

**Scanning Tunneling Spectroscopy Study of
Inhomogeneity, Granularity, & Segregation
in the Electronic Structure of
 $\text{Bi}_2\text{Sr}_2\text{CaCu}_2\text{O}_{8+d}$**

by

Kristine Michelle Lang

B.S. (Georgetown University) 1993
M.A. (University of California, Berkeley) 1998

A dissertation submitted in partial satisfaction of the
requirements for the degree of
Doctor of Philosophy

in

Physics

in the

GRADUATE DIVISION
of the
UNIVERSITY of CALIFORNIA at BERKELEY

Committee in charge:

Professor J.C. Séamus Davis, Chair
Professor Dung-Hai Lee
Professor Norman Phillips

Fall 2001

The dissertation of Kristine Michelle Lang is approved:

Chair Date

Date

Date

University of California at Berkeley

Fall 2001

Scanning Tunneling Spectroscopy Study of
Inhomogeneity, Granularity, & Segregation
in the Electronic Structure of
 $\text{Bi}_2\text{Sr}_2\text{CaCu}_2\text{O}_{8+\delta}$

Copyright Fall 2001
by
Kristine Michelle Lang

Abstract

Scanning Tunneling Spectroscopy Study of Inhomogeneity, Granularity, & Segregation in the Electronic Structure of $\text{Bi}_2\text{Sr}_2\text{CaCu}_2\text{O}_{8+\delta}$

by

Kristine Michelle Lang

Doctor of Philosophy in Physics

University of California, Berkeley

Professor J.C. Séamus Davis, Chair

After almost fifteen years of intensive study there is still no widely accepted fundamental theory of high temperature superconductivity (HTSC). There exists a wealth of experimental data which provides pieces of the puzzle. Many theories have been put forth as to how those pieces might fit together. But the theories and the experimental evidence have not come together in a cohesive picture of what makes these materials superconduct at such high temperatures. In this thesis I present experimental evidence which provides what may be definitive new pieces of the HTSC puzzle. Using a low temperature scanning tunneling microscope (STM), we studied the high temperature superconductor $\text{Bi}_2\text{Sr}_2\text{CaCu}_2\text{O}_{8+\delta}$. An STM is unique in that it provides real-space atomic-scale resolution imaging of both the positions of the atoms and the local electron density of states (LDOS). We have used this capacity of the STM to study in detail spatial variations in the local electronic structure of this material. In doing so, we find that the LDOS is inhomogeneous on a nanometer length scale. Such an observation was suggested by earlier work, which is reviewed in this thesis. However, the detailed studies

presented herein permit many additional and comprehensive observations. Essentially, the spatial variation of various properties of the LDOS is suggestive of discrete regions of distinct electronic structure which are termed *grains*. Further, it is found that the grains may be classified as one of two distinct types. This observation leads one to suggest that the electronic structure of BSCCO is not only *inhomogenous*, but is also *granular* and *segregated*. The objective of this thesis is to present as complete a description as possible of the phenomenology of inhomogeneity, granularity and segregation which we have observed by STM in the electronic structure of $\text{Bi}_2\text{Sr}_2\text{CaCu}_2\text{O}_{8+\delta}$.

A handwritten signature in black ink, reading "Seamus Davis". The signature is written in a cursive style with a large, sweeping initial 'S'.

Professor J.C. Séamus Davis
Dissertation Committee Chair

Acknowledgements

This thesis is dedicated to my parents- to my mother who kept me from 'spinning in' and to my father who kept me from going under. I cannot thank you enough for always being there for me. I am truly blessed to have such wonderful parents as you.

I would also like to thank and acknowledge my extended family who have spent so many happy times with me. Thank you especially to my brother and to Egin who have made me laugh through the years, to my Grandma and Grandpa Stanfield who provided such a wonderful retreat for me at the Lake House, and to my Grandma and Grandpa Lang who always made me feel so special.

I have also been blessed with supportive and loving friends who have shared the good times and the bad. To Corey, who always told me the truth even when I didn't want to hear it, I am so grateful for your loving support. For Eric who, with such patience taught me so much about physics and about life, I could not have hoped for a better teacher, mentor and friend. For Mia who shared so much heartache and laughter with me, I am so glad you came into my life when you did. To Kim and Becky, I so much appreciated and enjoyed the giggles and girl talk that we shared. To my study buddies, Robert and Robin, let's thank each other for pulling through 221! And to Robin, my companion in foreign adventures and my physics other half, I am so glad you are good at math! For Kamran who tried (unsuccessfully) to teach me to drink coffee and beer, wherever you are, I miss you here. And finally to Jen, thank you for margarita nights and barbecues on your deck, but mostly thank you for always being there for me.

I would be remiss if I didn't thank the wonderful staff of the physics department who fought the red tape, machined the parts, and processed the forms, and who were friends and teachers to me. To Abram Hardin, Paula Milano, Suzanne Pierce, Donna Sakima and Claudia Trujillo, who always cheerfully went above and beyond the call of duty to help me, thank you. To George Weber and John Davis, I so much appreciate your kind and patient tutoring in the ways of machining and electronics respectively. I am most especially grateful to Tom Pedersen, who always drilled a few extra holes in my parts 'to lighten them for me' and who never let me down when I needed advice, assistance or encouragement, and to Anne Takizawa, who was unfailingly kind and helpful in so many ways and who was always willing to lend a sympathetic ear.

Thanks goes as well to those who worked with me in my second graduate school activity-organizing SWPS. To Colette Patt, Annie Endozo, Susana Fernandez, Rupa Datta, and Jenny Hoffman, I appreciate all that you did to help make the organization a success.

I also wish to thank my professional colleagues. Hiroshi Eisaki and Shin-ichi Uchida provided the samples which I studied with the instrument built by Shuheng Pan and Eric Hudson. I appreciate very much the laughter and camaraderie I shared with my labmates: Andrew Schechter, Ray Simmonds, Sudeep Dutta, Joan Hoffmann, Jenny Hoffman, Kyle McElroy, Justin Mortara, Barry Barker, and Vidya Madhavan.

Finally, I would like to express my profound gratitude to my advisor, Seamus Davis, who challenged my intellect and my patience, who taught and inspired me, who appreciated my sometimes brutal honesty, and who always pushed me to become an ever better scientist, the results of which process are chronicled in these pages.

CURRICULUM VITAE

KRISTINE LANG

Department of Physics
University of California
Berkeley, CA 94720-7300

Phone: 510-643-4080
Fax: 510-643-8497
E-mail: kmlang@physics.berkeley.edu
<http://socrates.berkeley.edu/~kmlang>

Education:

Ph.D. Physics	University of California, Berkeley	Summer 2001
M.A. Physics	University of California, Berkeley	1998
B.S. International Affairs, Summa Cum Laude	Georgetown University, Washington, D.C.	1993

Experience:

Postdoctoral Researcher	J.C. Davis Group, Physics Department, U.C. Berkeley	Summer 2001- Feb 2002
Graduate Student Research Assistant	J.C. Davis Group, Physics Department, U.C. Berkeley	1996-2001
Coordinator and Founder	The Society for Women in the Physical Sciences, U.C. Berkeley	1997-2000
Research Assistant	Space Sciences Laboratory, Berkeley, CA	1995
Graduate Student Instructor	Physics Department, U.C. Berkeley	1994-1996
Office Manager	J.E. Austin Associates, Arlington, VA	1993-1994
Teaching Assistant	Physics Department, Georgetown University	1992-1994

Fellowships and Awards:

IBM Research Fellowship	IBM	1999-2001
Predocotrual Fellowship Award	Association for Women in Science	1999
Mentored Research Award	Graduate Division, U.C. Berkeley	1999-2000
Volunteer Service Award	Physics Department, U.C. Berkeley	1998 and 1999
Graduate Student Fellowship	National Science Foundation	1996-1999
Department of Education Graduate Student Fellowship	Physics Department, U.C. Berkeley	1994-1996
NASA Space Grant Summer Fellowship	Space Sciences Laboratory, Berkeley, CA	1995
Phi Beta Kappa	Georgetown University, Washington, D.C.	1992

Publications:

“Imaging the granular structure of high T_c superconductivity in underdoped $\text{Bi}_2\text{Sr}_2\text{CaCu}_2\text{O}_{8+\delta}$ ”, K.M. Lang, V. Madhavan, J.E. Hoffman, E.W. Hudson, H. Eisaki, S. Uchida, J.C. Davis. *To appear in Nature*.

“A four-unit cell periodic ‘checkerboard’ pattern of quasiparticle states surrounding vortex cores in $\text{Bi}_2\text{Sr}_2\text{CaCu}_2\text{O}_{8+\delta}$ ”, J.E. Hoffman, E.W. Hudson, K.M. Lang, V. Madhavan, H. Eisaki, S. Uchida, J.C. Davis. *To appear in Science*.

“Nanoscale one-dimensional scattering resonances in the CuO chains of $\text{YBa}_2\text{Cu}_3\text{O}_{6+x}$ ”, D.J. Derro, E.W. Hudson, K.M. Lang, S.H. Pan, J.C. Davis, J.T. Markert, A.L. de Lozanne. *To appear in Physical Review Letters*.

“Discovery of microscopic electronic inhomogeneity in the high- T_c superconductor $\text{Bi}_2\text{Sr}_2\text{CaCu}_2\text{O}_{8+x}$ ”, S.H. Pan, J.P. O’Neal, R.L. Badzey, C. Chamon, H. Ding, J.R. Engelbrecht, Z. Wang, H. Eisaki, S. Uchida, A.K. Gupta, K.-W. Ng, E.W. Hudson, K.M. Lang, J.C. Davis. *Nature* **413**, 282-285 (September 20, 2001).

“Interplay of magnetism and high- T_c superconductivity at individual Ni impurity atoms in $\text{Bi}_2\text{Sr}_2\text{CaCu}_2\text{O}_{8+\delta}$ ”, E.W. Hudson, K.M. Lang, V. Madhavan, S.H. Pan, H. Eisaki, S. Uchida, J.C. Davis. *Nature* **411**, 920-924 (June 21, 2001).

“Imaging the Effects of Individual Zinc Impurity Atoms on Superconductivity in $\text{Bi}_2\text{Sr}_2\text{CaCu}_2\text{O}_{8+\delta}$ ”, S.H. Pan, E.W. Hudson, K.M. Lang, H. Eisaki, S. Uchida, and J.C. Davis. *Nature* **403**, 746-750 (February 17, 2000).

Publications (cont.):

“A Detailed Scanning Tunneling Microscopy Study of the CuO Chains of $\text{YBa}_2\text{Cu}_3\text{O}_{7-\delta}$ ”, D.J. Derro, E.W. Hudson, K.M. Lang, S.H. Pan, J.C. Davis, K. Mochizuki, J.T. Markert, A. de Lozanne. *Physica C*, **341-348**, 425-428 (2000).

“STM of Quasiparticle Scattering Resonances in $\text{Bi}_2\text{Sr}_2\text{CaCu}_2\text{O}_{8+\delta}$ ”, E.W. Hudson, S.H. Pan, K.M. Lang, A.K. Gupta, K.-W. Ng, J.C. Davis. *Physica B*, **284-288**, p.969-970 (2000).

“Search for Superconductivity in Li.”, K.M. Lang, Ari Mizel, J. Mortara, E. Hudson, J. Hone, Marvin L. Cohen, A. Zettl, J.C. Davis. *Journal of Low Temperature Physics*, **114**, (No.5-6), p.445-54 (1999).

Presentations:

“An Electronic Nano-Mosaic in $\text{Bi}_2\text{Sr}_2\text{CaCu}_2\text{O}_{8+\delta}$: Evidence for Granular High- T_c Superconductivity?”
Special Seminar, Sandia National Laboratory, Livermore, August 2001.

“Electronic Nano-Domains and Granular Superconductivity in Underdoped $\text{Bi}_2\text{Sr}_2\text{CaCu}_2\text{O}_{8+\delta}$.”
Invited Talk, Aspen Center for Physics, Workshop on Emergent Behavior in Correlated Electron Materials, Aspen, July 2001.

“An Electronic Nano-Mosaic in $\text{Bi}_2\text{Sr}_2\text{CaCu}_2\text{O}_{8+\delta}$: Evidence for Granular High- T_c Superconductivity?”
Contributed Poster, Eleventh International Conference on Scanning Tunneling Microscopy/Spectroscopy and Related Techniques, Vancouver, July 2001.

“Electronic Nano-Domains and Granular Superconductivity in Underdoped $\text{Bi}_2\text{Sr}_2\text{CaCu}_2\text{O}_{8+\delta}$.”
Special Seminar, National Institute of Standards and Technology, Boulder, June 2001.

“Electronic Nano-Domains and Granular Superconductivity in Underdoped $\text{Bi}_2\text{Sr}_2\text{CaCu}_2\text{O}_{8+\delta}$.”
Condensed Matter Seminar, Los Alamos National Laboratory, June 2001.

“Nanometer Scale Spatial Variations in the Local Density of States of Underdoped BSCCO as Revealed by Low Temperature Scanning Tunneling Spectroscopy.”
Contributed Talk, APS March Meeting, Seattle, March 2001.

“Spatial Variations in the Superconducting Order Parameter of $\text{Bi}_2\text{Sr}_2\text{CaCu}_2\text{O}_{8+\delta}$ as Revealed by Low Temperature Scanning Tunneling Spectroscopy.”
Contributed Talk, Conference on New Theories, Discoveries, and Applications of Superconductors and Related Materials, Honolulu, January 2001.

Presentations (cont.):

“Ripples in a Still Pond: Imaging Single Atom Perturbations to High T_c Superconductivity.”

Condensed Matter Seminar, U.C. Davis Physics Department, June 2000.

“The Society for Women in the Physical Sciences: a Successful Mentoring Program at U.C. Berkeley.”

Invited Talk, APS April Meeting, Long Beach, April 2000.

“Spatial Variations in the Superconducting Order Parameter of $\text{Bi}_2\text{Sr}_2\text{CaCu}_2\text{O}_{8+\delta}$ as Revealed by Low Temperature Scanning Tunneling Spectroscopy.”

Contributed Talk, APS March Meeting, Minneapolis, March 2000.

“Scanning Tunneling Microscopy Study of Individual Ni and Zn Impurities in $\text{Bi}_2\text{Sr}_2\text{CaCu}_2\text{O}_{8+\delta}$.”

Contributed Talk, APS March Meeting, Minneapolis, March 2000.

“Imaging Single Atom Impurity Scattering in Doped $\text{Bi}_2\text{Sr}_2\text{CaCu}_2\text{O}_{8+\delta}$.”

Contributed Poster, 6th International Conference on Materials and Mechanisms of Superconductivity and High-Temperature Superconductors, Houston, February 2000.

“Mentoring Undergraduate Women in Physics: a Successful Program at U.C. Berkeley.”

Physics Departmental Colloquium, University of Nevada, Reno, September 1999.

“Mentoring Undergraduate Women in Physics: a Successful Program at U.C. Berkeley.”

Contributed Talk, APS March Meeting, Atlanta, March 1999.

“Search for Superconductivity in Li.”

Contributed Talk, APS March Meeting, Los Angeles, March 1998.

Community Service:

Society for Women in the Physical Sciences (SWPS), Founder and Coordinator, U. C. Berkeley, Fall 1997-Fall 2000.

SWPS sponsors monthly activities for women in the physical science departments at Berkeley. Past events have included discussion forums, socials, and workshops. SWPS also organizes a mentoring program which pairs 4-5 undergraduate women with a graduate student mentor. There are currently about 60 undergraduate women mentees in 13 mentoring groups. As coordinator I managed the mentoring program and organized all the events. For more details see the group’s website: <http://socrates.berkeley.edu/~swps>.

Table of Contents

PREAMBLE MOTIVATION, OBJECTIVE, & ORGANIZATION	1
P.1 The Puzzle of High-T_c Superconductivity	1
P.2 New Pieces for the HTSC Puzzle	2
P.3 Organization of this Thesis	3
P.4 Clarification of Nomenclature	4
P.4.1 Definition of Inhomogeneity, Granularity and Segregation	4
P.4.2 Pointillist Paintings: An Analogy for Understanding Inhomogeneity, Granularity and Segregation	4
CHAPTER 1 INTRODUCTION TO THE TECHNIQUE AND MATERIAL: SCANNING TUNNELING MICROSCOPY AND $\text{Bi}_2\text{Sr}_2\text{CaCu}_2\text{O}_{8+d}$	7
1.1 Fundamentals of the Operation of a Scanning Tunneling Microscope	7
1.2 Theory of Scanning Tunneling Microscopy	8
1.2.1 Tunneling Current Equation	8
1.2.2 Tunneling Matrix Element.....	9
1.3 A Brief Description of the STM System Used in this Study	10
1.4 A Few Remarks on $\text{Bi}_2\text{Sr}_2\text{CaCu}_2\text{O}_{8+d}$	10
1.4.1 Crystal Structure of $\text{Bi}_2\text{Sr}_2\text{CaCu}_2\text{O}_{8+\delta}$	11
1.4.2 Samples, Sample Preparation, and Cleavage Planes.....	11
1.5 Topographic Imaging with an STM	12
1.5.1 Topographic Scanning: Two Modes and Method.....	12
1.5.2 Typical Topography on $\text{Bi}_2\text{Sr}_2\text{CaCu}_2\text{O}_{8+\delta}$	13
1.6 Scanning Tunneling Spectroscopy	13
1.6.2 Practice of Scanning Tunneling Spectroscopy	14
1.6.3 Schematic for Understanding Spectroscopy	15
1.7 Spectroscopic Imaging with an STM	15
1.7.1 Spectral-Surveys	16
1.7.2 Spectrum.....	16
1.7.3 Linecut.....	16
1.7.4 Differential Conductance Map	17
1.8 Definition of Spectral Parameters	17
1.8.1 Definition of Δ	17
1.8.2 Definition of $A(\Delta)$	18
1.8.3 Definition of $\Sigma(V_a, V_b)$ and $\Sigma(\Delta)$	18
1.9 Parameter Maps	19
1.9.1 Δ , $A(\Delta)$, and Σ maps	19
1.9.2 Gradient Maps	19

1.10 A Discussion of the Relation Between Differential Conductance and LDOS	20
1.10.1 Origin of Variations in the Tip-Sample Separation Under Constant Current Normalization	20
1.10.2 Implications of Variations in the Tip-Sample Separation for Topography	21
1.10.3 Magnitude of Variations in the Tip-Sample Separation.....	22
1.10.4 Magnitude of Variations in the dI/dV-LDOS Proportionality Factor	22
1.10.5 Effect of Variations in the Tip-Sample Separation on Spectral Characteristics.....	23
1.11 Surface vs. Bulk Local Density of States.....	26
Chapter 1 Figures	27-62
CHAPTER 2 CATALOG OF DATA.....	63
2.1 Overview of the Data Presented in This Thesis.....	63
2.2 Description of The Data Catalog	65
2.2.1 Organization of the Data Catalog.....	65
2.2.2 Color Scales, Error in Sizes, Spatial Resolution, and Bad Pixels	65
2.2.3 Overview Maps and Histograms.....	66
2.2.4 Detail Maps.....	67
2.2.5 Linecuts.....	67
2.2.6 Summary of Spatial Interrelationships For Run 159 Data	68
Chapter 2 Figures	69-114
CHAPTER 3 INHOMOGENEITY IN THE ELECTRONIC STRUCTURE OF	
Bi₂Sr₂CaCu₂O_{8+d}	115
General Comments About the Data Presented in This Chapter	115
3.1 Linecuts Illustrating LDOS Spatial Inhomogeneity	116
3.1.1 Summary.....	117
3.2 Spatial Variation of D	118
3.2.1 Maps of Δ	118
3.2.2 Histograms of Δ	119
3.2.3 Summary.....	120
3.3 Diversity of Spectral Shapes	120
3.3.1 Representative Selected Spectra	120
3.3.2 Representative Average Spectra	121
3.3.3 Summary.....	122
3.4 Spatial Variation of A(D) and S.....	122
3.4.1 Interpretation of A(Δ) and Σ	122
3.4.2 Maps of A(Δ) and $\Sigma(\Delta)$	124
3.4.4 Maps of $\Sigma(\leq\Delta)$	126
3.4.5 A(Δ) and Σ at Positive vs. Negative Bias.....	126
3.4.6 Summary.....	127
3.5 Summary and Looking Ahead.....	127
Chapter 3 Figures	129-164

**CHAPTER 4 LITERATURE REVIEW: SCANNING TUNNELING
MICROSCOPY STUDIES OF INHOMOGENEITY IN $\text{Bi}_2\text{Sr}_2\text{CaCu}_2\text{O}_{8+d}$ 165**

4.1 Observation of Inhomogeneity by Topography and Non-Spatially Registered Spectroscopy 165

4.1.1 Coleman Group..... 165

4.1.2 Lieber Group 166

4.1.3 Goldman Group 167

4.2 Observation of Inhomogeneity by Spatially Registered Spectroscopy..... 167

4.2.1 Wolf Group..... 167

4.2.2 Nishida Group 169

4.2.3 Klein Group 169

4.2.4 Kapitulnik Group..... 170

4.3 Observation of Homogeneity in Recently Annealed Crystals 171

4.3.1 Lieber Group 171

4.3.2 Fischer Group 171

4.3.3 Discussion of the Lieber and Fischer Observations..... 172

4.4 Summary 173

Chapter 4 Figures 177-186

**CHAPTER 5 GRANULARITY AND SEGREGATION IN THE ELECTRONIC
STRUCTURE OF UNDERDOPED $\text{Bi}_2\text{Sr}_2\text{CaCu}_2\text{O}_{8+d}$ 187**

Rationale for Studying Underdoped Samples..... 187

General Comments About the Data Presented in This Chapter 188

5.1 Linecuts Illustrating Granularity and Segregation 189

5.1.1 Existence of Grains..... 189

5.1.2 Existence of Segregation 189

 An Analogy for Understanding Segregation..... 190

 Distinguishing Grains by the Value of D..... 190

 Distinguishing Grains by the Value and Spatial Variability of A(D)..... 191

 Distinguishing Grains by the Spatial Variability of D 191

 Distinguishing Grains by Spectral Shape 192

5.1.3 Boundaries Between the Grains..... 192

5.2 Maps Demonstrating Granularity and Segregation 194

5.2.1 Gapmap on Large Field of View 194

5.2.2 High Spatial Resolution Maps on Small Field of View..... 195

 D-map 195

$|\tilde{N} D|$ -map..... 195

 A(D)-map..... 195

$|\tilde{N} A(D)|$ -map 196

 S-map 196

 Analogous Set of Images..... 196

5.3 Quantifying the Properties of the α- and β- regions	196
5.3.1 Size of the α -Domains	197
5.3.2 Separation of the α -Domains	197
5.3.3 Characteristics of the α -Domains and β -Regions	198
5.4 Conclusion	199
5.4.1 Summary of α , β , γ Region Characteristics	199
5.4.2 A Few Concluding Remarks on the Observation of Inhomogeneity, Granularity & Segregation	200
Chapter 5 Figures	201-236
CHAPTER 6 ORIGIN AND SIGNIFICANCE OF INHOMOGENEITY, GRANULARITY, AND SEGREGATION	237
A Comment on the Basis for the Discussion in this Chapter	237
6.1 A Brief and Selected Discussion of the Current State of Knowledge in HTSC	237
6.1.1 Phenomenology as a Function of Doping	238
6.1.2 Phenomenology as a Function of Temperature	239
6.1.3 Papers Addressing Inhomogeneity, Granularity and/or Segregation	240
6.2 Origin of Inhomogeneity	242
6.2.1 Definition of Local Doping Level	242
6.2.2 Global Causality Implies Local Causality	243
6.2.3 Comparison of Global and Local Spectral Shapes	244
6.3 Origin of Granularity	244
6.3.1 Origin of Non-Uniform Local Hole Distribution	245
6.3.2 Non-Uniform Hole Distribution Implies Granularity	246
6.4 Origin of Segregation	247
6.5 Implications for Segregation	247
6.6 Summary	248
Chapter 6 Figures	251-266
CONCLUSION	267

APPENDIX 1	PEAK PICKING ALGORITHM	269
A.1	Description of the Peak Picking Algorithm With Examples	269
A.2	Dealing With Spectra Which Have No Peaks Out To the Highest Measured Energy	270
A.3	Estimate of the Error in the Value of D Chosen by the Peak Picking Algorithm.....	271
Appendix 1	Figures.....	273-282
APPENDIX 2	DATA ACQUISITION PARAMETERS	283
BIBLIOGRAPHY	285
GLOSSARY	293

List of Figures

PREAMBLE MOTIVATION, OBJECTIVE, & ORGANIZATION

P.1: Analogy to Understand Inhomogeneity, Granularity and Segregation -- La Grande Jatte by Georges Seurat	5
---	---

CHAPTER 1 INTRODUCTION TO THE TECHNIQUE AND MATERIAL: SCANNING TUNNELING MICROSCOPY AND $\text{Bi}_2\text{Sr}_2\text{CaCu}_2\text{O}_{8+d}$

1.1: Fundamental components of an STM.....	27
1.2: Current dependence and spatial coordinate definitions for a scanned STM tip.....	29
1.3: Schematic of tunneling from sample to tip.....	31
1.4: Schematic of the STM and cryostat.....	33
1.5: Diagram of the STM proper	35
1.6: Structure of $\text{Bi}_2\text{Sr}_2\text{CaCu}_2\text{O}_{8+\delta}$	37
1.7: STM feedback and data acquisition system.....	39
1.8: Constant current topographic mapping.....	41
1.9: Typical topography on the BiO surface of $\text{Bi}_2\text{Sr}_2\text{CaCu}_2\text{O}_{8+\delta}$	43
1.10: Schematic illustrating scanning tunneling spectroscopy	45
1.11: Technique for making a direct measurement of dI/dV	47
1.12: Data-sets which can taken with an STM	49
1.13: BSCCO spectra illustrating parameter definitions.....	51
1.14: Example of parameter maps from BSCCO	53
1.15: Fourier filtering the topography to find the relative variations in tip-sample separation	55
1.16: Measurement of s_0 - the current decay length-scale for tip withdrawal.....	57
1.17: Trend in $A(\Delta)$ as a function of tip-sample separation.....	59
1.18: Trend in $\Sigma(\Delta)$ as a function of tip-sample separation	61

CHAPTER 2 CATALOG OF DATA

2.1: Overview maps on as-grown oxygen doped BSCCO with approximately 0.6 % Zn impurities	71
2.2: Overview maps on as-grown oxygen doped BSCCO with 0.5% Ni impurities	73
2.3 - 2.5: Overview maps on oxygen underdoped BSCCO with no intentional impurities	75 - 79
2.6 - 2.10: Detail maps on oxygen underdoped BSCCO with no intentional impurities	83 - 91
2.11 - 2.12: Linecut & topo on BSCCO with as-grown oxygen doping and 0.6 % Znimps.....	95 - 97
2.13 -2.14: Linecut and topo on BSCCO with as-grown oxygen doping and 0.5 % Niimps.....	99 - 101
2.15 - 2.17: Linecut and topo on oxygen underdoped BSCCO with no intentionalimps.....	103 - 107
2.18: Interrelationships of the maps and linecuts which were taken in run 159 on oxygen underdoped BSCCO with no intentional impurities.....	111
2.19: Repeat of Figure 2.10 to show trajectories of the linecuts 01108c and 01109c	113

List of Figures

CHAPTER 3 INHOMOGENEITY IN THE ELECTRONIC STRUCTURE OF $\text{Bi}_2\text{Sr}_2\text{CaCu}_2\text{O}_{8+d}$

3.1: Extrinsic sources of disorder in high temperature superconductors: impurities, twin boundaries, and crystal defects	129
3.2: Linecut illustrating LDOS spatial inhomogeneity in BSCCO with as-grown oxygen doping.....	131
3.3: Linecut illustrating distinct Δ domains in BSCCO with as-grown oxygen doping.....	133
3.4: Linecut illustrating distinct Δ domains in underdoped BSCCO	135
3.5: Linecut illustrating spatial variation in $A(\Delta)$ in underdoped BSCCO	137
3.6: Gapmaps approximately 550 \AA square in size from two samples with different oxygen doping levels.....	139
3.7: Histograms of Δ from regions approximately 550 \AA square in size from two samples with different oxygen doping levels	141
3.8: Representative set of selected spectra which illustrate the variety of observed spectral shapes.....	143
3.9: Spectrum representative of type with no distinct peaks.....	145
3.10: Average spectra as a function of Δ	147
3.11: Standard deviation from the Δ -binned average spectra.....	149
3.12: Correlation of $\Sigma(\Delta)$ with spectral shape.....	151
3.13: $A(\Delta)$ maps approximately 550 \AA square in size from two samples with different oxygen doping levels.....	153
3.14: $\Sigma(\Delta)$ maps approximately 550 \AA square in size from two samples with different oxygen doping levels.....	155
3.15: Trends in average $A(\Delta)$ and $\Sigma(\Delta)$ vs. Δ from two samples with different oxygen doping levels.....	157
3.16: Trends in the standard deviation from the mean $A(\Delta)$ and $\Sigma(\Delta)$ vs. Δ from two samples with different oxygen doping levels.....	159
3.17: $\Sigma(\leq\Delta)$ maps approximately 550 \AA square in size from two samples with different oxygen doping levels.....	161
3.18: Compare $\Sigma(\Delta_+)/N_+$ to $\Sigma(\Delta_-)/N_-$ maps from two samples with different oxygen doping levels	163

List of Figures

CHAPTER 4 LITERATURE REVIEW- SCANNING TUNNELING MICROSCOPY STUDIES OF INHOMOGENEITY IN $\text{Bi}_2\text{Sr}_2\text{CaCu}_2\text{O}_{8+d}$

4.1: Linecut from the Wolf Group illustrating correlated spatial variation in Δ , $A(\Delta)$, and spectral shape	177
4.2: Spectra from the Nishida group which illustrate the three distinct spectral types observed	179
4.3: Spectra and linecut from the Klein group illustrating two observed spectral types and the transition between them	181
4.4: Gapmap and spectra from the Kapitulnik group illustrating the spatial variations in Δ and the two observed extremal spectral types	183
4.5: Data from the Fischer group showing spatially homogeneous spectroscopy	185

CHAPTER 5 GRANULARITY AND SEGREGATION IN THE ELECTRONIC STRUCTURE OF UNDERDOPED $\text{Bi}_2\text{Sr}_2\text{CaCu}_2\text{O}_{8+d}$

5.1: Linecut illustrating the observation of granularity in underdoped BSCCO	201
5.2: Linecut illustrating the behavior of Δ and $A(\Delta)$ in α - and β - grains	203
5.3: Second linecut illustrating the behavior of Δ and $A(\Delta)$ in α - and β - grains	205
5.4: Linecut illustrating the spatial variability of Δ in α - and β - grains	207
5.5: Linecut illustrating the border regions which exist between grains	209
5.6: Large field of view gapmap and histogram on underdoped BSCCO	211
5.7: High resolution maps of multiple spectral parameters on a small field of view	213
5.8: Set of Δ & $A(\Delta)$ traces and a linecut which correlate with the maps of the previous small field of view	215
5.9: Second large field of view gapmap and histogram on underdoped BSCCO	217
5.10: Set of high resolution maps of multiple spectral parameters on a second small field of view	219
5.11: Set of Δ & $A(\Delta)$ traces and a linecut which correlate with the maps of the second small field of view	221
5.12: Two-point correlation of a gapmap	223
5.13: Δ - and $A(\Delta)$ -maps with α -domains indicated	225
5.14: Δ - and $A(\Delta)$ -maps with β -regions indicated	227
5.15: Histogram of Δ values for α -domains, β -regions, and all regions	229
5.16: Representative α , β , and γ spectra	231
5.17: Linecut showing color coded α , β , and γ regions	233
5.18: Second linecut showing color coded α , β , and γ regions	235

List of Figures

CHAPTER 6 ORIGIN AND SIGNIFICANCE OF INHOMOGENEITY, GRANULARITY, AND SEGREGATION

6.1: High temperature superconductivity phase diagram.....	251
6.2: Trend in the spatially averaged value of Δ as a function of oxygen-doping	253
6.3: Trend in the spatially averaged value of $A(\Delta)$ as a function of oxygen-doping.....	255
6.4: Schematic illustrating the proposed relationship between local oxygen doping and local spectral properties	257
6.5: Trend in the spectral shape as a function of doping- local vs. global measurements.....	259
6.6: Schematic showing local oxygen atom distribution and proposed resulting local hole distribution	261
6.7: Schematic illustrating stripe ordering	263
6.8: Schematic illustrating how LDOS granularity can arise from a clustered distribution of holes	265

APPENDIX 1 PEAK PICKING ALGORITHM

A.1: Selected spectra for illustration of the peak picking algorithm.....	273
A.2: Detailed illustration of algorithm using single spectrum	275
A.3: Additional example spectra to demonstrate general functionality of algorithm	277
A.4: Spectrum with no peaks to highest measured energy	279
A.5: Parameter maps showing a patch of NP type spectra.....	281

List of Tables

2.1: Summary of Runs and Samples for Data Presented in this Thesis	64
2.2: Format of Data Filenames	64
4.1: Summary of STM observation of LDOS spatial variation	175
5.1: Summary of α - and β - region characteristics	199
5.2: Summary of γ - boundary region characteristics	199

Preamble

Motivation, Objective, & Organization

P.1 The Puzzle of High- T_c Superconductivity

Superconductivity was discovered in 1911 by H. Kamerlingh Onnes in mercury [Onnes 1911]. Subsequent decades of research into this phenomenon led to the discovery of a variety of new superconducting materials and to the development of a microscopic theory of the mechanism of *conventional superconductivity*, the BCS theory [Bardeen 1957]. Conventional superconductors have been used in a variety of practical applications such as high field magnets and SQUIDS, and many further potential applications have been envisioned. However, the utility of conventional superconductors has been limited by their low critical temperatures (T_c) which necessitate that they be cooled with great expense, usually by liquid helium, in order to exhibit superconductivity. By 1971 a superconductor had been produced with a T_c of 23 K; however, despite enormous efforts to produce a material with a higher critical temperature, there was no success. Many scientists believed that T_c could not be further increased^{1,2}.

Despite the widespread belief that T_c would forever remain near 20 K, some groups continued to look for superconductivity in new materials. In 1986 such efforts paid off for Bednorz and Müller who announced the discovery of superconductivity above 30 K in a new class of materials, the copper oxides [Bednorz 1986]. This discovery sparked a frenzy of research to find new compounds of this class with even higher T_c , as well as to map the phenomenology of the materials, and to develop a theoretical understanding of the mechanism of *high temperature superconductivity (HTSC)*³.

In the last fifteen years, intense study of high temperature superconductivity has produced a tremendous body of knowledge, and yet, to date a complete picture of this phenomenon has not emerged. In analogy to a child's jigsaw puzzle, it is as though we possess many of the pieces of the HTSC puzzle. Some of those pieces have even been fit together to produce small bits of the overall picture. A grasp of the whole picture seems tantalizingly close at hand. And yet, the puzzle remains disassembled and the image recorded in its pieces is still unknown.

¹ Even since the discovery of high temperature superconductivity, many scientists still did not believe that there could be a conventional superconductor with a substantially higher T_c . However, very recently quite a stir was created when what is believed to be conventional superconductivity was discovered in the compound MgB_2 at 39 K [Nagamatsu 2001].

² For nice review of the early history of high temperature superconductors see Chapter 13 of Simon 1988.

³ Two books each of which presents an excellent qualitative introduction to the phenomenology, theory, and history of superconductivity are by Simon & Smith [1988] and Ginzburg & Andryushin [1994].

It is then the enduring mystery of high temperature superconductivity which provides the motivation for the studies presented in this thesis. In particular, the goal of the experiments presented herein is to provide definitive new pieces of the puzzle.

P.2 New Pieces for the HTSC Puzzle

This thesis presents scanning tunneling microscopy studies of the high temperature superconductor $\text{Bi}_2\text{Sr}_2\text{CaCu}_2\text{O}_{8+\delta}$. With its unique viewpoint, scanning tunneling microscopy (STM) provides a wealth of new information which can help fill in the picture of HTSC. Such a viewpoint derives from three distinct aspects of STM. First, STM produces images in real space (as opposed to k-space), so that non-periodic structures can be studied. Second, STM can take such real space images with sub-Å spatial resolution. Finally, the distinctive advantage of STM derives from its ability to image not just the position of the atoms, but also the local density of states. Atomic length-scale real-space images of the local density of states are the unique viewpoint provided by the technique of scanning tunneling microscopy.

High temperature superconductors have been studied by scanning tunneling microscopy almost since they were discovered, and many illuminating STM studies of the HTSC BSCCO are reviewed in this thesis. However, such studies have been limited by the significant challenge of achieving long term spatial stability of the lateral location of the tip with respect to the sample. In order to study detailed spatial variations in the local density of states, one must be able to take thousands of spatially registered spectra with high spatial resolution over a large area. Such data-sets, which have been termed *spectral-surveys* in this thesis, can take days to acquire, and so extreme spatial stability is necessary to preserve the spatial interrelationship of spectra taken throughout the acquisition. The STM used to take the data presented in this thesis is one of the first in the world to achieve such spatial stability⁴ and consequently the spectral-surveys presented in this thesis are among the first of their kind.

The new and original results presented in this thesis originate from spectral-surveys taken on several different BSCCO samples. Using these maps, an analysis of the electronic structure of BSCCO has revealed that this material is spatially inhomogeneous. Such an observation was suggested by earlier work⁵. However, the detailed studies presented herein permit additional observations. Essentially, the spatial variation of various properties of the electronic structure is suggestive of discrete regions of distinct electronic structure which are termed *grains*. Further, it is found that the grains may be classified as one of two distinct types. This observation leads one to suggest that BSCCO is not only *inhomogeneous*, but is also *granular* and *segregated*. These observations constitute the new and original scientific contribution presented in this thesis.

⁴ This STM was developed by S.H. Pan and E.W. Hudson in the group of J.C. Séamus Davis at U.C. Berkeley. Some particulars of the instrument are discussed in Section 1.3 and further information can be found in the following references: Pan 1999, Hudson 1999.

⁵ This work is reviewed in Chapter 4.

P.3 Organization of this Thesis

The objective of this thesis is to present as complete a description as possible of the phenomenology of *inhomogeneity, granularity and segregation* which we have observed by STM in the electronic structure of $\text{Bi}_2\text{Sr}_2\text{CaCu}_2\text{O}_{8+d}$. This description is contained in the three data chapters, Chapters 2, 3, and 5. In addition, background and contextual information is presented in Chapters 1, 4, and 6. A more complete description of the chapters is as follows:

Chapter 1: Provides background for both the technique, STM, and the material studied, $\text{Bi}_2\text{Sr}_2\text{CaCu}_2\text{O}_{8+\delta}$.

- discussion of the fundamentals of scanning tunneling microscopy (STM) and spectroscopy (STS)
- BSCCO crystal structure and sample preparation
- short description of the STM used in these studies
- description of the types of data-sets which can be obtained via STM and STS
- relationship of STS data to the local density of states (LDOS)

Chapter 2: Presents a catalog of our data displayed in a uniform manner.

- large field of view *overview* maps
- small field of view *detail* maps
- linecuts

Chapter 3: Discusses the existence and phenomenology of the spatial *inhomogeneity* observed by us in the electronic structure of BSCCO.

- illustrative linecuts
- spatial variations in the gap and magnitude of the gap-edge peak
- spectra representative of the observed inhomogeneity

Chapter 4: Provides an overview of spatial inhomogeneity in BSCCO as observed in STM measurements made by other groups.

- early observations by topography and scattered spectra
- later observations by spatially resolved spectroscopic imaging
- role of annealing

Chapter 5: Demonstrates the existence of both *granularity* and *segregation* as observed by us in the electronic structure of underdoped BSCCO.

- demonstration of both granularity and segregation using both illustrative linecuts and parameters maps
- definition and quantification of the properties of the two distinct types of grains

Chapter 6: Discusses the context, origin, and significance of the observations

- background to high temperature superconductivity
- discussion of possibilities for the origin and significance of inhomogeneity, granularity and segregation

P.4 Clarification of Nomenclature

As stressed above, the objective of this thesis is to present as complete a description as possible of the phenomenology of the *inhomogeneity*, *granularity* and *segregation* which we have observed by STM in the electronic structure of $\text{Bi}_2\text{Sr}_2\text{CaCu}_2\text{O}_{8+\delta}$. Given the ubiquity and importance of these three terms in this thesis, I would like to present here a brief discussion of them. I will first carefully define each term and will then subsequently present an analogy for understanding these definitions.

P.4.1 Definition of Inhomogeneity, Granularity and Segregation

Inhomogeneity in the LDOS is defined as the existence of spatial variation in spectral parameters such as the energy gap and the height of the gap-edge peak.

Granularity in the LDOS is defined as inhomogeneity, plus the existence of regions within which the spectral parameters exhibit a common set of characteristics, which are distinct from the characteristics exhibited by neighboring regions⁶. The distinct regions are termed *grains*.

Segregation in the LDOS is defined as inhomogeneity and granularity, plus the existence of a finite number of distinct grain-types such that each observed grain may be classified as one of these types.

P.4.2 Pointillist Paintings: An Analogy for Understanding Inhomogeneity, Granularity and Segregation

If you have ever been to the Art Institute of Chicago (or even if you have not) you may remember the famous pointillist painting by Georges Seurat called *La Grande Jatte*. To refresh your memory, this painting is reproduced in Figure P.1. Recall that in a pointillist painting the image is created by applying small strokes or dots of color to a surface so that from a distance they blend together to make the picture. This type of painting provides an analogy for understanding the three terms which are being defined in this section. In this comparison, brushstroke and paint color are analogous to the local density of states.

⁶ Note that *granularity* should not be taken as synonymous to *granular superconductivity*. While the latter implies something about the nature of the distinct regions (namely that one is superconducting and the other is not), the former merely describes the structure of the electronic local density of states with no implications as to the nature of the distinct regions.

In this analogy then...

a *homogeneous* painting would consist of a perfectly uniform covering by a single color of paint on the canvas.

an *inhomogeneous* painting would consist of a textured covering of the canvas, such that some variation is observed, but still by a single color of paint.

a *granular* painting would consist of a covering of the canvas with little dots (grains) of a single color of paint.

a *segregated* painting would consist of a covering of the canvas with little dots of paint in which each dot was a distinct and classifiable color. This is exemplified in the Seurat pointillist painting seen below.

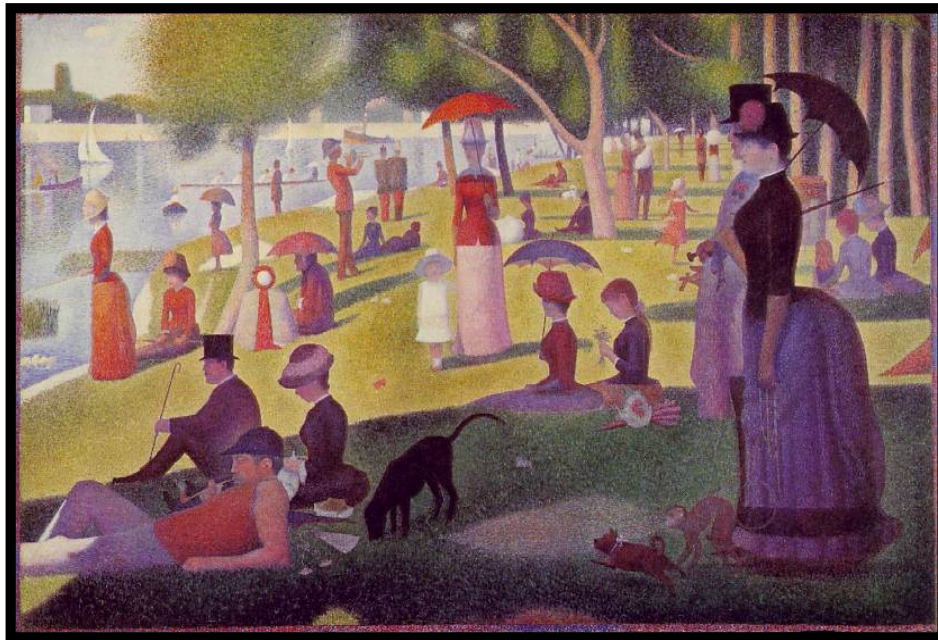


Figure P.1: Analogy to Understand Inhomogeneity, Granularity and Segregation: La Grande Jatte by Georges Seurat.

Chapter 1

Introduction to the Technique and Material: Scanning Tunneling Microscopy and $\text{Bi}_2\text{Sr}_2\text{CaCu}_2\text{O}_{8+d}$

All the results presented in this thesis were obtained on $\text{Bi}_2\text{Sr}_2\text{CaCu}_2\text{O}_{8+\delta}$ single crystals which were cleaved in cryogenic-UHV and subsequently studied in vacuum at 4.2 K using a scanning tunneling microscope (STM)⁷. The purpose of this chapter is to provide background information for both the technique, STM, and the material, $\text{Bi}_2\text{Sr}_2\text{CaCu}_2\text{O}_{8+\delta}$.

As an introduction to STM, I will present an explanation and some basic theory of the operation of this instrument. In addition I will make some brief comments on the particular system that was used to take the data presented herein. However, the focus in this chapter will be on the types of measurements which can be made with an STM, and on appropriate analysis and interpretation of those measurements.

Throughout the chapter I illustrate the STM techniques presented with typical examples obtained on BSCCO. This illustration, together with a brief discussion of some of the most important properties of BSCCO, will serve as an introduction to this material.

1.1 Fundamentals of the Operation of a Scanning Tunneling Microscope

For all the wealth of information which can be obtained with an STM, it is in principle a remarkably simple instrument. The basic principle of operation of an STM is shown in the schematic in Figure 1.1. Essentially, a sharp wire, which is commonly referred to as the tip⁸, is brought within a few angstroms of the sample surface. A bias voltage⁹ is applied between the tip and the sample¹⁰ and a current flows by tunneling through the vacuum gap that separates them. The current signal is amplified and subsequently recorded.

The amount of current that flows between the tip and sample depends on a number of factors. First, it depends on the magnitude of the applied bias voltage (V). Second, it depends on the distance between the tip and the sample surface (s). And finally, it depends on the *local* density of electronic states (LDOS) both of the tip and of the region of the sample directly beneath the tip.¹¹

⁷ See Appendix 2 for a complete description of the data acquisition parameters.

⁸ All data in this thesis were taken with an etched tungsten tip which was cleaned in situ by field emission.

⁹ All data in this thesis were taken with the tip at a virtual ground and the sample at a finite bias, and thus all data in this thesis is given in terms of sample bias. Recall that, negative sample bias probes filled sample states and positive sample probes empty sample states.

¹⁰ Both the tip and sample must be conducting materials.

¹¹ In practice, the DOS of the metallic tip is a constant with respect to energy within the narrow range of energies we consider, and thus the important dependence of the current is on the *sample* LDOS.

The real power of STM therefore derives from the ability to measure the current, and thus to measure both the LDOS and the vertical displacement of the sample, as the tip is scanned across the sample surface. This ability is depicted in the schematic presented in Figure 1.2. In this schematic regions with different LDOS are represented in different colors. First, notice that for tip x-positions 1,2, and 3, which are all above the “green” LDOS region, different values of the current are recorded depending on s , the separation between the tip and the sample surface. Second, notice that for constant s , different values of the current are recorded for tip x-positions 3 and 4 which are in the green and red LDOS regions respectively.

1.2 Theory of Scanning Tunneling Microscopy

1.2.1 Tunneling Current Equation

A simple model for determining the analytic dependence of the current on the three parameters, V , s , and LDOS, is given in the tunneling theory which was first proposed by Bardeen [1960] and later applied to STM by Tersoff and Hamann [Tersoff 1983, Tersoff 1985]. In this model of tunneling, the tip and sample are treated as two separate systems whose wave functions slightly overlap. Perturbation theory can then be used to determine the rate of electron transfer between the systems. Assuming that any electron which tunnels does not change its energy so that energy is conserved in the tunneling process (elastic tunneling), then the current is given by the following equation:

$$\begin{aligned}
 I &= I_{sample \rightarrow tip} - I_{tip \rightarrow sample} \\
 &= \frac{4\pi e}{\hbar} \int_{-\infty}^{\infty} |M|^2 \mathbf{r}_s(x, y, E_s) \mathbf{r}_t(E_t) \{f(E_s)[1 - f(E_t)] - f(E_t)[1 - f(E_s)]\} d\mathbf{e}
 \end{aligned} \tag{1.1}$$

where e is the electron charge, \hbar is Planck’s constant over 2π , $|M|$ is the tunneling matrix element, and ρ is the local density of states for either the sample (s) or the tip (t). The Fermi function, $f(E)$, is given by:

$$f(E) = (1 + \exp[\frac{E - E_f}{k_B T}])^{-1} \tag{1.2}$$

in which E_f is the Fermi energy, k_B is Boltzmann’s constant, and T is temperature.

An intuitive way to understand Equation 1.1 is illustrated in Figure 1.3. For each electron in the sample at energy ϵ , there is some chance that that electron will tunnel to the tip, thus creating an electron current from the sample to the tip. The probability that such tunneling will occur depends on the number of states that the electron could tunnel to, or more precisely, the number of empty states available at energy ϵ in the tip. In other words, the electron tunneling current from the sample to the tip at a given energy ϵ is given by the product of the number of full sample-states (number of electrons that could tunnel) with the number of empty tip-states (number of states each electron could go to).

To obtain Equation 1.1 above, recall that the number of full sample-states is given by the product of the sample density of states with the Fermi function, both evaluated at energy ϵ . One can similarly obtain the a relation for the number of empty tip-states. This gives the first term in the equation. To obtain the net total current from the sample to the tip, one must then subtract the reverse (tip to sample) current at that energy ϵ , and finally sum over all energies. In doing so, one arrives at Equation 1.1.

Equation 1.1 can be rewritten by taking all energies relative to the Fermi energy of the respective system, and then setting the Fermi energy equal to zero. In addition, the two Fermi energies can be offset from one another by the application of a sample bias voltage. The energies are then given by: $E_s = \epsilon - eV$ and $E_t = \epsilon$. Such manipulation results in the following expression for the tunneling current:

$$I = \frac{4\pi e}{\hbar} \int_{-\infty}^{\infty} |M|^2 \mathbf{r}_s(x, y, \mathbf{e} - eV) \mathbf{r}_t(\mathbf{e}) [f(\mathbf{e} - eV) - f(\mathbf{e})] d\mathbf{e} \quad (1.3)$$

1.2.2 Tunneling Matrix Element

All that remains is to establish an expression for the tunneling matrix element which is given by:

$$|M|^2 \propto \exp\left(-2 \frac{\sqrt{2m\mathbf{j}}}{\hbar} s\right) \approx \exp\left(-\sqrt{\mathbf{j}} (eV) s (\text{\AA})\right) \quad (1.4)$$

in the approximation that $V \ll \phi$, where ϕ is the convoluted work function of the tip and sample¹² and m is the electron mass.

Although the derivation of this matrix element will not be discussed here, it can also be understood intuitively. An electron in the sample encounters a potential barrier between itself and the tip. The electron's chances of getting through the barrier depend on the value of its wave function once it reaches the tip proper. However, from simple quantum mechanics of a particle at a step we know that the sample-electron wave function is decaying exponentially inside the barrier. Thus, the chance that the electron will tunnel diminishes exponentially with the width of the barrier (tip-sample separation). Or in other words, the current depends exponentially on the separation between the tip and the sample. A simple explanation of this dependence can be found in the excellent book by Chen [p. 3 Chen 1993].

The exponential dependence of the current on tip-sample separation, in combination with the assumption that the tunneling matrix element is independent of energy, allows one to rewrite Equation 1.3 in the following manner often seen in the literature.

$$I = I_0 \exp\left(-\frac{s}{s_0}\right) \quad (1.5)$$

¹² For the data presented in this thesis $\phi \sim 3\text{-}4$ eV.

Equation 1.3 and 1.4 taken together provide an analytic form that gives the dependence of the tunneling current on the three important parameters, V , s and sample LDOS. Sections 1.5 - 1.7 describe how these dependencies can be used to make both topographic and spectroscopic maps of the sample surface.

1.3 A Brief Description of the STM System Used in this Study

Having provided a brief overview of how an STM works, I would now like to stay a few words about the specific system that was used for the studies presented in this thesis. This section will be very brief since the details of this instrument have been thoroughly described elsewhere [Pan 1999, Hudson 1999B].

A schematic of the system used is presented in Figure 1.4. The home-built scanning tunneling microscope is mounted on a ^3He refrigerator which can achieve a base temperature of 240 mK.¹³ The system is equipped with a magnet which can produce fields up to 7.25 T parallel to the STM tip.¹⁴ The system provides for sample exchange during a run and sample cleavage in cryogenic ultra-high vacuum (UHV) via a sample manipulator rod.

A schematic of the STM used in the system is provided in Figure 1.5. The STM employs as its coarse tip-sample approach mechanism a shear-piezo slip-stick “Pan walker/motor” [Pan 1993]. Fine tip-sample separation control and scanning capabilities are provided by a piezoelectric scan tube.

The primary benefit of this STM over other instruments is its extreme spatial stability. When optimally stabilized before a scan, the lateral drift in the system is less than about 1 Å per hour for about 10 hours. The drift after that time is negligible. In addition, the tip can be withdrawn from the surface by more than half a millimeter, and upon reapproach the lateral displacement will be found to be less than 100 Å. Such withdrawal (although not over such large distances) is necessary when transferring helium into the dewar for example. Such stability upon withdrawal means that the same region of the sample, or even the same single atom, can be studied for weeks or months at a time.

1.4 A Few Remarks on $\text{Bi}_2\text{Sr}_2\text{CaCu}_2\text{O}_{8+d}$

Before beginning to describe the types of measurements which can be made with an STM, I would like to make a few introductory remarks about $\text{Bi}_2\text{Sr}_2\text{CaCu}_2\text{O}_{8+\delta}$ in general, and the samples we use in particular. This section is included at this point since BSCCO data will be used to illustrate the techniques presented in the following sections.

¹³ As noted earlier, all the data in this thesis was taken at 4.2 K.

¹⁴ All the data in this thesis was taken in zero field unless otherwise noted.

1.4.1 Crystal Structure of $\text{Bi}_2\text{Sr}_2\text{CaCu}_2\text{O}_{8+d}$

Superconductivity in $\text{Bi}_2\text{Sr}_2\text{CaCu}_2\text{O}_{8+\delta}$ was discovered in 1988 by Maeda *et al.* The crystal structure of this system was reported by Subramanian *et al* [1988] and a schematic of the structure is given in Figure 1.6.

Although there is occasionally some confusion in the literature over the labeling of the crystal axes in this material, the orientation shown in the schematic is the most common one and will be used throughout this thesis. In this labeling the **a** and **b** axes are at 45° to the Cu-O bond direction. The unit cell in the **a** or **b** direction is 5.4 \AA . The **c** axis is perpendicular to the planes, and the unit cell in this direction is 30.7 \AA . The direction along the Cu-O bonds is commonly referred to as the **x** axis. All the results reported in this thesis are c-axis tunneling.

The actual crystal structure is made a good deal more complicated by the existence of an incommensurate *supermodulation* which runs throughout the bulk BSCCO crystal. The wavelength of this modulation is about $4.8*b$ (26 \AA) and the wave vector points along the **b** axis (successive crests and troughs are parallel to the **a** axis) [Yamamoto 1990]. This supermodulation is easily seen in STM topographic images as we will see in Section 1.5.

1.4.2 Samples, Sample Preparation, and Cleavage Planes

The single crystals used in our studies were made with the floating zone method and were provided by Dr. H. Eisaki and Prof. S. Uchida of Tokyo University. Any deliberate changes in the oxygen doping away from ‘as-grown’ samples were also done by this group. The samples are typically oxygen annealed several weeks to months before they are studied and are kept in a desiccated environment at room temperature in the intervening time. In this thesis I report on samples which are either as-grown, which is typically close to optimally doped, or $79 \text{ K } T_c$ underdoped.

To study the samples, we first glue them with conducting epoxy¹⁵ to a sample stud. One end of a small aluminum rod is glued to the front face of the sample, so that the sample is between the rod and the stud. This object is then inserted into the refrigerator and cooled to $<30 \text{ K}$. After the cooling, and in the cryogenic UHV environment, the sample is cleaved by holding the sample stud fixed while the rod is hit sharply. This generally leaves a flat clean surface for study. The sample is immediately inserted into the STM. Topographic images are then taken to ascertain the quality of the sample surface and tip, and if all is well, then spectroscopic images may be taken.

BSCCO has four superconducting CuO_2 planes per unit cell, and it is the physics of these planes that we wish to probe with our spectroscopy. The cleaving process discussed above generally exposes the BiO plane [Lindberg 1989], although we do sometimes see terraces [Pan 1998]. Topographies taken on the BiO plane show the positions of the Bi

¹⁵ Two conducting epoxies have been used, EPO-TEK 417 and EPO-TEK H20E. Both are manufactured by Epoxy Technology, Inc.

atoms, but not the O atoms [Kirk 1988]. Since each Bi atom is above a Cu atom, these topographies also give the positions of the Cu atoms. For spectroscopy, the predominant physics observed is believed to originate in the CuO_2 plane, because vortex core states, which are inextricably linked with superconductivity, and impurity resonances, which correspond to atoms that are known to substitute for Cu, are both seen [Pan 2000A, Pan 2000B, Hudson 2001]. However, the influence of the SrO and BiO planes on the tunneling process is still not completely understood.

1.5 Topographic Imaging with an STM

In the preceding sections I described the fundamentals of the operation of an STM and the particular STM used in these studies, as well as the material under study, $\text{Bi}_2\text{Sr}_2\text{CaCu}_2\text{O}_{8+\delta}$. With this preliminary information in hand, we can now proceed to what is the focus of this chapter- a description of the types of measurements which can be made with an STM, illustrated by typical examples obtained on BSCCO. In general an STM is used in either *topographic* or *spectroscopic* mode. This section will focus on the former method while subsequent sections will focus on the latter.

1.5.1 Topographic Scanning: Two Modes and Method

In practice, there are two ways to scan the STM tip across the sample surface, *constant height mode* and *constant current mode*. In both cases the tip-sample voltage is fixed¹⁶ at a certain value which is referred to as the *set point voltage* or V_{set} .

Referring to the variable labeling of Figure 1.2, in *constant height mode*, the tip is scanned across the surface as z is held fixed. The value of the current and any desired spectroscopic information is recorded at each x,y position.

In *constant current mode*, the total current is fixed at the *set point current* or I_{set} for each x,y position by changing the tip-sample separation, s . Subsequently, the value of z and any desired spectroscopic information is then recorded for that position. Maintaining a constant current during the course of a scan requires that the z position of the tip be controlled by a feedback circuit. A schematic of this circuit is given in Figure 1.7. Constant current mode is the most usual method of operation for an STM, and all data in this thesis were obtained in that mode.

The fundamental technique involved in making a topographic map using an STM in constant current mode is illustrated in Figure 1.8. The tip is scanned across the surface while the total current is held fixed at I_{set} for a given tip-sample voltage V_{set} . Holding the current constant is, to first approximation, equivalent to holding the tip-sample

¹⁶ For spectroscopic imaging, discussed in the next sections, the bias voltage is not always fixed, but V_{set} is nonetheless used to determine and fix the vertical position of the tip for each position at which a spectroscopic measurement is made.

separation, s , constant.¹⁷ During the scan, the value of z is recorded at each pixel. If we assume that the tip-sample separation, s , is a constant¹⁷, then a plot of z ($=h+s$) is, for the purposes of relative comparisons, equivalent to a plot of h . Plotting z as a function of x,y position on the surface produces a topographic map or *topography*.

1.5.2 Typical Topography on $\text{Bi}_2\text{Sr}_2\text{CaCu}_2\text{O}_{8+d}$

A typical topography with $V_{\text{set}} < 200$ mV taken on the BiO plane of a BSCCO surface is shown in Figure 1.9. There are three aspects of this image which I would like to point out, and these will be discussed in subsequent paragraphs.

First, I would like to point out the clear atomic resolution. To aid the reader, a small number of atoms are marked with yellow circles in the upper left hand corner of the image¹⁸. This type of atomic resolution in the topography implies that we have commensurate spatial resolution in taking spectroscopy. More broadly speaking and in general, the quality of the topographic image can convey a sense of the quality of the spectroscopic data.

The second feature to notice in Figure 1.9 is the supermodulation which was discussed in the previous section. Successive troughs of this structure have been marked with red lines at the top of the image.

The third feature to notice in Figure 1.9 is the presence of non-periodic and apparently randomly shaped maxima and minima, two of which are circled in red. These features are manifestations of the spectroscopic LDOS inhomogeneity which show up in the topography. They result from the constant current method of imaging. Essentially, although holding the current constant holds s constant to first order; nonetheless, there are slight variations in s due to variations in the local density of states. These variations in s show up in the topography because the topography is a not a map of h directly, but rather it is a map of z , which is the sum of $h+s$. This topic will be revisited in Section 1.10.2.

1.6 Scanning Tunneling Spectroscopy

The most scientifically interesting measurement which can be made with an STM is a measurement of the *local density of states* (LDOS). Such measurements are often referred to as *scanning tunneling spectroscopy* (STS) and were first demonstrated by Stroscio *et al* [1986] on Si (100). Beginning with Equation 1.3 and making a few simplifying assumptions, we can see how an STM can measure the LDOS.

¹⁷ The tip-sample separation is not in fact constant if there are local variations in the LDOS; however, in practice this variation does not generally affect the qualitative observations drawn from the data. See Section 1.10 on set points and normalization for more information on this point.

¹⁸ Recall that although this is the BiO plane, the atoms visible in this topography are only the Bi atoms since the orbital energies of the oxygen atoms prevent us from imaging them.

1.6.1 Theory of Scanning Tunneling Spectroscopy

Assuming small sample bias (V), the tunneling matrix element may be considered a constant with respect to energy and removed from the integral yielding:

$$I \propto \frac{4\pi e}{\hbar} \int_{-\infty}^{\infty} \mathbf{r}_s(x, y, \mathbf{e} - eV) \mathbf{r}_t(\mathbf{e}) [f(\mathbf{e} - eV) - f(\mathbf{e})] d\mathbf{e} \quad (1.6)$$

We further assume that the density of states of the tip is a constant over the energy range in which the remainder of the integrand gives a significant contribution. We also assume that the temperature is low enough such that the Fermi function can be treated as a step function, $\theta(\epsilon)$. These assumptions yield:

$$I \propto \int_{-\infty}^{\infty} \mathbf{r}_s(x, y, \mathbf{e} - eV) [\mathbf{q}(\mathbf{e} - eV) - \mathbf{q}(\mathbf{e})] d\mathbf{e} = \int_0^{eV} \mathbf{r}_s(x, y, \mathbf{e} - eV) d\mathbf{e} \quad (1.7)$$

Taking a derivative of this equation with respect to yields:

$$\frac{dI}{dV}(x, y, s, V) \propto \mathbf{r}_s(x, y, eV) \quad (1.8)$$

Thus a measurement of the differential tunneling conductance, dI/dV , yields a quantity which is proportional to the local density of states, given the validity of the assumptions outlined above. The factor that relates dI/dV to ρ_s is a function of, among other things, the tip-sample separation, s . The explicit form of the dependence of this factor on s can be obtained from an examination of the equation for the tunneling matrix element, 1.4. Using this equation, we can write:

$$\frac{dI}{dV}(x, y, s, V) = A \exp\left(-\frac{s}{s_0}\right) \mathbf{r}_s(x, y, eV) \quad (1.9)$$

where A does not depend on s , but might exhibit some dependence on x and y .

1.6.2 Practice of Scanning Tunneling Spectroscopy

Given that dI/dV is proportional to the LDOS, we would like to have a means to measure dI/dV as a function of x, y position on the surface and as a function of bias voltage, V . This would then be equivalent to measuring the LDOS as a function of x, y position and energy assuming that s is a constant. Section 1.10 will discuss the degree to which s is constant and the consequent implications, but for the purposes of this discussion it is helpful to ignore this complication and consider s to be constant. There are two means to measure $dI/dV(x, y, V)$.

In the first method, a measurement is made of the total current $I(x,y,V)$ for a range of bias voltages, and then a numerical derivative is taken to get dI/dV . In practice this can result in fairly noisy spectra given the usual troubles with numerical derivatives.

A better method is to measure dI/dV directly by using a lock-in amplifier, and this is the method employed for all the data presented in this thesis. For this method, the tip-sample separation is fixed by requiring a total current of I_{set} for the bias voltage V_{set} (=constant current normalization discussed above). After the set point current has been established at a given x,y position, the feedback is turned off and the vertical position of the tip no longer varies. Then a small sinusoidal AC voltage is added to the DC bias voltage. The current thus acquires a small AC component and can now be rewritten as a Taylor series:

$$I(V + dV \sin(\omega t)) \approx I(V) + \left. \frac{dI}{dV} \right|_V \cdot dV \sin(\omega t) \quad (1.10)$$

The AC component of the current can be read directly using a lock-in amplifier and is proportional to the differential conductance (dI/dV) and hence to the LDOS. If the DC bias voltage is varied, the AC current component can be measured as a function of bias voltage or equivalently the LDOS can be measured as a function of energy. This LDOS measurement can be carried out at successive x,y positions, and the result is *scanning tunneling spectroscopy (STS)*: $dI/dV(x,y,V) \Rightarrow \text{LDOS}(x,y,E)$. A schematic of this technique is given in Figure 1.10.¹⁹

1.6.3 Schematic for Understanding Spectroscopy

A schematic of the acquisition of a spectrum at a single x,y location by direct measurement of dI/dV is illustrated in Figure 1.11. In this figure, the tip is negatively biased with respect to the sample. This moves the Fermi level of the tip up with respect to that of the sample, and the net electron flow is from the tip to the sample. The amount of current flow depends on the product of the number of full tip states (red hatched areas) which are opposite empty sample states (white hatched areas). Adding an AC bias modulation, whose amplitude is given by the height of a gray shaded area, produces an AC current which is proportional to the product of the gray shaded areas. Since the value of the bias modulation (height of the two gray areas) is known and the tip DOS (width of tip gray shaded area) is a constant, the magnitude of the sample DOS curve (width of the sample gray shaded area) can be determined by a measurement of the AC current.

1.7 Spectroscopic Imaging with an STM

In this section I will discuss the variety of data sets which can be obtained using an STM. Figure 1.12 is a schematic which shows these data sets, and the rest of this section will essentially consist of an explanation of this figure. As in previous sections, I will illustrate the various measurements with data from $\text{Bi}_2\text{Sr}_2\text{CaCu}_2\text{O}_{8+\delta}$.

¹⁹ The algorithm used to take the data presented in this thesis is given by Hudson 1999B Appendix A.3.

As discussed in the previous section, using STS one can measure $dI/dV(x,y,V)$. The dependence of dI/dV on these three parameters is shown schematically as the series of stacked planes in Figure 1.12(a). In this image, each plane represents a different voltage and the lateral position on the plane indicates different x,y positions. At each different x,y position on each different energy plane one could make a measurement of dI/dV , so $dI/dV(x,y,V)$ can be obtained.

1.7.1 Spectral-Surveys

The most complete data-set would consist of a measurement of the differential conductance at all x,y positions within some area and at all energies within some range²⁰. Such a data set will be referred to as a *spectral-survey*. Spectral-surveys can provide a wealth of information, and much of the data contained in this thesis is derived from them. For example, the parameter maps discussed in Section 1.9 are derived from spectral-surveys.

However, this wealth of information has a cost, and that cost is long data-set acquisition times. Taking each spectral-survey in this thesis required from 17- 48 hours of continuous data acquisition for the 128 pixels x 128 pixels x 101 energy layers typically acquired. In taking data over such a long period of time, lateral tip-sample drift can be a serious problem for many instruments²¹, and it is for this reason that this type of data-set is very rarely encountered in the literature. In practice, one takes subsets of this complete data-set and these subsets are the subject of the subsequent paragraphs.

1.7.2 Spectrum

The first data-subset I will describe is a *spectrum*. To take a spectrum one fixes the x,y position of the tip and takes a measurement of the differential conductance at a finite set of energies in a certain range. Differential conductance is then plotted as a function of bias voltage as shown in Figure 1.12(b). This panel shows a spectrum one might find studying BSCCO.

Typically, it takes from a few seconds to a few minutes to take a single spectrum. The few second variety of spectra are usually part of a spectral-survey, whereas the few minute variety are taken as single point spectra or as part of a linecut.

1.7.3 Linecut

Another spectroscopic data-set which can be taken with an STM is a *linecut*, which is shown in Figure 1.12(c). A linecut is a series of spectra taken at discrete sequential positions along a line. Typically, the spectra are displayed by offsetting them from one another vertically as shown in the figure. When they are displayed like this, the y-axis

²⁰ Of course, in practice one does not make a measurement of “all” x,y positions, but rather one lays a grid on the surface of some finite spacing, and then takes a measurement at each node point in the grid. Similarly for energy, one takes a measurement every so many mV.

²¹ See Section 1.3 for the lateral drift specifications of the instrument used in these studies.

gives both distance along the line and differential conductance for individual spectra. The x-axis gives voltage as is usual for a spectrum. The panel 1.12(c) shows a linecut taken on a Zn-doped BSCCO crystal, and the large peak in differential conductance near 0 mV indicates the location of a Zn impurity.

Each spectrum in a linecut takes a few minutes to acquire, and the time to take the entire linecut depends on the number of spectra desired.

1.7.4 Differential Conductance Map

A *differential conductance or dI/dV map* is another spectroscopic data-set, and this is shown in Figure 1.12(d). A dI/dV map is a measure of the differential conductance at each x,y location in a given area for a single voltage. Such maps are particularly useful for imaging the spatial evolution of a single peak in the spectrum. For example, the spatial evolution of the resonance near an impurity atom (as shown in the linecut of 1.12(c)) can be imaged this way, and such a map is shown for a Zn atom in BSCCO.

The time it takes to make a differential conductance map depends on the number of pixels in the map, but to give a sense, a 256x256 pixel map would take about 2 hours of overhead time (moving the tip and stabilizing it at each x,y position) and then 40 minutes for each distinct voltage for which a map was desired.

1.8 Definition of Spectral Parameters

Although a wide variety of spectral shapes are found in a typical spectral-survey of $\text{Bi}_2\text{Sr}_2\text{CaCu}_2\text{O}_{8+\delta}$, certain characteristics are recognizable in the large majority of the spectra. The purpose of this section is to identify and define those characteristics in order to parameterize them.

Parameterization is necessary because spectral-surveys contain thousands of spectra and it is not possible to view all these spectra individually. Instead, a computer program is used to extract parameters from each spectrum in the survey in order to create parameter maps, which are discussed in the next section.

1.8.1 Definition of D

Figure 1.13 shows two BSCCO spectra with different shapes. On each spectrum, several of the same characteristics are observed. At zero bias voltage the differential conductance is low. Moving in either direction from zero, the differential conductance rises and achieves a maximum. Still moving away from zero, the differential conductance then falls, which defines a peak. The voltage at which this peak occurs is identified in the figure as either Δ_- or Δ_+ depending on the polarity of the bias voltage. The energetic separation between the two peaks is defined as 2Δ ²² so that:

²² While Δ_- and Δ_+ are signed values which are negative and positive respectively, Δ should be considered as a magnitude and is thus always positive.

$$\Delta \equiv \frac{\Delta_+ - \Delta_-}{2} \quad (1.11)$$

From a physically intuitive standpoint, Δ generically gives the width of the energy gap which is centered around the Fermi energy. Therefore, in this thesis, Δ will be referred to as the *[energy] gap*. For a spectrum taken on a superconductor, Δ would give the magnitude of the superconducting gap. For a material with a charge density wave, Δ would give the magnitude of the charge density wave gap, and so on.

1.8.2 Definition of A(D)

The value of the differential conductance at any given voltage is defined as $G(V)$. The value of the differential conductance at Δ_{\pm} gives the *amplitude of the gap-edge peaks*. These amplitudes will be referred to as $A(\mathbf{D}_{\pm})$. For reasons that will be discussed later in this chapter, generically I will define:

$$A(\Delta) \equiv A(\Delta_{\pm}) \quad (1.12)$$

For a spectrum taken on a superconductor, $A(\Delta)$ would give the height of the coherence peak.

1.8.3 Definition of S(V_a,V_b) and S(D)

A third spectral parameter, $\Sigma(V_a, V_b)$, is defined in equation 1.13.

$$\Sigma(V_a, V_b) \equiv \frac{\sum_{i=a}^{i=b} G(V_i)}{|b-a|} \approx \frac{\int_{V_a}^{V_b} G(V) dV}{|V_b - V_a|} \quad (1.13)$$

As one can see from the equation, Σ represents the average value of the differential conductance between two given voltages, V_a and V_b . In practice, since successive values of $A(V)$ are measured with fixed finite energy spacing, the quantity Σ is strictly defined as a sum. However, if the energy intervals are small enough, the sum may be thought of as continuous, in which case it becomes an integral as indicated in the equation. In this case, Σ is proportional to the area under the spectrum between V_a and V_b , and this area is shown as the hatched region in the graphs.

Whenever the quantity Σ is used, the voltages V_a and V_b will be specified in the description of the figure. In the text of this thesis, however, I will often use a shorthand notation, $\Sigma(\Delta)$. This notation will be used if the chosen voltages V_a and V_b span all values of Δ for all spectra for which Σ is computed and if essentially the entire gap-edge peak is included in this energy range for all those spectra.

From a physically intuitive standpoint, if V_a and V_b are both negative then Σ is proportional to the number of occupied states in the specified energy range. Conversely

if V_a and V_b are both positive, Σ is proportional to the number of filled states. I would like to add one cautionary note at this point. Although Σ is always proportional to the number of states, the constant of proportionality is, ironically, not always constant. This means that care must be taken when comparing relative values of Σ between different spectra. This issue will be discussed in detail in the subsequent sections in this chapter.

1.9 Parameter Maps

In the previous section I defined several spectral parameters. Given these definitions, each spectrum in a spectral-survey can be analyzed and the value of that parameter extracted. The value of the parameter can then be plotted as a function of x,y position, so that the spatial evolution of the parameter can be studied. Such a map will be generically referred to as a *parameter map*. Figure 1.14 shows an example from BSCCO of the parameter maps discussed in this section. These maps will be presented again in later chapters and discussed in the context of the physics they represent.

1.9.1 D , $A(D)$, and S maps

Using the definitions of Δ , $A(\Delta)$, and Σ in the previous section, maps of these parameters can be extracted from a spectral-survey. In particular, we can make a map of the value of Δ as a function of x,y position. This will be referred to as a *D -map* or a *gapmap*. We can also make a map of $A(\Delta)$, which will be referred to as a *$A(D)$ -map* or *peakmap*. Finally, we can make a map of Σ , which will be referred to as a *S -map* or an *intmap*.

As each spectral-survey presented in this thesis generally contains 128×128 (=16384) individual spectra, the extraction of these parameters must be accomplished by a computer. The value of Δ and $A(\Delta)$ both rely on an algorithm for picking the peak in a spectrum, which is discussed in Appendix 1. This appendix also discusses a few issues which need be considered when viewing Δ and $A(\Delta)$ maps.

The value of Σ is independent of the peak-picking algorithm, and depends only on an algorithm which implements the definition of Σ as presented in equation 1.13. The independence of Σ from the peak-picking algorithm means that Σ can be used an independent check of that algorithm in addition to being an interesting independent quantity.

1.9.2 Gradient Maps

As the purpose of the Δ , $A(\Delta)$, and Σ maps is to study the spatial evolution of these parameters, it seems useful to make maps which indicate regions of change in these quantities. A map of the gradient of a given parameter would serve such a purpose. Such maps have been generated using the following definition for the gradient at a y,x position at which spectrum i,j has been acquired:

$$\nabla P_{y,x} \equiv \left| \left(\bar{\nabla} P \right) \right|_{i,j} = \frac{\sqrt{\left(P_{i+1,j} - P_{i-1,j} \right)^2 + \left(P_{i,j+1} - P_{i,j-1} \right)^2}}{l} \quad (1.14)$$

$P_{i,j}$ is the value of the parameter at position i,j , and l is a constant which relates the number of pixels in the image to the size of the image in angstroms.

Maps of the gradient of a parameter will generally be referred to as \tilde{N} -maps. Specifically, a map of the gradient of Δ will be a $\tilde{N}D$ -map, a map of the gradient of $A(\Delta)$ will be a $\tilde{N}A(D)$ -map, and a map of the gradient of Σ will be a $\tilde{N}S$ -map.

The $\bar{\nabla}$ -maps are, of course, also produced by an automated computer analysis of the data, which implements an algorithm based on the definition of $\bar{\nabla}$ presented above. Appendix 1 discusses a few issues which need to be considered when viewing these $\bar{\nabla}$ -maps.

1.10 A Discussion of the Relation Between Differential Conductance and LDOS

In a parameter map and in general, there are several characteristics which one might study as function of x,y position. Three of these characteristics are the parameters discussed above, Δ , $A(\Delta)$, and Σ . These characteristics can be extracted from the dI/dV spectra. A final characteristic one might study as a function of x,y position is the overall shape of the dI/dV spectrum.

The motivation for studying characteristics of dI/dV spectra is, of course, that there exists a relationship between dI/dV and the physically meaningful quantity, local density of states. What one would *really* like to know is how spectral characteristics vary in the actual LDOS spectra. The purpose of this section is to elaborate on the relationship between dI/dV and LDOS, and thus to afford the reader a more accurate physically intuitive interpretation of variations in dI/dV spectral characteristics

Before considering the physical interpretation for any particular spectral characteristic, we need to carefully examine the role of the tip-sample separation, s . Thus, I will begin by discussing why s can vary as a function of x,y position under the constant current normalization scheme used in taking the data presented in this thesis. I subsequently discuss in general the effects of this variation on the relationship between the dI/dV spectra and the physically meaningful LDOS. Finally, I will discuss the effects of this variations on the specific spectral characteristics Δ , $A(\Delta)$, Σ , and spectral shape.

1.10.1 Origin of Variations in the Tip-Sample Separation Under Constant Current Normalization

Variations in the tip-sample separation under constant current normalization are due to variations in the integrated LDOS, where the integral ranges from the Fermi energy at 0 meV to the set point voltage at V_{set} . The remainder of this section will be devoted to justifying this statement.

Recall that in constant current imaging, at each x,y tip-position, the z^{23} tip-position is determined by using feedback to maintain the current at the constant value, I_{set} . So variations in z and by extension, variations in s, should be explained by examining an expression for the total current at V_{set} . Using equations 1.3-1.5 and 1.7 we may trivially obtain such an equation for I_{set} which includes an explicit s dependence:

$$I_{set} = A \exp\left(-\frac{s}{s_0}\right) \int_0^{eV_{set}} \mathbf{r}_s(x, y, \mathbf{e} - eV_{set}) d\mathbf{e} \quad (1.15)$$

This equation shows that the total current is determined by the number of LDOS states between the Fermi energy at $V=0$ and the voltage set point, V_{set} .

The implication of this becomes clear if one considers that the tip is above a region in which the LDOS has relatively more states in the energetic region $V=0$ to V_{set} . In this case, s must be increased in order to keep the total current constant at I_{set} . Conversely, in regions in which the integral of the LDOS from $V=0$ to V_{set} is relatively lower, then s must be decreased in order to keep the total current constant at I_{set} . So under constant current normalization, forcing the current to be I_{set} for all x,y positions means that s varies in order to offset variations in the integrated LDOS.

1.10.2 Implications of Variations in the Tip-Sample Separation for Topography

Recall that a topography is a map of z ($= h+s$)²³. If s is a constant, then the z positions of the tip will track perfectly the real topographic features in the sample as reflected by h, and maps of z and h will be equivalent. However, if s is varying as a function of lateral tip position, then these variations will be visible in a map of z. Since variations in s are due to variations in the integrated LDOS, an STM topography (defined as a map of z) will then reflect a convolution of the real topographic features and spectroscopic information.

This discussion explains the large (compared to the atoms) non-periodic high and low patches in topographies taken on BSCCO. Examples of these patches are circled in red in Figure 1.9 and were mentioned in the discussion of that figure. In short, these non-periodic high and low patches are due to variations in s and reflect changes in the integrated number of LDOS states between 0 and V_{set} .

²³ Please see Figure 1.2 and 1.8 for a definition of x, y, z, s, and h.

1.10.3 Magnitude of Variations in the Tip-Sample Separation

In the previous sub-section it was established that the non-periodic high and low patches in the topographies of BSCCO were due to variations in the tip-sample separation, s . Thus, these patches represent a means to measure the *relative* variations in s ²⁴ if their signal can be separated from the ‘real’ topographic signal (h).

This can be accomplished if we assume that we know the periodicity of all features which contribute to h . In the case of BSCCO, these are the atoms and the supermodulation whose wavelengths are known and were discussed in Section 1.4. To extract relative s values, a BSCCO topography is Fourier transformed, and then the wavelengths which correspond to the atoms and supermodulation are cut out. The resulting image is then inverse Fourier transformed producing a map of variations in relative s ²⁵. A histogram of the values in this map may be made, and the width of this histogram provides an estimate for variations in s about \bar{s} .

Figure 1.15 shows the results of such an exercise using a typical topography taken on BSCCO. Panel (a) shows the original topography. Panel (c) shows the image which results when all wavelengths which correspond to the atoms and the supermodulation are removed from the topography. For completeness, panel (b) shows the image which results from keeping only the wavelengths which correspond to the atoms and the supermodulation. The histogram of the s values contained in the image in panel (c), is shown in panel (d).

1.10.4 Magnitude of Variations in the dI/dV -LDOS Proportionality Factor

The reason for quantifying the variations in s , as in the previous section, is to permit quantification of the corresponding variations in the proportionality factor which relates dI/dV and LDOS. In this section then I will estimate the variations in that proportionality factor.

Equation 1.9, which relates dI/dV to LDOS, is repeated here for convenience.

$$\frac{dI}{dV}(x, y, s, V) = A \exp\left(-\frac{s}{s_0}\right) \mathbf{r}_s(x, y, eV) \quad (\text{Repeat 1.9})$$

²⁴ Using this method we are not able to measure the actual tip-sample separation, but rather measure *relative* variations in the tip-sample separation (σ_s) about some unknown mean value, \bar{s} . We may estimate \bar{s} to be an angstrom or two based on (1) the value of s_0 as determined in the next paragraph and (2) the physically intuitive argument that tunneling occurs only if the tip and sample wave functions overlap, and since these are ultimately atomic wave functions, their spatial extent is of the order of a few angstroms.

²⁵ Note that the atoms are not perfectly periodic due to the presence of the supermodulation. Thus this filtering can not remove the entire atomic signal; however, it works very well nonetheless.

This equation indicates that dI/dV and ρ_s are proportional to one another, with a proportionality factor that depends on s . Consider now two x,y positions designated by 1 and 2. We assume that position 1 is located at a point which has the mean tip-sample separation, \bar{s} , and position 2 is arbitrary. Using the equation above we may write:

$$\frac{r_{s_2}}{r_{s_1}} = \exp\left(\frac{s_2 - \bar{s}}{s_0}\right) \frac{\frac{dI}{dV_2}}{\frac{dI}{dV_1}} \quad (1.16)$$

An estimate of an upper bound for the exponential factor in the equation above gives the maximum amount of variation which could be expected in the dI/dV -LDOS proportionality factor as compared to the mean proportionality factor. We may obtain this upper bound as follows.

From the distribution of s values in Figure 1.15, we find the standard deviation of s from the mean value, σ . Recall that for a Gaussian distribution 95% the values in the distribution are within 2σ of the mean value. Taking this as a guide, we expect that $|s_2 - \bar{s}| < 2\sigma_s$ gives an approximate upper bound on the deviations in s from the mean. For the field of view of Figure 1.15 then, we find $2\sigma_s \sim 2 * 0.13 \text{ \AA} \sim 0.26 \text{ \AA}$.

The value of s_0 can be found by measuring an I vs. s curve and then using equation 1.5 to extract s_0 . Such an exercise generally produces $s_0 \sim 0.5 \text{ \AA}$ as shown in Figure 1.16 for two different tips and samples.

Having found an estimate for the terms in the proportionality factor of Equation 1.16, we may now plug them in to find for the field of view of Figure 1.15:

$$\exp\left(\frac{s_2 - \bar{s}}{s_0}\right) < \exp\left(\frac{0.26}{0.5}\right) = 1.68 \quad (1.17)$$

Thus for this field of view, variations in the tip-sample separation produced changes in the dI/dV -LDOS proportionality factor of no more than a factor 1.7 as compared to the mean proportionality factor.

A second field of view (this one 590 \AA square) from a second sample showed a standard deviation about the mean value of s of $2\sigma_s \sim 0.4 \text{ \AA}$. For this field of view then, variations in the tip-sample separation produced changes in the dI/dV -LDOS proportionality factor of no more than a factor 2.2 as compared to the mean proportionality factor.

1.10.5 Effect of Variations in the Tip-Sample Separation on Spectral Characteristics

Having established generally why and how much the tip-sample separation varies as function of x,y position, let us now consider the effects of such variation on particular

spectroscopic measurements. I now consider the spectral characteristics, Δ , $A(\Delta)$, Σ and spectral shape, and discuss how variations in s and the dI/dV -LDOS proportionality factor affect comparisons of these characteristics.

When comparing dI/dV spectra, one must consider that potentially a different factor of proportionality relates each spectrum to the physically meaningful LDOS. Although this situation might seem to render meaningful comparisons between distinct dI/dV spectra difficult if not impossible, this is definitely not the case. Meaningful comparisons between distinct dI/dV spectra can be made provided that one keeps in mind the considerations which are discussed in the remainder of this section.

Effect of s Variations on Δ

The first characteristic to be considered is Δ . While variations in s can affect the magnitude of the differential conductance peak located at a particular energy, such variations cannot affect the energetic location of that peak. This means that the parameter Δ is insensitive to variations in s . A second concern regarding Δ would arise if the dI/dV -LDOS proportionality factor contained an energy dependent term, but it does not²⁶. Taken together these facts indicate that any conclusion about the spatial variation of Δ which is derived from a dI/dV spectral-survey, is equivalent to the conclusion which could be drawn given the commensurate LDOS spectral-survey. In other words, observations about spatial variations of Δ which are derived from dI/dV spectral-surveys should be considered quantitatively physically meaningful.

Effect of s Variations on $A(\Delta)$ and Σ

We next consider the two characteristics, $A(\Delta)$ and Σ , which depend on the magnitude of the differential conductance. Such characteristics are most likely to be affected by variations in s ; however, let us examine how they are affected by these variations. Figure 1.17(e) shows a scatter plot of $A(\Delta)$ vs. s from panels (c) and (d) respectively of the same figure. The map of s is found by Fourier filtering the topography as described above in Section 1.10.3. Although there is a great deal of scatter, nonetheless, this figure demonstrates a clear trend for spectra with high $A(\Delta)$ to be associated with high s values. Although I do not suggest that the data is linear, a line has been fit to the data to illuminate the trend.

²⁶ One might argue that there could be some energy dependence in ‘ A ’ of Equation 1.9, which derived from an energy dependence of the tunneling matrix element, M . However, in order for such energy dependence to shift the apparent position of the peak for a given dI/dV spectrum as compared to the “real” position of the peak in the LDOS spectrum, the tunneling matrix element would have to vary rapidly within an energy which is on the order of the width of the peaks (~ 10 mV). Such rapid variation seems intuitively unlikely. Further, even if M did vary this rapidly as a function of E , this would just produce a systematic error in the apparent position of the peak in the dI/dV spectra. In other words, the peak positions for all dI/dV spectra would appear shifted by the same energy as compared to the “real” peak position in the LDOS spectra. Such a shift would not invalidate observations about the relative spatial variation of Δ .

For the remainder of this discussion I am going to use as examples the spectra presented in Figure 1.13. The use of these specific examples is to aid the reader in appreciating the arguments made; however, the discussion should be taken as being more generally applicable.

The trend in $A(\Delta)$ vs. s suggests that, generally speaking, spectra which look like Figure 1.13(a) are associated with higher s values (s_a), whereas spectra which look like 1.13(b) are associated with lower s values (s_b). So in general, $s_a > s_b$ and therefore $\exp(s_a - s_b/s_0) > 1$, and using equation 1.16 with $s_2 \rightarrow s_a$ and $s_1 \rightarrow s_b$ we have:

$$\frac{\mathbf{r}_{sa}}{\mathbf{r}_{sb}} > \frac{\frac{dI}{dV_a}}{\frac{dI}{dV_b}} \quad (1.18)$$

Since we are concerned with relative change, we can choose one type of spectrum to be the baseline point of comparison. Choosing the spectrum with low $A(\Delta)$ in 1.13(b) for this, and to assist in the clarity of this argument, assuming that $\rho_{sb} = dI/dV_b$, we obtain:

$$\mathbf{r}_{sa} > \frac{dI}{dV_a} \quad (1.19)$$

The implication of the equation above is the following. For dI/dV spectra with high $A(\Delta)$, like that in Figure 1.13(a), the effect of variations in s is generally to suppress the measured value of $A(\Delta)$ relative to the real peak height value one would obtain given a means to measure the LDOS spectra directly.

More generally, the variations in s which arise due to the constant current normalization scheme reduce the size of any signal present in $A(\Delta)$ by reducing the measured height of high peaks and increasing the measured height of low peaks as compared to the real heights of such peaks in an actual LDOS spectrum²⁷.

The preceding discussion has been made for one particular differential conductance, $A(\Delta)$. However, as figure 1.18(e) shows, the same trend is present for $\Sigma(\Delta)$ vs. s as was present for $A(\Delta)$ vs. s , and so the same series of arguments can be made for relative values of $\Sigma(\Delta)$.

In general, when making a comparison of different dI/dV spectra one must remember that the multiplicative proportionality factor which converts those spectra to LDOS may be different for different spectra. However, the differences in the factor are not random, but rather they are such as to reduce the contrast in any signal present in $A(\Delta)$ and Σ . Thus, any qualitative conclusions drawn regarding relative trends of $A(\Delta)$ and Σ are valid.

²⁷ As is seen in Figure 1.17(e), this statement may not be valid for every individual spectrum in a spectral-survey; however, it is valid for the vast majority of the spectra.

Effect of s Variations on Spectral Shape

Having discussed the effect of s -variations on Δ , $A(\Delta)$, and Σ , I would now like to comment on the effect of these variations on overall spectral shape. Quite simply, since the dI/dV -LDOS proportionality factor does not depend on energy, the shape of a differential conductance spectrum is the same as that of the respective LDOS spectrum.

The implication of this statement can be understood by again taking the spectra presented in Figure 1.13 as an example. One can easily appreciate that the spectrum in 1.13(a) is qualitatively a very different shape than the spectrum in 1.13(b). The variations in s mean that to quantitatively compare these two spectra we might need to multiply one of them by an overall factor; however, there is no possible way that multiplying the spectrum in 1.13(b) by any overall factor could ever make it look like the spectrum in Figure 1.13(a). Thus, qualitative observations of spectral shape are insensitive to issues of variations in s .

Summary

In summary, in this section I have presented a detailed discussion of the consequences of constant current normalization and the ensuing variations in the tip-sample separation, s . The essence of the findings is that observations and conclusions derived from studies of differential conductance spectra may be taken as comparable to the observations and conclusions one would derive from a study of the commensurate LDOS spectra. Having thus established that the differential conductance data presented in this thesis can be used to make valid observations of a physically meaningful quantity, LDOS, the remainder of this thesis concentrates on detailing such observations.

1.11 Surface vs. Bulk Local Density of States

Scanning tunneling spectroscopy is a probe of the local density of states at the *surface* of the material under study. There is a very real possibility that the surface LDOS may be somewhat or even significantly different than the bulk LDOS. There is, unfortunately, no direct means to verify to what degree the LDOS measured by STS probes the bulk. Since the electronic structure probed by ARPES represents the same near surface electronic states, comparison of STM data with that from with ARPES also cannot answer this question. However, some inferences can be made using indirect means. For example, STS results may be compared to other bulk measurements such as heat capacity, NMR, conductivity, or neutron scattering. A brief discussion of such a comparison of the data presented in this thesis with such bulk measurements is given in our forthcoming paper [Lang 2001]. Much further work using comparison between bulk techniques and surface sensitive techniques will be required to define both the interrelationship between these measurements and the degree to which STM studies reveal bulk properties in HTSC.

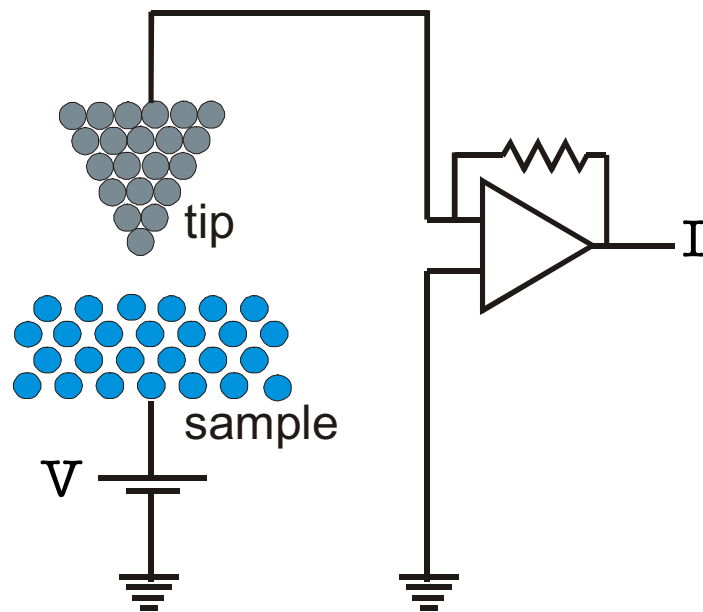


Figure 1.1: Fundamental components of an STM.

A metal tip is held within a few angstroms of the sample to be studied. When the sample is voltage biased, a current flows by tunneling across the vacuum barrier separating the tip and sample. This current is amplified and then recorded.

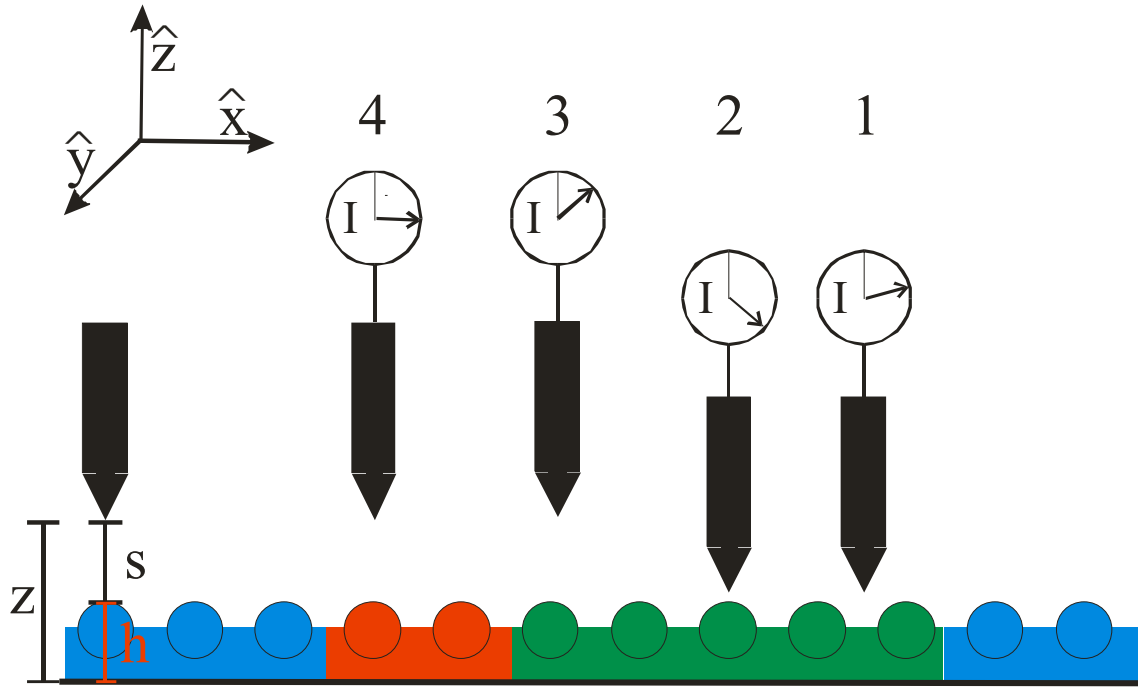


Figure 1.2: Current dependence and spatial coordinate definitions for a scanned STM tip.

As the tip is scanned across the surface (x - y plane) with a fixed tip-sample voltage, the current may vary due to changes in the tip-sample separation (s) or to changes in the local density of states, LDOS, (indicated schematically by color in this diagram).

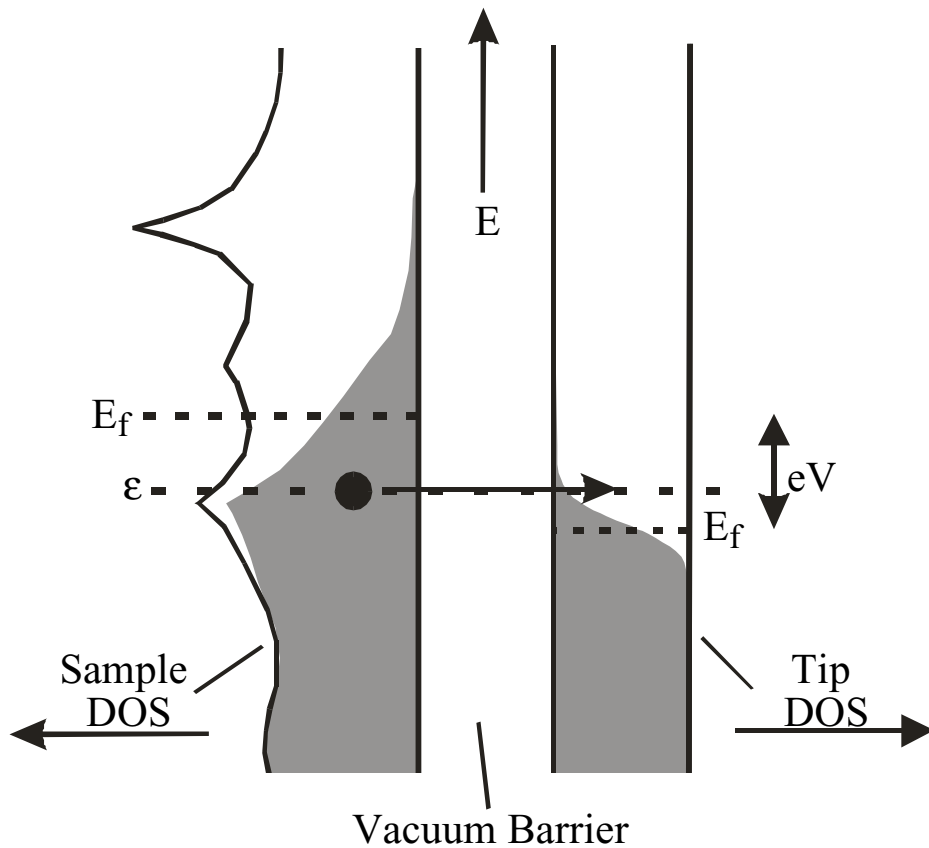


Figure 1.3: Schematic of tunneling from sample to tip. The density of states of the sample and tip is given by the black outlines. Filled states, as determined by the Fermi function, are indicated by gray shading. A given electron in the sample at energy ϵ may tunnel if there is a state for it at ϵ in the tip. Thus, the total number of electrons tunneling at energy ϵ will depend on the product of the number of filled sample-states at that energy (number of electrons available for tunneling) with the number of empty tip-states at that energy (number of states available for electrons to go to).

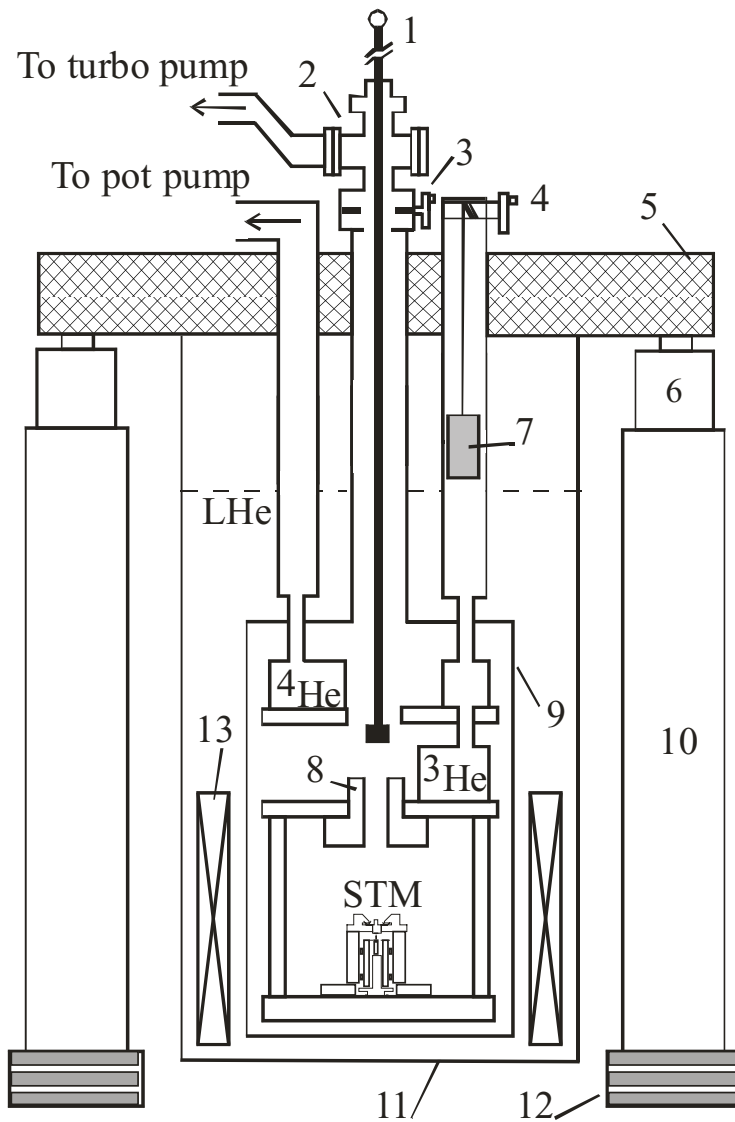


Figure 1.4: Schematic of the STM and cryostat.

Schematic is not to scale. The numbered components are as follows: (1) Sample manipulator rod, (2) Load-lock chamber, (3) Gate-valve, (4) Charcoal sorption pump lift/lowering mechanism, (5) Lead filled table top for vibration isolation, (6) Air-spring, (7) Activated charcoal sorption pump, (8) Mechanical sample cleavage stage, (9) Vacuum chamber, (10) Supporting table leg, (11) Superinsulation dewar, (12) Stacked rubber and steel pads, (13) 7.25 T Magnet.

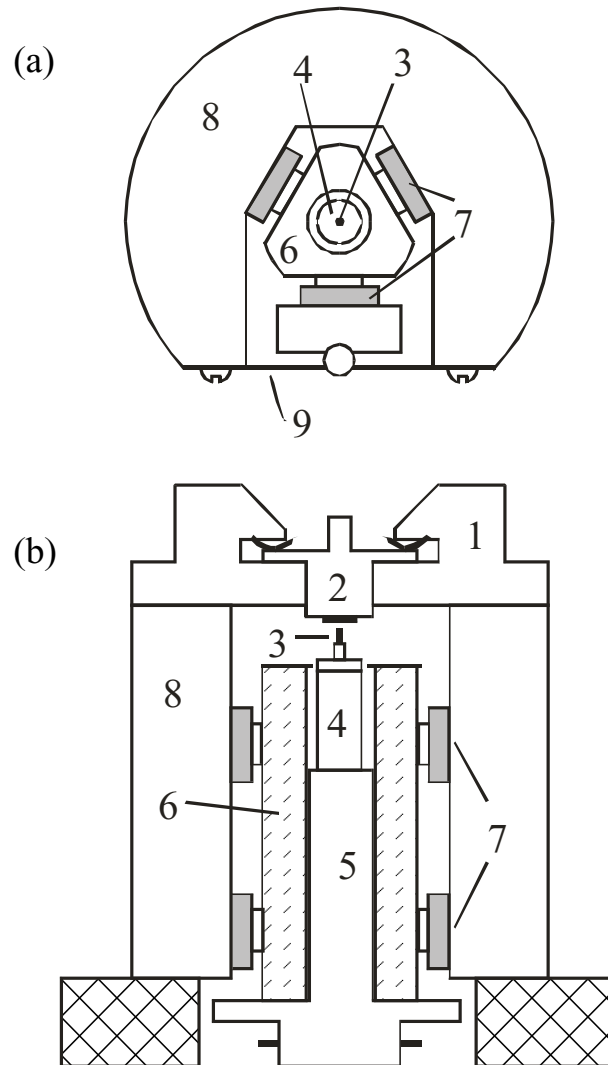


Figure 1.5: Diagram of the STM proper.

(a) top view (with sample receptacle removed for clarity) and (b) side view. The diagram is not to scale, but the actual overall dimensions of the STM are 1.5" in diameter by 1.75" high. The numbered components are as follows: (1) Sample Stud Holder, (2) Sample Stud, (3) Tip, (4) Tube Scanner, (5) Scanner Holder, (6) Sapphire Prism, (7) Shear Piezo Stacks, (8) Macor Body, (9) Spring Plate.

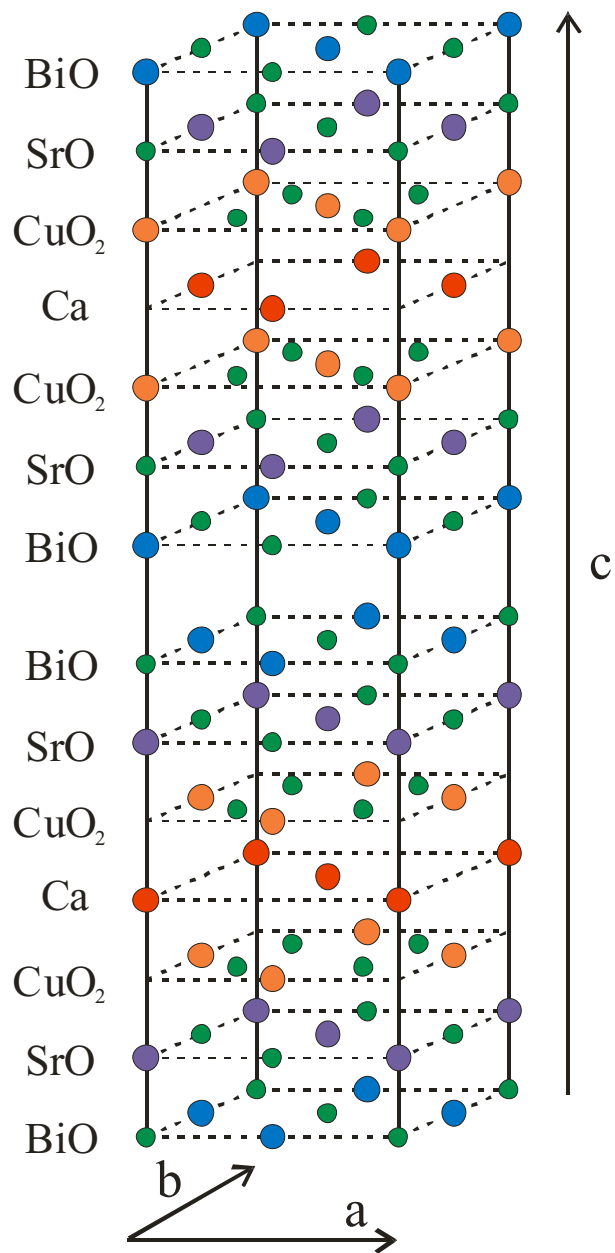


Figure 1.6: Structure of $\text{Bi}_2\text{Sr}_2\text{CaCu}_2\text{O}_{8+\delta}$. The diagram shows a single unit cell of BSCCO. The smaller green circles represent oxygen atoms.

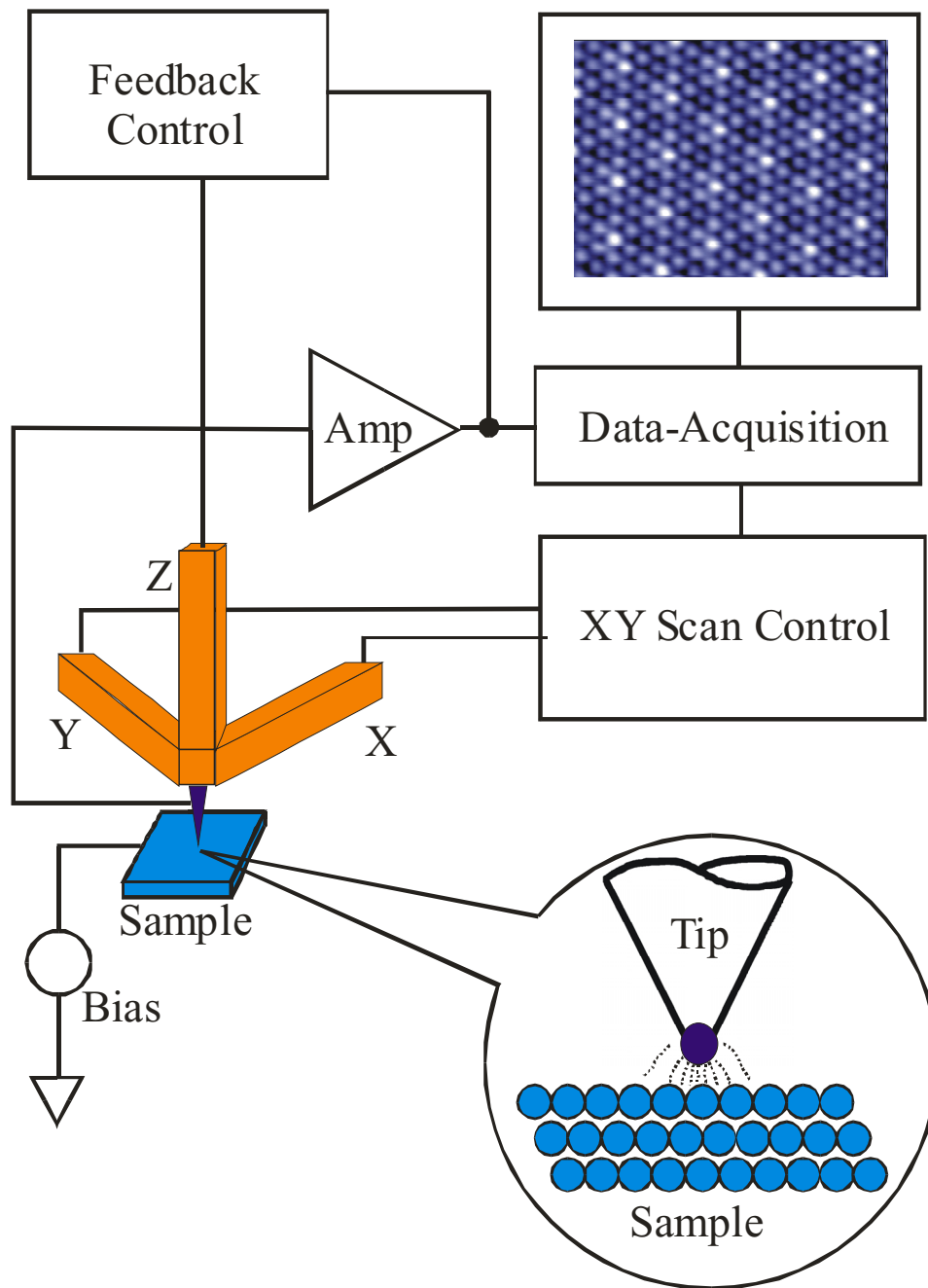


Figure 1.7: STM feedback and data acquisition system.

As the XY Scan Control scans the tip over the sample, the Feedback Control adjusts the z-position of the tip in order to hold the current constant. Both the z-position and the current can be recorded as a function of x,y tip position by the Data Acquisition module.

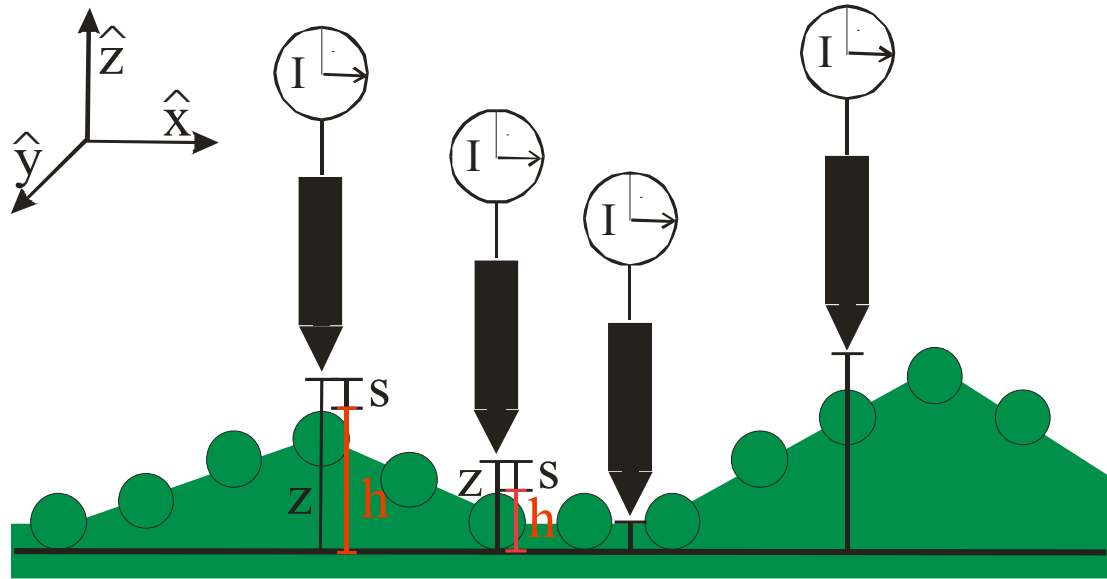


Figure 1.8: Constant current topographic mapping.

The tip is scanned across the surface while feedback holds the current fixed. To first order this is equivalent to holding s fixed as well. The value of z is recorded for each x, y position. This results in a topographic map of the surface since z is offset from h by the constant s .

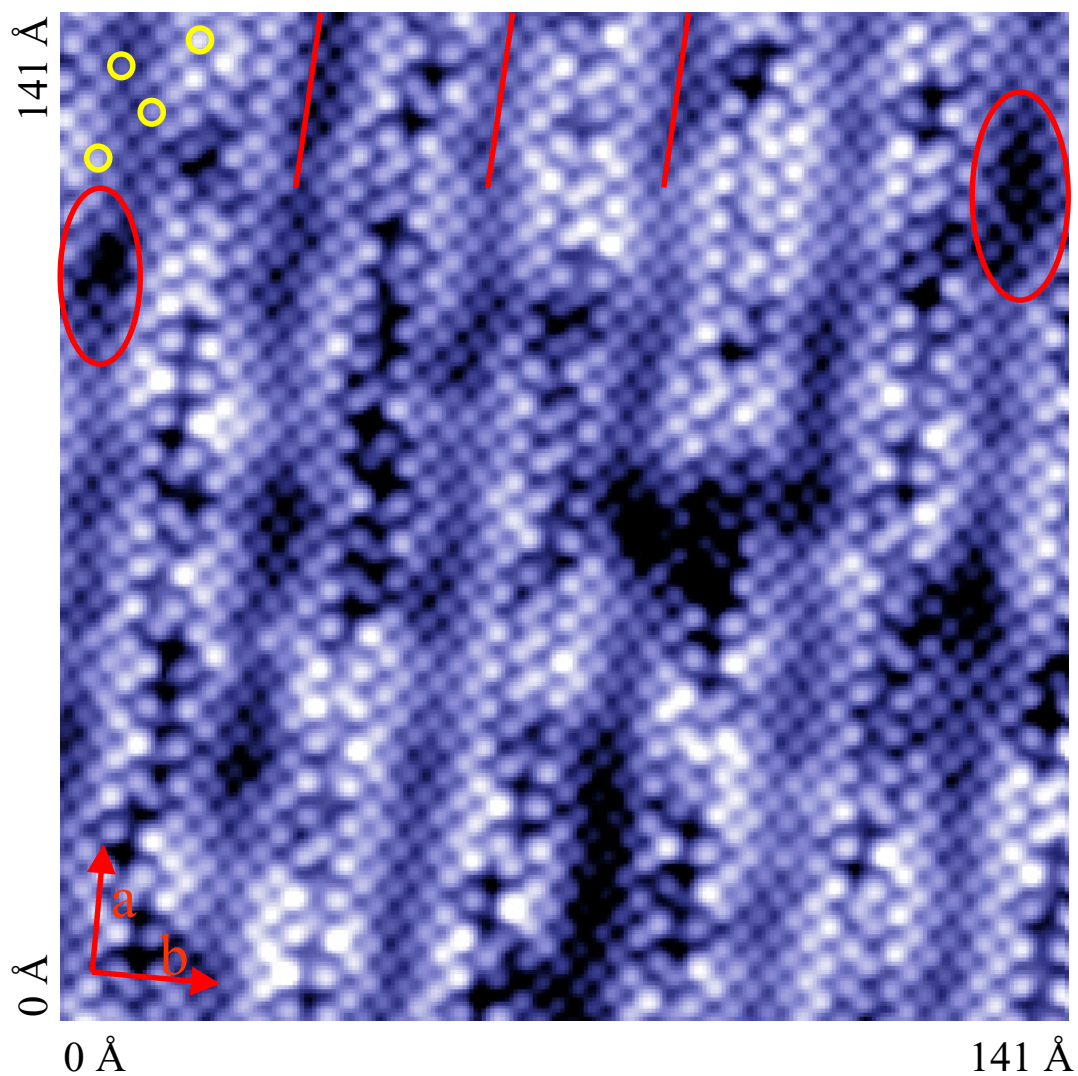


Figure 1.9: Typical topography on the BiO surface of $\text{Bi}_2\text{Sr}_2\text{CaCu}_2\text{O}_{8+\delta}$. The atoms are clearly resolved in this topography. The positions of several atoms are indicated by the small yellow circles. The supermodulation is also clearly visible. Three successive troughs of this wave-like modulation are indicated by the three parallel red lines. Finally, spectroscopic information is apparent in this topography as evidenced by the randomly shaped and distributed dark and light patches. Two of these patches are circled in red.
 Run = 147, File = 91116f03 crop from center, $V_{\text{set}} = -100$ mV, $I_{\text{set}} = 100$ pA

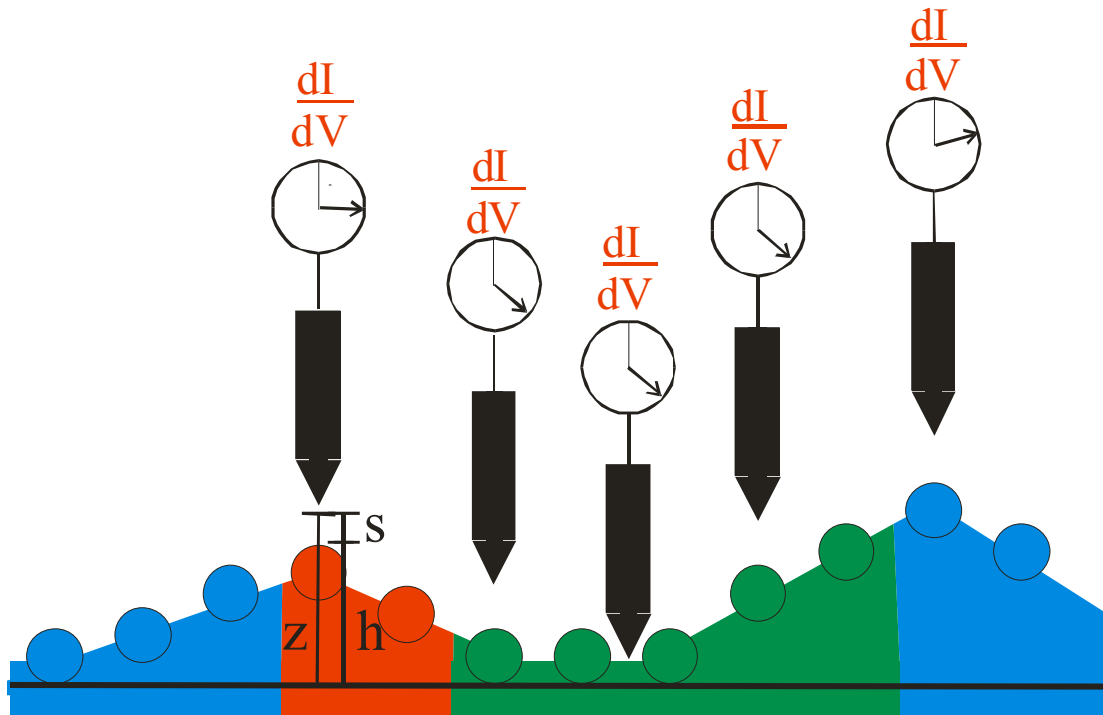


Figure 1.10: Schematic illustrating scanning tunneling spectroscopy. In this diagram LDOS is given schematically by color. Regions with different LDOS produce different values of dI/dV as indicated by the meters attached to each tip. Measurement of dI/dV is achieved in the following manner. At each x,y location where spectroscopic information is desired, the z position of the tip is adjusted so that the set point current is established. Then the feedback is turned off and the tip z -position is fixed. A small AC voltage (dV) is added to the DC bias voltage creating an AC modulation in the current (dI) which is measured with a lock-in amplifier. The dI signal is recorded for each voltage (V) at which spectroscopic information is desired. After the spectroscopic measurements are complete at that location, the feedback is turned back on and the next x,y position is sought. Thus dI/dV is measured as function of x,y position and bias voltage.

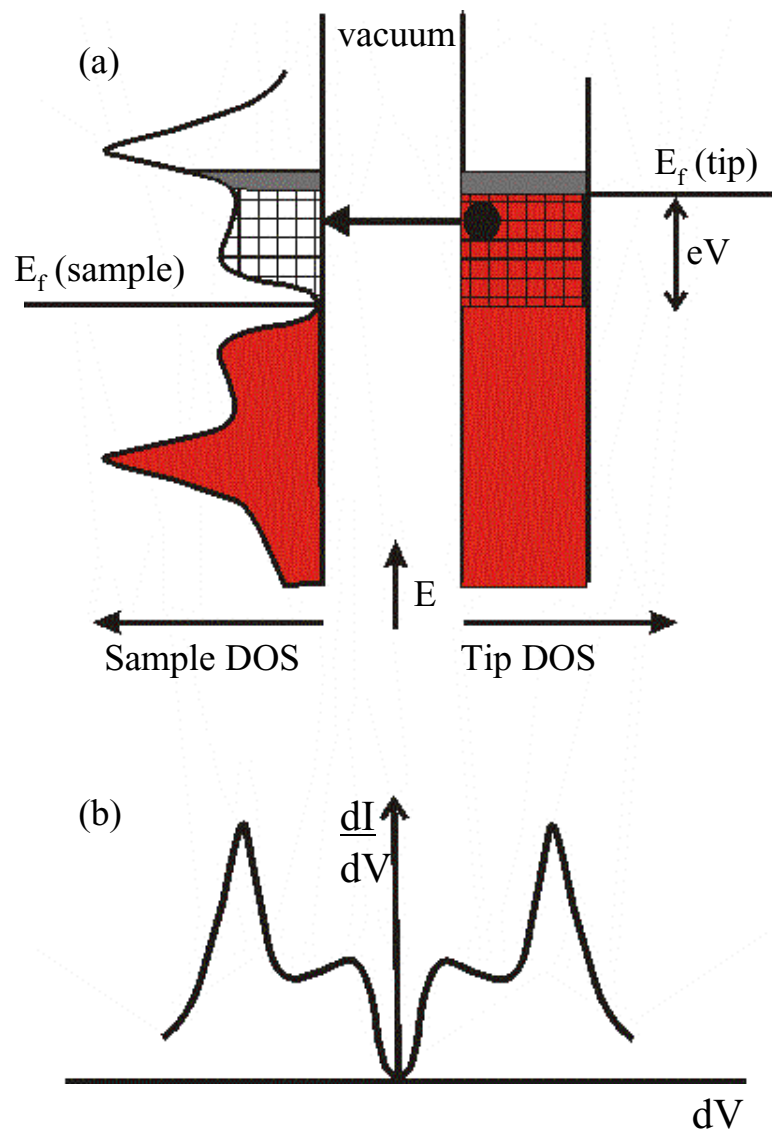


Figure 1.11: Technique for making a direct measurement of dI/dV . (a) Diagram indicating how to make a direct measurement of dI/dV . The black outlines indicate the density of states. Filled states are given in red. The total current which flows depends on the product of the hatched areas. When the bias is modulated by an amount given by the height of a gray shaded area, a modulated current signal is detected which is proportional to the product of the two gray shaded areas. Given knowledge of the magnitude of the bias modulation and the assumption that the tip LDOS is constant, the sample LDOS may then be determined from this measurement of the modulated current signal. (b) Shows the resulting plot of dI/dV vs. V which can be generated from such a direct measurement of differential conductance.

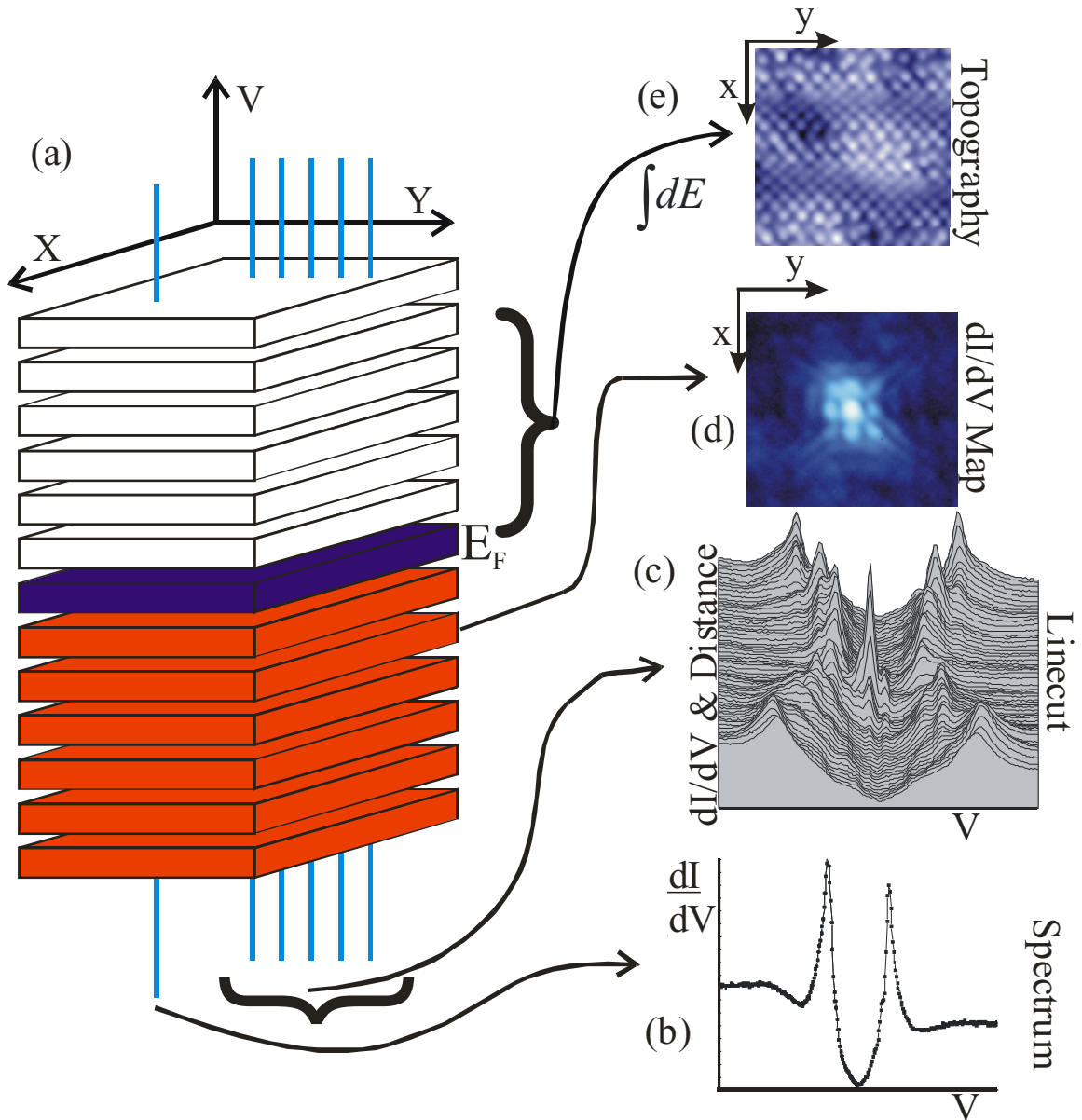


Figure 1.12: Data-sets which can be taken with an STM.

(a) Since an STM can measure $dI/dV(x,y,V)$, this figure schematically represents the x,y and V values at which an STM can measure the differential conductance. Each plane represents a different value of the tip-sample bias V , and the lateral position on the plane gives the x,y position of the tip. Filled states are given in red. The plane at the Fermi energy ($V=0$) is shown in blue. Panels (b) - (e) show subsets of this full data-set. The relation of the subset to the full data-set is shown schematically, and the name of each subset and a typical example of each from BSCCO is shown.

Topography: Run =124, File =90419a13, $V_{\text{set}} = -100$ mV, $I_{\text{set}} = 100$ pA

dI/dV Map: Zn resonance, Run 124, File =90410b01, $V_{\text{set}} = -200$ mV, $I_{\text{set}} = 200$ pA

Linecut: Run = 122, File = 90302i:0-121, $V_{\text{set}} = -100$ mV, $I_{\text{set}} = 100$ pA

Spectrum: Run = 147, File = 91126153, $V_{\text{set}} = -200$ mV, $I_{\text{set}} = 200$ pA

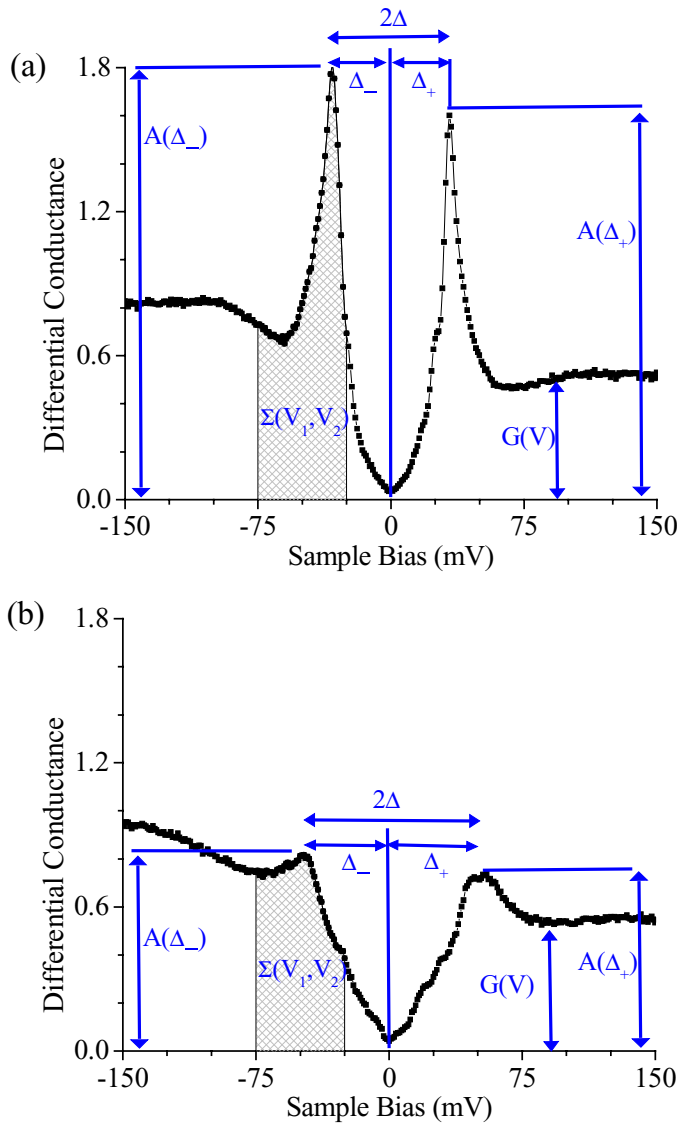


Figure 1.13: BSCCO spectra illustrating parameter definitions.

Panels (a) and (b) show two qualitatively differently shaped spectrum which nonetheless share several characteristics. Both spectra have low differential conductance near zero bias. Moving in either direction from zero bias, the differential conductance rises and then falls creating a peak. The energetic position of this peak is defined as Δ and the height of this peak at negative bias as $A(\Delta)$. The area under the curve between the two specified voltages is $\Sigma(V_1, V_2)$.

Run = 147, File = 91126a68 & 91126153, $V_{\text{set}} = -200$ mV, $I_{\text{set}} = 200$ pA

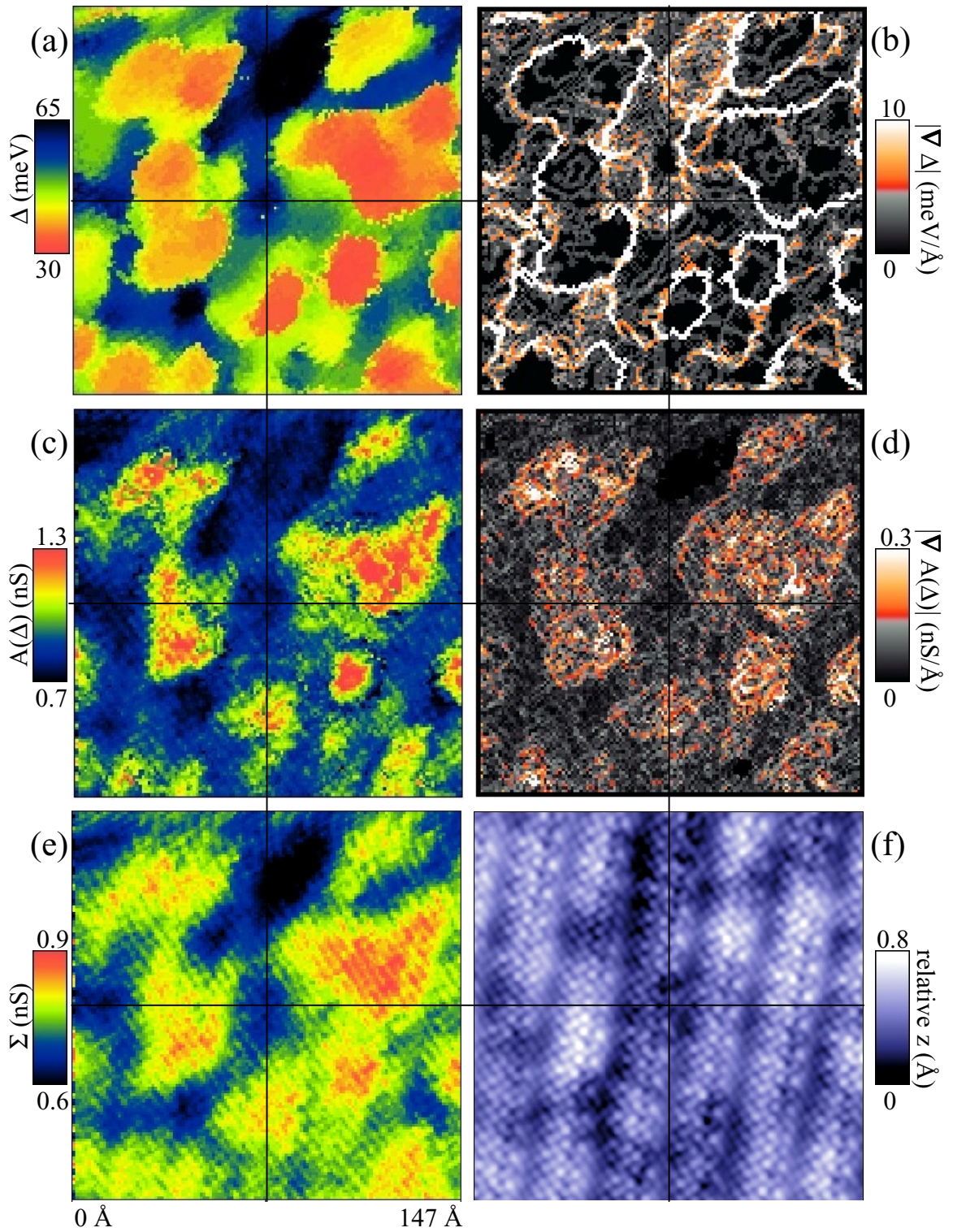


Figure 1.14: Example of parameter maps from BSCCO.

All the parameter maps shown here were extracted from a single spectral survey and thus represent the same area. The parameter which is mapped in each panel is shown next to the colorbar. (f) is a topography of the same area.

Run = 159, File = 01104b03 & 01105a00, $V_{\text{set}} = -200$ mV, $I_{\text{set}} = 200$ pA

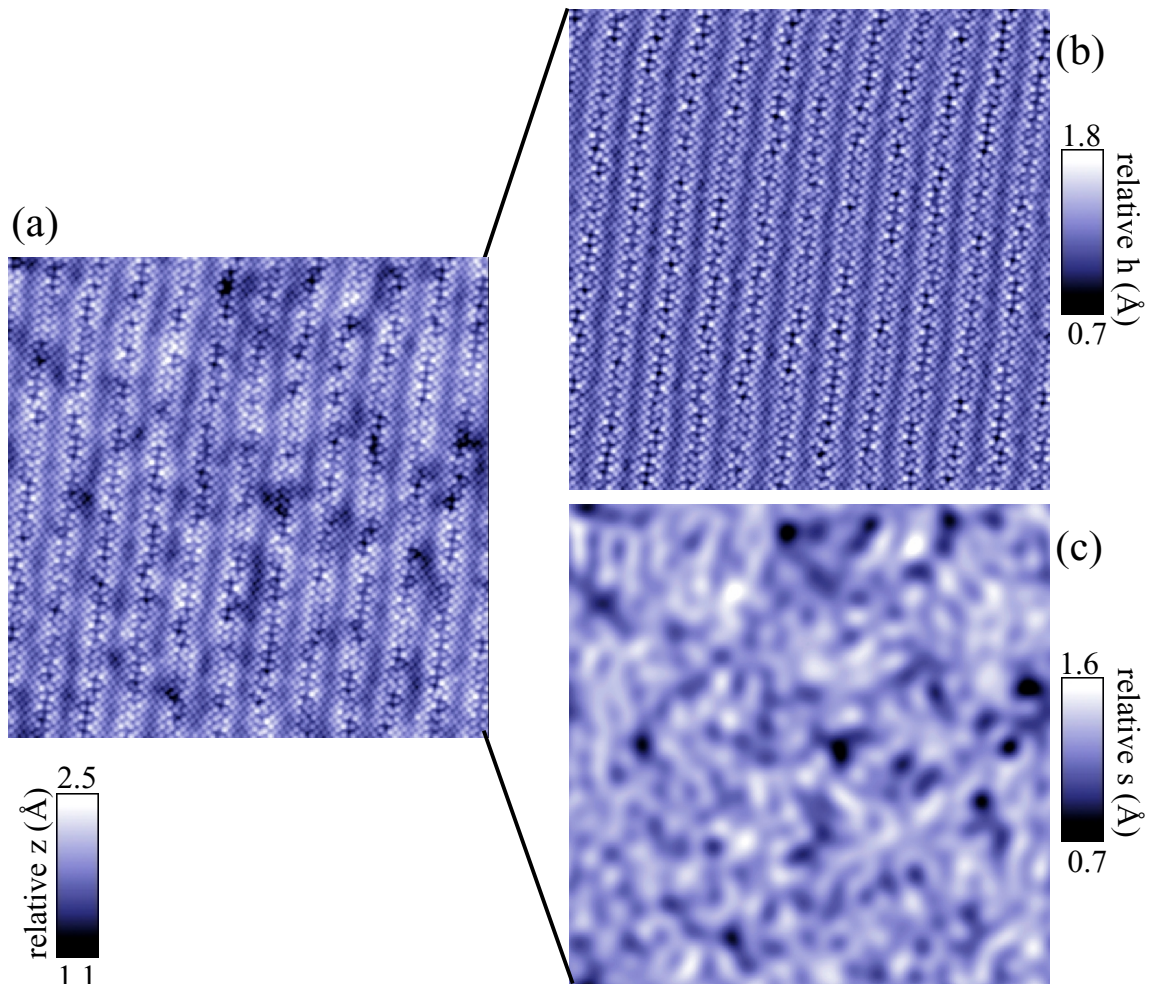


Figure 1.15: Fourier filtering the topography to find the relative variations in tip-sample separation. (a) shows the original 283 Å square topography which is a map of z . This topography is Fourier transformed and only those wavelengths which correspond to the atomic corrugation and to the supermodulation are kept/removed. The resulting image is inverse Fourier transformed to produce panel (b)/(c) which is a map of h/s . (d) shows a histogram of the values of s found in (c). The histogram shows variations with respect to the mean value, \bar{s} .

Run = 147, File = 91116f01, $V_{\text{set}} = -100$ mV, $I_{\text{set}} = 100$ pA

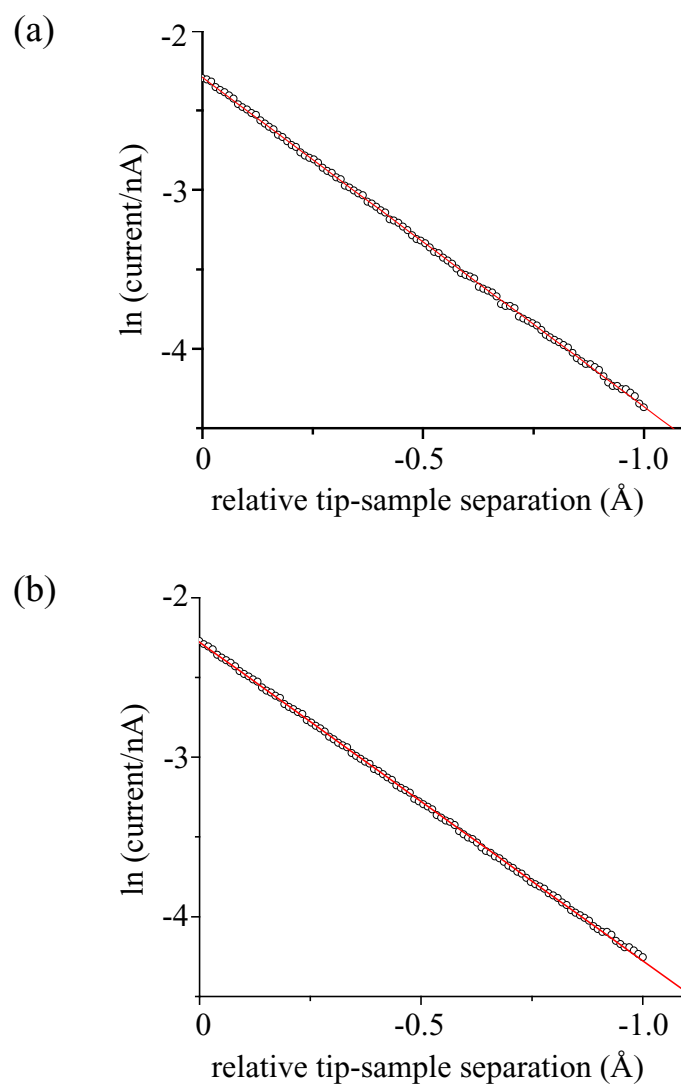


Figure 1.16: Measurement of s_0 - the current decay length-scale for tip withdrawal. Given Equation 1.5: $I = I_0 \exp(-s/s_0)$, s_0 may be found by plotting $\ln(I)$ against the tip-sample separation, s . Such plots are shown for two different tips and samples in (a) and (b) above. The red line is a fit to the data, which in both cases yielded an s_0 of 0.5 \AA .

(a) Run = 159, File = 01017a03, $V_{\text{set}} = -100 \text{ mV}$, $I_{\text{set}} = 100 \text{ pA}$

(b) Run = 147, File = 91112a01, $V_{\text{set}} = -100 \text{ mV}$, $I_{\text{set}} = 100 \text{ pA}$

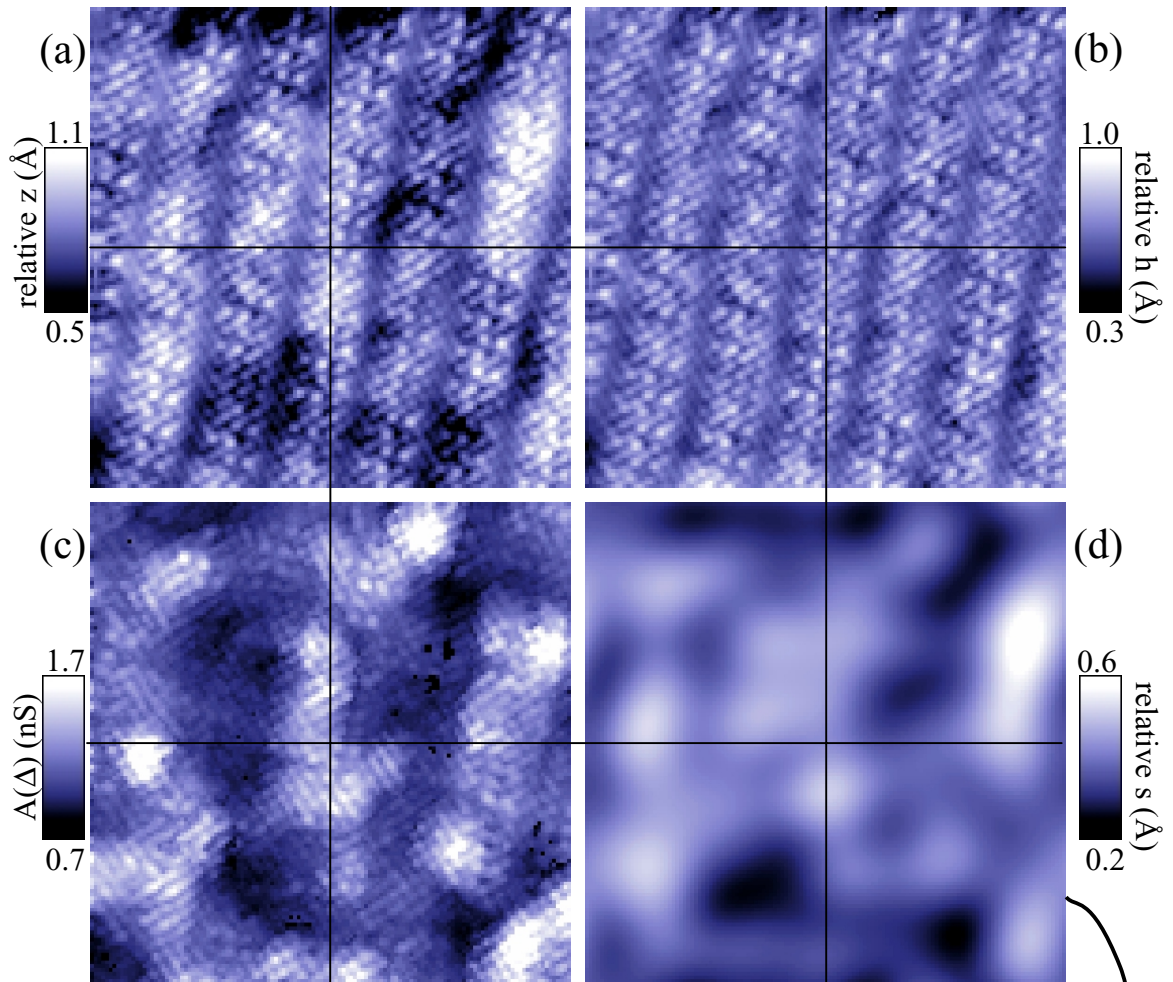


Figure 1.17: Trend in $A(\Delta)$ as a function of tip-sample separation.

(a): 147 Å square topography as measured by STM. (b): Fourier filtered version of (a) keeping only atomic and supermodulation wavelengths. (c): $A(\Delta)$ -map of the same region. Map was extracted from a simultaneously acquired spectral-survey. (d): Fourier filtered version of (a) with atomic and supermodulation wavelengths removed.

(e): Plot of a random selection of 20% of the points in (c) against the corresponding points in (d). The trend in (e) demonstrates that in general points with higher $A(\Delta)$ were taken with higher relative tip-sample separation, s . The red line is a fit to the data. The black lines are guides to the eye.

Run = 159, File = 01025d02, $V_{\text{set}} = -200$ mV, $I_{\text{set}} = 200$ pA

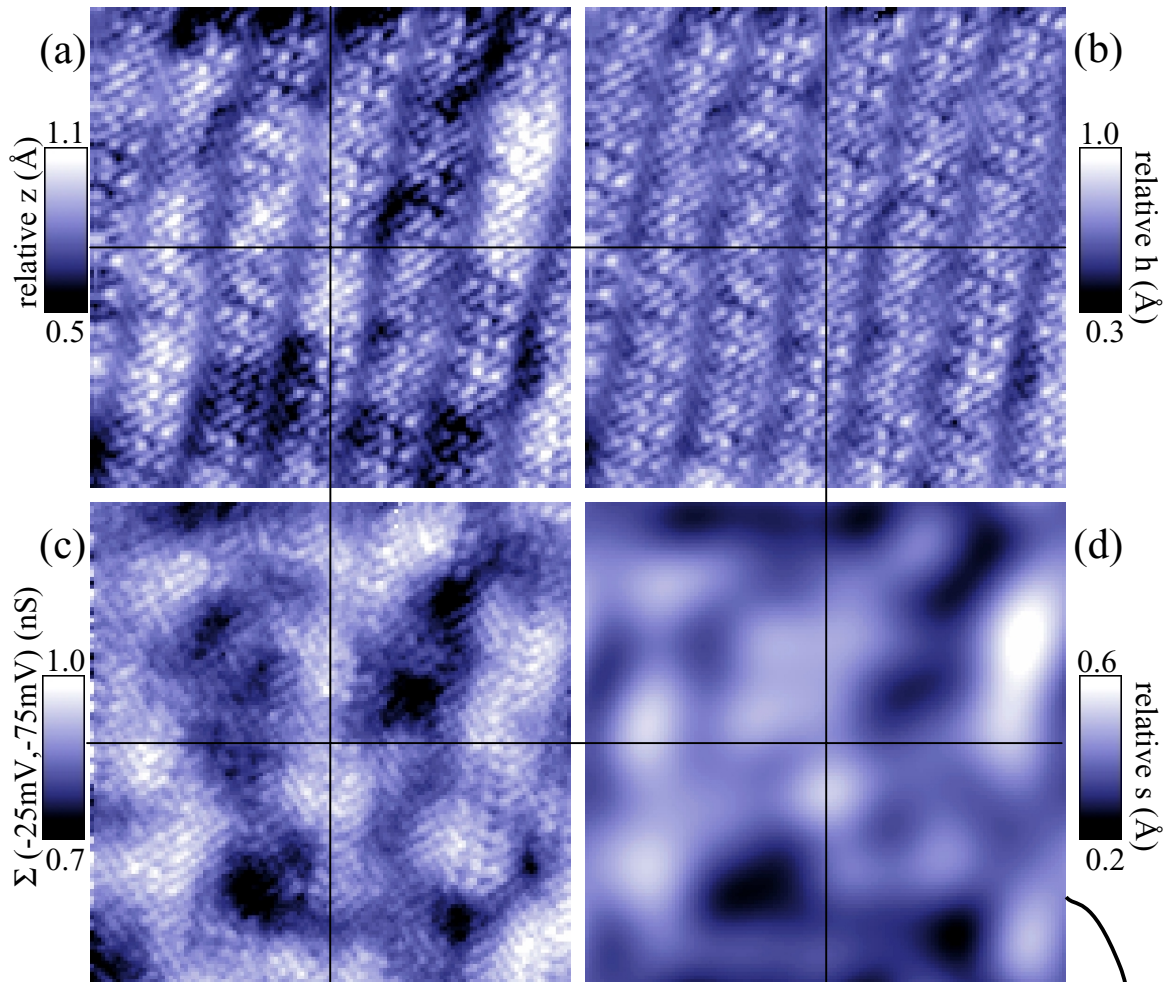


Figure 1.18: Trend in $\Sigma(\Delta)$ as a function of tip-sample separation.

(a): 147 Å square topography as measured by STM. (b): Fourier filtered version of (a) keeping only atomic and supermodulation wavelengths. (c): $\Sigma(\Delta)$ -map of the same region. Map was extracted from a simultaneously acquired spectral-survey. (d): Fourier filtered version of (a) with atomic and supermodulation wavelengths removed.

(e): Plot of a random selection of 20% of the points in (c) against the corresponding points in (d). The trend in (e) demonstrates that in general points with higher $\Sigma(\Delta)$ were taken with higher relative tip-sample separation, s . The red line is a fit to the data. The black lines are guides to the eye.

Run = 159, File = 01025d02, $V_{\text{set}} = -200$ mV, $I_{\text{set}} = 200$ pA

Chapter 2

Catalog of Data

The purpose of this chapter is to provide a catalog of data which is presented in as uniform and objective manner as is possible. Such a catalog serves several purposes. First, it makes generally available a large amount of data for future study and interpretation by others in the field. Second, in the chapters following this one, I will present a hypothesis about the nature of the electronic structure of BSCCO. In support of this hypothesis I will use carefully chosen data which is presented in a particular format in order to most clearly illustrate the several points which make up the hypothesis. Thus, an additional purpose of this catalog is to permit readers to view a large quantity of uniformly presented data, in order to determine the general validity of the points for themselves.

The remainder of this chapter is concerned with the following two topics. First, I give a general overview of the data presented both in the data catalog and in the thesis as a whole. This overview explains the meaning of run number and file names used throughout the thesis. The second section is description of the figures in the data catalog.

2.1 Overview of the Data Presented in This Thesis

All the results presented in this thesis were obtained on UHV cold-cleaved $\text{Bi}_2\text{Sr}_2\text{CaCu}_2\text{O}_{8+\delta}$ single crystals which were studied in vacuum at 4.2 K using a scanning tunneling microscope (STM)²⁸. The data has been collected in the course of many data-runs, on many samples, and over a number of years by myself and several colleagues. The chart below summarizes the runs which produced data *presented* in this thesis. In addition there were multiple runs resulting in data which are not given in the chart since that data was not presented in this thesis. The run number should be taken to be equivalent to a sample number since in each data run we study a single sample using a single STM tip²⁹.

Within a given run each distinct data set (topography, linecut, spectral-survey, etc.) is given a filename. The format of the filename is [YMMDDSNN] as explained in the chart below.

In this entire thesis, for all figures which contain data, the run number and filename will be given in the figure caption. Use of the run number and filename in conjunction with the two charts in this section should permit the reader to determine the context of the data, including its temporal relationship to other data presented.

²⁸ See Appendix 2 for a complete description of the data acquisition parameters.

²⁹ The tip is cleaned by field emission against a gold target at the beginning of the run. The tip is subsequently not deliberately altered during the course of the run, although there are occasionally small spontaneous 'tip changes' which are probably due to a slight relocation of an atom on the end of the tip.

Table 2.1: Summary of Runs and Samples for Data Presented in this Thesis³⁰

Run	Dates	Sample impurity-doping % Cu sites	Sample oxygen-doping	T _c (width) in K	Data primarily collected by
122	March 2 - 10, 1999	~0.6% ³¹ Zn	as-grown	84 (4) ^{31,32}	Pan ³³ , Hudson ³⁴
124	April 7 - 19, 1999	0.6 % Zn ³⁵	as-grown	84 (4) ³²	Hudson
147	Nov 9 -Dec 15, 1999	0.5 % Ni ³⁵	as-grown	83 (4) ^{32,36}	Hudson, Lang
155	Aug 13-20, 2000	none ³⁷	underdoped	79 (5)	Lang
159	Oct 12 - Dec 1, 2000	none ³⁷	underdoped	79 (5)	Lang

Table 2.2: Format of Data Filenames

Y	MM	DD	S	NN
year	month	day of the	series within	number within
9 = 1999	e.g. 03 = March	month	the day	the series
0 = 2000	12 = December			

The three earlier data sets presented in this thesis (122, 124, 147) were collected in the course of our studies of impurity atoms in BSCCO [Pan 2000A, Hudson 2001]. The BSCCO samples studied contained either Zn or Ni impurities at some relatively low concentration. Outside of the region of influence of these impurities (< 15 % of the area), we assume that we see the intrinsic properties of pure BSCCO. This assumption is based on the observation that the spectra and phenomena observed in these impurity doped samples are comparable to those in samples with no impurities. In addition, we showed that the signature of the impurity atoms is only seen in a very limited region [Pan 2000A, Hudson 2001]. Thus these data sets are useful for studying the intrinsic inhomogeneity in the electronic structure of BSCCO which is the focus of this thesis.

The two later data sets on underdoped BSCCO (155, 159) were taken specifically for the study of inhomogeneity in electronic structure. Of the two data sets, run 159 is the most extensive and comprises the majority of the data presented in this thesis. Much of the

³⁰ The runs listed here are only those which produced the data presented in this thesis. There are numerous other runs that produced data which supports the conclusions presented in this thesis.

³¹ This number is an estimate.

³² The value of T_c for an impurity doped sample is not an accurate representation of the oxygen doping level in the sample since the presence of the impurities lowers T_c.

³³ Shuheng Pan. Present affiliation: Dept. of Physics, Boston University, Boston, MA 02215, USA.

³⁴ Eric Hudson. Present affiliation: Dept. of Physics, MIT, Cambridge, MA 02139-4301, USA.

³⁵ The percent given is defined as nominal percent substitution of Cu atoms by the given impurity. The actual percentage of substitution by these impurities may be somewhat lower than this value.

³⁶ The transition width is an estimate. Due to the presence of the magnetic Ni impurities, it is difficult to find a width for the transition when T_c is measured in a magnetometer.

³⁷ There are no deliberately doped impurities in these samples. They do contain a very small percentage (<0.1%) of unknown impurities.

data in run 159 is interconnected (i.e. multiple data sets covering the same region) and the interrelationship of the data is given in Figures 2.18 & 2.19 in the data catalog.

Although we do plan to look at other oxygen doping levels in future experiments, we chose to focus our first experiment on studies of inhomogeneity in *underdoped* BSCCO for several reasons. First, we already had some data on essentially optimally doped crystals (albeit in crystals with impurities), and we wished to study a significantly different doping. Second, the pseudogap state is found in the underdoped regime. Since the origin of this state and its interrelationship with superconductivity and the superconducting gap is still unexplained, we hoped to shed some light on these issues with our studies. Finally, since we conjectured that the random distribution of dopant oxygen atoms could be the origin of the inhomogeneity in the electronic structure, we thought it would be interesting to study a doping in which the statistics of small numbers of dopant atoms might lead to significant variations in local doping levels.

2.2 Description of The Data Catalog

2.2.1 Organization of the Data Catalog

The data presented in this catalog is organized into three sections with a summary section at the end. The three sections are arranged, roughly speaking, in order of diminishing sample coverage area and corresponding increase in detail. The first section contains *overview* maps which cover a relatively large (compared to the characteristic features discussed later) area. Each of the map-sets covers an area of about 550 Å square. The second section contains *detail* maps which cover a much smaller field of view than the overview maps, about 150 Å square, and have much higher spatial resolution. The third section contains linecuts which present data only along a single one-dimensional line; however, the advantage of these data-sets is that the raw spectral data can be viewed. The final summary section contains figures which show the interrelationship between all run 159 data.

Many specifics regarding the data presented are contained in the discussion in the remainder of this section 2.2. In general, information which is common to all figures in a given section is contained in the subsequent discussion in this section, and the figure captions contain only information which is specific to that figure.

2.2.2 Color Scales, Error in Sizes, Spatial Resolution, and Bad Pixels

This section consists of a few miscellaneous comments that are common to all the data of a particular type in the catalog.

For all linear dimensions given, the size quoted is determined by calibrating the scanner tube using the known lattice spacing of BSCCO. Multiple calibrations on the same sample and run generally produce calibrations within 3 % of one another. Thus all linear dimensions given in this chapter and elsewhere in this thesis are accurate to within this 3% margin of error.

All topographies are square and have a resolution of about $0.25 \text{ \AA} - 1 \text{ \AA}$ per pixel. All topographies are presented in a linear gray scale in which black is low and white is high. The histogram of values present in the topography has been centered on the color scale. The topographies have not been processed in any way except to flatten them. Flattening means that a plane has been fit to the topography and then subtracted in order to account for the overall slope of the sample.

All parameter maps are square and contain 128×128 pixels independent of their size in angstroms. All parameter maps are presented in the same linear gray scale as was used for the topographies. For all maps except Δ maps, lower values of the parameter are black and higher values are white. For Δ -maps the converse is true. For all parameter maps except Δ -maps, the histogram of values present in the map has been centered on the color scale. For all Δ -maps, the color scale runs from 25 meV to 70 meV independent of the histogram of Δ values present in the map.

All parameter maps have been created using the algorithm described in Appendix 1. In this catalog and throughout the thesis, for reasons discussed previously, Δ is always defined as $(\Delta_+ - \Delta_-)/2$. $A(\Delta)$ is defined as the height of the gap edge peak at negative bias, and Σ is the integral on the negative bias side of the spectrum between the stated energies.

I would like to make a few comments here about bad pixels that may appear in parameter maps (Δ , $A(\Delta)$, $\nabla \Delta$, and $\nabla A(\Delta)$ - maps) which rely on the peak picking algorithm. Appendix 1 provides a description of that algorithm and details pertaining to the origin of bad pixels. At this point, I will confine the comments on this topic to the statement that a bad pixel is created when the peak picking algorithm either fails to find a peak anywhere in the entire spectrum or when the algorithm picks an energy which doesn't correspond to the predominant gap-edge peak.. In either case, a bad pixel will appear as incongruously-discontinuous speckle. Such speckle, which can be a single pixel or a few pixels, appears as pure white in the Δ -maps and as pure black in the $A(\Delta)$ -maps. The reason for this is discussed in the Appendix. This comment is included here to aid the reader in distinguishing these bad pixels when viewing the data in this chapter.

2.2.3 Overview Maps and Histograms

The first section in the data catalog (Section 2.3) contains overview maps and corresponding histograms. For a given figure all the panels represent the same area of the sample. Specific dimensions are given on each figure, but all areas in this section are approximately 550 \AA square. All maps contain 128×128 pixels so the spatial resolution of maps in this section is approximately 4 \AA per pixel. The spatial resolution of the topography is approximately 1 \AA per pixel unless otherwise noted. Specifically, the panels show:

Panel (a): Δ -map.

Panel (b): Histogram of the values of Δ from panel (a). The mean and standard deviation for Δ are given.

Panel (c): $A(\Delta)$ -map.

Panel (d): Histogram of the values of $A(\Delta)$ from panel (c). The mean and standard deviation for $A(\Delta)$ are given.

Panel (e): Topography.

2.2.4 Detail Maps

The second section of the data catalog (Section 2.4) contains more detailed maps. For a given figure all the panels represent the same area of the sample. All areas in this section are 147 \AA^2 square. All parameter maps contain 128×128 pixels so the spatial resolution of maps in this section is 1.1 \AA per pixel. The spatial resolution of the topographies in this section is 0.29 \AA per pixel unless otherwise noted. Specifically, the panels show:

Panel (a): Δ -map.

Panel (b): $|\tilde{N} \Delta|$ -map.

Panel (c): $A(\Delta)$ -map.

Panel (d): $|\tilde{N} A(\Delta)|$ -map.

Panel (e): $\Sigma(-25 \text{ mV}, -75 \text{ mV})$ -map.

Panel (f): Topography.

2.2.5 Linecuts

The third section of the data catalog (Section 2.5) contains linecuts and corresponding topographies. Specifically, the panels show:

Panel (a): Linecut shown with sample bias -200 mV to $+200 \text{ mV}$.

Panel (b): Same linecut as in panel (a), but now shown with sample bias -80 mV to $+80 \text{ mV}$.

Panel(c): Topography with black line indicating the trajectory of the linecut.³⁸ The black circle at one end of the trajectory corresponds to the position of the thick black curve shown in panels (a) and (b).

³⁸ The error in determining the trajectory of a linecut on a topography is generally about $\pm 2 \text{ \AA}$ due to lateral drift between the tip and sample during the acquisition of the linecut data.

2.2.6 Summary of Spatial Interrelationships For Run 159 Data

The final section of the data catalog (Section 2.6) contains two figures which give the spatial interrelationships for the Run 159 Data.

Figure 2.18 shows the spatial interrelationships of all the Δ -maps from run 159. The file number for each panel is given on the panel. Recall that the file number gives the date that the file was taken, and so this figure also gives the temporal relationship between the data.

Figure 2.19 is a repeat of Figure 2.10; however the current figure shows the trajectories of two linecuts from run 159 on all the panels in the figure. As in the linecut section of the catalog, the circle at one end of the trajectory corresponds to the thick black curve in the corresponding linecut.

Section 2.3: Overview Parameter Maps and Histograms

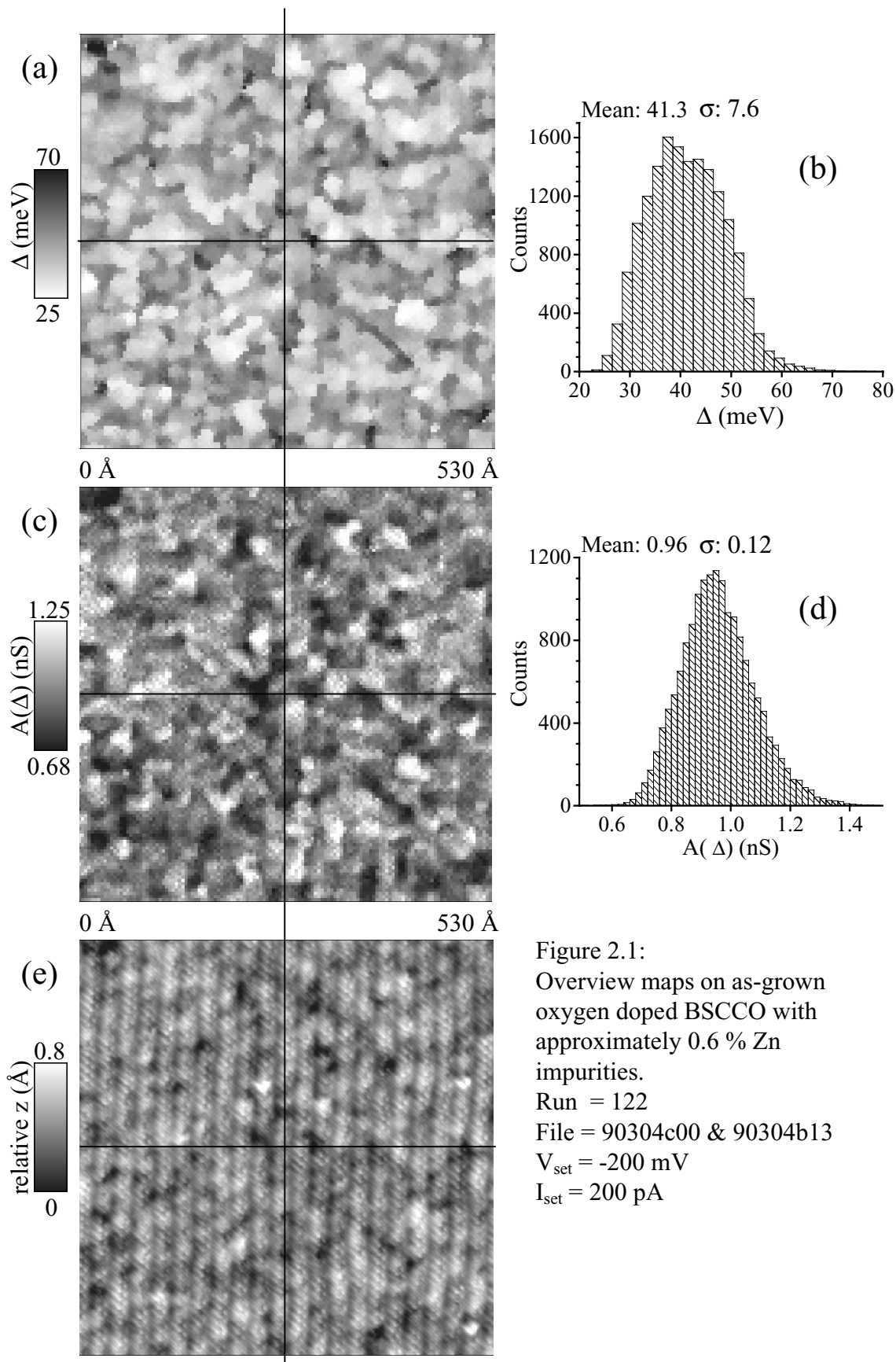


Figure 2.1:
 Overview maps on as-grown oxygen doped BSCCO with approximately 0.6 % Zn impurities.
 Run = 122
 File = 90304c00 & 90304b13
 $V_{\text{set}} = -200$ mV
 $I_{\text{set}} = 200$ pA

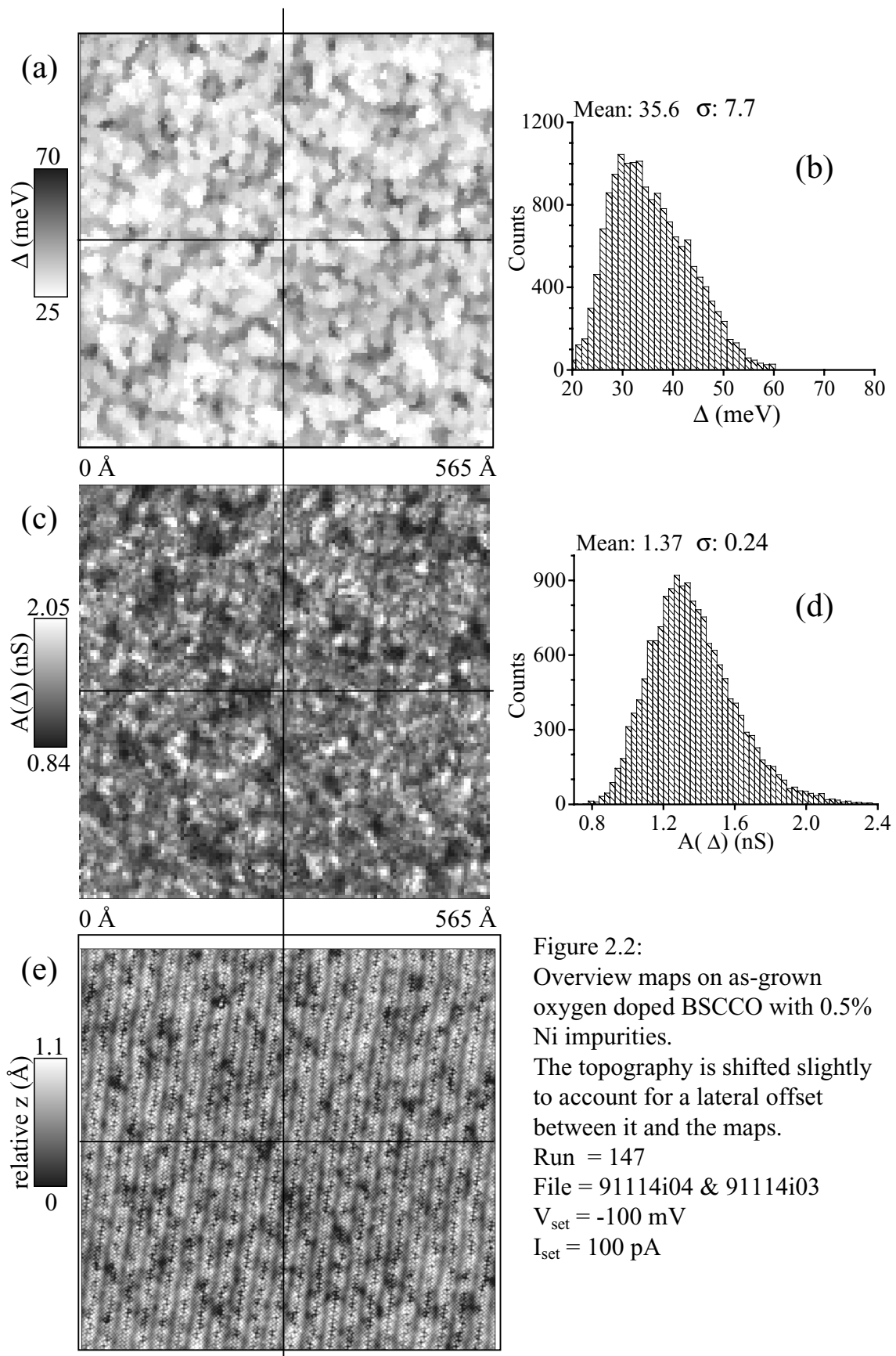


Figure 2.2:
 Overview maps on as-grown oxygen doped BSCCO with 0.5% Ni impurities.
 The topography is shifted slightly to account for a lateral offset between it and the maps.
 Run = 147
 File = 91114i04 & 91114i03
 $V_{\text{set}} = -100$ mV
 $I_{\text{set}} = 100$ pA

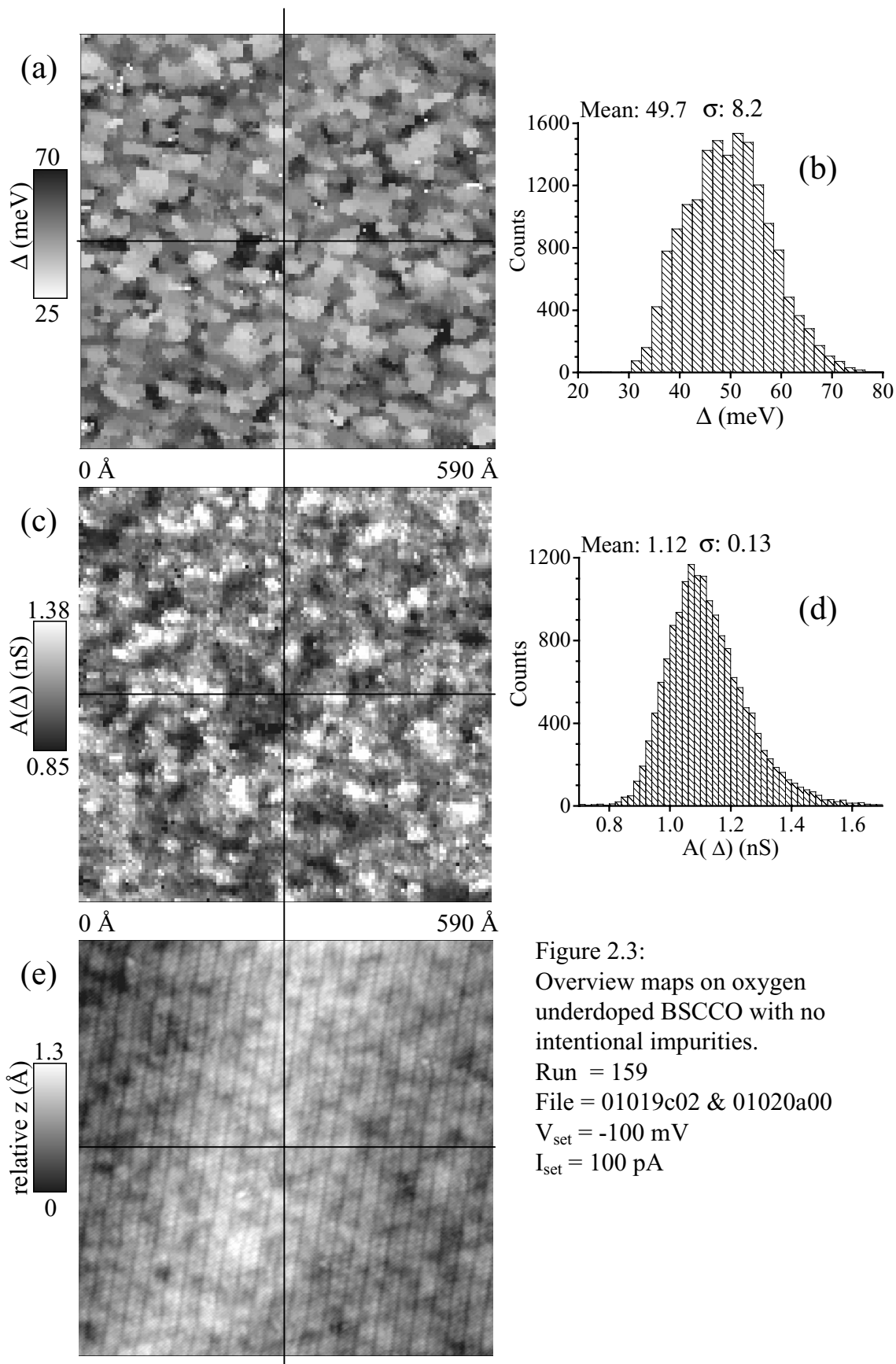


Figure 2.3:
 Overview maps on oxygen underdoped BSCCO with no intentional impurities.
 Run = 159
 File = 01019c02 & 01020a00
 $V_{\text{set}} = -100$ mV
 $I_{\text{set}} = 100$ pA

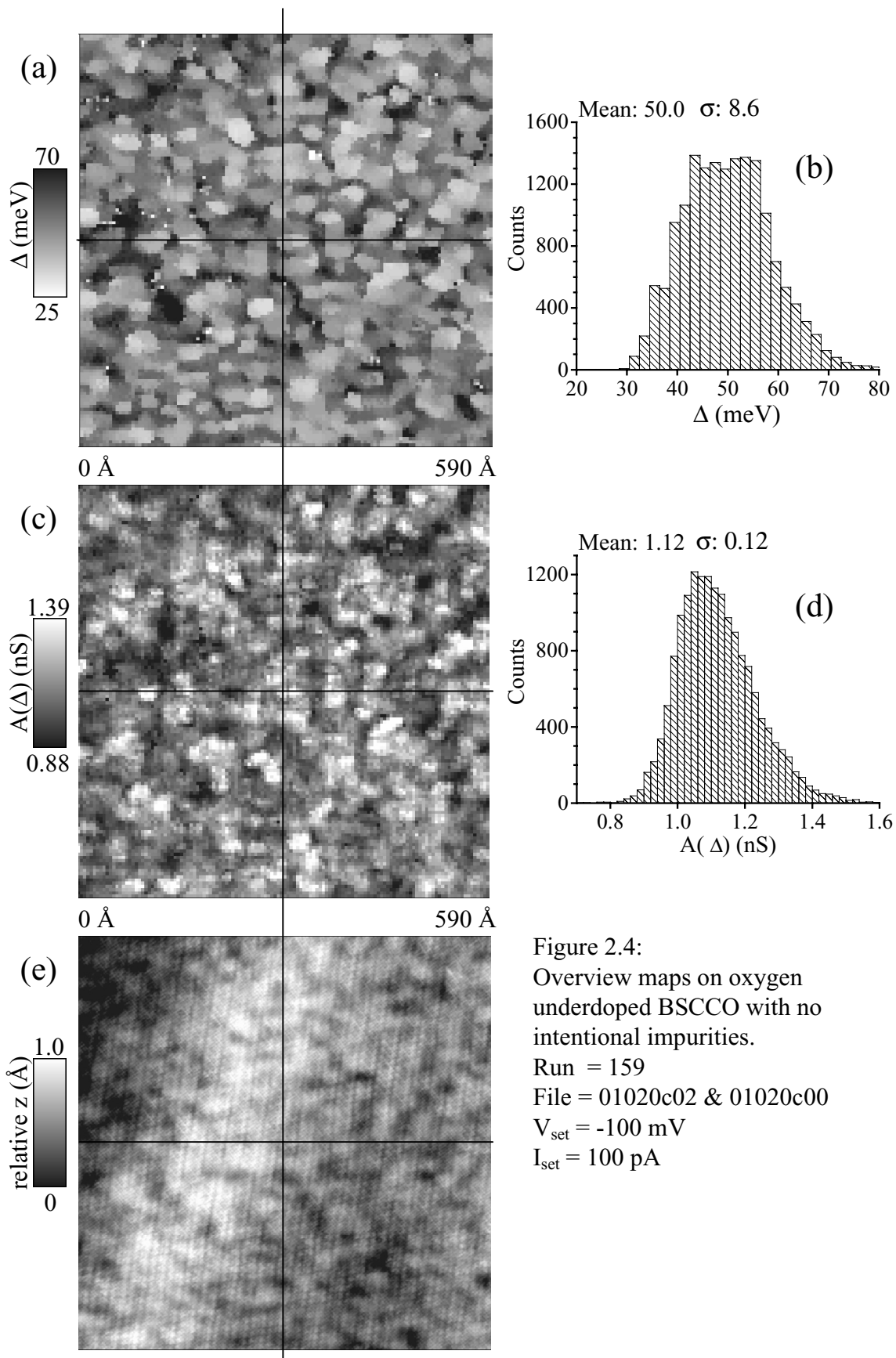


Figure 2.4:
 Overview maps on oxygen
 underdoped BSCCO with no
 intentional impurities.
 Run = 159
 File = 01020c02 & 01020c00
 $V_{\text{set}} = -100$ mV
 $I_{\text{set}} = 100$ pA

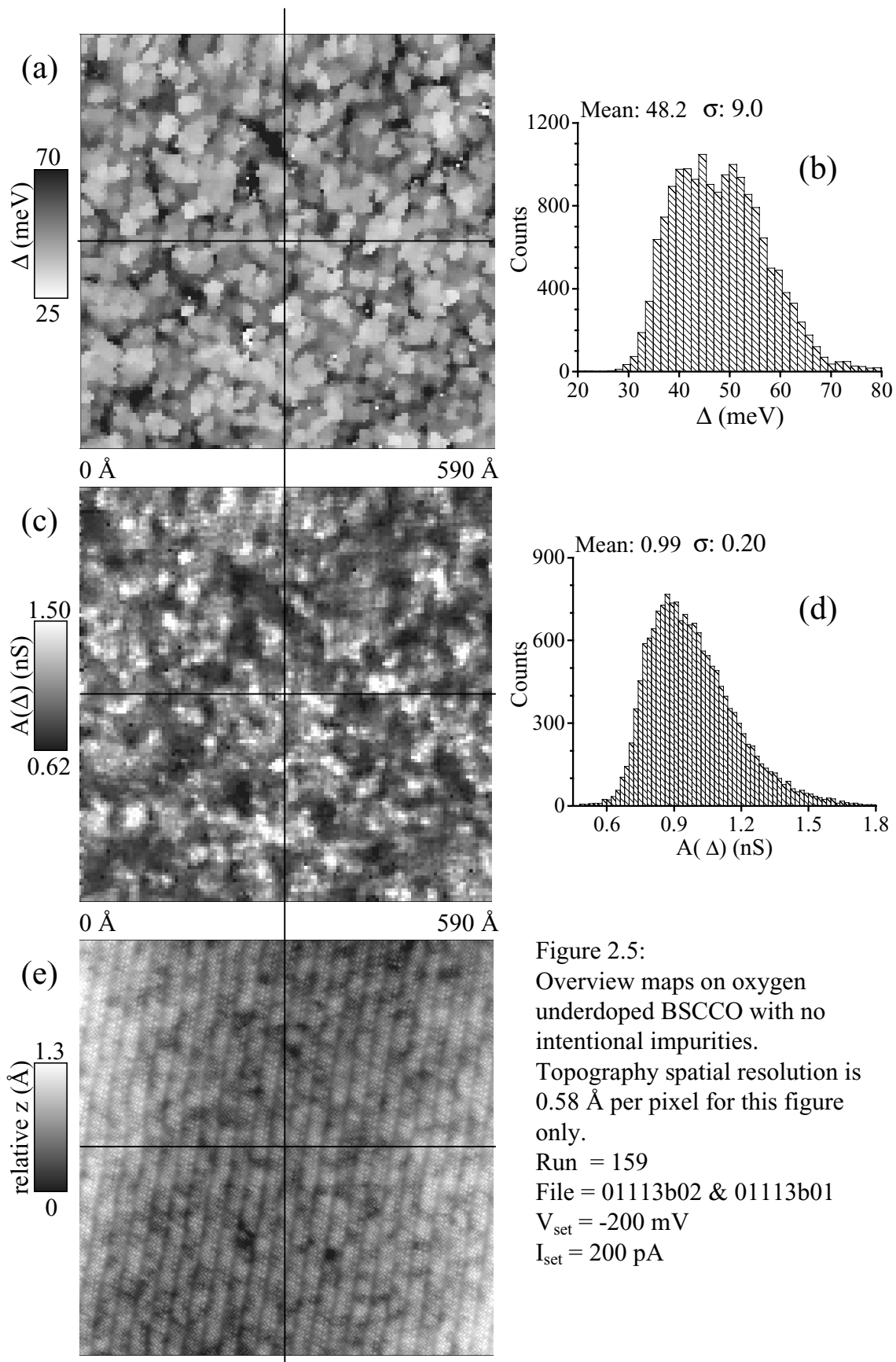


Figure 2.5:
 Overview maps on oxygen underdoped BSCCO with no intentional impurities.
 Topography spatial resolution is 0.58 Å per pixel for this figure only.
 Run = 159
 File = 01113b02 & 01113b01
 $V_{\text{set}} = -200$ mV
 $I_{\text{set}} = 200$ pA

Section 2.4: Detail Parameter Maps

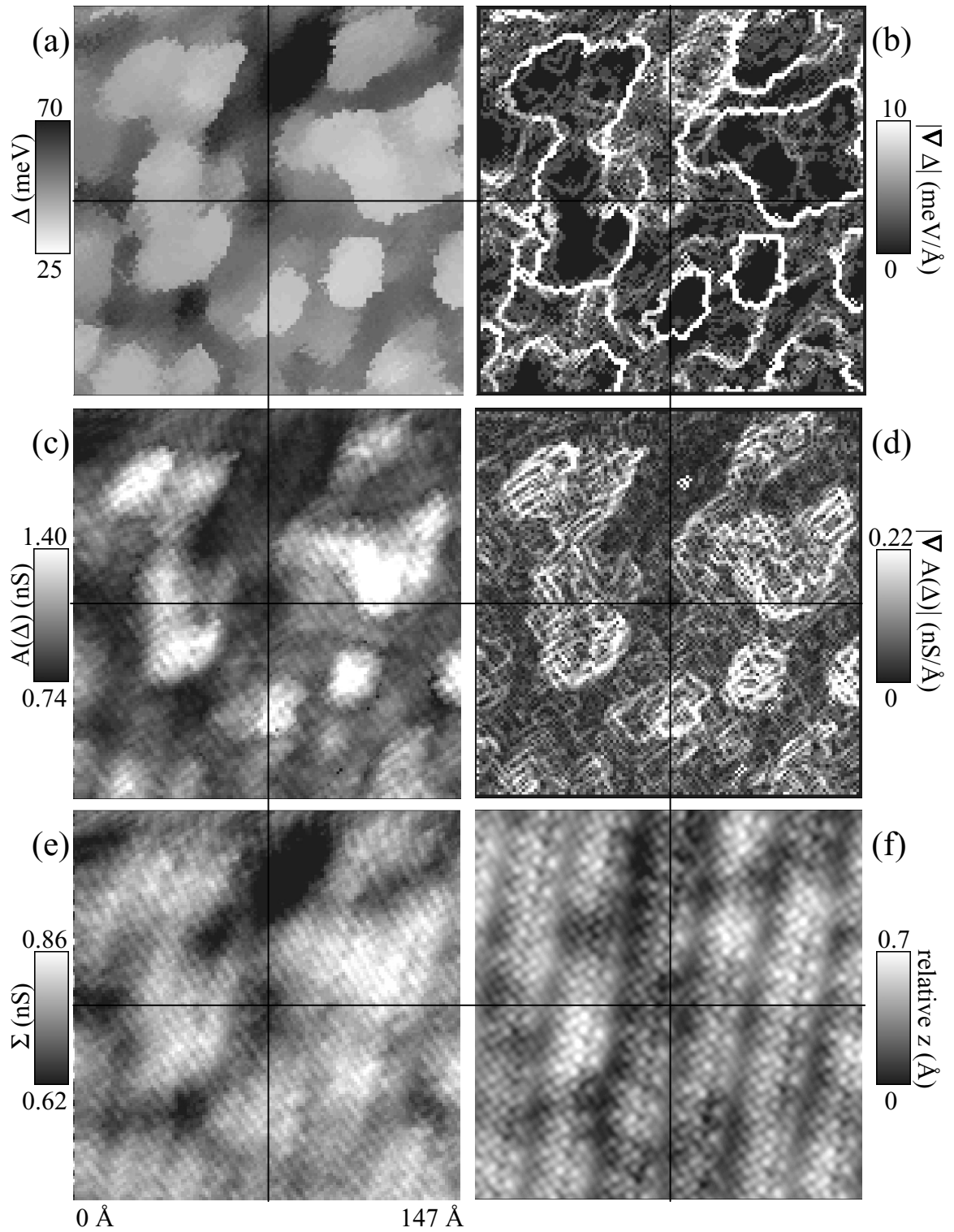


Figure 2.6: Detail maps on oxygen underdoped BSCCO with no intentional impurities. Run = 159, File = 01104b03 & 01105a00, $V_{\text{set}} = -200$ mV, $I_{\text{set}} = 200$ pA

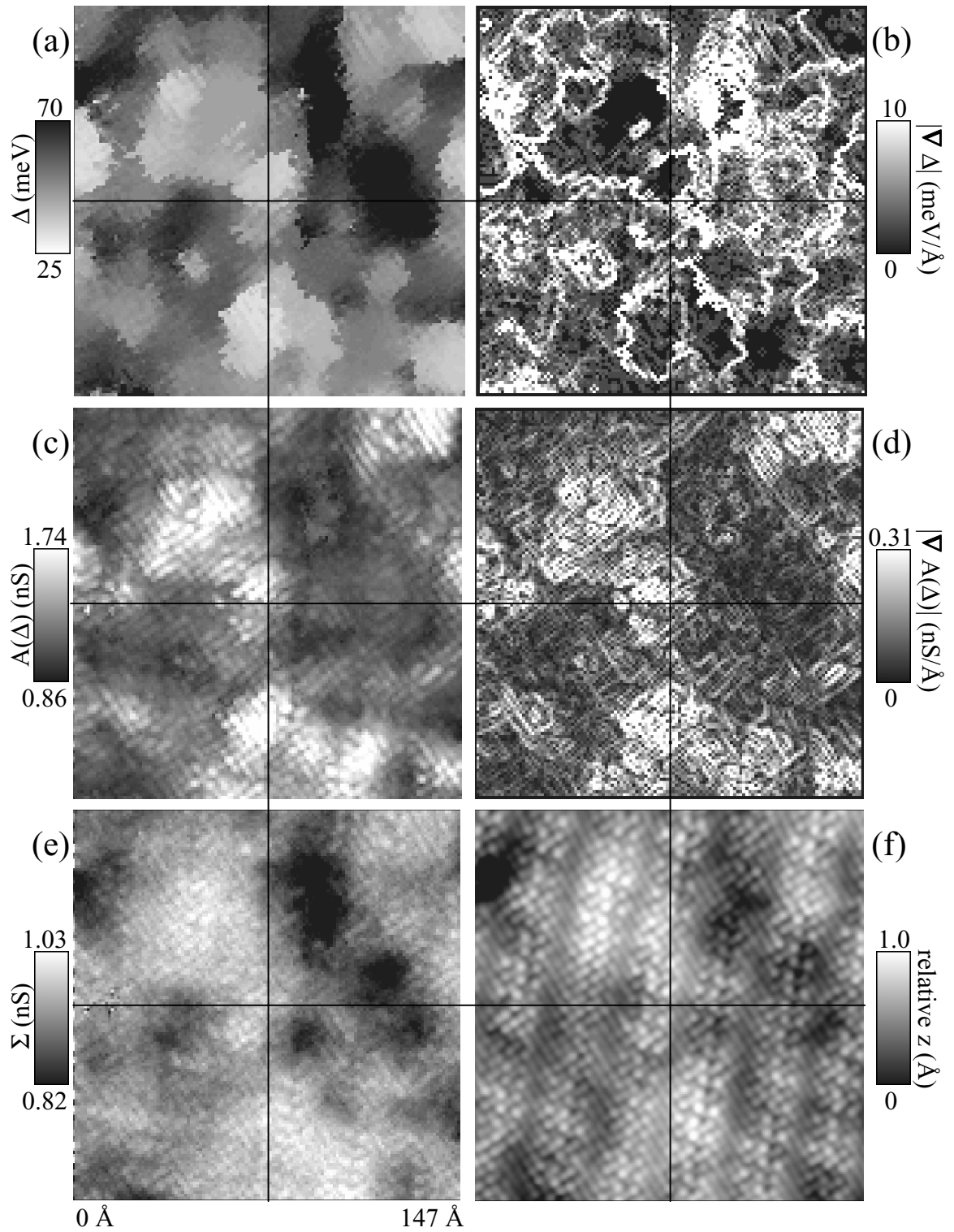


Figure 2.7: Detail maps on oxygen underdoped BSCCO with no intentional impurities. Topography spatial resolution is 0.58 \AA per pixel for this figure. Run = 159, File = 01021b02 & 01022a00, $V_{\text{set}} = -100 \text{ mV}$, $I_{\text{set}} = 100 \text{ pA}$

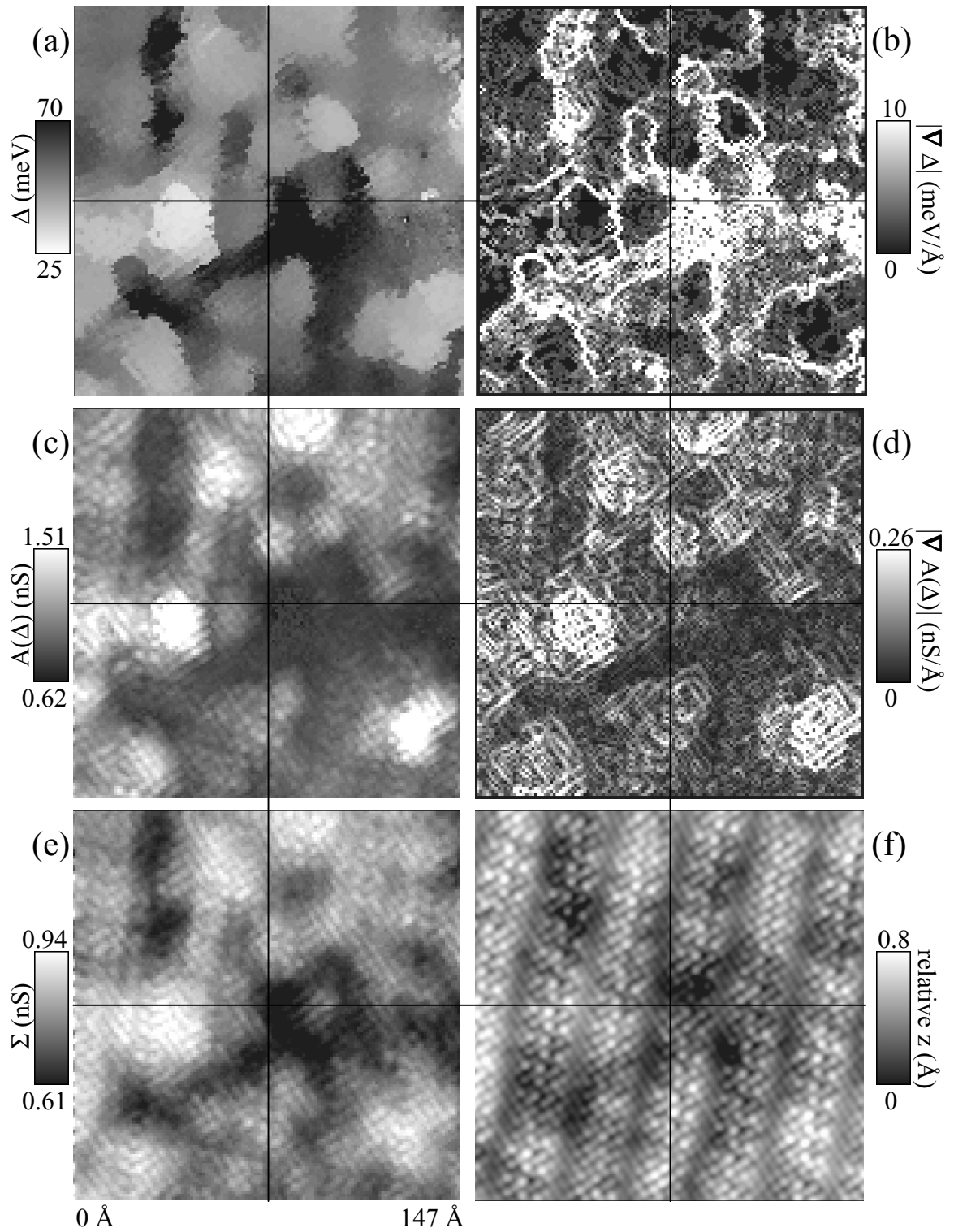


Figure 2.8: Detail maps on oxygen underdoped BSCCO with no intentional impurities. Run = 159, File = 01024n02 & 01025a00, $V_{\text{set}} = -200$ mV, $I_{\text{set}} = 200$ pA

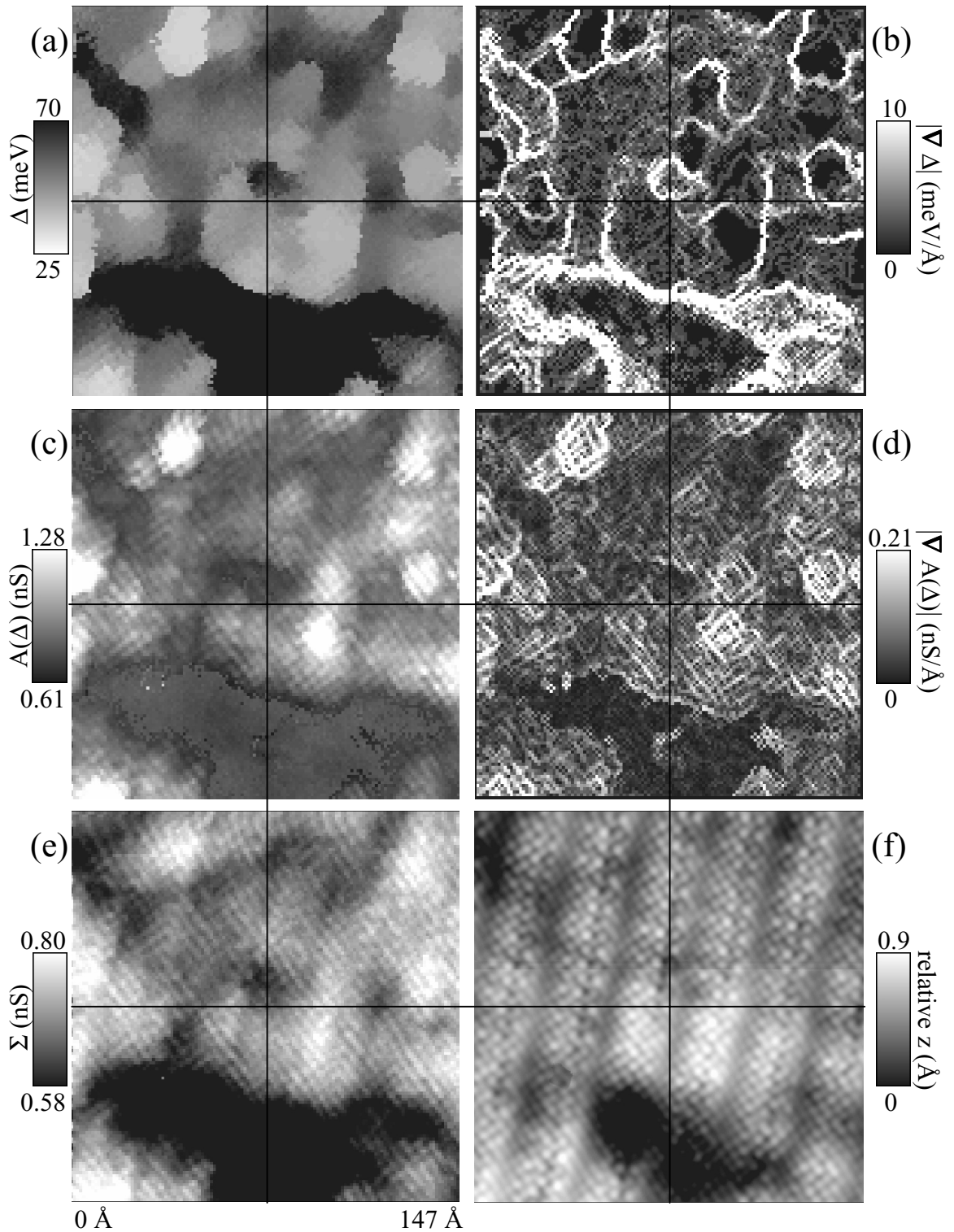


Figure 2.9: Detail maps on oxygen underdoped BSCCO with no intentional impurities. The large black region at the bottom of the maps consist of NP type spectra. See Figure 3.9 for an example of this type of spectrum and see Section A.1 for a discussion. Run = 159, File = 01103b02 & 01104a00, $V_{\text{set}} = -100$ mV, $I_{\text{set}} = 100$ pA

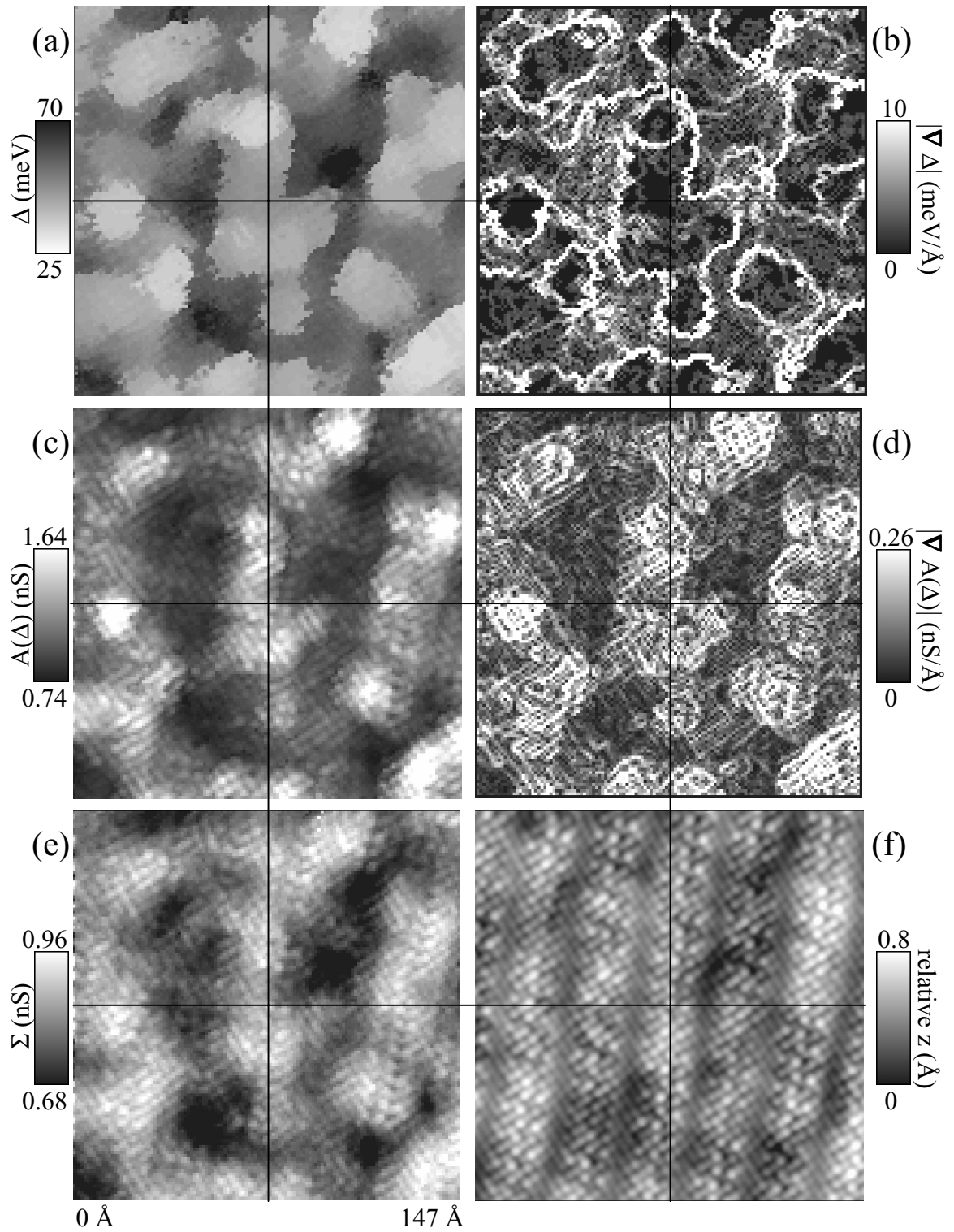


Figure 2.10: Detail maps on oxygen underdoped BSCCO with no intentional impurities. Run = 159, File = 01025d02 & 01026a00, $V_{\text{set}} = -200$ mV, $I_{\text{set}} = 200$ pA

Section 2.5: Linecuts

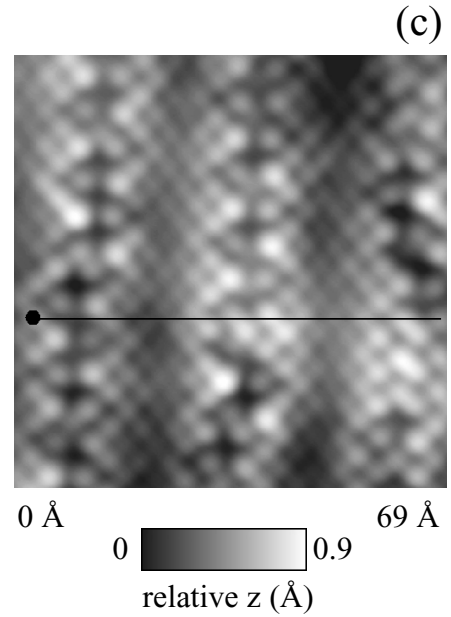
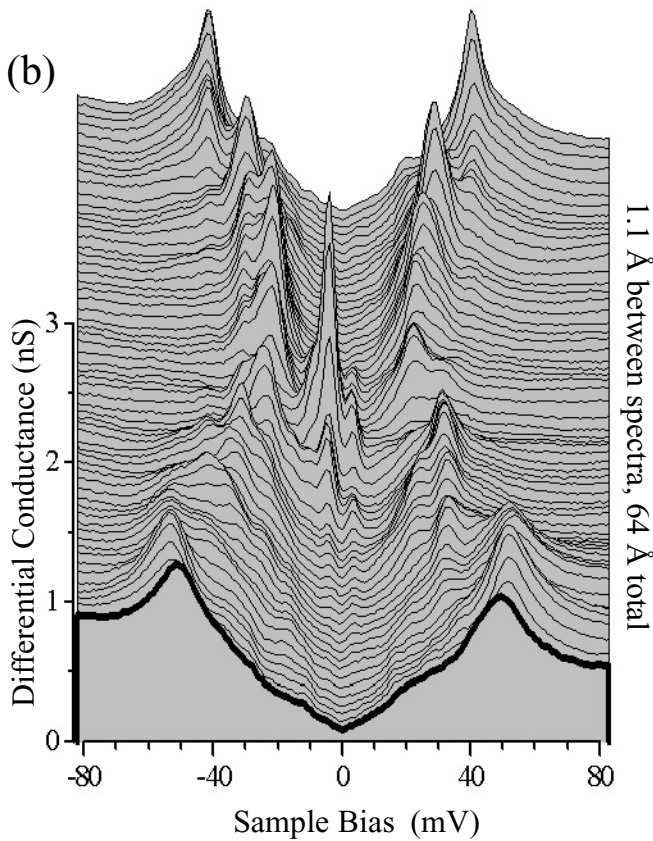
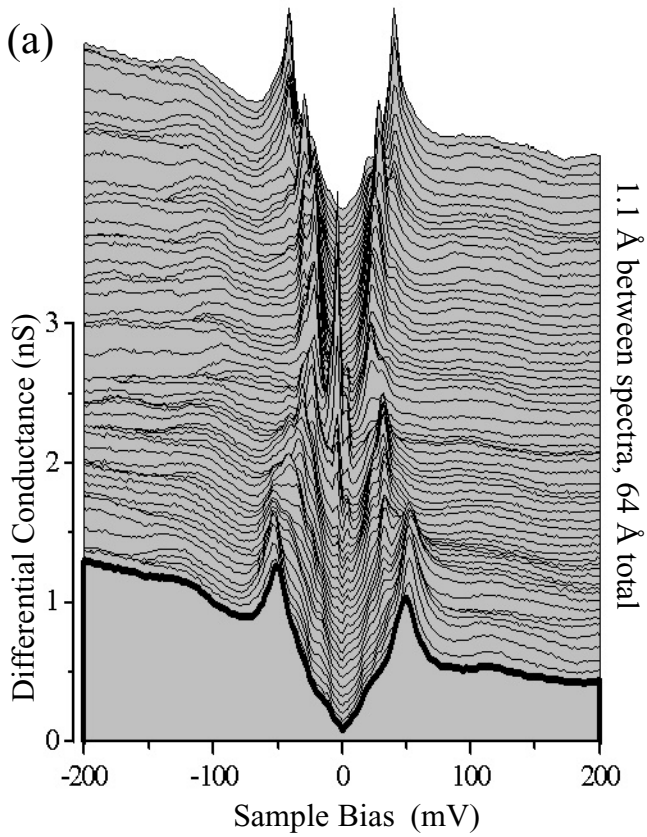


Figure 2.11:
 Linecut and topography on
 BSCCO with as-grown oxygen
 doping and approximately 0.6 %
 Zn impurities. The trajectory of
 the line traverses a single Zn
 impurity as indicated by the large
 resonance near zero bias.
 Run = 122
 File = 90302i:0-121 & 90303a00
 $V_{\text{set}} = -100$ mV
 $I_{\text{set}} = 100$ pA

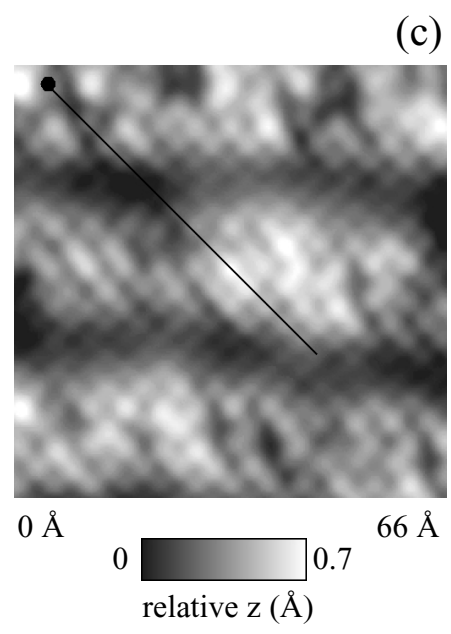
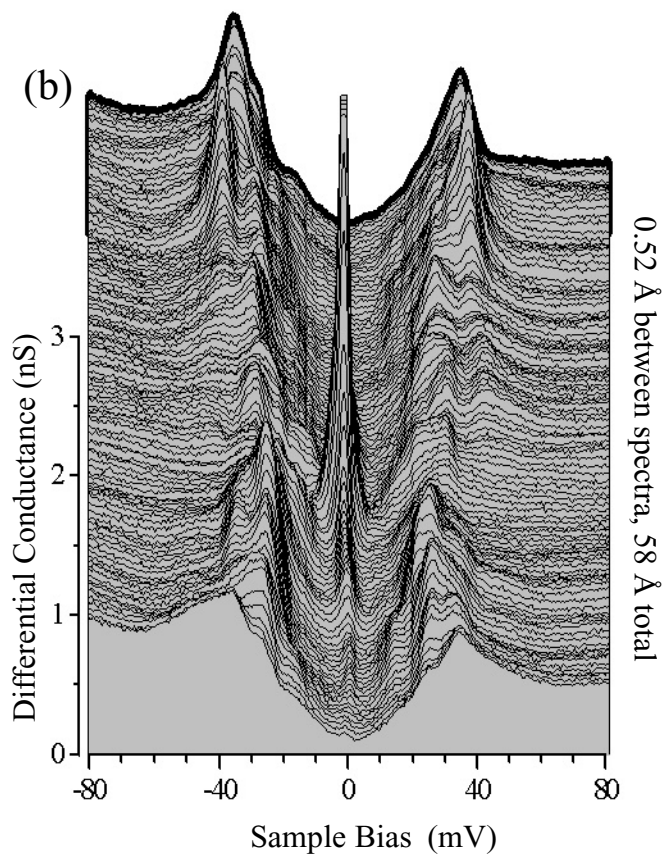
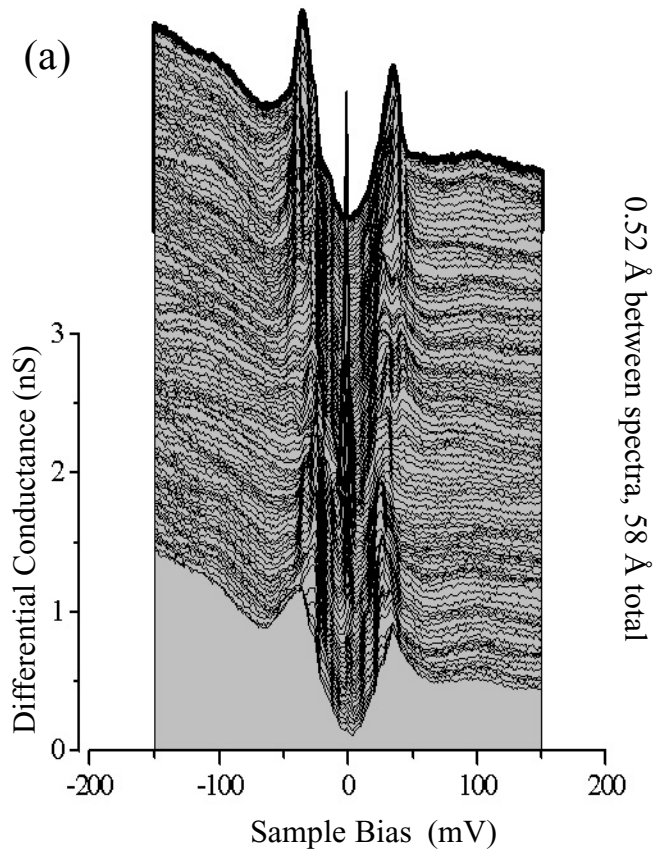


Figure 2.12:
 Linecut and topography on
 BSCCO with as-grown oxygen
 doping and 0.6 % Zn impurities.
 The trajectory of the line
 traverses a single Zn impurity as
 indicated by the large resonance
 near zero bias.
 Run = 124
 File = 90408a:0-112 & 90407g01
 $V_{\text{set}} = -200$ mV
 $I_{\text{set}} = 200$ pA

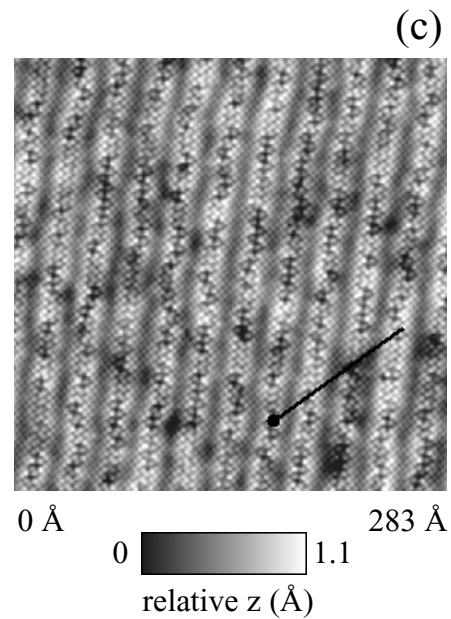
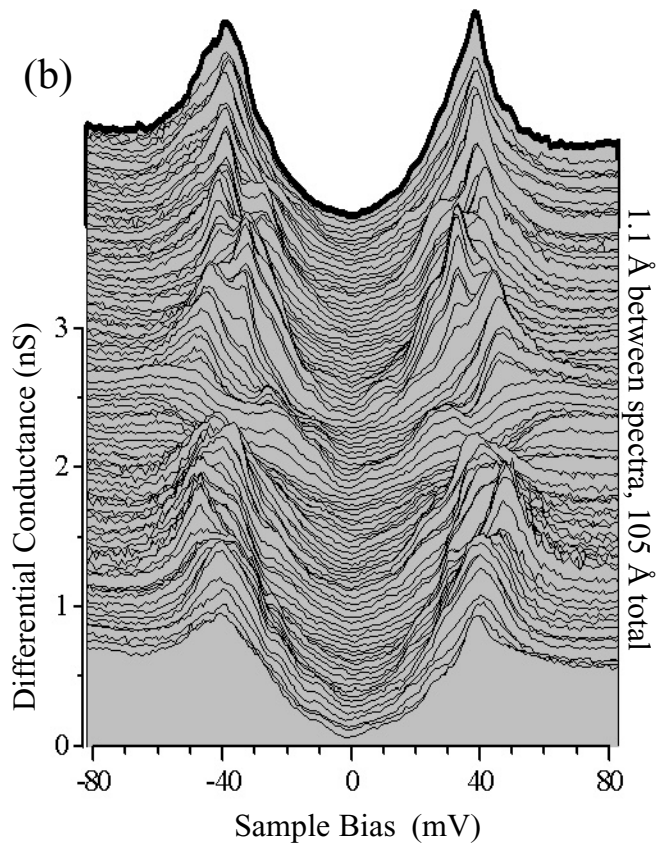
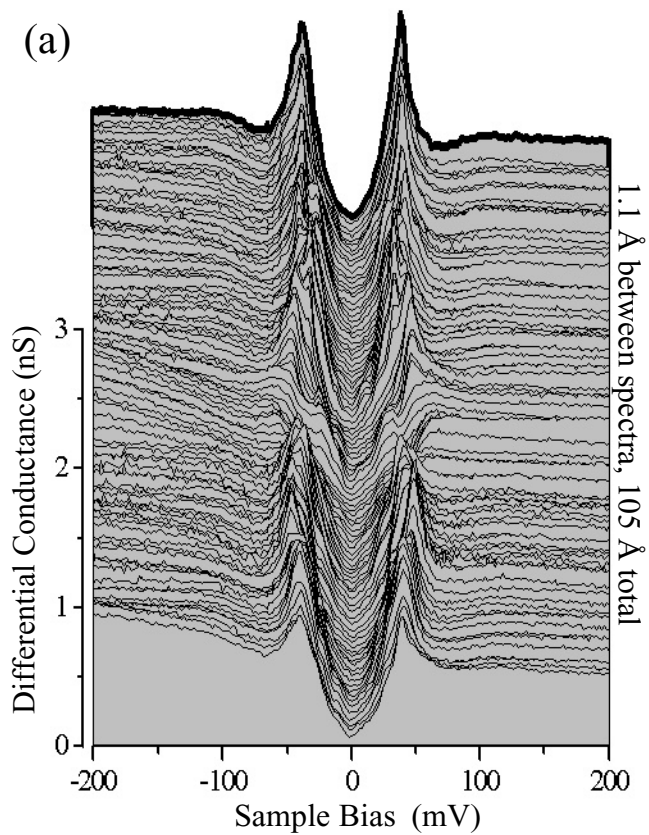


Figure 2.13:
 Linecut and topography on
 BSCCO with as-grown oxygen
 doping and 0.5 % Ni impurities.
 The trajectory of the line avoids
 the region of influence of all Ni
 impurity atoms.
 Run = 147
 File = 91124b:25-120 &91125a00
 $V_{\text{set}} = -200$ mV
 $I_{\text{set}} = 200$ pA

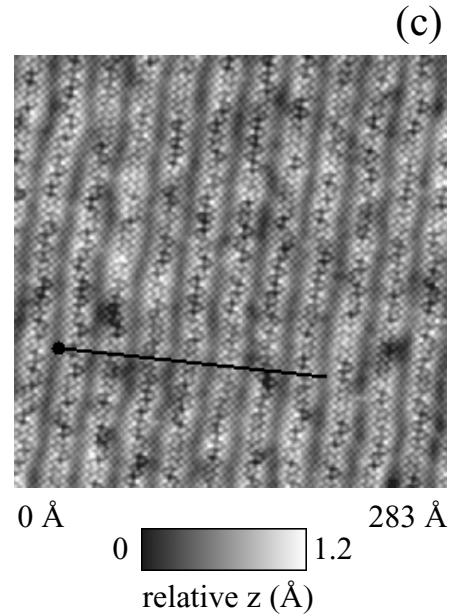
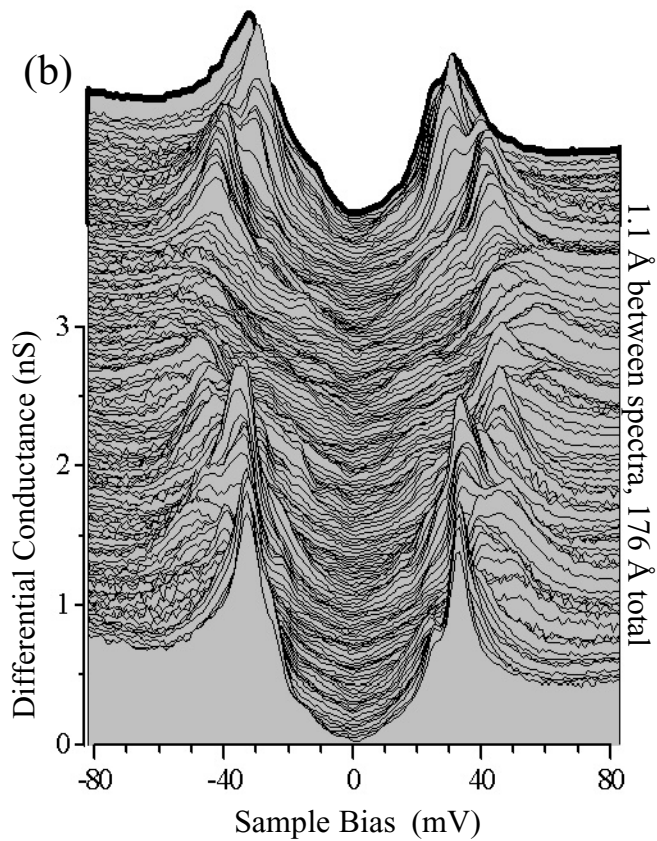
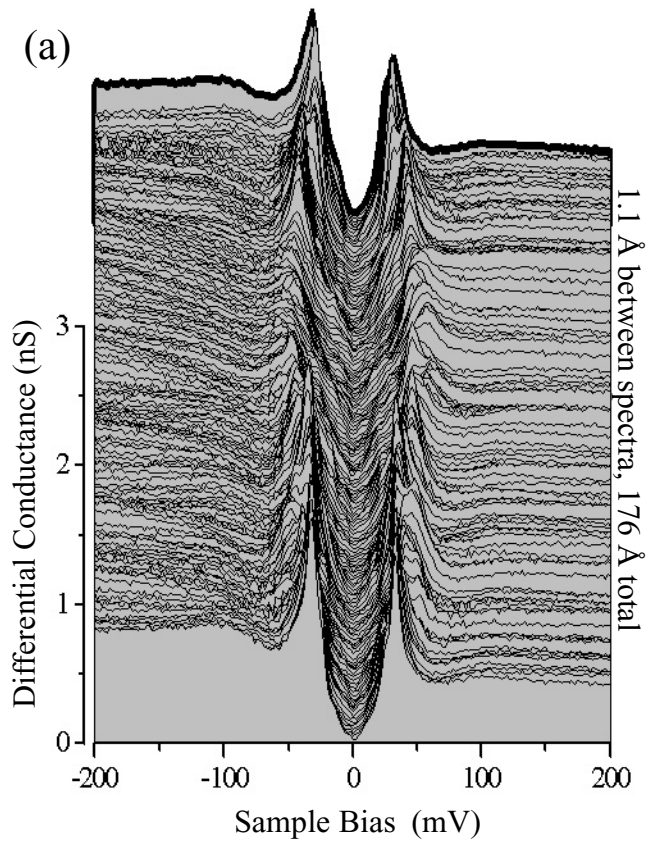


Figure 2.14:
 Linecut and topography on
 BSCCO with as-grown oxygen
 doping and 0.5 % Ni impurities.
 The trajectory of the line avoids
 the region of influence of all Ni
 impurity atoms.
 Run = 147
 File = 91126a0-159 & 91126b00
 $V_{\text{set}} = -200$ mV
 $I_{\text{set}} = 200$ pA

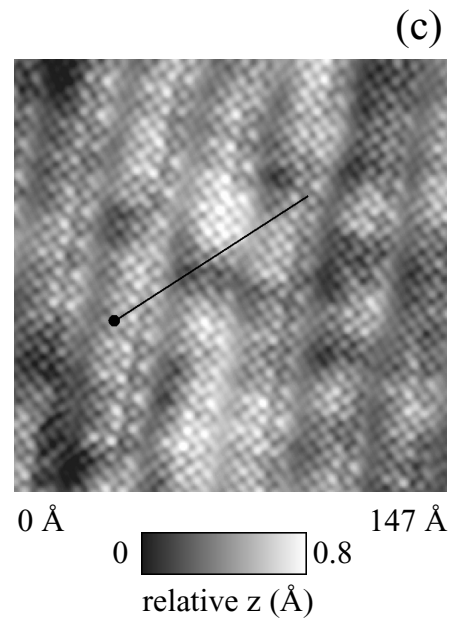
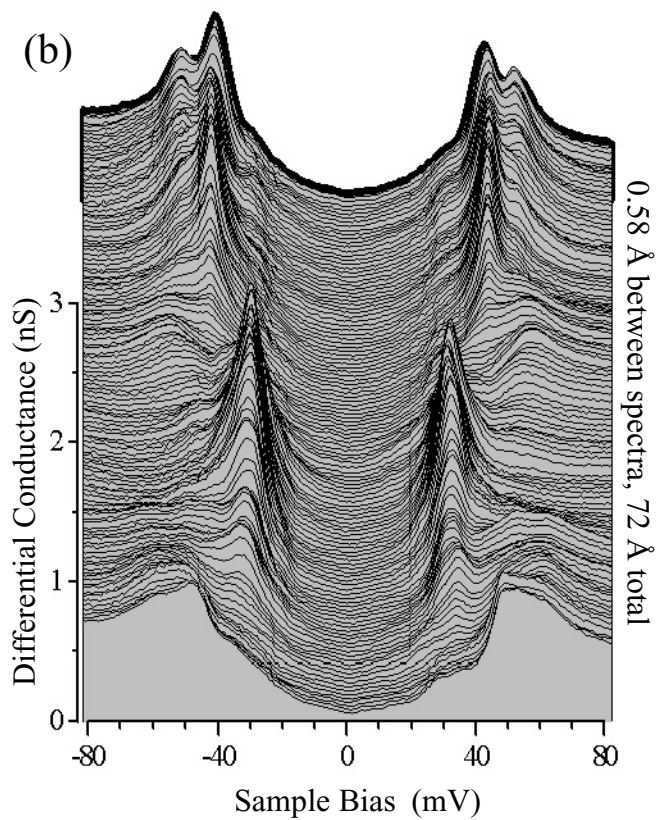
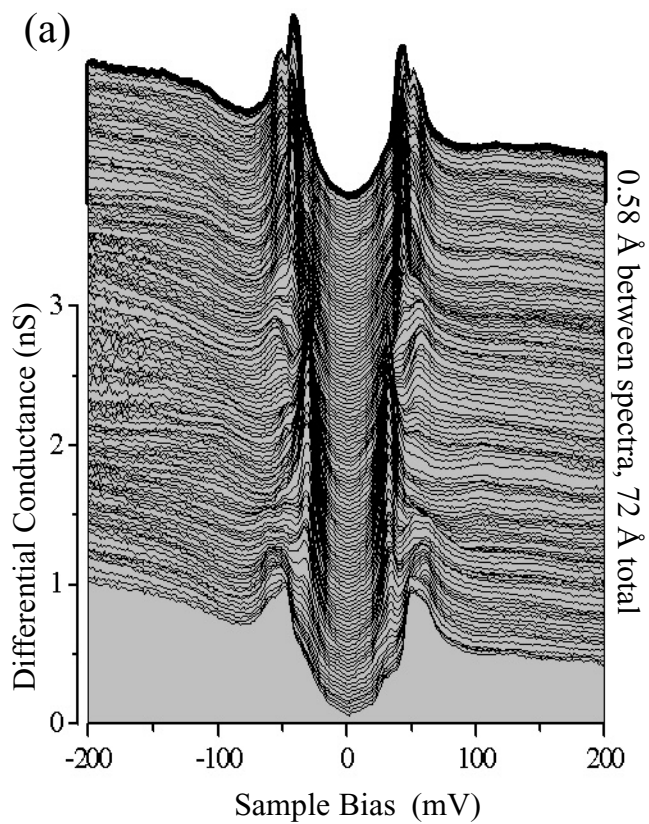


Figure 2.15:
 Linecut and topography on
 oxygen underdoped BSCCO with
 no intentional impurities.
 Run = 159
 File = 01101d:0-250 even only
 & 01101b02
 $V_{\text{set}} = -200$ mV
 $I_{\text{set}} = 200$ pA

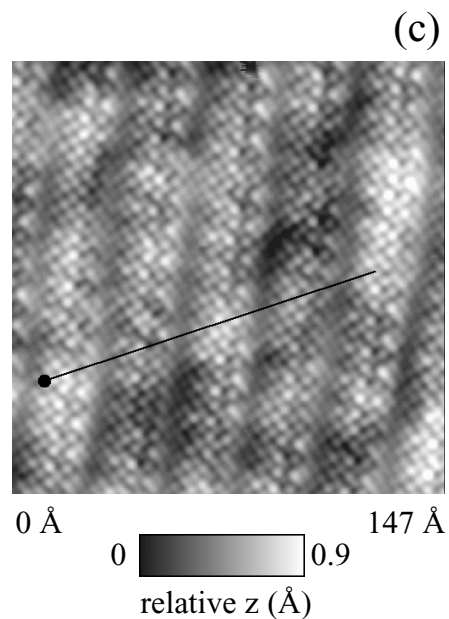
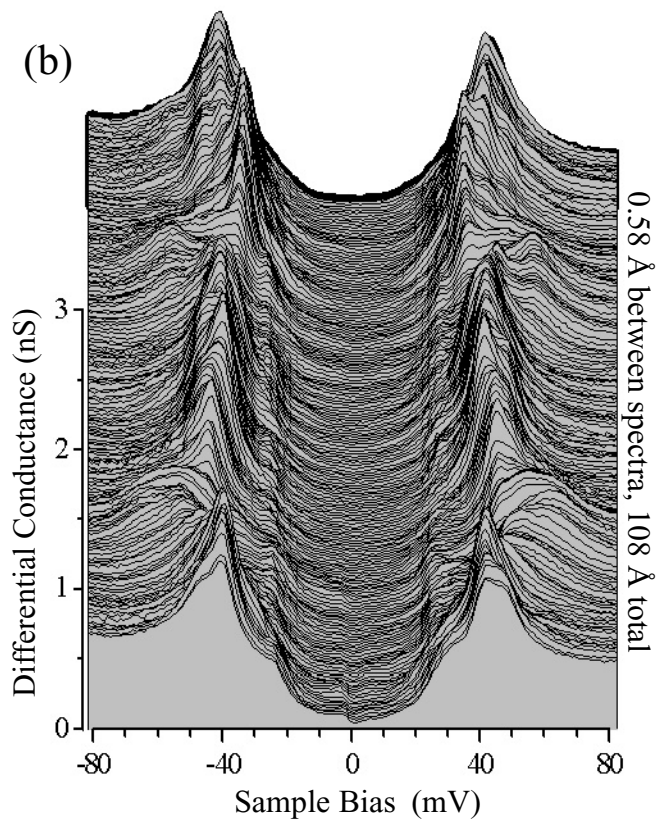
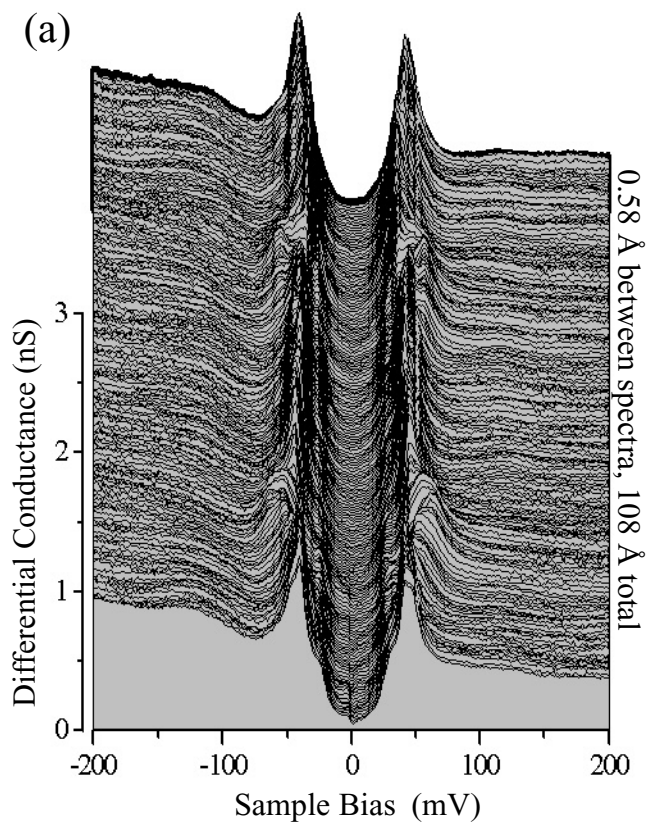


Figure 2.16:
 Linecut and topography on
 oxygen underdoped BSCCO with
 no intentional impurities.
 Run = 159
 File = 01108c:0-376 even only
 & 01109a00
 $V_{\text{set}} = -200$ mV
 $I_{\text{set}} = 200$ pA

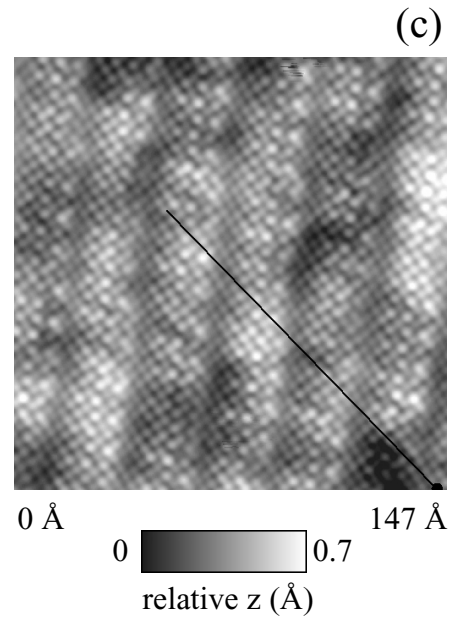
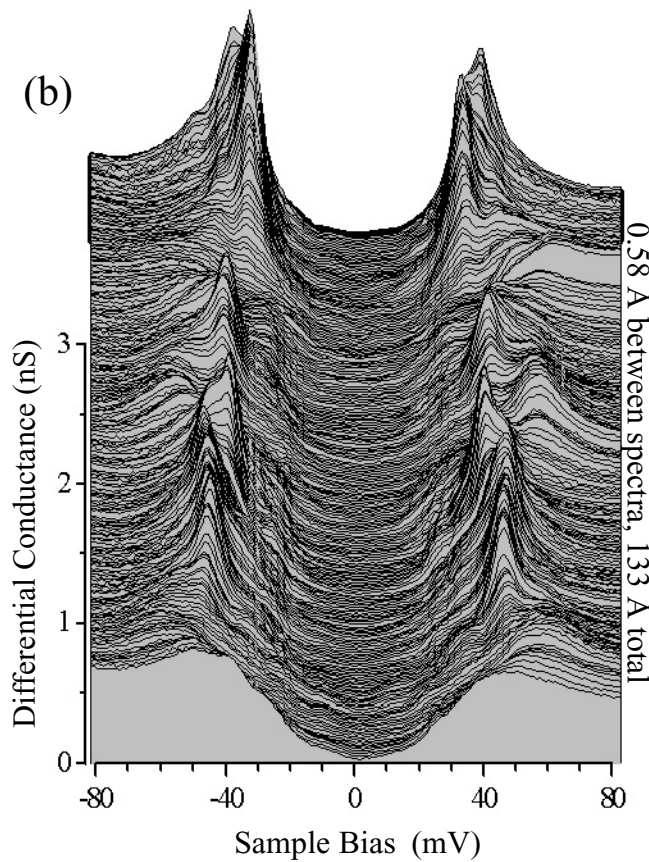
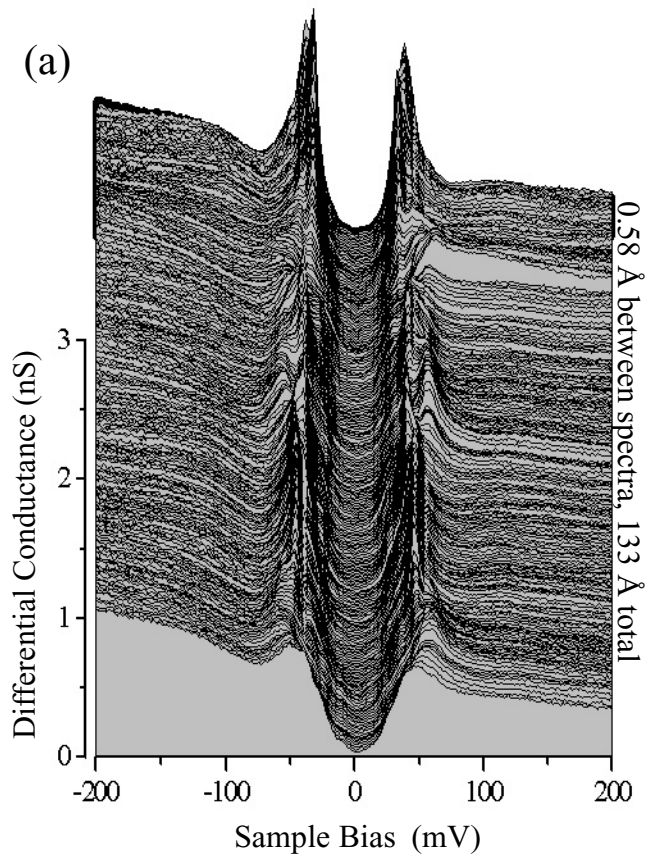


Figure 2.17:
 Linecut and topography on
 oxygen underdoped BSCCO with
 no intentional impurities.
 Run = 159
 File = 01109c:0-465 even only
 & 01110a00
 $V_{\text{set}} = -200$ mV
 $I_{\text{set}} = 200$ pA

Section 2.6: Summary of Spatial Interrelationships For Run 159 Data

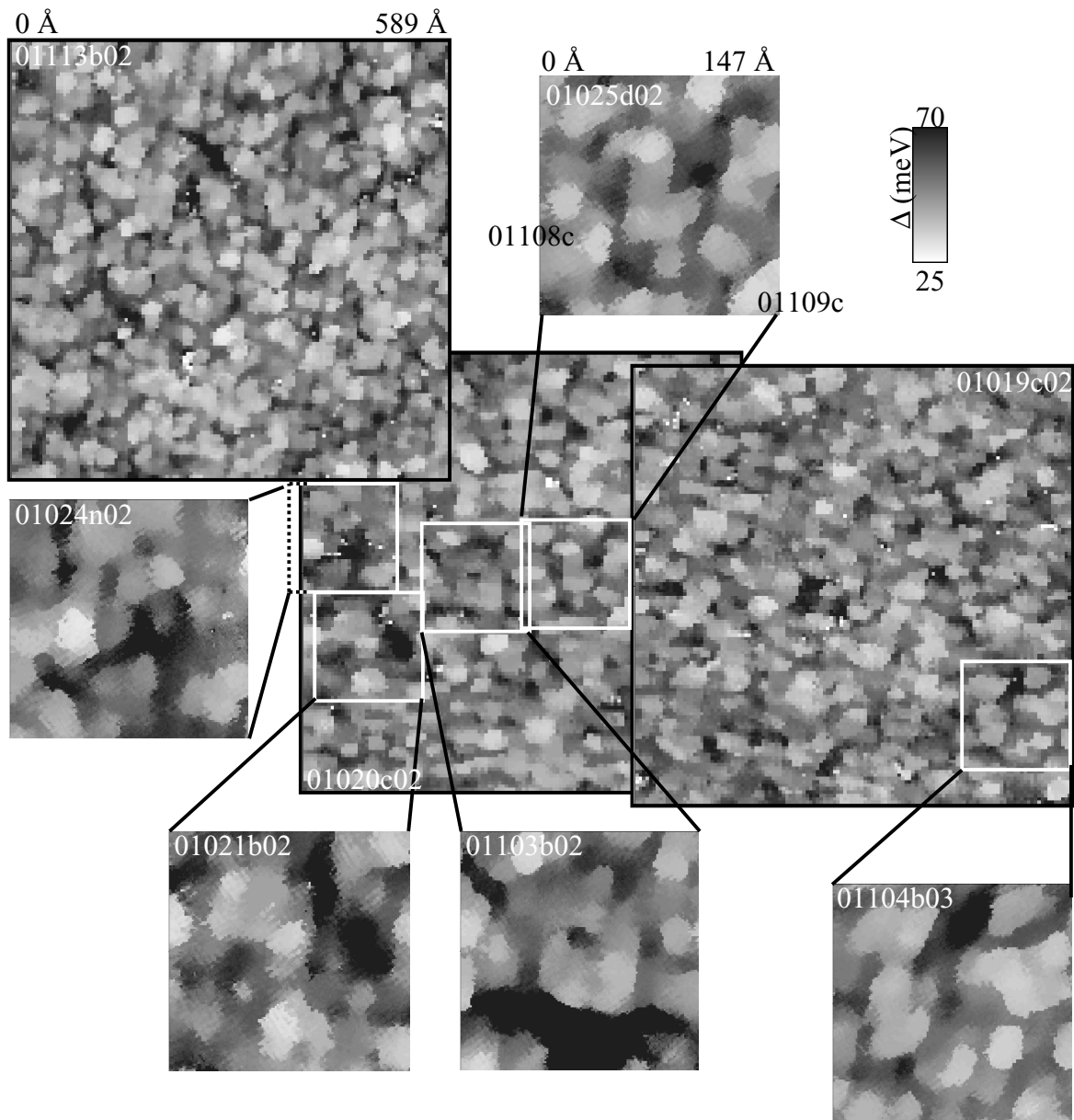


Figure 2.18: Interrelationships of the maps and linecuts which were taken in run 159 on oxygen underdoped BSCCO with no intentional impurities. All maps shown are Δ -maps. The trajectories of two linecuts are shown on 01025d02. The file name of each panel is given to aid in cross-referencing with other figures in this chapter and thesis.

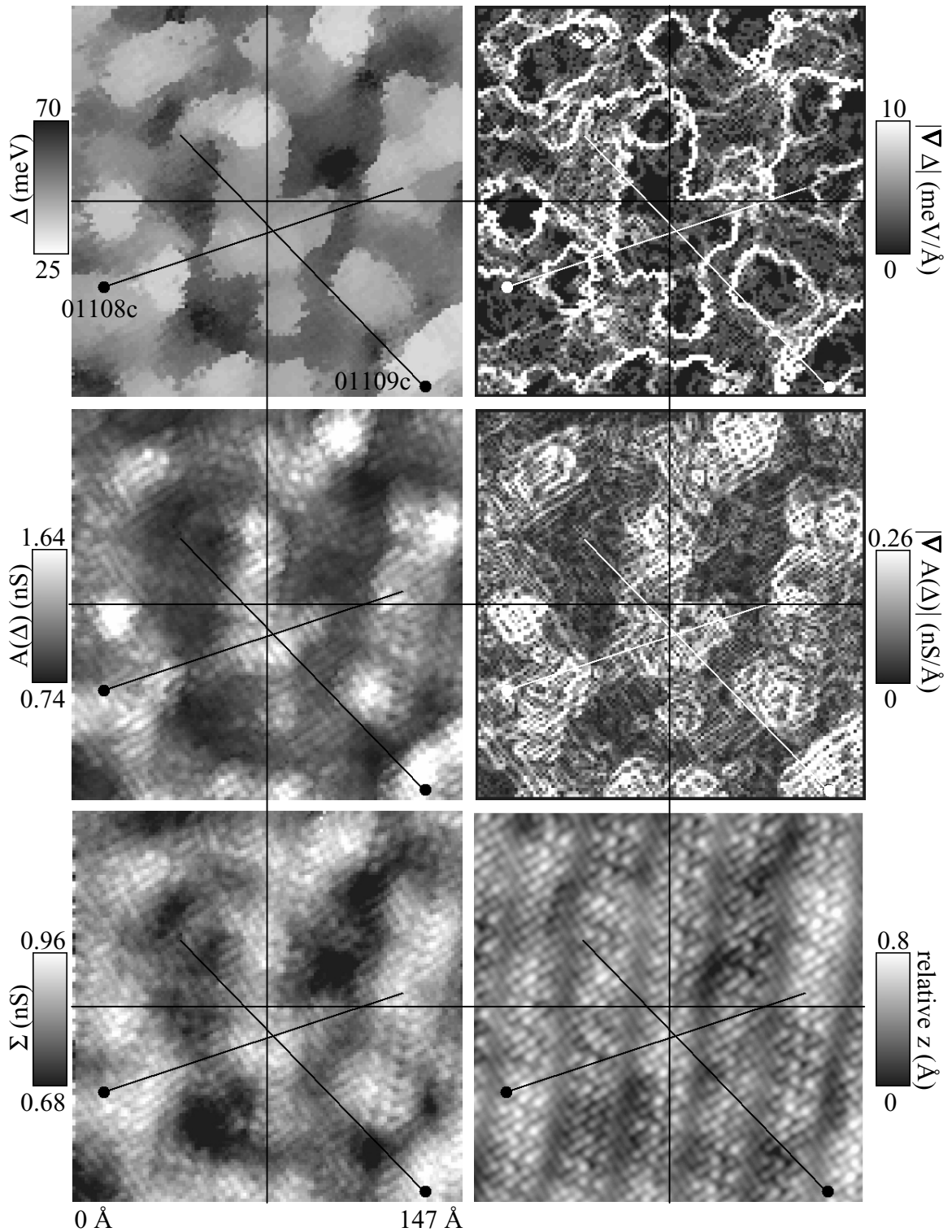


Figure 2.19: Repeat of Figure 2.10 to show trajectories of the linecuts 01108c and 01109c. Detail maps on oxygen underdoped BSCCO with no intentional impurities. Run = 159, File = 01025d02 & 01026a00, $V_{\text{set}} = -200$ mV, $I_{\text{set}} = 200$ pA

Chapter 3

Inhomogeneity in the Electronic Structure of $\text{Bi}_2\text{Sr}_2\text{CaCu}_2\text{O}_{8+d}$

There are many reasons why the local density of states (LDOS)³⁹ may vary as a function of position in a material. Much of our recent research has focussed on variations in the local density of states of $\text{Bi}_2\text{Sr}_2\text{CaCu}_2\text{O}_{8+\delta}$ due to the presence of impurity atoms [Hudson 1999A, Pan 2000A, Hudson 2001]. There are of course other reasons why the local density of states may vary, including crystal defects and grain boundaries. An example of each of these sources of variation is given in Figure 3.1. In the course of our study of BSCCO, we discovered, however, that even far from these obvious and identifiable sources of disorder still the local density of states varies dramatically as a function of position. In particular, both the size of the energy gap, Δ , the height of the gap-edge peaks, $A(\Delta)$, and the integrated spectral weight, $\Sigma(\Delta)$ ⁴⁰, show significant spatial *inhomogeneity*.

In this chapter I will present data which demonstrates the existence and ubiquity of this native spatial inhomogeneity in the local density of states of BSCCO. In addition, I will describe the general phenomenology of the observed spatial inhomogeneity⁴¹.

General Comments About the Data Presented in This Chapter

Much of the data presented in this chapter is contained in the Data Catalog in Chapter 2. The re-rendering of specific examples permits the reader to more clearly see the evidence for a given assertion⁴². Although selected data has been re-rendered to highlight specific features of the data, in general the reader may refer to the figures in Chapter 2 for further evidence for any assertion. In some cases specific references will be made to figures from that chapter which are particularly illuminating.

The reader should be aware that many of the maps and plots in this chapter were derived from the same two spectral-surveys, one on underdoped and one on as-grown doped BSCCO. This was done to facilitate cross comparison between the two different doping-

³⁹ Although all the data presented in this thesis comprises measurements of the local *differential conductance*, nonetheless in this chapter and subsequently in this thesis, *local density of states (LDOS)* will be used synonymously with *differential conductance (dI/dV)*. The clarity and comprehensibility of presenting a discussion in terms of the physically meaningful quantity LDOS is the impetus for this nomenclature. The strictly proportional relationship between differential conductance and LDOS is the justification. Details of the relationship between differential conductance and LDOS are given in Chapter 1, and in particular the reader's attention is directed to Section 1.10 which discusses how to interpret inter-comparisons between distinct spectra measured at different locations.

⁴⁰ See Fig 1.13 for a definition of these quantities.

⁴¹ For the work of other groups in this area please see Chapter 4.

⁴² The data file numbers, which are given in all figure captions, permit a comparison between the present figure and any previous presentation of the same data.

levels and between the different views of the data presented. The figures which are derived from these spectral-surveys are as follows: 3.6, 3.7 3.10, 3.11, 3.13 3.14, 3.15, 3.16, 3.17. Other views of these spectral-surveys may also be found in the Data Catalog in Figures 2.1 and 2.5.

3.1 Linecuts Illustrating LDOS Spatial Inhomogeneity

The primary purpose of this section is to present *raw* dI/dV spectra, in the form of several linecuts, in order to illustrate spatial inhomogeneity. The secondary purpose is to facilitate initial observations of the phenomenology of the spatial inhomogeneity. All observations introduced in this section will be revisited subsequently; however, discussion of the observations in conjunction with presentation of the linecuts permits the reader to study the raw data in the context of the proposed phenomenology. The final purpose of this section is to demonstrate the repeatability of the phenomena by showing a multitude of linecuts which span multiple samples, years of operation, and operators, and which come from crystals with two significantly different oxygen-doping levels⁴³.

Figure 3.2 shows a linecut taken on a Ni doped BSCCO sample with *as-grown* oxygen doping. Much of the early data in which we observed spatial variation in the LDOS was taken on impurity-doped samples. Although, the impurities do create local LDOS spatial variation, we know that each impurity influences a roughly circular region with a radius on the order of the coherence length ($\sim 15 \text{ \AA}$). By looking at the LDOS outside of the radius of impurity influence, we observe the *intrinsic* spatial variation in these impurity-doped samples. This linecut and the others in this section were taken, with one noted exception, completely outside the region of influence of any impurity atoms.

As Figure 3.2 very clearly demonstrates, there is considerable spatial variation in the LDOS, and in particular both the energy gap and the height of the gap-edge peaks are varying. A closer inspection of the linecut permits several observations.

We first observe that at low energy ($|E| \lesssim 15 \text{ meV}$), there is very little variation in the LDOS. This observation holds true at high energies ($|E| \gtrsim 80 \text{ meV}$) as well⁴⁴. In short, the energies at which we see significant spatial variation are those near the gap energy ($E \sim \Delta$). Consequently, subsequent discussion will focus on observations of spectral properties in this energy range.

We begin with observations regarding the spatial evolution of the size of the gap (Δ)⁴⁵. In particular, one observes that Δ does not vary continuously. Rather, Δ has one relatively constant value for a certain distance. It then changes over some relatively short length to a different constant value which persists over a certain distance, and so on. This

⁴³ See Table 2.1 and Appendix 2 for more details about the samples used.

⁴⁴ The constant current normalization scheme described in Chapter 1 and in particular in section 1.5.1 can enhance the apparent homogeneity observed at low and high energies, and so these observations should be qualified with a discussion of the effects of this scheme. Such a discussion is found in Wang 2001A and indirectly in Section 1.10.

⁴⁵ See Figure 1.13 for a definition of Δ and other spectral parameters.

phenomenon is very clear in Figure 3.3. In this figure a resonance which indicates the presence of Zn impurity is seen in the middle of the line cut. Beyond that resonance there are three clearly distinct regions, each with a different value of Δ from its neighboring regions. A third linecut which illustrates the discontinuous variation in Δ is shown in Figure 3.4. In this linecut there are five distinct Δ regions which are marked with vertical arrows.

The value of Δ is not the only spectral characteristic which exhibits spatial inhomogeneity. A second spatially varying parameter is the magnitude of the LDOS for $E \sim \Delta$. In particular we may examine variations in the height of the gap-edge peaks, $A(\Delta)$. Variation in $A(\Delta)$ can be seen in all the linecuts thus far presented, but it is more easily observed when a linecut is viewed from a different angle. Accordingly, the front half of the linecut shown in Figure 3.4 is re-rendered in Figure 3.5. In this view it is clear that the gap-edge peak is rising and falling dramatically in certain regions. Closer inspection of this and other linecuts reveals that peaks in regions with lower values of Δ exhibit the most pronounced variation. Witness Figure 3.5, in which the middle domain, which has a lower value of Δ than either of the surrounding domains, is the one with pronounced and dramatic peak height variation. This observation will be discussed in more detail in Chapter 5.

The observation of variation in the LDOS begs the question of its origin. This question will be addressed in detail in Chapter 6. At this point, I confine remarks on this topic to what is probably not the origin, namely the atomic corrugation and the supermodulation. Recall from Section 1.4.1 and Section 1.5.2 that the supermodulation is the wave-like buckling of crystal layers which is seen in the topography of Figure 3.2 (3.4) as roughly horizontal (diagonal) crests and troughs. The red line drawn on the topography shows the trajectory of the associated linecut. Comparing the trajectory with the spectra in the linecut reveals no obvious shared periodicity between the spectral variations and either the atomic corrugation or the supermodulation. Thus, whatever effect these periodic structures may exert on the LDOS is not the dominant factor but is rather of second order.

3.1.1 Summary

In summary, in this section the following observations have been made and discussed. The LDOS of $\text{Bi}_2\text{Sr}_2\text{CaCu}_2\text{O}_{8+\delta}$ in the energetic region $E \sim \Delta$ varies spatially, which is to say, the LDOS is inhomogenous. In particular, both the magnitude of the gap and the height of the gap-edge peaks vary in a characteristic way. As to the variation of the gap size, Δ is relatively constant in a given region, and then changes rapidly over a short distance to a different relatively constant value. As to the variation of the gap-edge peak, for regions of low Δ , $A(\Delta)$ rises significantly and then falls again as the Δ region is crossed. For regions with high Δ , $A(\Delta)$ is low and constant.

3.2 Spatial Variation of Δ

Having shown examples of raw data to generally demonstrate spatial variation in the LDOS, I now focus on a more systematic presentation of the variations of Δ . The purpose of this section is to show the magnitude of variations in the gap, and also to present a more complete view of the spatial interrelationships of the variation both in general and as a function of doping. To this end, in this section and in much of the remainder of the chapter, many of the maps and plots are derived from the same two spectral-surveys, one on underdoped and one on as-grown doped BSCCO.

3.2.1 Maps of Δ

Figure 3.6 shows two *gapmaps*, one from the underdoped and one from the as-grown sample. The same maps are shown both in gray scale and in color scale. Figure 3.7 shows the respective histograms for the values of Δ which are found in these areas. The topographies, $A(\Delta)$, and Σ maps which correspond to these same areas are given in Figure 2.1, 2.5, and in later figures in this chapter.

Before discussing the content of the images, I would like to explain why I present them in two different color palettes. A continuous color scale, such as the gray scale, is a slightly more objective presentation of the data, which better facilitates individual readers forming their own opinions about the observations discussed herein. The multi-color palettes used are designed to enhance the described features of the data and to make it easier to see them. While the use of multi-color palettes does nothing to alter the data itself, they could be inferred as a subjective presentation. To avoid this issue, I present this image and several others in a dual palette. For this and subsequent images in this thesis, a gray scale version of the image is also often available in the Data Catalog in Chapter 2.

Returning to a discussion of the content of Figure 3.6, we wish to examine the spatial interrelationships which exist between different values of Δ . As was illustrated earlier with the linecuts, one observes that Δ is not continuously varying in these maps, but rather is relatively constant within a given region and then changes over a fairly short length scale to a different relatively constant value. This observation is manifest in the images as a ‘patchwork’ or ‘granular’ impression, in which one observes regions that consist of contiguous patches of a single color. Several other $\sim 550 \text{ \AA}$ square gapmaps are shown in Section 2.3, and all give the same impression of a patchwork of Δ values. Given this view of a relatively large (compared to the size of the patches) area, we infer that the relative constancy of Δ within a given patch⁴⁶ is a general feature of the material

⁴⁶ Further discussion of the patchwork nature of the Δ regions is found in Chapter 5 and in particular in Section 5.3. Here I foretell the conclusions of that section to provide some quantitative context to the statement of the constancy of Δ within a patch of a given size. The approximate size of the patches is 28 \AA . For patches with $\Delta \leq 50 \text{ meV}$, the gap size is maintained at a single value to within 5%. For patches with $\Delta \geq 35 \text{ meV}$, the gap size exhibits a slow characteristic spatial variation in which Δ changes by $\sim 10 \text{ meV}$ across the patch.

(and not just a singular observation found only in the limited field of view of the linecuts).

In addition to noting the general impression of a patchwork, one can examine the qualitative shape of the regions in the gapmaps as a function of Δ . Several regions of low Δ are roughly outlined with red circles on the map for each sample. The outline of these low- Δ regions is given as a closed curve, because in general regions of low Δ are compact and discrete, particularly in the underdoped sample. In contrast, a contiguous yet non-compact high- Δ region is indicated by white lines on the gapmaps. In the underdoped sample this region is not at all closed; however, in the as-grown sample the region is more bounded as indicated by the two semi-closed regions in the curve.

A helpful analogy is to consider the low- Δ regions to be *islands* in a *sea* of high- Δ regions, or more scientifically speaking, the high- Δ regions are percolative whereas the low- Δ regions are discrete. This percolative vs. discrete nature of the high vs. low- Δ regions is clearly evident in the underdoped sample. In the as-grown sample the two regions appear more spatially equivalent.

3.2.2 Histograms of Δ

Although both the underdoped and the as-grown sample exhibit a Δ -patchwork, the values of Δ present in that patchwork are different for the differently doped crystals. Essentially the Δ values present in the underdoped sample correspond to having blue, green and yellow as the predominant colors in its gapmap image. This is in contrast to the Δ values present in the as-grown sample, which correspond to having green, yellow and orange as the predominant colors in its gapmap image. To see the shift in Δ values clearly, one must examine the histograms of Δ values derived from these images which are given in Figure 3.7.

The histograms in Figure 3.7 confirm that the values of Δ found in both samples span a fairly large range, but that the range is shifted for one doping as compared to the other. For the underdoped data, Δ ranges from 30 meV to 70 meV with a mean of 48.2 meV and a width (= two standard deviations) of about 18 meV. For the as-grown doped data, Δ ranges from 25 meV to 65 meV with a mean of 41.3 meV and a width of about 15.2 meV.

A gaussian has been fit to the histograms; however, rather than providing a good fit, it serves to highlight the lack of symmetry in these plots. The distributions are not symmetric about their means, rather, there is a slower falloff on the high side of the mean as compared to the low side. This is particularly the case for the underdoped data. The origin and significance of the observations regarding the gapmaps and their histograms will be discussed in Chapter 6.

3.2.3 Summary

In summary, in this section the following observations have been made and discussed. The two-dimensional data in the gapmaps supports the previous observation that Δ is relatively constant within a given region, changing rapidly only in the borders between regions. This is manifest in the patchwork impression of the gapmap image and is true for both doping levels presented. However, the range of Δ values for the different doping-levels is different. In particular, the underdoped histogram is shifted to higher values of Δ as compared to the as-grown histogram. While neither histogram is symmetric about its mean, the underdoped histogram exhibits greater asymmetry.

3.3 Diversity of Spectral Shapes

The previous section discussed spatial variation in the size of the gap. However, as was discussed in section 3.1, Δ is not the only characteristic of the LDOS spectra which varies. In fact, the whole shape of the spectrum can be qualitatively different at different locations. The purpose of this section is to present a representative spectra to illustrate the variety of spectral shapes which we observe.

3.3.1 Representative Selected Spectra

To illustrate the variety of observed spectral shapes with selected, but spatially registered spectra, the linecut of Figure 3.4 is re-rendered in a different view (both forward and backward) in Figure 3.8(a&b). Several curves are highlighted by distinct colors in the linecut and are numbered. These spectra are shown in the panels at the side and serve to represent the variety of spectra which we observe. Although there is a continuous variation of spectral properties, very roughly speaking, there are six qualitatively different spectral shapes observed, which are enumerated in the next sentence. Each spectrum has either (i) no distinct peaks, or (ii) two or (iii) four sharp high peaks, or (iv) two or (v) four low broad peaks, or (vi) four peaks with two of them low & broad and two high & sharp⁴⁷. Specific examples of these types will be given in the subsequent paragraphs.

Starting at the front of the view in Figure 3.8(a) and with the spectra in Panel (c), the red (1) spectrum represents shape *4LB* with four peaks which are low and broad. The following green (2) and blue (3) spectra represent shape *2HS* with 2 peaks which are high and sharp. The turquoise (4) spectrum has four peaks with one pair low & broad and the second pair high & sharp, and thus it is of type *4LB-HS*. For the spectra in Panel (b), the pink (5) spectrum is of *4LB* type. It is followed by the yellow (6) spectrum which is of type *2LB* with two low broad peaks. The orange (7) spectrum is again *4LB*. In Panel (c), the purple (8) and the teal (9) spectra are both of *2HS* type. Finally, the brown (10) spectrum is of *4HS* type with 4 high sharp peaks.

⁴⁷ In very complicated situations in which several regions come together at one point, spectra may exist with more than four peaks. However, these situations represent only a very small (< 1 %) fraction of the total spectra.

The one characteristic spectral shape which is not found in the linecut of Figure 3.8 is illustrated in Figure 3.9. There are some regions where the spectra have no distinct peaks out to the highest energy at which we measure (typically ± 200 meV), and this type of spectra is designated as *NP*.

3.3.2 Representative Average Spectra

In the previous discussion I have presented selected individual spectra in order to demonstrate the variety of spectra we see. It is also interesting to look at average spectra in order to get a broader sense of the phenomenology. Figure 3.10 shows average spectra which come from the fields of view whose gapmaps were presented in Figure 3.6. These average spectra are generated as follows. All the 16384 spectra in a given field of view are sorted based on Δ ⁴⁸, and are then assigned to a bin, which in this case has a width of 6 meV. All the spectra in a given bin are averaged to produce the curves shown in Figure 3.10. The table gives the percentage of the total spectra found in each bin. There are several observations which can be drawn from this figure, and they are discussed in the following paragraphs.

As a first observation, a contrast can be drawn between the low, $E \lesssim 15$ meV, and higher energy, $15 \text{ meV} \lesssim E \lesssim 80$ meV, characteristics of the curves. Strikingly, at low energies all the curves lie on top of one another, whereas at higher energy ($E \sim \Delta$) the curves are very different from one another⁴⁴. This reaffirms the observation about the spatial homogeneity of the low energy LDOS which was suggested by the linecuts in Section 3.1. This issue will be revisited in Section 3.4.

As a second observation from Figure 3.10, there is a clear trend visible in the curves such that the lower the value of Δ , the higher and sharper are the gap edge peaks, and conversely. This observation is augmented by a re-examination of the spectra in Figure 3.8. This figure shows low Δ curves with both low and high $A(\Delta)$ (see the blue (3), green (2) and red (1) curves of Figure 3.8), whereas high Δ curves have only low $A(\Delta)$ (see the pink (5), yellow (6) and orange (7) curves of Figure 3.8). These observations taken together suggest that there may be significantly more variation in the peak height for low Δ curves.

This suggestion is confirmed by Figure 3.11 which shows the standard deviation for the spectra averaged to produce Figure 3.10⁴⁹. As suggested, we indeed see a trend such that the lower the value of Δ , the greater is the standard deviation for energies near that value of Δ . In other words, curves with low values of Δ have a wide range of peak heights; whereas, curves with high values of Δ have a limited range of peak heights. This observation is consistent with the previous observation that regions which have lower

⁴⁸ Spectra with four distinct peaks are generally sorted into the bin corresponding to the energy of the higher peak; however, these spectra make up a fairly small fraction of the total field of view so the effect on the average is negligible.

⁴⁹ The large peak in the standard deviation near zero bias for the as-grown doping case is due to the presence of Zn impurities in this sample. As the Zn resonance is very high, [Pan 2000A] averaging in spectra from even a few Zn impurities can significantly affect the standard deviation at low bias.

values of Δ , exhibit greater spatial variation of $A(\Delta)$ within those regions, as illustrated in Figure 3.5.

As a final observation from Figure 3.10, there is a clear kink in the curves at about ± 30 meV for those spectra with $\Delta \geq 50$ meV. This kink is most visible on the positive bias side, but can also be seen on the negative bias side.

3.3.3 Summary

In summary, in this section the following observations have been made and discussed. There are six prototypical spectral shapes which arise from classifying the observed spectra by the number of peaks they exhibit and by the shape of those peaks. To recapitulate, each spectrum has either (i) no distinct peaks, or (ii) two or (iii) four sharp high peaks, or (iv) two or (v) four low broad peaks, or (vi) four peaks with two of them low & broad and two high & sharp⁵⁰. With regard to a correlation between the value of Δ and the height of the gap-edge peaks, we find that spectra with lower values of Δ tend to have higher sharper gap-edge peaks whose height may vary significantly. Conversely, spectra with higher values of Δ tend to have lower broader gap-edge peaks whose height does not vary significantly.

3.4 Spatial Variation of $A(D)$ and S

As discussed in the preceding sections, the value of Δ , the height of the gap-edge peaks, and the overall spectral shape all vary as a function of position in $\text{Bi}_2\text{Sr}_2\text{CaCu}_2\text{O}_{8+\delta}$. In Section 3.2, Δ -maps were presented, and the spatial interrelationship of different Δ regions was discussed. In the preceding section, selected and average spectra were used to illustrate the range of $A(\Delta)$ and spectral shape. In this section the spatial interrelationship of the variation in $A(\Delta)$ and spectral shape is examined and discussed. Maps of $A(\Delta)$ and Σ are used to study this spatial interrelationship and also to discuss the correlation of these quantities with Δ .

3.4.1 Interpretation of $A(D)$ and S

Prior to discussing $A(\Delta)$ and Σ maps, in this section I briefly discuss the interpretation of these variables. Additional discussion of these quantities, including the mathematical definitions for $A(\Delta)$ and $\Sigma(V_1, V_2)$, can be found in Section 1.8.

Recall that $A(\Delta)$ is the value of the LDOS at the gap energy, or in other words the height of the gap-edge peak. While the physical interpretation of $A(\Delta)$ for HTSC remains unclear, for a *conventional* superconductor the gap-edge peak is generally referred to as the coherence peak.

⁵⁰ In very complicated situations in which several regions come together at one point, spectra may exist with more than four peaks. However, these situations represent only a very small ($< 1\%$) fraction of the total spectra.

The quantity Σ provides a measure of trends in the LDOS magnitude which occur over a wide range of energies. Strictly speaking, $\Sigma(E)$ is defined as the integral of the LDOS curve for energies near E , or equivalently, as the average value of the spectrum for those energies. More colloquially, $\Sigma(E)$ may be thought of as the spectral weight contained in the energy range near E .

Given the observations detailed earlier in this chapter, Σ will generally be used to study the trends in the LDOS magnitude for $E \lesssim \Delta$ or for $E \sim \Delta$ with these quantities given as $\Sigma(\lesssim \Delta)$ and $\Sigma(\Delta)$ respectively. Considering specifically these two energy ranges, $E \lesssim \Delta$ is taken to mean a range of energy whose upper bound is either less than or approximately equal to the lowest value of Δ found in a given sample, whereas $E \sim \Delta$ means the range of energy which encompasses at least 95% of the total range of Δ values found in a given sample. As for the usefulness of these two quantities, $\Sigma(\lesssim \Delta)$ can be used to support the earlier observation that the low energy LDOS is spatially homogenous under the constant current normalization scheme, while the quantity $\Sigma(\Delta)$ is related to spectral shape as is discussed in the remainder of this section.

Recall the two canonical spectral shapes HS (high and sharp) and LB (low and broad). It is possible that $\Sigma(\Delta)$ is the same for these two shapes, since the spectral weight contained in the height of the HS peak could be preserved in the width of the LB peak if this peak encompasses a very large energy range. Such a scenario is generally referred to as *conservation of spectral weight*. Alternatively, $\Sigma(\Delta)$ could be different for these two shapes, if the spectral weight contained in the height of the HS peak is spread out over such a wide range of energies that it is effectively no longer contained in the width of the LB peak. In the first case in which spectral weight is conserved, $\Sigma(\Delta)$ is not a good indicator of spectral shape since it is a constant. However, in the second case, $\Sigma(\Delta)$ does indicate spectral shape as it would be higher for the HS spectral type than for the LB. The question then arises as to which scenario exists for the observed spectra.

Figure 3.12 is a re-rendering of the selected spectra of Figure 3.8 with the colors and numbering of that figure preserved. The spectra are now plotted on one graph with no offset so that the relative spectral weight and spectral shape can be observed simultaneously, in order to determine if there is a correlation. A qualitative inspection suggests that those spectra with lower, but broader, peaks contain less spectral weight in the Δ -energy range than those with higher and sharper peaks⁵¹. The chart presented with the figure confirms this observation. The spectra in the chart are given in order of increasing $\Sigma(\Delta)$; however, this order is also approximately the order of increasingly higher and sharper gap-edge peaks as can be observed in the corresponding spectra. Two different integration ranges are given for Σ , and the observation holds for both. Thus, the higher the value of $\Sigma(\Delta)$, independent of the exact range of integration, the higher and sharper are the gap-edge peaks for that spectrum.

⁵¹ The observations in this section are most properly made with respect to the negative bias side of the spectrum, because the set point bias is negative, and thus the negative side is uniformly constant-current normalized by definition. See Section 1.5.1 and Section 1.10 for a discussion of constant current normalization.

To reiterate and clarify then, the observations in the preceding paragraph imply the following. $\Sigma(\Delta)$ provides a rough measure of spectral shape, such that higher values of $\Sigma(\Delta)$ mean that the gap-edge peaks are higher and sharper for that spectrum. It is important also to consider this observation from the opposite side. Namely, spectra with higher gap-edge peaks have relatively more spectral weight in the Δ -energy range than those spectra with lower gap-edge peaks.

3.4.2 Maps of $A(\Delta)$ and $S(\Delta)$

Having discussed in the previous section the interpretation of $A(\Delta)$ and $\Sigma(\Delta)$, I now turn to a presentation of observations derived from these quantities. Figure 3.13 and 3.14 show maps of $A(\Delta)$ and $\Sigma(\Delta)$ respectively. These maps are derived from the same spectral-surveys as those used to produce the gapmaps of Figure 3.6, and thus all three figures show the same two regions of the same two samples.

As in the case of Figure 3.6, the maps in Figures 3.13 and 3.14 are presented in both color and gray scale. Note that for the gapmap of Figure 3.6, the lowest values of Δ are shown in red/white for the colored/grayscale maps; however, for the $A(\Delta)$ and $\Sigma(\Delta)$ maps the highest values are shown in these colors. The reason for inverting the color scales for the $A(\Delta)/\Sigma(\Delta)$ maps as compared to the Δ -maps will become clear in the following paragraphs. Taken together then, the maps in Figures 3.6, 3.13, and 3.14 permit one to make the several observations discussed in the following paragraphs.

As a first observation, the maps demonstrate a clear spatial correlation between low values of Δ , high values of $A(\Delta)$ and high values of $\Sigma(\Delta)$, and vice versa. This is evidenced by the observation that wherever a region of low Δ is found, in that same region $A(\Delta)$ and $\Sigma(\Delta)$ are both high, and conversely. Qualitatively speaking, this observation is made by noting that the same spatial patterns and shapes are easily recognized in all three maps.

In particular, the low/high Δ regions outlined in red/white in Figure 3.6 are shown as well on the $A(\Delta)$ and $\Sigma(\Delta)$ maps of these figures. Inside the red circles, the $A(\Delta)$ and $\Sigma(\Delta)$ maps both show a high region of roughly the same shape as the low Δ region in the gapmaps. Similarly, in the regions indicated by the white curves, the $A(\Delta)$ and $\Sigma(\Delta)$ maps both show a low region of roughly the same shape as the high Δ region in the gapmaps.

A second observation regards the relative size of the qualitative shapes and spatial patterns in the three maps. In comparing the parameter maps, it is interesting to note that while the same qualitative shapes and spatial patterns are present in the Δ , $A(\Delta)$ and $\Sigma(\Delta)$ maps, again qualitatively speaking, those shapes are not the same apparent size in all three maps. For the low- Δ regions, the Δ and $\Sigma(\Delta)$ maps indicate regions of the same approximate size; however, in the $A(\Delta)$ map these same regions appear much smaller.

The reason for this is clear if one considers the representative red circled regions, which in the Δ and $\Sigma(\Delta)$ maps contain a comparatively uniform value of the respective quantity as compared to the same circled regions in the peak-amplitude maps, inside which $A(\Delta)$ varies significantly. Thus, the significant spatial variation of $A(\Delta)$ within a low- Δ region, which has been noted earlier, is responsible for the apparently smaller low- Δ region size in the $A(\Delta)$ vs. the Δ and $\Sigma(\Delta)$ maps.

A further implication of the apparent size of the respective regions derives from recalling that $\Sigma(\Delta)$ indicates spectral shape. Taken together with the fact that the Δ and $\Sigma(\Delta)$ maps show regions of the same approximate size, this implies that the spectral shape in a given Δ region is relatively uniform.

3.4.3 Trends in $A(D)$ and $S(D)$ as a Function of D

An examination of the $A(\Delta)$ and $\Sigma(\Delta)$ maps can give a sense of spatial interrelationships; however, for a more quantitative sense it is useful to examine average trends of these variables as a function of Δ , as presented in Figures 3.15 and 3.16. The graphs in these figures are generated from the same two spectral-surveys which were used to create the maps discussed in the previous section, and thus represent the same two regions of the same two samples.

The graphs in Figures 3.15 and 3.16 were generated in the following manner. All the 16384 spectra in a given field of view are sorted based on Δ^{48} and are then assigned to a bin, which in this case has a width of 6 meV. The bins and spectral-surveys are the same as that used to produce Figure 3.10, and thus the chart in that figure gives the percent of total spectra in each bin. The mean and standard deviation for the appropriate quantity for all the spectra in a given bin is then found to produce the curves shown in Figure 3.15 and 3.16. There are several observations which can be drawn from this figure, and they are discussed in the following paragraphs.

Figure 3.15 shows the trend in both $A(\Delta)$ and $\Sigma(\Delta)$ as a function of Δ . As was observed in the maps and linecuts discussed earlier in this chapter, there is a trend for low Δ regions to have higher values of both $A(\Delta)$ and $\Sigma(\Delta)$, and vice versa. This trend is clearly visible in this representation of the data. Given that $\Sigma(\Delta)$ is a measure of spectral shape, this representation is another way of observing that high $\Sigma(\Delta)$ is associated with low Δ which implies spectra with high sharp gap-edge peaks for that regime, and conversely. High values of $A(\Delta)$ are also seen to be associated with low Δ , and conversely, which is consistent with earlier observations.

An additional observation which can be derived from Figure 3.15 is the trend in the standard deviation from the mean of these quantities. The standard deviation is shown as error bars in Figure 3.15, but to facilitate comparison it is plotted vs. Δ in Figure 3.16. For the standard deviation from $\overline{A}(\Delta)$ there is a very clear trend for this quantity to be larger for lower values of Δ . This is consistent with earlier observations that there is more variability in the height of the gap-edge peak across the low Δ domains.

3.4.4 Maps of $\Sigma(\leq D)$

Having examined the behavior of the LDOS amplitude in the energetic region near Δ , we now turn to an examination of this behavior for low energies, $E \lesssim \Delta$. For this purpose, maps of the variable $\Sigma(\leq \Delta)$ are given in Figure 3.17. The maps of $\Sigma(\leq \Delta)$ in this figure are derived from the same spectral-surveys as were used to create Figures 3.6, 3.13, 3.14 and other figures in this chapter. For convenience, the maps of $\Sigma(\Delta)$ from Figure 3.14 are reproduced in Figure 3.17. For ease of comparison of the relative changes between the two Σ -maps for a given sample, the colorbar-maximum-value minus the colorbar-minimum-value is the same for both the $\Sigma(\leq \Delta)$ and the $\Sigma(\Delta)$ maps for that sample.

Focussing first on the as-grown oxygen doped $\Sigma(\leq \Delta)$ map, Figure 3.17(c), there are about 25 compact regions with high $\Sigma(\leq \Delta)$ in the field of view. These are the Zn impurity atoms which are visible in this map due to their large low energy resonance. As the impurities are compact ($\sim 25 \text{ \AA}$ diameter) and occupy a relatively small fraction of the field of view ($\sim 5 \%$), they comprise a local perturbation, but do not determine the overall properties of this map.

Looking at both $\Sigma(\leq \Delta)$ -maps, and ignoring the purely localized perturbation of the Zn impurities in the as-grown map, we find that both these maps show $\Sigma(\leq \Delta)$ relatively constant, as compared to the variations present in the $\Sigma(\Delta)$ -maps, for the entire field of view. This observation supports the earlier suggestion that the LDOS is relatively spatially constant at low energies, $E \lesssim \Delta$, under the constant current normalization scheme.

3.4.5 $A(D)$ and S at Positive vs. Negative Bias

In this section and elsewhere in this thesis, for any quantity involving LDOS magnitudes, the value shown is generally for negative bias. For example, an $A(\Delta)$ -map is always a map of $A(\Delta_-)$. This is done because the bias set point is generally negative, which means that the negative side of the spectrum is *experimentally* constant current normalized *a priori*. Thus, no numerical processing is required to render the normalization spatially uniform for LDOS magnitudes on the negative side of the spectrum. However, it is interesting to ask whether $A(\Delta)$ and Σ for positive bias exhibit the same behavior as is observed at negative bias, and which was discussed previously in this section. To answer this question most consistently, the negative and positive bias values of $A(\Delta)$ and Σ should both be numerically normalized and then compared.

The results of such numerical normalization are given in Figure 3.18, which shows maps of $\Sigma(\Delta_+)/N_+$ and $\Sigma(\Delta_-)/N_-$ derived from both the spectral-surveys which have been used to generate many of the figures in this chapter, including 3.6, 3.13, and 3.14. One sees from this figure that for a given sample, the maps of $\Sigma(\Delta_+)/N$ and $\Sigma(\Delta_-)/N$ are both similar to one another in the spatial patterns present, and are similar to the non-numerically normalized map of $\Sigma(\Delta_-)$ shown in Figure 3.14. From this observation we

conclude that in general the behavior of $\Sigma(\Delta)$ is qualitatively the same regardless of the polarity of the bias. Although, figures for $A(\Delta_+)/N$ and $A(\Delta_-)/N$ are not shown, the same independence of bias polarity is observed for this quantity as well.

3.4.6 Summary

In summary, in this section the following observations have been made and discussed. The quantity $\Sigma(\Delta)$ relates to spectral shape such that higher values of this quantity imply spectra with higher and sharper gap-edge peaks. Maps of $\Sigma(\Delta)$ and $A(\Delta)$ display the same qualitative spatial shapes and patterns as maps of Δ from the same region. Specifically, regions of low Δ are found to also be regions of high $A(\Delta)$ and $\Sigma(\Delta)$. This observation indicates a correlation between these three quantities, which is supported by the Δ -binned and averaged values of $A(\Delta)$ and $\Sigma(\Delta)$, which increase with decreasing Δ . In addition, the variations in these quantities, particularly $A(\Delta)$, increase with decreasing Δ on average. Maps of $\Sigma(\leq\Delta)$ confirm earlier suggestions that the low energy LDOS magnitude is relatively spatially uniform. Finally, the qualitative observations made throughout this section are found to be independent of bias polarity.

3.5 Conclusion

3.5.1 Summary

In this chapter I have presented evidence for intrinsic spatial variation in the local density of states observed in both underdoped and as-grown doped $\text{Bi}_2\text{Sr}_2\text{CaCu}_2\text{O}_{8+\delta}$. I have also described the phenomenology of this spatial variation in some detail. Here, I recapitulate the most important aspects of the phenomenology.

- The local density of states varies as a function of position in all observed samples of $\text{Bi}_2\text{Sr}_2\text{CaCu}_2\text{O}_{8+\delta}$ far from obvious sources of disorder such as impurities, topological defects and grain boundaries.
- This variation is ubiquitous and has been observed in a wide variety of samples including both oxygen underdoped and as-grown doped samples and samples from multiple sources.
- For energies below the range of gap energies, $E \leq \Delta$, the local density of states is spatially uniform given constant current normalization.
- The overall shape of the LDOS spectrum changes as a function of position for energies on the order of the gap energies, $E \sim \Delta$. In particular both the width of the gap, Δ , the height of the gap-edge peak, $A(\Delta)$, and the integrated local density of states, $\Sigma(\Delta)$ vary spatially.
- Spatial maps of Δ , and to a lesser degree maps of Σ , indicate that variation in these parameters is not continuous, but rather is suggestive of grains within which these properties have well defined values.
- The phenomenology of the spatial variation is different for regions that have relatively low values of Δ as compared to those that have higher Δ values. These differences are summarized as follows.

- A histogram of Δ values is not symmetric, but rather falls off markedly more rapidly on the low Δ side than on the high Δ side.
- The lower the value of Δ for a given region, the higher the value of $A(\Delta)$ and $\Sigma(\Delta)$.
- The lower the value of Δ , the higher and sharper is the average gap-edge peak for that region.
- In regions with lower Δ , $A(\Delta)$ varies dramatically whereas in regions with relatively higher Δ values, $A(\Delta)$ is relatively constant.
- On average, spectra with $\Delta > 50$ meV show a clear kink at ± 30 meV whereas those with $\Delta < 50$ meV show no such kink.

3.5.2 Looking Ahead

In conclusion, the observations presented in this chapter demonstrate the existence and ubiquity of native spatial *inhomogeneity* in the local density of states of BSCCO. The phenomenology of this variation has been observed and described in some detail as summarized above.

The details of the phenomenology in this chapter permit us to make a comparison of our observations to the work of other groups in this field. Although the results in this chapter represent a comparatively comprehensive study of the native inhomogeneity in BSCCO, subsets of the observations detailed herein were made by several groups studying BSCCO by STM over the last fifteen years. Such observations are discussed and compared to those herein in Chapter 4 of this thesis.

In addition, some aspects of the phenomenology described in this chapter suggest that an even more detailed study of the spatial variation of the LDOS may produce additional significant observations. In particular, the phenomenology suggests that the variations in some parameters imply of a spatial division of the material into regions with distinct electronic structure. This phenomenon, termed *granularity*, will be discussed in Chapter 5.

Additionally, a disparity between the low Δ and high Δ behavior of the LDOS further suggests that these electronically distinct regions may not form a continuum of behavior as a function of Δ , but rather may be classified as one of two or more types. This phenomenon, termed *segregation*, will also be discussed in Chapter 5.

Finally, Chapter 6 will provide some interpretation of the observations detailed in this and the next two chapters in the context of the overall knowledge and study of high temperature superconductors.

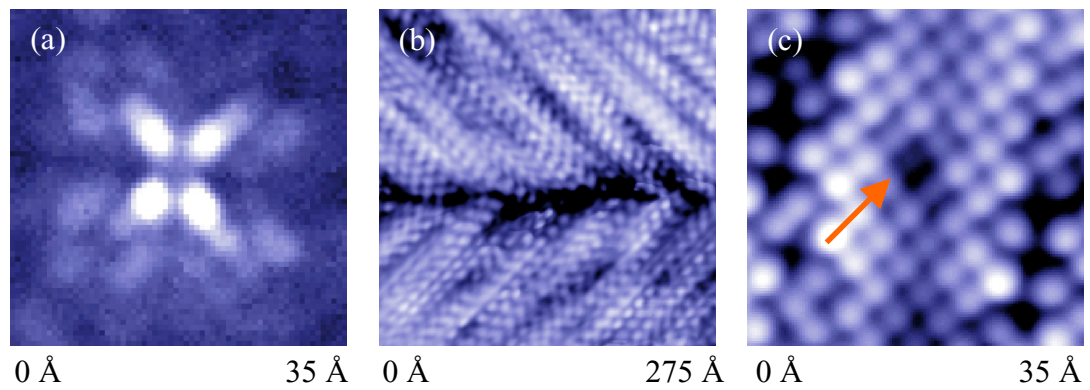


Figure 3.1: Extrinsic sources of disorder in high temperature superconductors: impurities, twin boundaries, and crystal defects.

(a) Differential conductance map of -9 mV Ni impurity resonance in $\text{Bi}_2\text{Sr}_2\text{CaCu}_2\text{O}_{8+\delta}$. (b) Topography of a twin boundary in $\text{YBa}_2\text{Cu}_3\text{O}_{7-\delta}$. (c) Topography showing a 'missing' atom crystal defect in $\text{Bi}_2\text{Sr}_2\text{CaCu}_2\text{O}_{8+\delta}$.

(a) Run =147, File =91118a00, $V_{\text{bias}} = -9$ mV, $V_{\text{set}} = -100$ mV, $I_{\text{set}} = 100$ pA

(b) Run =138, File =90715a00, $V_{\text{set}} = -100$ mV, $I_{\text{set}} = 100$ pA

(c) Run =147, File =91121f00, $V_{\text{set}} = -100$ mV, $I_{\text{set}} = 100$ pA

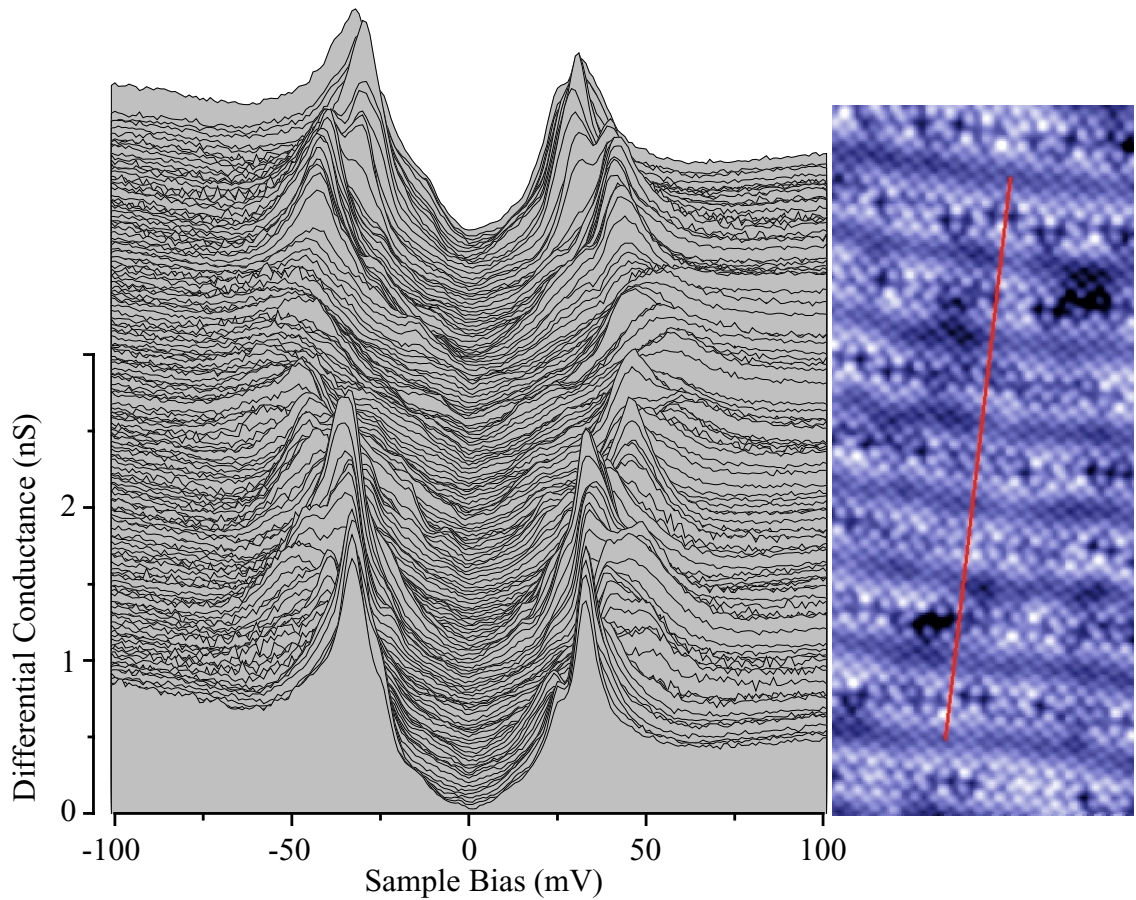


Figure 3.2: Linecut illustrating LDOS spatial inhomogeneity in BSCCO with as-grown oxygen doping.

This series of spectra was taken at 1.1 \AA intervals along a 176 \AA line. The spectra are vertically offset for clarity. The trajectory of the line is along the b-axis and is indicated on the topography. This linecut was taken on a BSCCO sample containing Ni impurities; however, its trajectory avoids the region of influence of all impurity atoms.

Run =147, File =91126a00-159 & 91124a, $V_{\text{set}} = -200 \text{ mV}$, $I_{\text{set}} = 200 \text{ pA}$

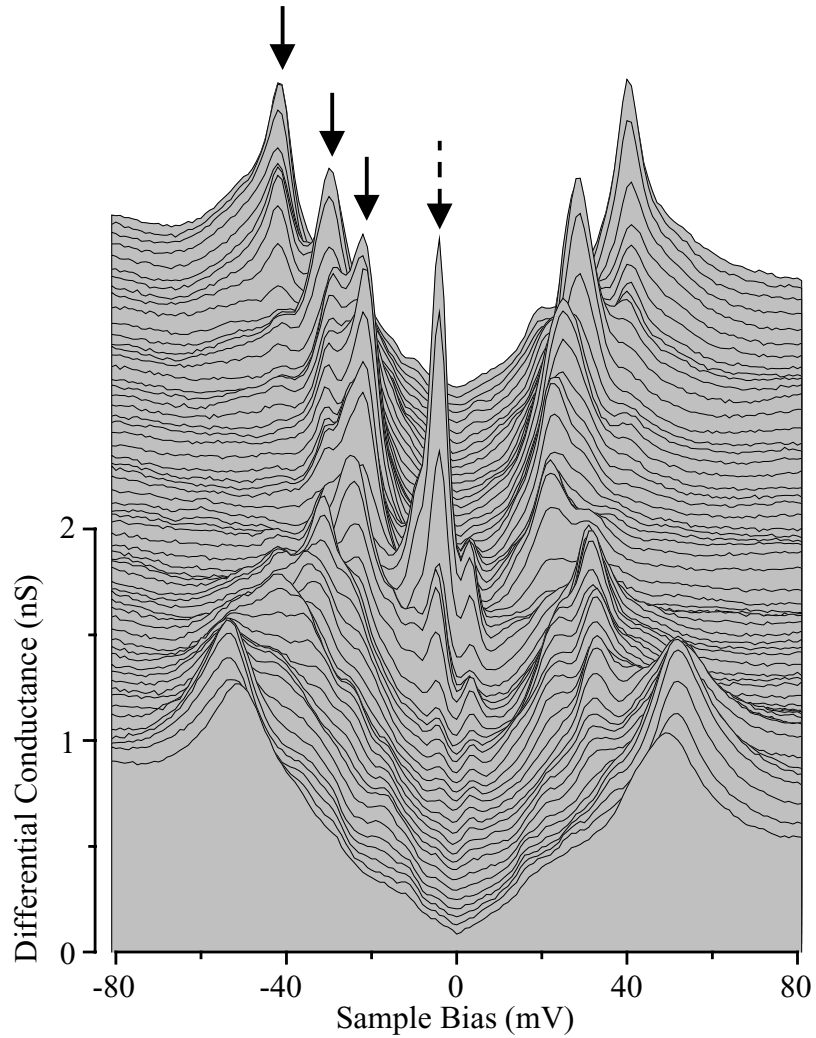


Figure 3.3: Linecut illustrating distinct Δ domains in BSCCO with as-grown oxygen doping.

This series of spectra was taken at 1.1 \AA intervals along a 64 \AA line. The spectra are vertically offset for clarity. The trajectory of the line is along the b-axis. This linecut was taken on a BSCCO sample containing Zn impurities. The trajectory of the linecut passes through a single Zn impurity which manifests as a high resonance peak at low energy (indicated by the dashed arrow). There are four distinct Δ domains outside the region of influence of the Zn atom, and three of these domains are indicated by arrows.

Run =122, File = avg 90302i series, $V_{\text{set}} = -100 \text{ mV}$, $I_{\text{set}} = 100 \text{ pA}$

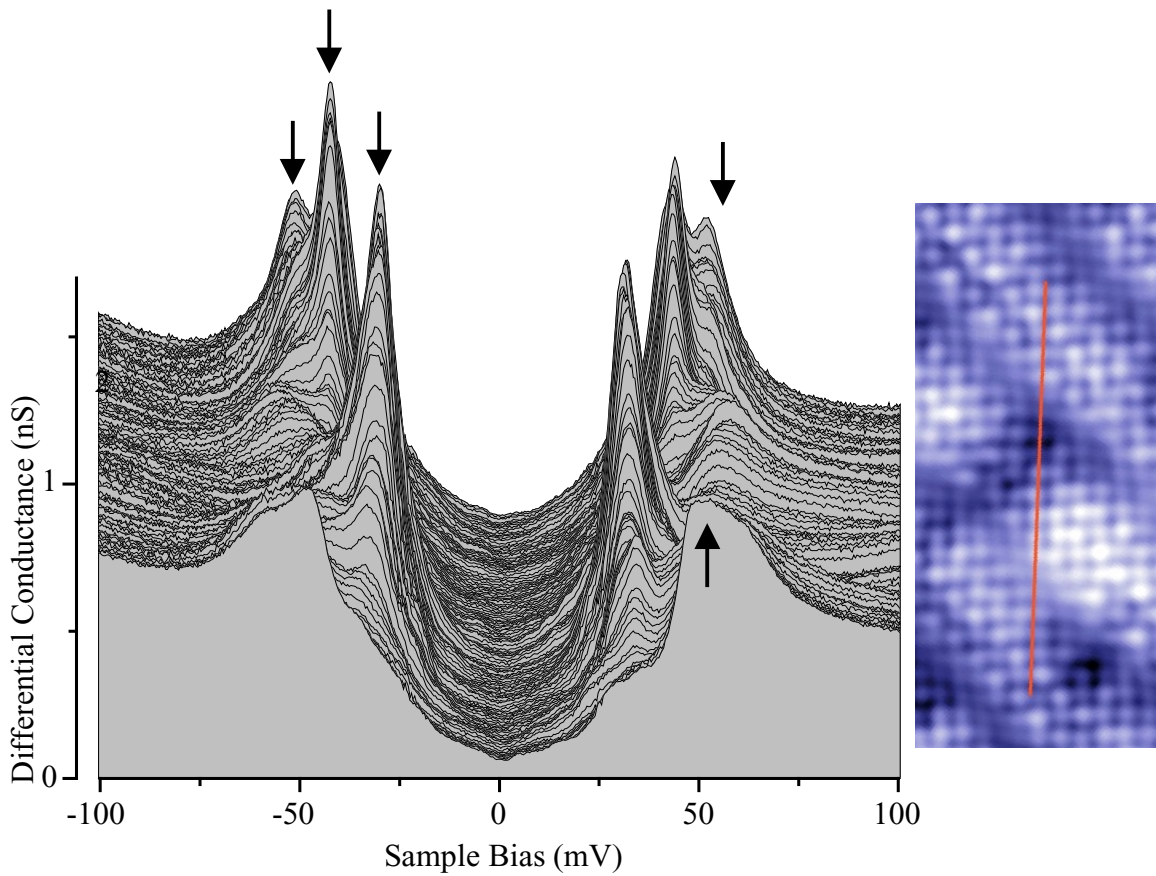


Figure 3.4: Linecut illustrating distinct Δ domains in underdoped BSCCO. This series of spectra was taken at 0.58 \AA intervals along a 71 \AA line. The spectra are vertically offset for clarity. The trajectory of the line is approximately along the x-axis and is indicated on the topography. The line passes through five distinct Δ domains each of which is marked with an arrow. This linecut was taken on an underdoped BSCCO sample containing no deliberately doped impurities. Run =159, File = 01101d00-250 every 2nd curve, $V_{\text{set}} = -200 \text{ mV}$, $I_{\text{set}} = 200 \text{ pA}$

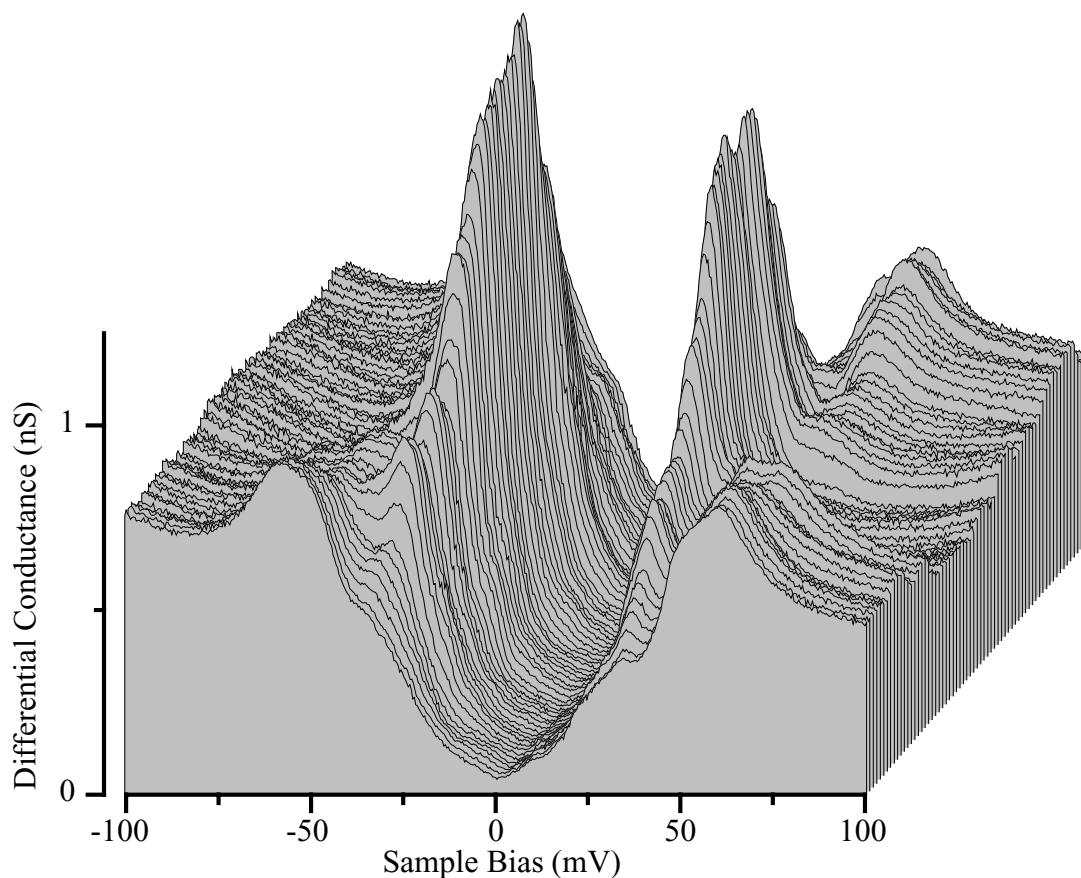


Figure 3.5: Linecut illustrating spatial variation in $A(\Delta)$ in underdoped BSCCO. The front of the linecut from Figure 3.4 is re-rendered here from a different angle to facilitate observation of variations in $A(\Delta)$. The spectra were taken at 0.58 \AA intervals along a 37 \AA line. The spectra are both vertically and horizontally offset for clarity. The trajectory of the line is approximately along the x-axis and is indicated on the topography in the previous figure. The line passes through three distinct Δ domains. The first and last domains in which Δ is larger each show little variation in $A(\Delta)$. This is in contrast to the middle domain in which Δ is lower, and the gap-edge peak rises and falls dramatically as the domain is crossed. This linecut was taken on a BSCCO sample containing no deliberately doped impurities.

Run =159, File = 01101d104-232 every 2nd curve, $V_{\text{set}} = -200 \text{ mV}$, $I_{\text{set}} = 200 \text{ pA}$

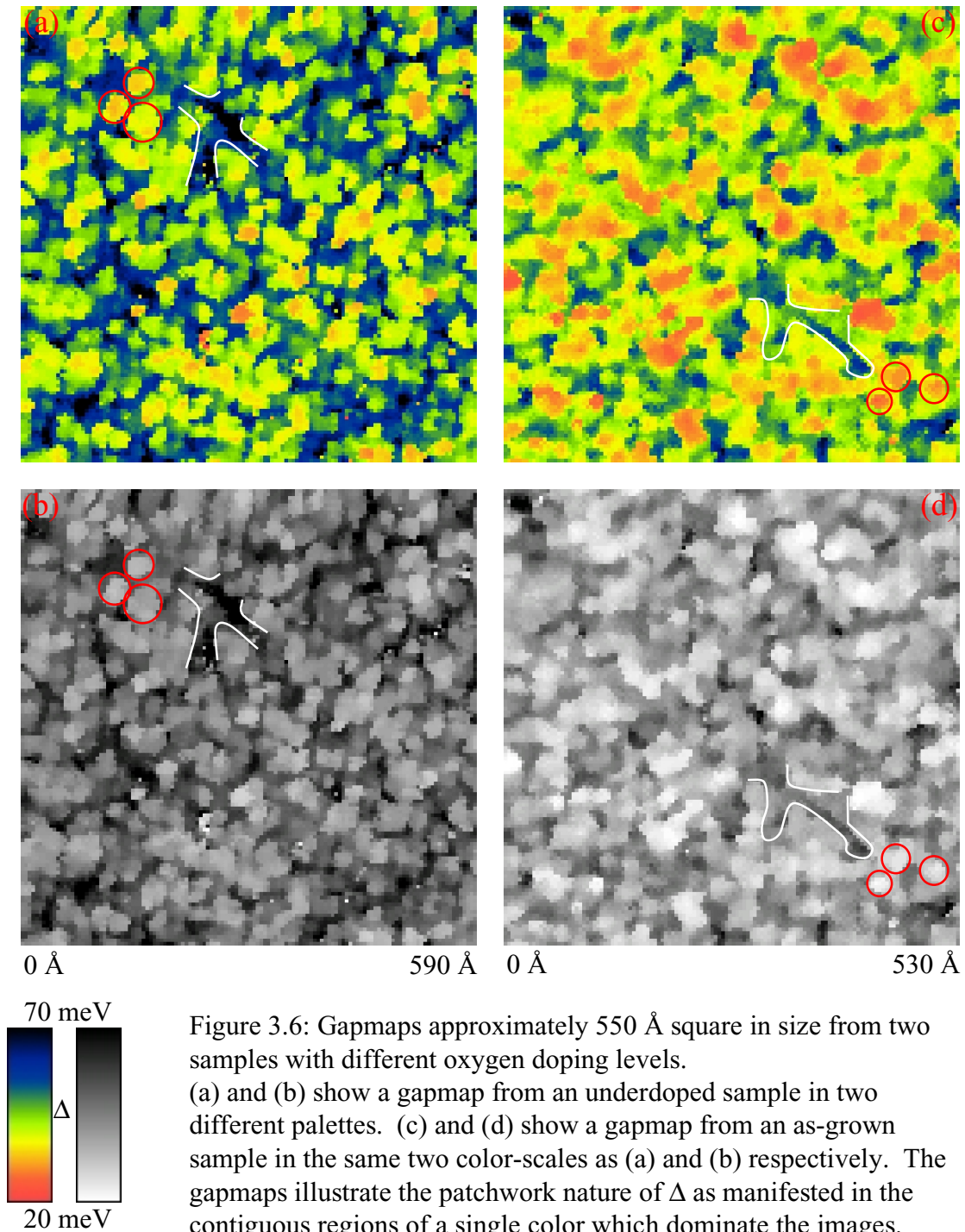


Figure 3.6: Gapmaps approximately 550 Å square in size from two samples with different oxygen doping levels. (a) and (b) show a gapmap from an underdoped sample in two different palettes. (c) and (d) show a gapmap from an as-grown sample in the same two color-scales as (a) and (b) respectively. The gapmaps illustrate the patchwork nature of Δ as manifested in the contiguous regions of a single color which dominate the images. Regions of low Δ are more compact and discrete, and several of these regions are roughly indicated by red circles. Regions of high Δ are more extended and percolative, particularly in the underdoped sample, and some are roughly indicated by white outlines. (a) and (b) Run = 159, File = 01113b02, $V_{\text{set}} = -200$ mV, $I_{\text{set}} = 200$ pA (c) and (d) Run = 122, File = 90304c00, $V_{\text{set}} = -200$ mV, $I_{\text{set}} = 200$ pA

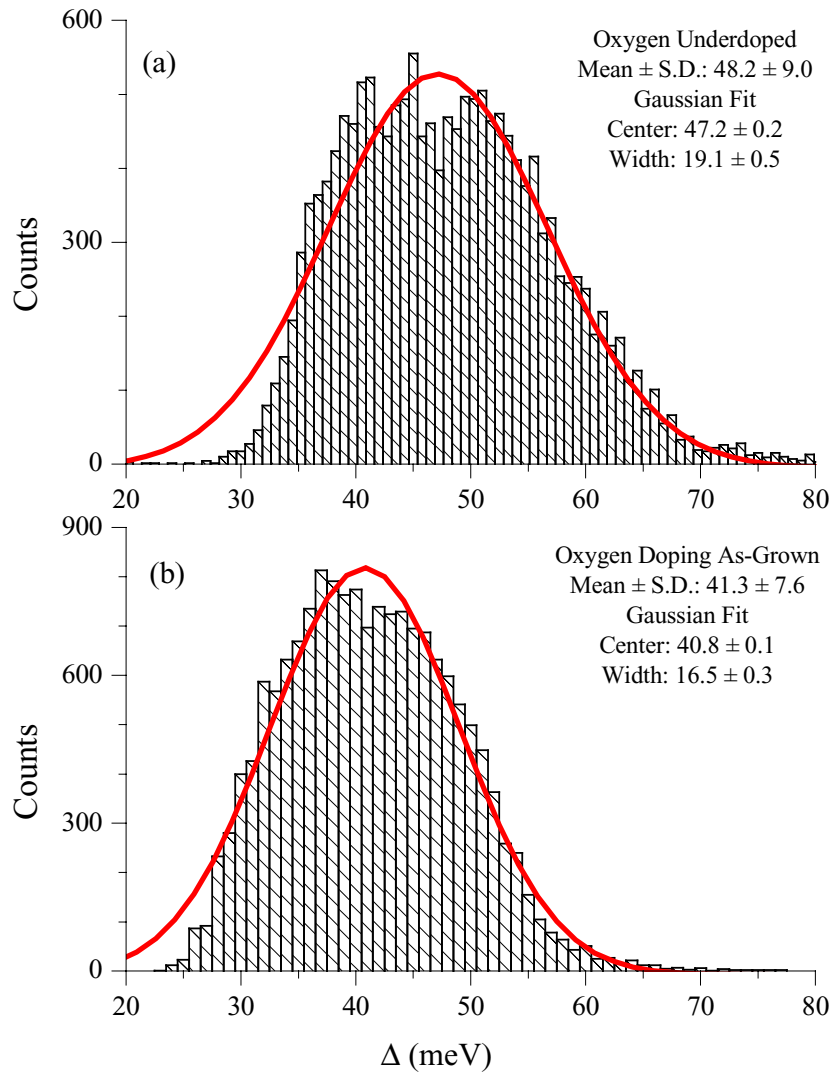


Figure 3.7: Histograms of Δ from regions approximately 550 \AA square in size from two samples with different oxygen doping levels. (a) gives the histogram of Δ values found in the region whose gapmap is shown in Figure 3.6 (a&b). (b) gives the histogram of Δ values found in the region whose gapmap is shown in Figure 3.6 (c&d). The histogram for the underdoped sample is shifted significantly toward higher values of Δ as compared to that for the as-grown doping sample. Neither histogram is symmetric about its center, but rather the falloff on the low- Δ side is much steeper than on the high- Δ side, in particular for the underdoped sample.
 (a) Run =159, File = 01113b02, $V_{\text{set}} = -200 \text{ mV}$, $I_{\text{set}} = 200 \text{ pA}$
 (b) Run =122, File = 90304c00, $V_{\text{set}} = -200 \text{ mV}$, $I_{\text{set}} = 200 \text{ pA}$

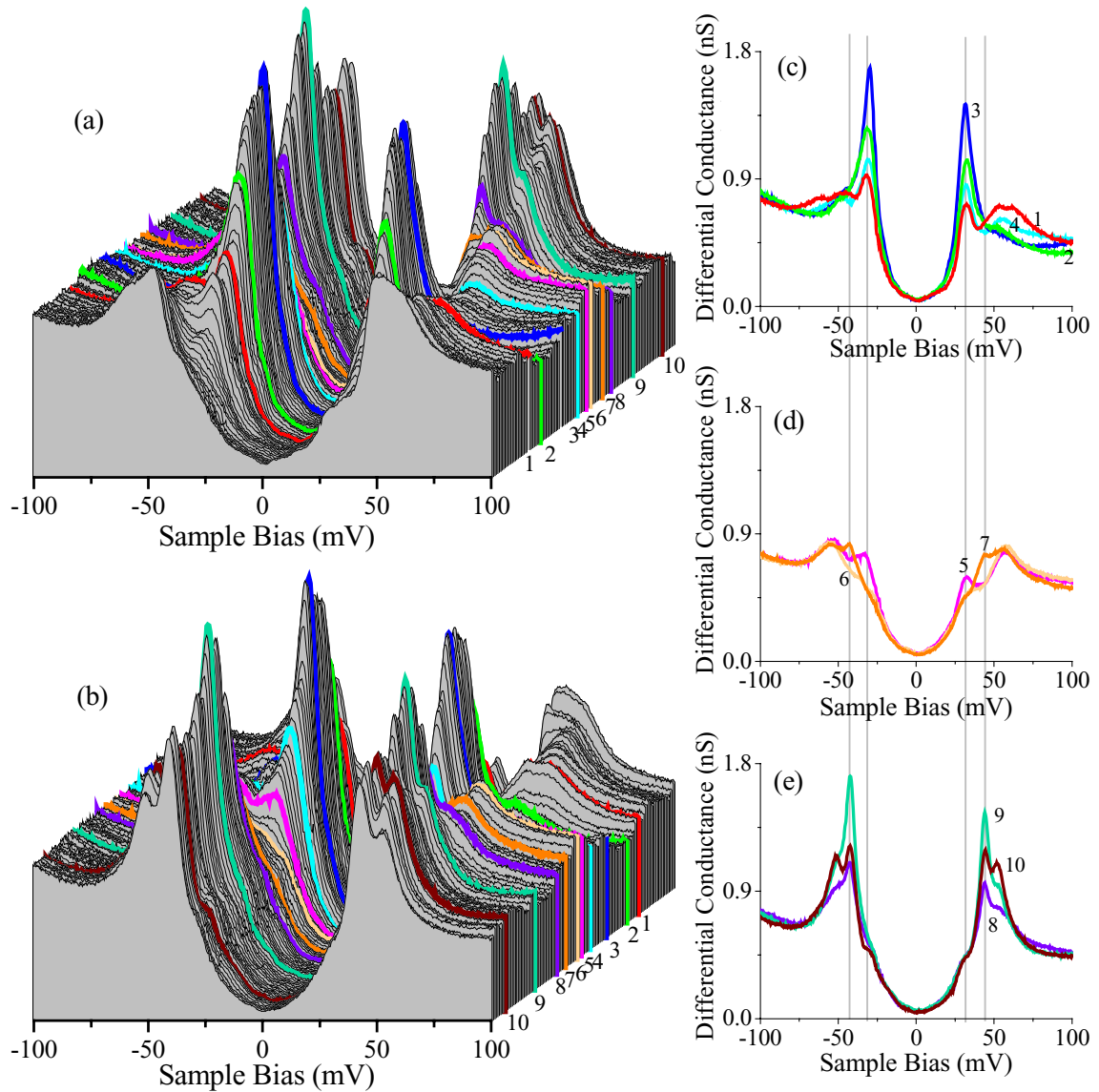


Figure 3.8: Representative set of selected spectra which illustrate the variety of observed spectral shapes.

(a) shows a different view of the linecut shown in Figure 3.4. (b) shows the same spectra as (a) but in the reverse order. The spectra in (a&b) are offset both vertically and horizontally for clarity. Selected spectra in (c,d,&e) are taken from the linecut as indicated by corresponding numbers and colors. These spectra illustrate the following qualitative spectral classes (see the text or the glossary for a definition of the classes): 1 = 4LB, 2 = 2HS, 3 = 2HS, 4 = 4LB-HS, 5 = 4LB, 6 = 2LB, 7 = 4LB, 8 = 2HS, 9 = 2HS, 10 = 4HS.

(a&b) Run = 159, File = 01101d00-250 every 2nd curve, $V_{\text{set}} = -200$ mV, $I_{\text{set}} = 200$ pA

(c) Run = 159, File = 01101d 200, 184, 156, 134, $V_{\text{set}} = -200$ mV, $I_{\text{set}} = 200$ pA

(d) Run = 159, File = 01101d 122, 116, 100, $V_{\text{set}} = -200$ mV, $I_{\text{set}} = 200$ pA

(e) Run = 159, File = 01101d 88, 58, 18, $V_{\text{set}} = -200$ mV, $I_{\text{set}} = 200$ pA

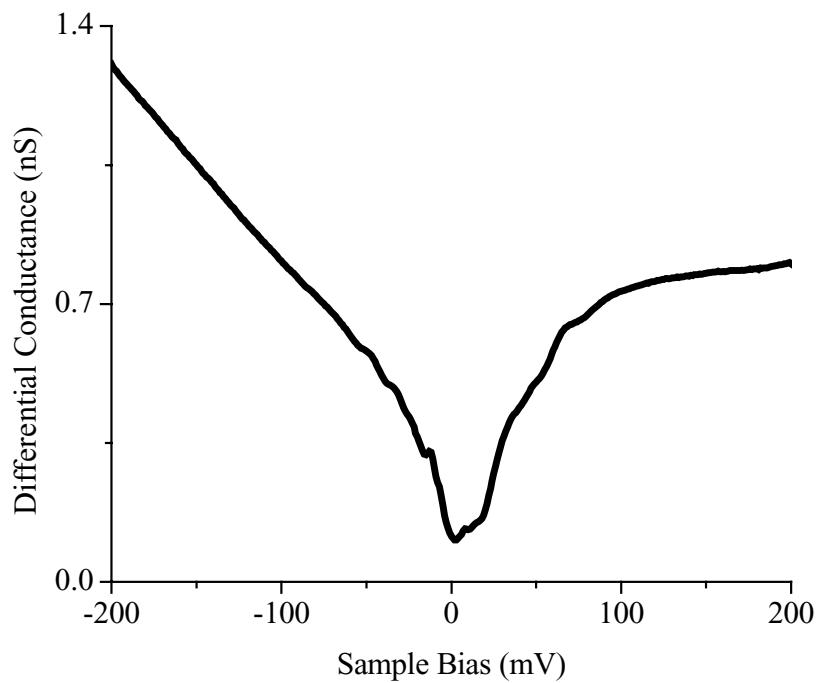
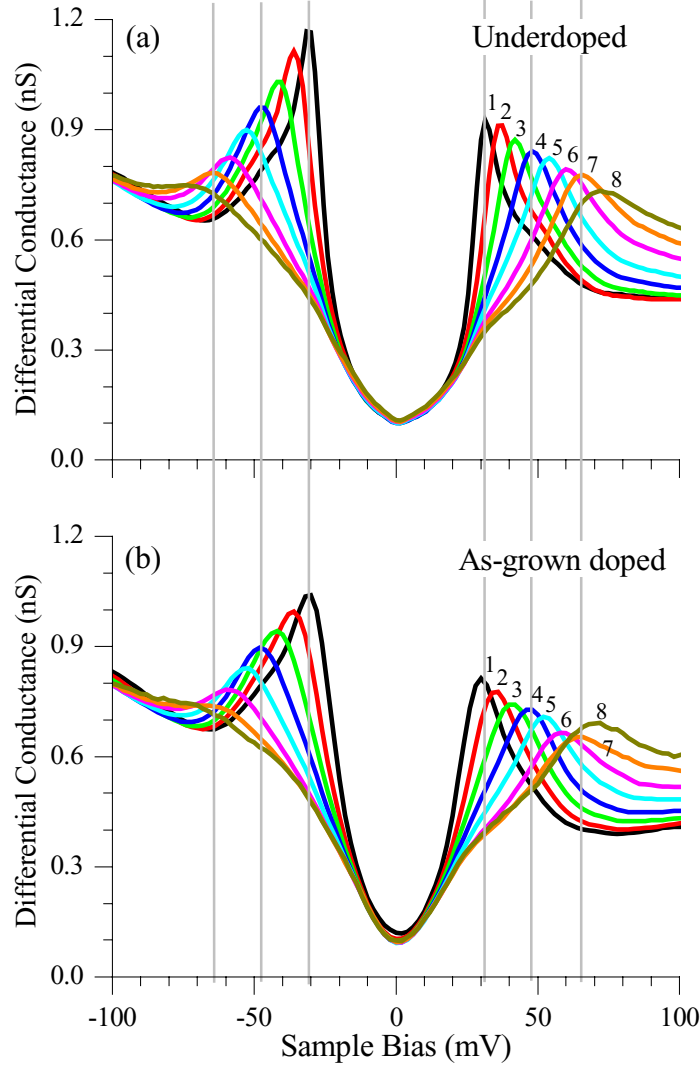


Figure 3.9: Spectrum representative of type with no distinct peaks.
This spectrum illustrates the type NP, in which no distinct peaks are observed out to the highest energy measured.
Run =159, File = 01024c, $V_{\text{set}} = -200$ mV, $I_{\text{set}} = 200$ pA



	Δ Bin(meV)	% in bin (UD)	% in bin (AGD)
1	26.5 to 32.5	1.2	12.4
2	32.5 to 38.5	13.9	25.9
3	38.5 to 44.5	23.7	27.2
4	44.5 to 50.5	23.2	22.5
5	50.5 to 56.5	20.9	9.7
6	56.5 to 62.5	11.5	1.8
7	62.5 to 68.5	4.6	0.45
8	68.5 to 74.5	1.1	0.11

Figure 3.10: Average spectra as a function of Δ . Spectral maps, from which the gapmaps of Figure 3.6 are also calculated, are used to generate these average spectra as follows. All 128^2 spectra in a given $\sim 550 \text{ \AA}$ square map are sorted on Δ . All the spectra in a given Δ bin are then averaged to produce the curves shown.

The table gives the bin ranges as well as the percent of the total spectra which are found in that bin. The clear trend indicated by this figure is that spectra with lower values of Δ have higher sharper gap-edge peaks, and conversely, spectra with higher values of Δ have lower broader gap-edge peaks.

(a) Run = 159, File = 01113b02, $V_{\text{set}} = -200 \text{ mV}$, $I_{\text{set}} = 200 \text{ pA}$

(b) Run = 122, File = 90304c00, $V_{\text{set}} = -200 \text{ mV}$, $I_{\text{set}} = 200 \text{ pA}$

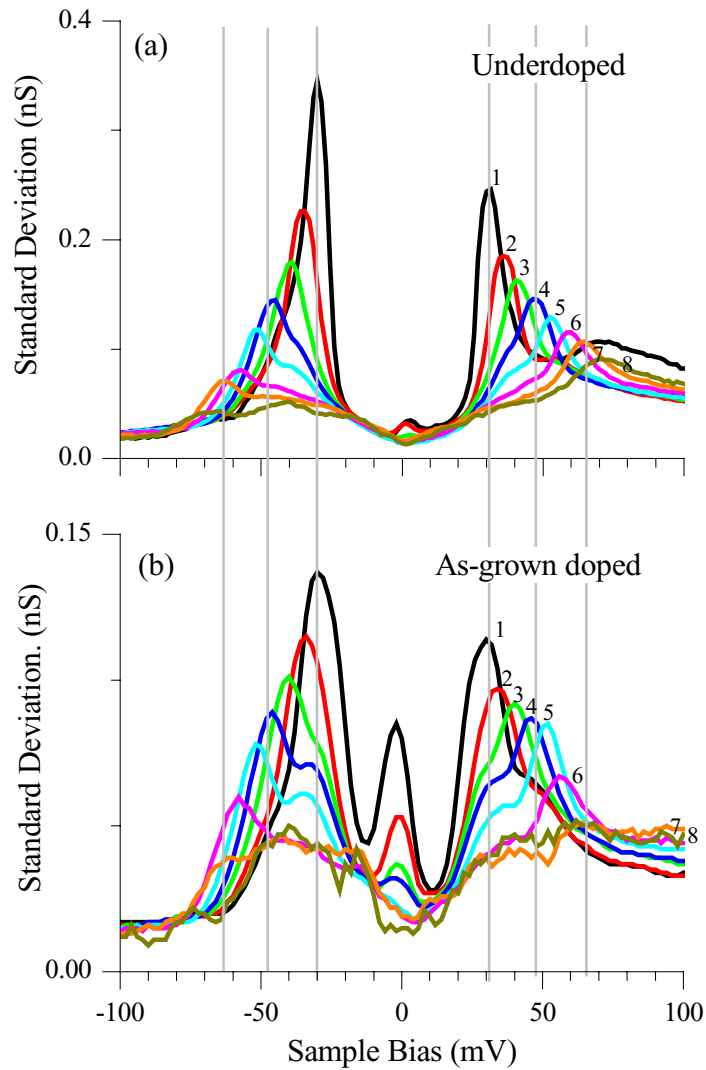
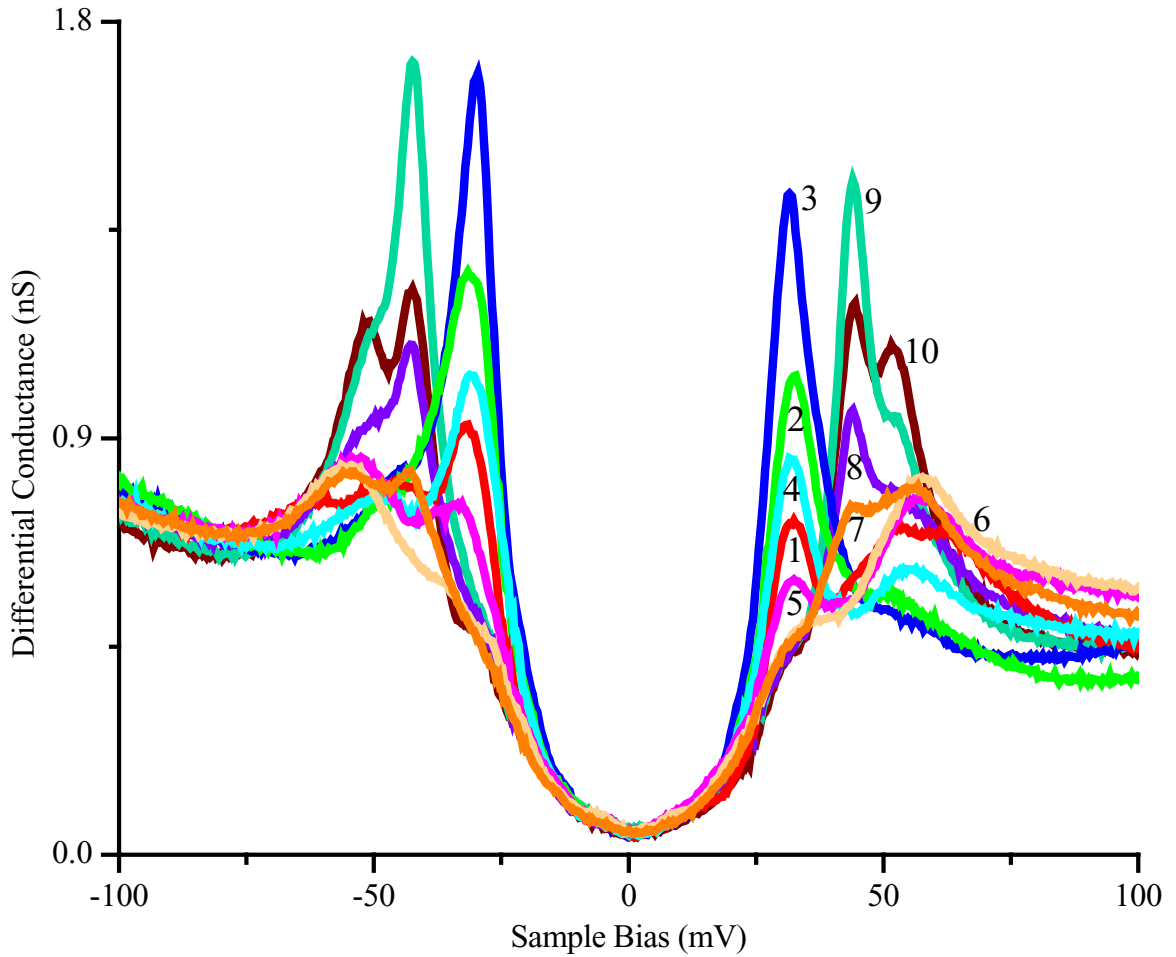


Figure 3.11: Standard deviation from the Δ -binned average spectra. These graphs show the standard deviation from the average spectra given in Figure 3.10. The binning, color scheme, and numbering are the same in this figure as in Figure 3.10, so see the table in that figure for the legend. The clear trend indicated by this figure is that spectra with lower values of Δ exhibit more variation in the height of their gap-edge peaks than do spectra with higher values of Δ . The large peak in the standard deviation near zero bias for the as-grown doping case is due to the presence of Zn impurities in this sample.

(a) Run =159, File = 01113b02, $V_{\text{set}} = -200$ mV, $I_{\text{set}} = 200$ pA

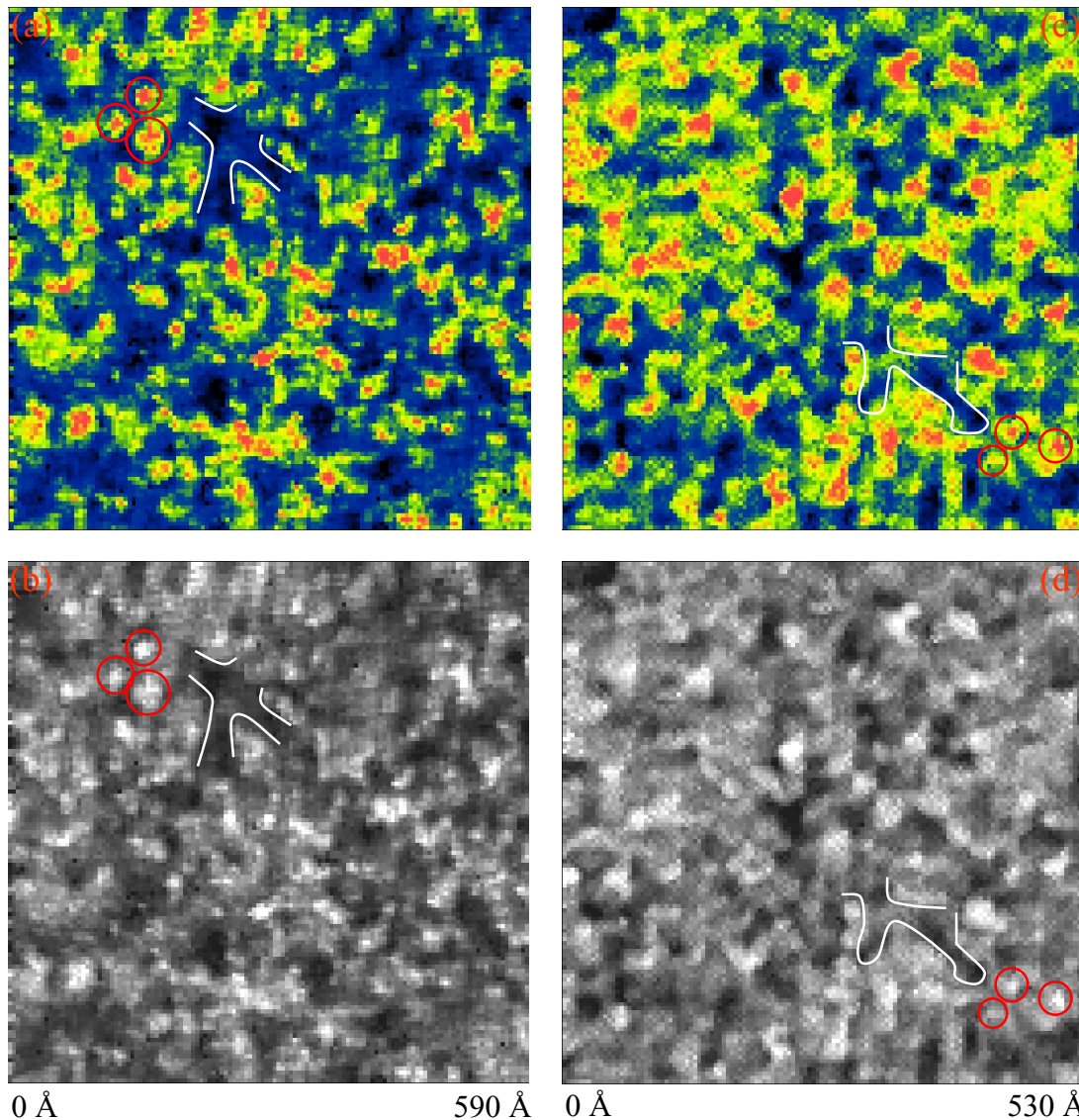
(b) Run =122, File = 90304c00, $V_{\text{set}} = -200$ mV, $I_{\text{set}} = 200$ pA



Spectrum	Σ (-15,-65)	Σ (-20,-75)
6	0.59	0.65
7	0.61	0.66
5	0.66	0.71
8	0.69	0.73
1	0.69	0.74
4	0.71	0.74
10	0.72	0.76
2	0.76	0.79
9	0.82	0.84
3	0.83	0.85

Figure 3.12: Correlation of $\Sigma(\Delta)$ with spectral shape. The selected spectra of Figure 3.8(c,d,&e) are reproduced here with the same color and number scheme. There is no offset for the spectra so that correlations between the spectral weight and spectral shape can be observed. Examination of the spectra in the figure in conjunction with the table at left implies that those spectra with higher and sharper gap-edge peaks generally have higher spectral weight in the Δ energy range, independent of the exact energy range chosen. Thus the value of $\Sigma(\Delta)$ is an indication of spectral shape.

(a) Run = 159, File = 01101d 18, 58, 88, 100, 116, 122, 134, 156, 184, 200,
 $V_{\text{set}} = -200$ mV, $I_{\text{set}} = 200$ pA

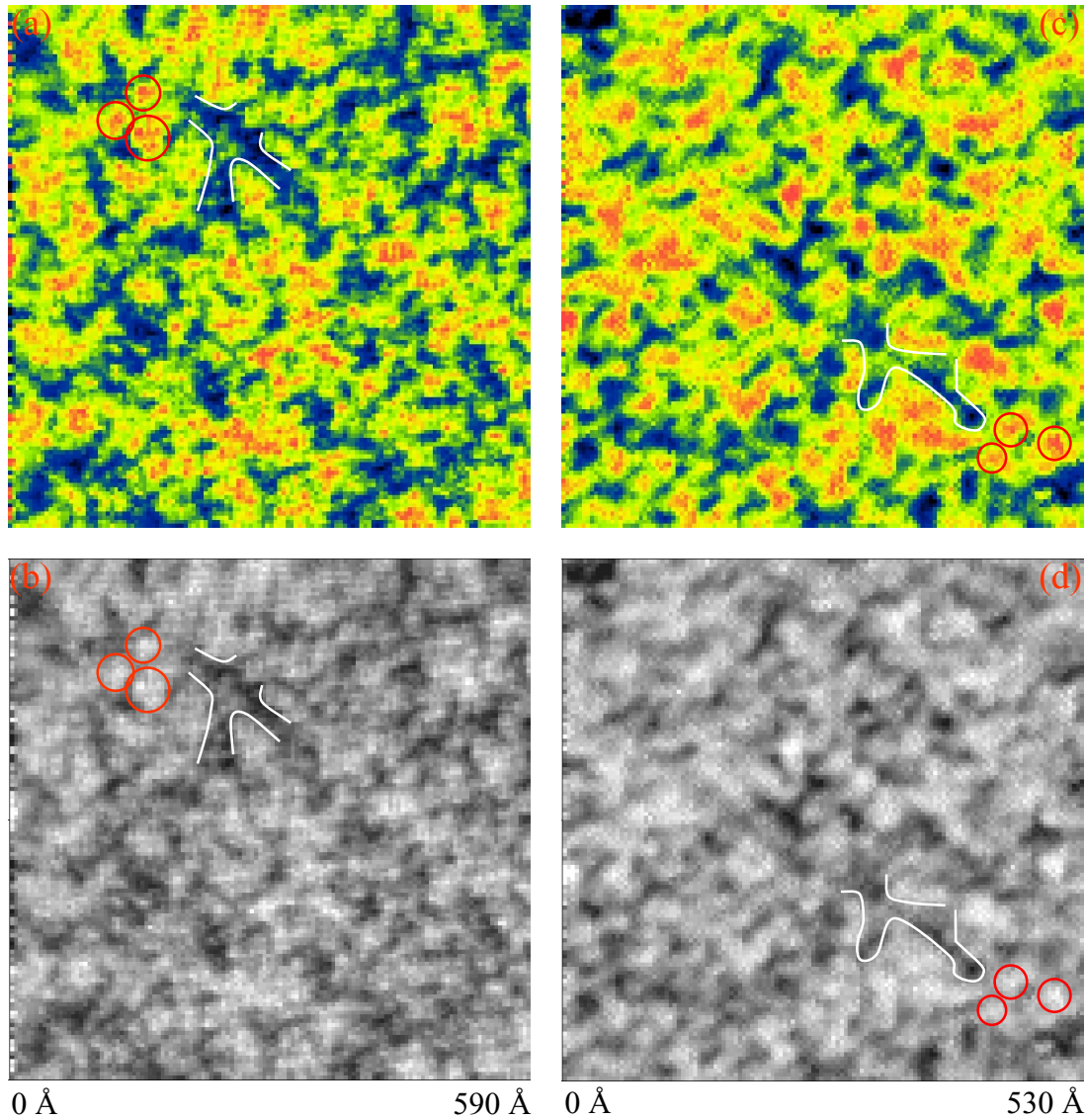


(a&b) 1.61 nS
(c&d) 1.29 nS
A(Δ)
(a&b) 0.61 nS
(c&d) 0.66 nS

Figure 3.13: $A(\Delta)$ maps approximately 550 Å square in size from two samples with different oxygen doping levels.

(a) and (b) show an $A(\Delta)$ -map from an underdoped sample in two different palettes. (c) and (d) show an $A(\Delta)$ -map from an as-grown sample in the same two palettes as (a) and (b). These maps are derived from the same spectral-surveys as those used to produce the gapmaps of Figure 3.6, and thus represent the same two regions of the same two samples. Comparison of these maps to the gapmaps of Figure 3.6 indicates a clear correlation, as manifested by a similarity of spatial shapes and patterns in the maps. This correlation is such that regions of low Δ are associated with regions of high $A(\Delta)$. The red and white curves which indicate characteristic regions of low and high Δ respectively, are the same as those given in Figure 3.6.

(a) and (b) Run =159, File = 01113b02, $V_{\text{set}} = -200$ mV, $I_{\text{set}} = 200$ pA
(c) and (d) Run =122, File = 90304c00, $V_{\text{set}} = -200$ mV, $I_{\text{set}} = 200$ pA



(a&b) 0.86 nS
 (c&d) 0.86 nS

 $\Sigma(\Delta)$
 (a&b) 0.43 nS
 (c&d) 0.52 nS

Figure 3.14: $\Sigma(\Delta)$ maps approximately 550 Å square in size from two samples with different oxygen doping levels. (a) and (b) show a $\Sigma(-15$ mV, -65 mV)-map from an underdoped sample in two different palettes. (c) and (d) show a $\Sigma(-15$ mV, -65 mV)-map from an as-grown sample in the same two palettes as (a) and (b). These maps are derived from the same spectral-surveys as those used to produce the maps of Figure 3.6 and 3.13, and thus represent the same two regions of the same two samples. Comparison of these maps to the gapmaps of Figure 3.6 indicates a clear correlation, as manifested by a similarity of spatial shapes and patterns in the maps.

This correlation is such that regions of low Δ are associated with regions of high $\Sigma(\Delta)$. The red and white curves, which indicate characteristic regions of low and high Δ respectively, are the same as those given in Figure 3.6 and 3.13.

(a) and (b) Run = 159, File = 01113b02, $V_{\text{set}} = -200$ mV, $I_{\text{set}} = 200$ pA
 (c) and (d) Run = 122, File = 90304c00, $V_{\text{set}} = -200$ mV, $I_{\text{set}} = 200$ pA

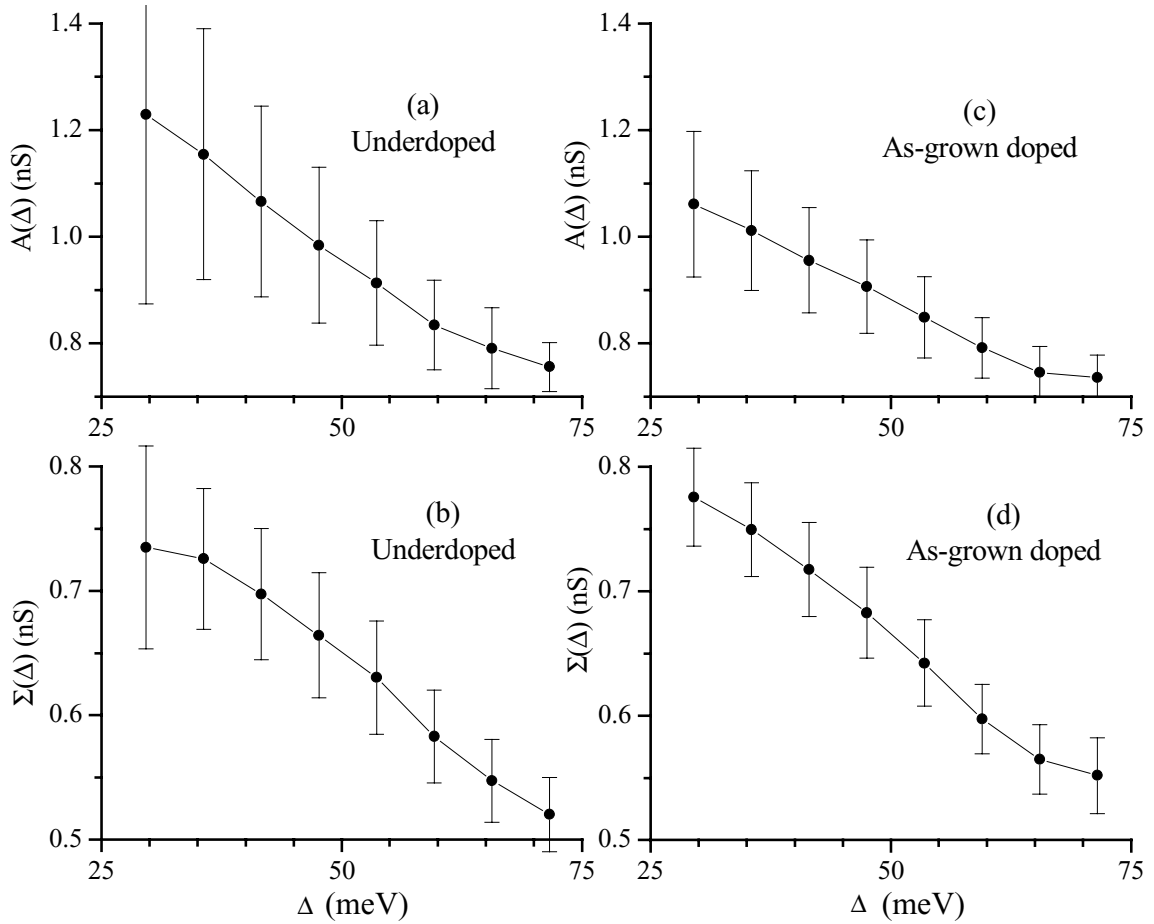


Figure 3.15: Trends in average $A(\Delta)$ and $\Sigma(\Delta)$ vs. Δ from two samples with different oxygen doping levels.

Spectral maps, from which the maps of Figures 3.6, 3.13, & 3.14 are also calculated, are used to generate these plots of the average trends in $A(\Delta)$ and $\Sigma(-15$ mV, -65 mV) as follows. All 128^2 spectra in a given ~ 550 Å square map are sorted on Δ . The average and standard deviation of the given quantity is then determined from all the spectra in a bin, and the average is plotted vs. Δ with the error bars given by standard deviation. The bins are the same as those used to produce Figure 3.10, and thus the table in that figure gives the percentage of total spectra in each bin. The plots show a clear trend such that $A(\Delta)$ and $\Sigma(\Delta)$ are both increasing for decreasing values of Δ .

(a) and (b) Run = 159, File = 01113b02, $V_{\text{set}} = -200$ mV, $I_{\text{set}} = 200$ pA

(c) and (d) Run = 122, File = 90304c00, $V_{\text{set}} = -200$ mV, $I_{\text{set}} = 200$ pA

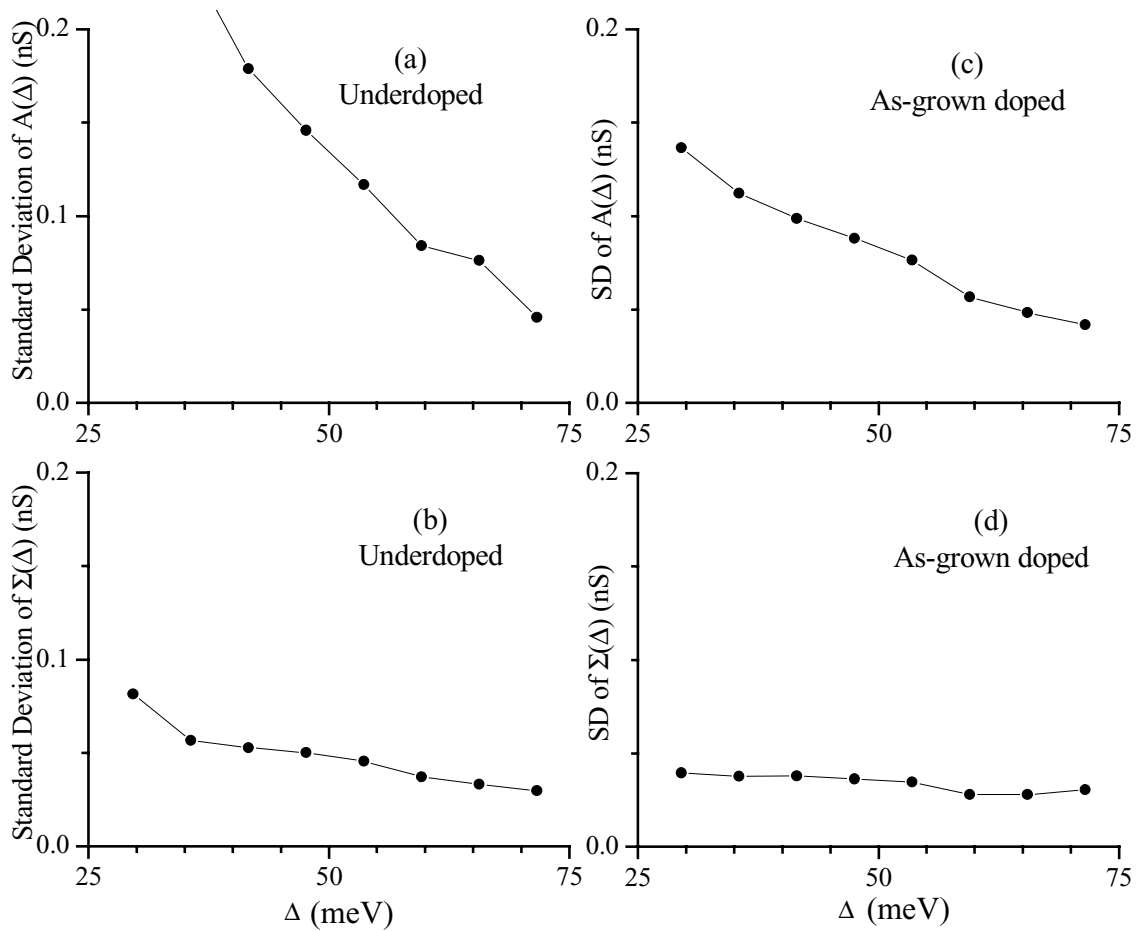
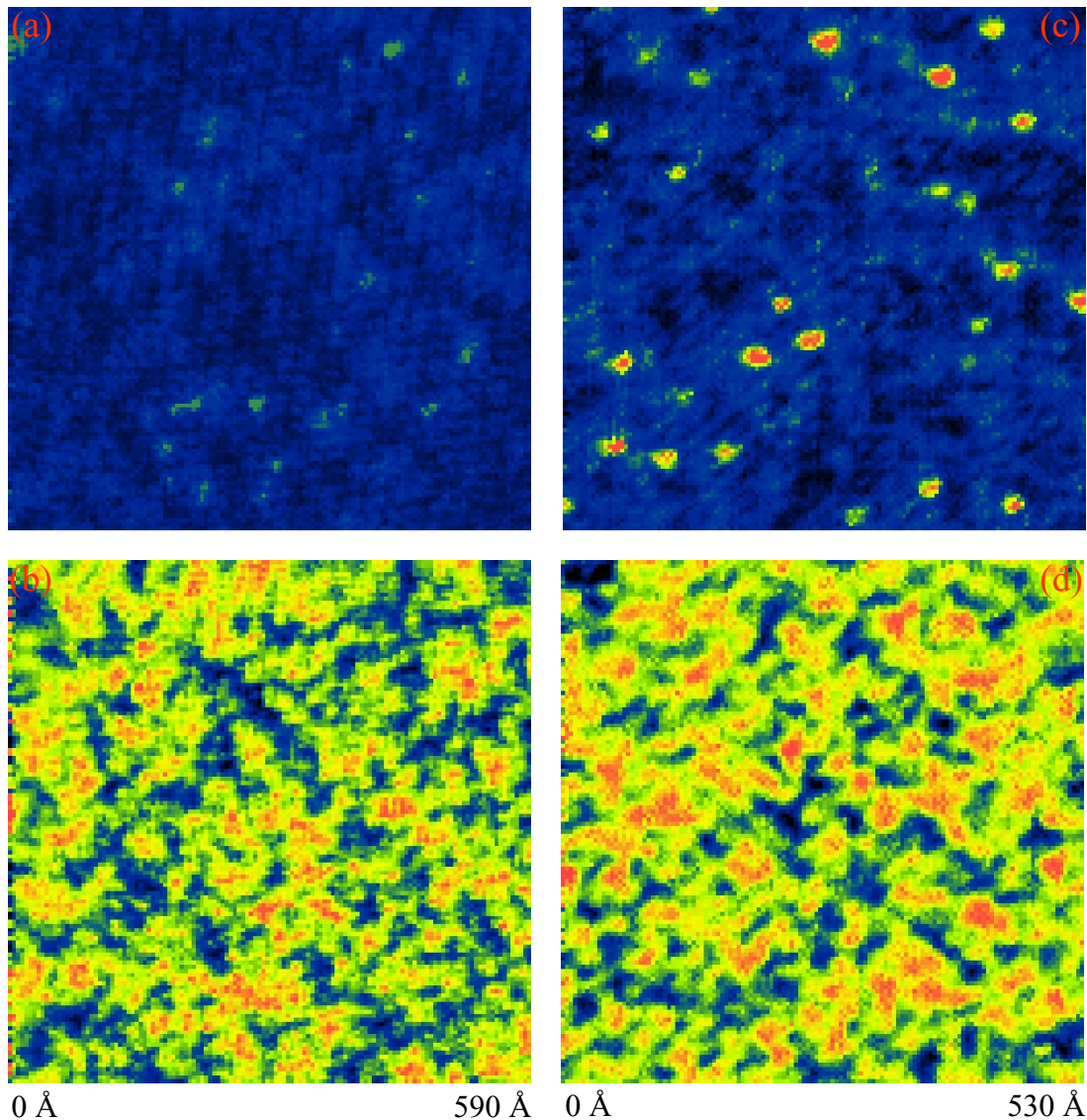


Figure 3.16: Trends in the standard deviation from the mean $A(\Delta)$ and $\Sigma(\Delta)$ vs. Δ from two samples with different oxygen doping levels.

Spectral maps, from which the maps of Figures 3.6, 3.13, 3.14, & 3.15 are also calculated, are used to generate these plots of the trends in the standard deviation (SD) from the mean $A(\Delta)$ and $\Sigma(-15 \text{ mV}, -65 \text{ mV})$, as detailed in the caption to Figure 3.15. The plots show a clear trend such that $SD-A(\Delta)$, and to a much lesser degree $SD-\Sigma(\Delta)$, are both increasing for decreasing values of Δ . This observation is consistent with the observation that the gap-edge peak increases and then decreases as a low- Δ region is traversed.

(a) and (b) Run =159, File = 01113b02, $V_{\text{set}} = -200 \text{ mV}$, $I_{\text{set}} = 200 \text{ pA}$

(c) and (d) Run =122, File = 90304c00, $V_{\text{set}} = -200 \text{ mV}$, $I_{\text{set}} = 200 \text{ pA}$



(a)0.5;(c)0.46
 (b)0.86;(d)0.86
 ↑ ↑
 +x Σ +y
 ↑ ↑
 (a)0.07;(c)0.12
 (b)0.43;(d)0.52

Figure 3.17: $\Sigma(\lesssim\Delta)$ maps approximately 550 Å square in size from two samples with different oxygen doping levels.

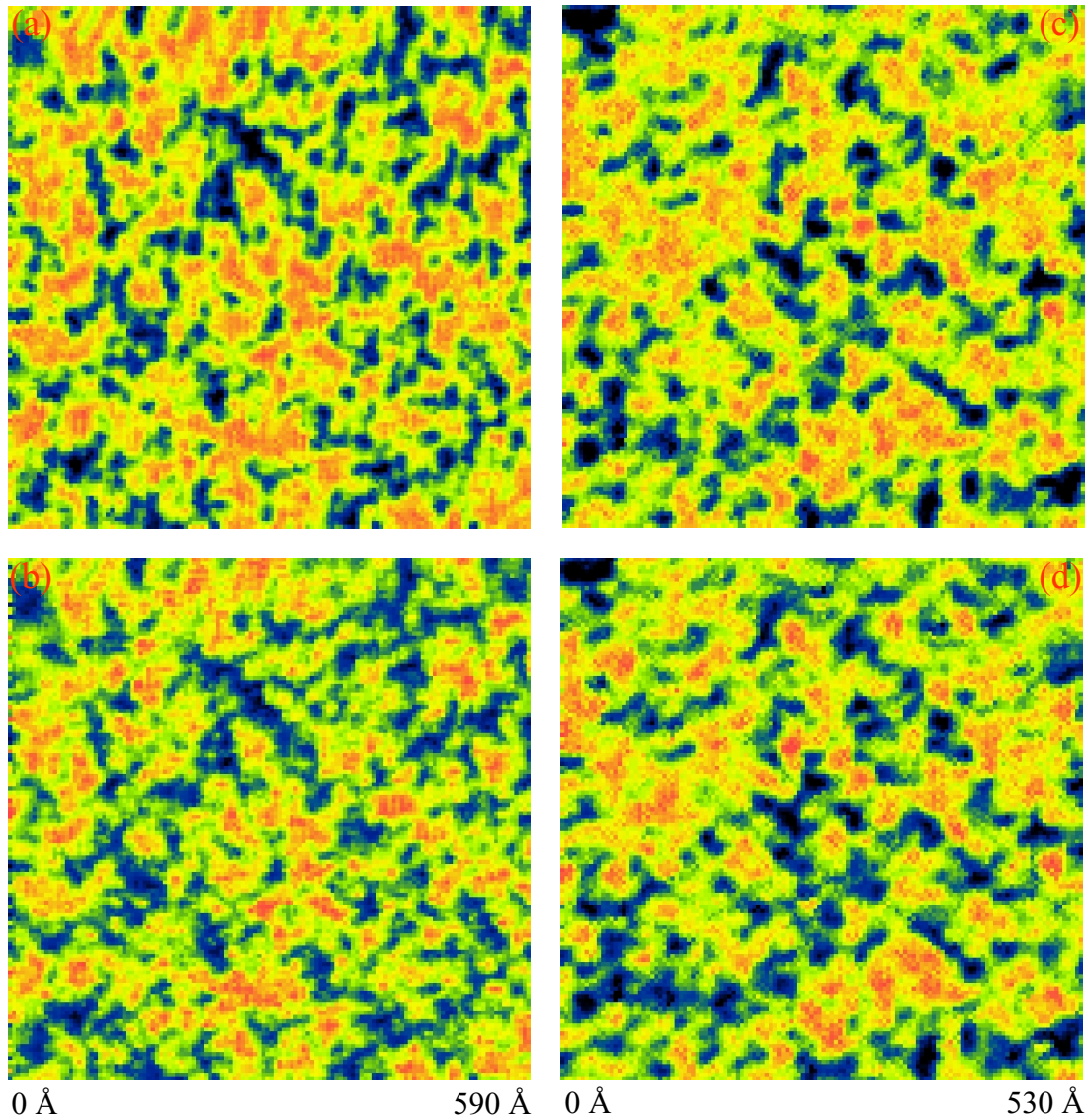
(a) and (c) show $\Sigma(0 \text{ mV}, -15 \text{ mV})$ -maps from an underdoped and as-grown doped sample respectively. For convenience the $\Sigma(-15 \text{ mV}, -65 \text{ mV})$ -maps of these same two regions are repeated from Figure 3.14 and are given in (b) and (d). These maps are derived from the same spectral-surveys as Figure 3.6 and 3.13. The ~ 25 compact regions in (c) are the localized effects of Zn atoms.

Ignoring these local perturbations, the $\Sigma(\lesssim\Delta)$ -maps show little spatial variation as compared to the $\Sigma(\Delta)$ -maps. Note that as with

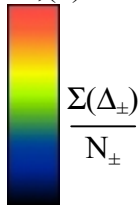
all the data in this thesis, these maps were taken with constant current normalization. (See Section 1.5.1 & 1.10.) For ease of comparison, the span of the colorbar is the same for both maps of the same sample. All data is in units of nS.

(a) and (b) Run =159, File = 01113b02, $V_{\text{set}} = -200 \text{ mV}$, $I_{\text{set}} = 200 \text{ pA}$

(c) and (d) Run =122, File = 90304c00, $V_{\text{set}} = -200 \text{ mV}$, $I_{\text{set}} = 200 \text{ pA}$



(a)1.46;(c)1.34
 (b)1.17;(d)1.23



(a)0.71;(c)1.0
 (b)0.69;(d)1.0

Figure 3.18: Compare $\Sigma(\Delta_+)/N_+$ to $\Sigma(\Delta_-)/N_-$ maps from two samples with different oxygen doping levels.

(a) and (c) show $\Sigma(+15 \text{ mV}, +65 \text{ mV})/N_+$ -maps from an underdoped and as-grown doped sample respectively. (b) and (d) show $\Sigma(-15 \text{ mV}, -65 \text{ mV})/N_-$ -maps of the same two regions, and are a numerically normalized version of Figure 3.14(a&c). The normalization factor, N_{\pm} , is equivalent to $\Sigma(0 \text{ mV}, \pm E_{\text{max}} \text{ mV})$ where E_{max} is the largest energy for which spectral data exists. For the underdoped/as-grown sample, E_{max} is 150 mV/100 mV. A qualitative comparison of the $\Sigma(\Delta_+)$ and $\Sigma(\Delta_-)$ maps reveals the same spatial patterns and shapes, which indicates that the behavior of $\Sigma(\Delta)$ is qualitatively the same independent of the polarity of the bias.

(a) and (b) Run =159, File = 01113b02, $V_{\text{set}} = -200 \text{ mV}$, $I_{\text{set}} = 200 \text{ pA}$
 (c) and (d) Run =122, File = 90304c00, $V_{\text{set}} = -200 \text{ mV}$, $I_{\text{set}} = 200 \text{ pA}$

Chapter 4

Literature Review:

Scanning Tunneling Microscopy Studies of Inhomogeneity in $\text{Bi}_2\text{Sr}_2\text{CaCu}_2\text{O}_{8+d}$

In Chapter 3 a detailed and extensive exposition of the phenomenology of inhomogeneity in the electronic structure of $\text{Bi}_2\text{Sr}_2\text{CaCu}_2\text{O}_{8+\delta}$ was presented based on data taken by myself and other members of the Davis Group at Berkeley. In addition, some of these results will be published [Pan 2001, Lang 2001], and more publications are forthcoming. Although the results presented in Davis Group publications and in Chapter 3 of this thesis represent a comparatively comprehensive study, more limited subsets of the observations detailed therein were made by several groups over the last fifteen years. In particular, papers by several groups have addressed the issue of spatial inhomogeneity observed in $\text{Bi}_2\text{Sr}_2\text{CaCu}_2\text{O}_{8+\delta}$ by scanning tunneling microscopy and spectroscopy. The purpose of this chapter is to present these papers and to discuss them in the context of the observations presented in Chapter 3.

In terms of the organization of this chapter, the several papers which represent the work of a single group, generally determined by the last author of the paper, will be presented together. The groups will be presented in approximately chronological order based on their most significant or extensive observations. For a single group, I will first present the observations made by that group by direct reference to or quotation from their papers. I will then discuss the observations of that group in the context of our observations as presented in Chapter 3.

4.1 Observation of Inhomogeneity by Topography and Non-Spatially Registered Spectroscopy

4.1.1 Coleman Group

An early suggestion that the electronic structure of BSCCO was not spatially homogenous came from the Coleman group at the University of Virginia, Charlottesville [Wang 1990]. Using a 4.2 K STM operating in a liquid helium environment, they obtained both topographic and spectroscopic data on optimally doped ($T_c = 95$ K) $\text{Bi}_2\text{Sr}_2\text{CaCu}_2\text{O}_{8+\delta}$ single crystals cleaved in air.

In their topographies they observed broad maxima and minima in apparent surface height which were distinct from the atomic corrugation. They state that the response “*can result from a variation in local electronic structure in the layers below the surface...*” [p. 8900]. In taking spectra at various locations, they find that “*The I versus V and dI/dV versus V curves generally show the presence of a strong gap structure, but the width and shape of this structure is strongly influenced by variations in the density of states below the gap*”

edge as well as variations in the position of the gap edge.” [p. 8900]. The paper goes on to describe difficulty in measuring a consistent value for the energetic size of the gap.

The results from Wang *et al* are consistent with the results presented in this thesis. Like them, we observe broad maxima and minima in our topographies as described in Section 1.5.2 and shown in Figure 1.9. As discussed in that section, these features are manifestations of the spectroscopic information which show up in the topography due to the constant current normalization scheme employed. As to their spectroscopic measurements, given an inhomogeneous sample it is to be expected in a random sampling of spectra that a variety of spectral shapes and gap values would be found. Certainly, their observations are suggestive of spatial inhomogeneity in the electronic structure and are consistent with our results.

4.1.2 Lieber Group

A second paper which addressed the issue of spatial inhomogeneity came from the Lieber group then at Columbia University [Wu 1991]. Using a room temperature STM operating in an argon environment they obtained topographic images of single crystal $\text{Bi}_2\text{Sr}_2\text{CaCu}_2\text{O}_{8+\delta}$ cleaved in situ. They studied both superconducting (as grown oxygen doping, $T_c = 85$ K) and non-superconducting (oxygen depleted) BSCCO.

They found that topographies taken on the *non-superconducting* samples with set point bias voltages in the range $-300 \text{ mV} > V > +500 \text{ mV}$ exhibited “*new non-periodic features in addition to a contribution from the superstructure...*” [p. 8731]. The approximate x-y plane size of these features is given as 20 - 30 Å, and the apparent vertical corrugation associated with them is reported to be ~ 5 times larger than the supermodulation, rendering them by far the dominant features in the images. Images taken with the same parameters on the *superconducting* crystals showed no such non-periodic features.

The results from Wu *et al* are consistent with the results reported in this thesis in that it seems likely that they are reporting a different phenomenon from the one we observe. Like Wu, we do not observe non-periodic structures with apparent vertical height much greater than the supermodulation in topographies taken on superconducting crystals. As discussed in Section 1.5.2 & Section 1.10.2 and shown in Figure 1.9, we do see a manifestation of the LDOS inhomogeneity in our topographies; however, these features have apparent z modulation which is about the same as or less than the corrugation due to the supermodulation.

There is no comment in the Wu paper on the existence of such smaller features, but one might imagine that they did not focus on such small features in light of the dominant features that they do report in the non-superconducting crystals. Additionally, as the features we see are associated with a gap which is found only at lower temperatures, the Wu observations which are made at room temperature may not be relevant to the work presented in this thesis.

4.1.3 Goldman Group

The Goldman group at the University of Minnesota also addressed the issue of electronic inhomogeneity in $\text{Bi}_2\text{Sr}_2\text{CaCu}_2\text{O}_{8+\delta}$ [Liu 1991]. They studied BSCCO single crystals with $T_c = 85$ K. The doping level is not stated, but is presumably as-grown. The crystals were cleaved at room temperature in air and then studied by STM in vacuum at 4.2 K.

After taking spectra at various sites, they conclude that Δ can vary significantly from location to location. Their paper includes a histogram of 36 Δ values, which range from 27 meV to 51 meV. In addition to reporting that Δ is spatially varying, they comment on a relationship between Δ and the shape of the spectra, saying, “*Traces exhibiting the largest gaps were those which were most broadened. The best-defined peaks in the conductance were those with the lowest gaps...*” [p. 2197].

In terms of an interpretation of their findings, they state that “*The many I-V characteristics obtained in this work were different, certainly the result of the tip being positioned at locations with different atomic environments...Alternatively, there may be inclusions at a particular location of other Bi-Sr-Ca-Cu-O phases with different (higher) transition temperatures.*” [p. 2197].

The observations of Liu *et al* are consistent both qualitatively and quantitatively with our observations. Although they do not state explicitly the oxygen doping of the crystal they study, if one assumes that it was as-grown, then it would have roughly the same oxygen concentration as that of the as grown samples we use. As shown in Figure 3.7, the histogram of Δ values obtained by us on an as-grown sample gives a range for Δ of 25 meV to 60 meV with 90% of observations concentrated between 27 meV and 51 meV. Our finding is thus quantitatively consistent with the Goldman histogram given the statistical fluctuations which arise from their small sample size.

Additionally, the statement in the Liu paper that spectra with larger gaps show broader peaks is born out in our observations. Figure 3.10 which shows the average curve shape for different values of Δ , demonstrates a clear trend for large Δ gap-edge peaks to be significantly broadened compared with the high sharp gap-edge peaks found for spectra with lower values of Δ .

4.2 Observation of Inhomogeneity by Spatially Registered Spectroscopy

4.2.1 Wolf Group

Early observation of electronic inhomogeneity derived from spatially resolved spectroscopic measurements comes from the Wolf group at the Polytechnic University in Brooklyn [Chang 1992, Wolf 1994, Wolf 1996]. Using an STM operating in a liquid helium environment at 4.2 K, the group studied 90 K T_c single crystal $\text{Bi}_2\text{Sr}_2\text{CaCu}_2\text{O}_{8+\delta}$ which was cleaved in air.

In terms of the range of Δ values observed, they state that, “*Analysis of 10^4 $G(V)$ spectra shows a large gap D_c in the range of 36-41 meV...with $\sim 20\%$ variations on as small a scale as $\sim 50 \text{ \AA}$...*” [p. 5697 Chang 1992]. They also find a range of values for the height of the gap-edge peak up to a height that is 1.9 times the value of the normal DOS [p. 356 Wolf 1994]. They comment upon a correlation between these observations saying, “*the ‘highly peaked’ $G(V)$ correlates a maximum of $G_{peak}(x,y)$ and minimum in $V_{peak}(x,y)$ with a maximum of z at [one point]*”⁵² [p. 5694 Chang 1992]. Figure 4.1 illustrates these observations with a linecut from their data.

In terms of the origin and significance of these observations, they speculate saying, “*We believe that spatial variation in $G(V,x,y)$...certainly reflects local variations in the superconductivity at the surface. It is likely that the latter reflects variations in the local stoichiometry...*” [p. 5695 Chang 1992].

The observations from Wolf *et al* are consistent both qualitatively and quantitatively with our observations. They do not comment on any deliberate oxygen doping of their crystal from which one can assume that the crystals had as-grown doping. Thus the range of Δ values they obtain should be comparable to those obtained by us on as grown crystals. As reported by us in Figure 3.7, we obtain for as-grown crystals a value for Δ of 41.3 meV \pm 18.4% which agrees remarkably well with their reported value.

We also find comparable variation in peak height. For an as-grown sample, Figure 2.1 gives the histogram of peak height values we obtain, which range up to about 1.4 nS. As shown in Figure 3.10, the normal DOS value, as observed at the edge of the spectrum, is about 0.8 nS for this same tip and sample. This gives us a range of values for the height of the gap-edge peak up to a height that is 1.75 times the value of the normal DOS, which agrees well with their reported value.

Wolf *et al* report an approximate length scale of variations as 50 \AA which larger than the $\approx 28 \text{ \AA}$ diameter patches reported by us in Section 5.3.1. However, the $> 5 \text{ \AA}$ spatial resolution of their data could account for this discrepancy if they were unable to resolve distinct but neighboring patches.

Finally, their linecut of Figure 4.1 and their report of a correlation between highly peaked spectra and low values of Δ is qualitatively consistent with our observations. Figure 4.1 clearly shows that larger values of Δ are associated with spectra with lower and broader gap-edge peaks which are relatively constant in height. Conversely, in that figure, smaller values of Δ are associated with regions in which the gap-edge peaks are sharper and vary from low to high and back to low as the region is crossed. Qualitatively speaking, these trends are consistent with our observations as discussed in this chapter. In particular, Figure 4.1 should be compared to Figures 3.4 and 5.1.

⁵² Translating from the notation used by Wolf *et al* to the notation used in this thesis: $G(V)$ is equivalent to $A(V)$, G_{peak} is equivalent to $A(\Delta)$, and V_{peak} is equivalent to Δ , and z is the apparent vertical height as recorded in the topography.

4.2.2 Nishida Group

A second group which studied $\text{Bi}_2\text{Sr}_2\text{CaCu}_2\text{O}_{8+\delta}$ by spatially registered scanning tunneling spectroscopy was the Nishida group at the Tokyo Institute of Technology [Kaneko 1998]. Using an STM operating at 4.2K in vacuum, the group studied slightly overdoped 86 K T_c BSCCO single crystals which were cleaved at 4.2K in cryogenic UHV. The STM used had a coarse sample translation stage, thus permitting the study of widely separated regions of a single sample.

The group reports on surveys of two such widely separated regions, each 5000 Å on a side. In one region they find that the “*the shape of the tunneling spectra does not depend on the position in the scanned area and the scattering of data is very small among the spectra.*” [p. 107]. The spectra in this region show a nearly constant gap value of $\Delta = 40$ meV. In the second region they find that the spectral shape varies greatly with position, saying, “...*the spectra...do not show good spatial reproducibility. Peak voltages at the superconducting gap edge take different values from position to position, ranging from 30 meV to 50 meV...*” [p. 107]. Considering together all the regions studied, the group concludes that, “*these tunneling spectra can be classified into three types as in [the] Fig [reproduced here as 4.2]...*” [p. 109].

As to the origin of the variations observed, the group comments, “*We think that the difference between the tunneling spectra comes from an inhomogeneous distribution of oxygen content in the sample: the oxygen content will be homogeneous in the length scale of at least 500 nm, but not in the scale of a sample size (~ mm).*” [p. 114].

The observations of Kaneko *et al* are consistent with our observations in that they do report inhomogeneity in spectral shape for some regions of their sample. The range of Δ values which they report for their slightly overdoped sample is centered on the same value as, but somewhat narrower than the distribution that we report for an as-grown sample in Figure 3.7. The three spectral types reported by them in panels a/b/c of Figure 4.2 are similar in shape to the 2HS/2LB/NP spectral types shown by us in Figure 3.8 and 3.9.

The regions of their sample which are homogeneous are probably related to the reports of the Lieber and Fischer groups (see below) of homogeneity in recently annealed samples.

4.2.3 Klein Group

Another observation of electronic inhomogeneity by spatially registered spectroscopy in BSSCO comes from the Klein group at the University of Paris [Cren 2000]⁵³. Using an STM operating at 4.2 K in a low pressure helium gas environment, the group studied 93K T_c (55K transition width) thin films of $\text{Bi}_2\text{Sr}_2\text{CaCu}_2\text{O}_{8+\delta}$. The films were grown to a thickness of 300 Å by MBE with two Bi-O layers terminating the growth, thus the top layer is the same as is usual for a cleaved single crystal [Pan 1998].

⁵³ A second paper by this group reports similar observations in $\text{Bi}_{2-x}\text{Pb}_x\text{Sr}_2\text{CaCu}_2\text{O}_{8+\delta}$ [Cren 2001].

The group reports variation in the gap size, saying, “*we find that the peak-to-peak gap value $2D$ varies significantly from one region to another; from roughly $D = 25$ meV to about 55 meV, while within a given region, the gap remains unchanged.*” [p. 148]. With regards to an observed variety of spectral shapes, they report, “*three different types of regions according to the local spectra.*” [p. 147]. The first type of spectrum, termed “superconducting,” is shown in Figure 4.3(a), and a second type, termed “pseudogap,” is shown in Figure 4.3(b). Finally there is a third type termed “semiconducting,” which has a “V shape” showing no peaks in the LDOS out to ± 100 meV.

As for spatial structure of the inhomogeneity, they report discrete regions in which one of these three types of spectra are manifest throughout the region. In particular they state, “*we find superconducting islands, bordered by pseudogap regions, dispersed on a dominating semiconducting sample surface.*” [p. 150]. Two regions are shown in their linecut, reproduced here in Figure 4.3(c). Starting in the back, this linecut shows a “superconducting” region which transitions to a “pseudogap” region.

The observations from Cren *et al* are qualitatively consistent with our observations. They report a range of gap values which is roughly the same as that observed by us on an as-grown sample, as shown in Figure 3.7. Their report that within a given region the gap value remains unchanged is consistent with our findings as illustrated in the linecut of Figure 3.4.

As for the three spectral shapes which they report, their ‘superconducting’/‘pseudogap’ spectrum of Figure 4.3(a/b) is qualitatively similar to our type 2HS/2LB spectra of Figure 3.8, and their ‘semiconducting’ spectrum is qualitatively similar to our NP type spectrum of Figure 3.9. Their linecut of Figure 4.3(c) is roughly comparable to those presented in Figures 3.2-3.5 of this thesis. The size of the ‘superconducting’ region at the rear of the linecut of Figure 4.3(c) is somewhat larger than what we observe for regions with comparable spectral shapes; however, from a single their linecut it is difficult to draw any definitive conclusions.

4.2.4 Kapitulnik Group

A recent observation of spatial inhomogeneity by spatially registered STS comes from the Kapitulnik group at Stanford University [Howald 2001]. Using an STM operating in a UHV environment at 8 K, the group studied slightly underdoped 80 K T_C single crystal $\text{Bi}_2\text{Sr}_2\text{CaCu}_2\text{O}_{8+\delta}$ which was cleaved in UHV at room temperature. Their spectroscopic data was taken using constant current normalization.

The group reports that “*behavior at the gap energy is inhomogeneous, [while] at low energies the sample appears to be homogeneous.*” [p. 2]. By plotting the gap value as a function of position on the surface for a 60 Å square region, reproduced here in Figure 4.4(a), they find regions about 20-30 Å across which are spectrally distinct from one another. The distinction is determined both by the value of Δ and by the overall shape for a given spectrum. They report, “*two extremal spectra: those from the center of these*

regions and those far away...the two extreme shapes are separated by a distance of ~ 30 Å.” [p. 2]. The two extremal spectra observed are reproduced here in Figure 4.4(b).

As for the origin of the inhomogeneity they state, “We argue that this inhomogeneity is a consequence of electronic phase separation into regions that are proximity -coupled to give a continuous variation of the tunneling spectroscopic features.” [p. 1].

The observations from Howald *et al* are consistent both qualitatively and quantitatively with our observations. Like them, we find a homogeneous LDOS at energies below the lowest gap energy for constant current normalization, as illustrated in Figure 3.17. As discussed in Section 5.3.1, the approximate size of the regions we observe in our gapmaps is 28 Å, which is consistent with their reported region size. Finally, the two extremal spectra they report as ‘a’ and ‘b’ of Figure 4.4(b) are qualitatively similar to the 2HS and 2LB spectra reported by us in Figure 3.8.

4.3 Observation of Homogeneity in Recently Annealed Crystals

4.3.1 Lieber Group

The Lieber group at Harvard made early studies of $\text{Bi}_2\text{Sr}_2\text{CaCu}_2\text{O}_{8+\delta}$ by spatially resolved spectroscopy [Zhang 1993, Liu 1994]. They studied 85.5 K T_c single crystal BSCCO which was cleaved in air at room temperature just prior to cooling. Measurements were made at 4.2 K in a low pressure helium gas environment. Although they used an STM for their studies, all their measurements were made with the STM tip in contact with the sample surface.

For crystals which were oxygen annealed in 540° C shortly prior to study, the group concludes, “we have found that the gap structure is reproducible at different surface positions for these oxygen-annealed crystals” [p. 3425 Zhang 1993]. They find this statement to be true also for different overall oxygen doping levels, stating, “These results show that within experimental error ($\pm 1\text{s}$) the magnitude of $2D$ is constant in high-quality samples with T_c 's varying nearly 15 K” [p. 6236 Liu 1994]. However, they find that this spatial homogeneity does not exist for samples which have *not* been recently annealed, stating, “It is interesting that this well-developed gap structure is observed reproducibly over the surface of O_2 -annealed BSCCO samples. In contrast, we observe a wide range of I - V behavior on as-grown BSCCO samples...” [p. 3424 Zhang 1993].

4.3.2 Fischer Group

The Fischer group at the University of Geneva also made STS studies of $\text{Bi}_2\text{Sr}_2\text{CaCu}_2\text{O}_{8+\delta}$ [Renner 1994, Renner 1995, Fischer 1998, Renner 1998] with results similar to those of the Lieber group. They studied 92 K T_c BSCCO single crystals, which were cleaved in UHV at room temperature, using an STM which operated near 4.2 K in a low pressure helium gas environment. The single crystals that they used were grown by

the directional solidification technique and were oxygen annealed just prior to study [Fischer 2001].

Although the observations contained in these papers are extensive, those germane to the present work are discussions of the spatial reproducibility of the spectra. The Fischer group reports that, “[when we] let the tip scan the surface at a constant height and take spectra at regular intervals along the surface...the spectra do not vary appreciably from one spot to the next along the whole [34 nm] line.” [p. 490 Fischer 1998]. The figure to which this comment is referred is reproduced here in Figure 4.5(a&b), and it shows a spatially invariant spectrum with a gap and high sharp gap-edge peaks. It is worth noting that this is not the only spectral shape observed. The group sometimes encounters samples in which the spatially invariant spectrum appears “semiconducting” as shown in Figure 4.5(c).

However, regardless of which of the two spectral shapes are observed in a particular sample, they find that, “The spectra are reproducible as a function of time and location on the surface within the 4 μm range of our STM...” [p. 9210 Renner 1995]. Furthermore they state that, “We measured the same surface for a period of up to four weeks, without any significant altering of the spectra. We also found that the tunneling spectra did not change after thermal cycling the sample through room temperature.” [p. 150 Renner 1998].

Recently, the Fischer group has begun to report some inhomogeneity, saying, “[there is] a certain inhomogeneity (on a scale larger than 100 Å) of some of the samples which we would characterize as moderately homogeneous.” Although they go on to state that, “In fact large-scale homogeneity has also been obtained, using an optimum oxygenation procedure.” [p. 2 Hoogenboom 2001].

4.3.3 Discussion of the Lieber and Fischer Observations

The observations of Lieber *et al* and Fischer *et al* seem contradictory with the observations presented in this thesis in that they report spatially invariant spectra and a homogenous density of states for BSCCO. However, I suggest that there is one crucial distinction between their measurements and ours which accounts for this difference in observations. Whereas both the Lieber and Fischer groups report homogeneous results on crystals which have been oxygen-annealed just prior to observation, our inhomogeneous results are found on crystals which are annealed several weeks to months prior to study.

In fact both the Lieber and Fischer groups do observe variations in the spectra on samples which have not been recently annealed. The published statements from both groups on this topic are given above. In addition, Prof. Fischer has confirmed verbally that his group does observe some variation in the local spectroscopy, particularly when the samples are studied some while after they are annealed [Fischer 2001]. A comparison of the details of the variations observed by these groups and us must await the publication of inhomogeneity data by these groups.

Although one could debate whether recently-annealed or not recently-annealed represents the “intrinsic” properties of this material, I believe that any practical use will comprise material which has not been recently annealed, and thus it is this state which we seek to understand. In addition, since an annealed crystal kept at room temperature will evolve from the homogeneous state toward the inhomogeneous state, one might assume that the homogeneous state is a meta-stable state, whereas the inhomogeneous state is the ground state of the system. This argument provides a reason for studying crystals which have not been recently annealed.

4.4 Summary

In Chapter 3 observations made by us which demonstrated the existence and ubiquity of native spatial *inhomogeneity* in the local density of states of BSCCO were presented. The phenomenology of the variation was also described. Although these results represent a comparatively comprehensive study, more limited subsets of the observations detailed therein were made by several groups over the last fifteen years. The purpose of this chapter was to summarize those results and compare them to our results as presented in Chapter 3. A summary of this literature review is to be found in Table 4.1.

Notes to Table 4.1.

¹ Abbreviations used are as follows: NR = not reported, RT = room temperature, UHV = ultra-high vacuum, CUHV = cryogenic ultra-high vacuum, LHe = liquid helium environment, GHe = gaseous He environment, SD = standard deviation

² All samples are single crystals except as otherwise noted.

³ In our studies we find patches of a certain size and separation as specified in Section 5.3. However, in general the authors of the other papers summarized here were not specific in indicating the exact quantity to which their length scale referred. Consequently, the length scale given here may not refer to exactly the same phenomena in all cases, and so the number here should be taken as a rough approximation to the length scale of the variation.

⁴ The following quantities are defined: “center” = the average value of Δ observed, or if no average value is explicitly given then the average of the max and min values given. “sd” = standard deviation from the average value. “range” = (max - min)/2.

⁵ The three spectral types are 2HS, 2LB and NP, and they are shown in Figures 3.8 and 3.9. In addition, spectra with four peaks are found on the borders between distinct regions. These three additional border types are 4LB, 4HS, and 4LB-HS and are shown in Figure 3.8.

⁶ The authors do not state whether this film was grown in-situ in UHV or was cleaved.

⁷ This length scale comes from Cren 2001 which reports data taken on Bi_2 -

$\text{Pb}_x\text{Sr}_2\text{CaCu}_2\text{O}_{8+\delta}$ single crystals.

⁸ This group sees a homogeneous LDOS in samples which have been recently oxygen annealed. The report of inhomogeneity is in samples which have not been recently oxygen annealed. According to verbal reports from the Fischer group, “recently” means that the crystals have been stored at RT no more than a week or two before study at low temperature.

Table 4.1: Summary of STM observation of LDOS spatial variation¹.

Group	T _c and O-doping	Cleave conditions ²	Study conditions	See inhomogeneity?	Length Scale of Variations ³	Observed values of Δ (meV) ⁴		# distinct spectral types
						Center	Range	
Davis	79 K underdoped	4.2 K in CUHV	4.2 K in CUHV	yes	28 Å (size of patch)	48.2	±20 SD: 9.0	3 (see endnote 5)
Davis	as-grown (~opt-doping)	4.2 K in CUHV	4.2 K in CUHV	yes	28 Å (size of patch)	41.3	±18 SD: 7.6	3 (see endnote 5)
Coleman	95 K opt-doped	RT in air	4.2 K in LHe	yes	NR	NR	NR	NR
Goldman	85 K as-grown?	RT in air	4.2 K in CUHV	yes	NR	39	±12	NR
Wolf	90 K as-grown?	RT in air	4.2 K in LHe	yes	50 Å	36-41	±7.7	NR
Nishida	86 K overdoped	4.2 K in CUHV	4.2 K in CUHV	yes	NR	40	±10	3
Klein	93 K	MBE thin film ⁶	4.2 K in GHe	yes	30 Å ⁷	40	±15	3
Kapitulnik	80 K underdoped	RT in UHV	8 K in CUHV	yes	20-30 Å	NR	NR	2
Lieber	85.5 K	RT in air	4.2 K in GHe	yes ⁸	NR	NR	NR	NR
Fischer	92 K	RT in UHV	4.2 K in GHe	yes ⁸	>100 Å	NR	NR	NR

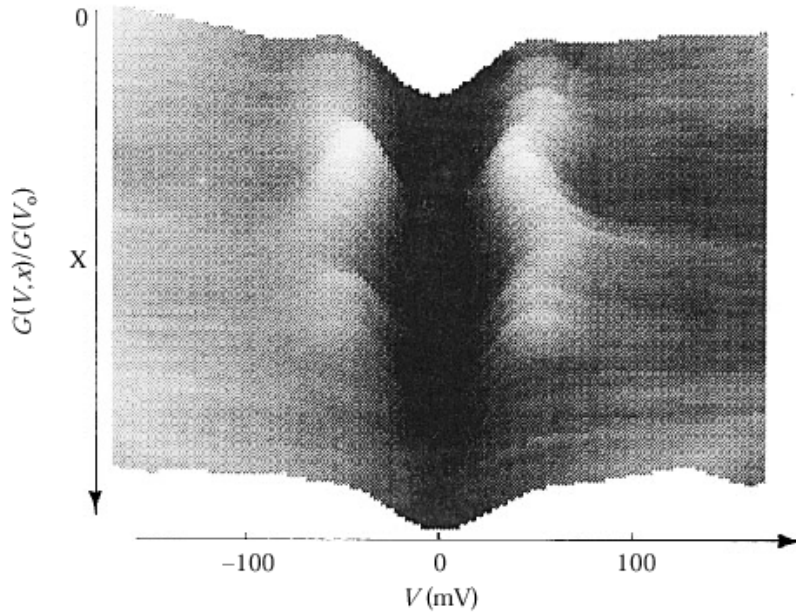


Figure 4.1: Linecut from the Wolf Group illustrating correlated spatial variation in Δ , $A(\Delta)$, and spectral shape.

This data was taken at 4.2 K on single crystal $\text{Bi}_2\text{Sr}_2\text{CaCu}_2\text{O}_{8+\delta}$. Curves were taken at 5 Å intervals over 500 Å length with averaging of the curves over a width of 25 Å. The gray-scale range is 0.12–1.36. The linecut shows the local variation of $A(V,x,y)/A(168 \text{ mV})$ and should be compared to linecuts in this thesis, in particular see Figures 3.4 and 5.1. The following similarities between this figure and the work in this thesis should be noted. This figure clearly shows that larger values of Δ are associated with spectra with lower and broader gap-edge peaks which are relatively constant in height. Conversely, smaller values of Δ are associated with regions in which the gap-edge peaks are sharper and vary from low to high and back to low as the region is crossed. These same observations were made with regard to the data presented in this thesis.

Reference: Figure 2 from Wolf 1996.

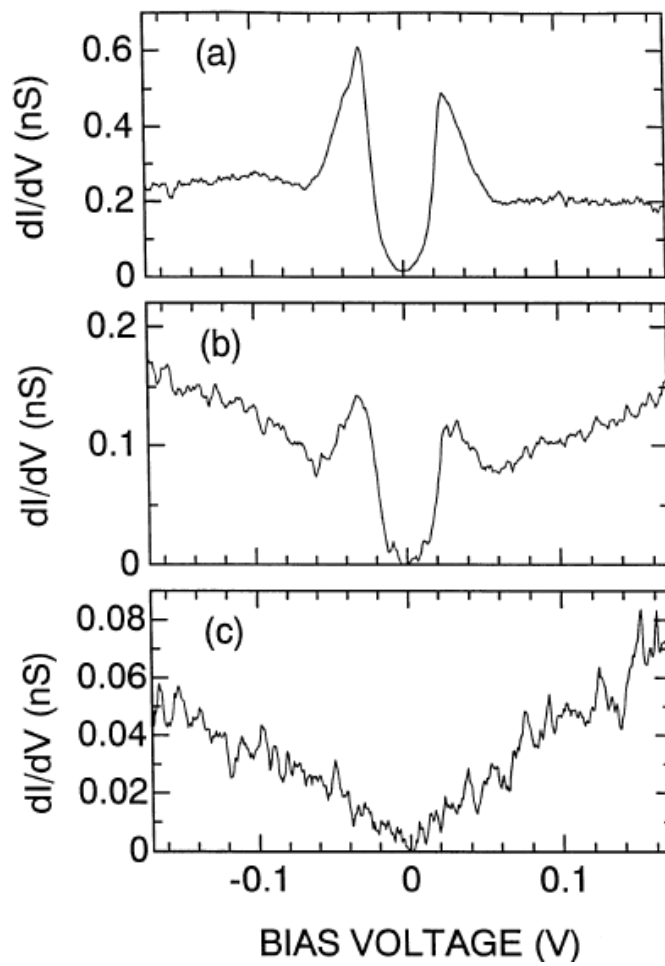


Figure 4.2: Spectra from the Nishida group which illustrate the three distinct spectral types observed.

This data was taken at 4.2 K on single crystal $\text{Bi}_2\text{Sr}_2\text{CaCu}_2\text{O}_{8+\delta}$. From a survey of large sample areas this group identified three distinct spectral types which are shown here. Qualitatively speaking, we observe the same three spectral types. The spectrum shown in (a/b) is similar in shape to the 2HS/2LB spectrum shown in this thesis in Figure 3.8. The spectrum shown in (c) is similar in shape to the spectrum shown in Figure 3.9.

Reference: Figure 6 from Kaneko 1998.

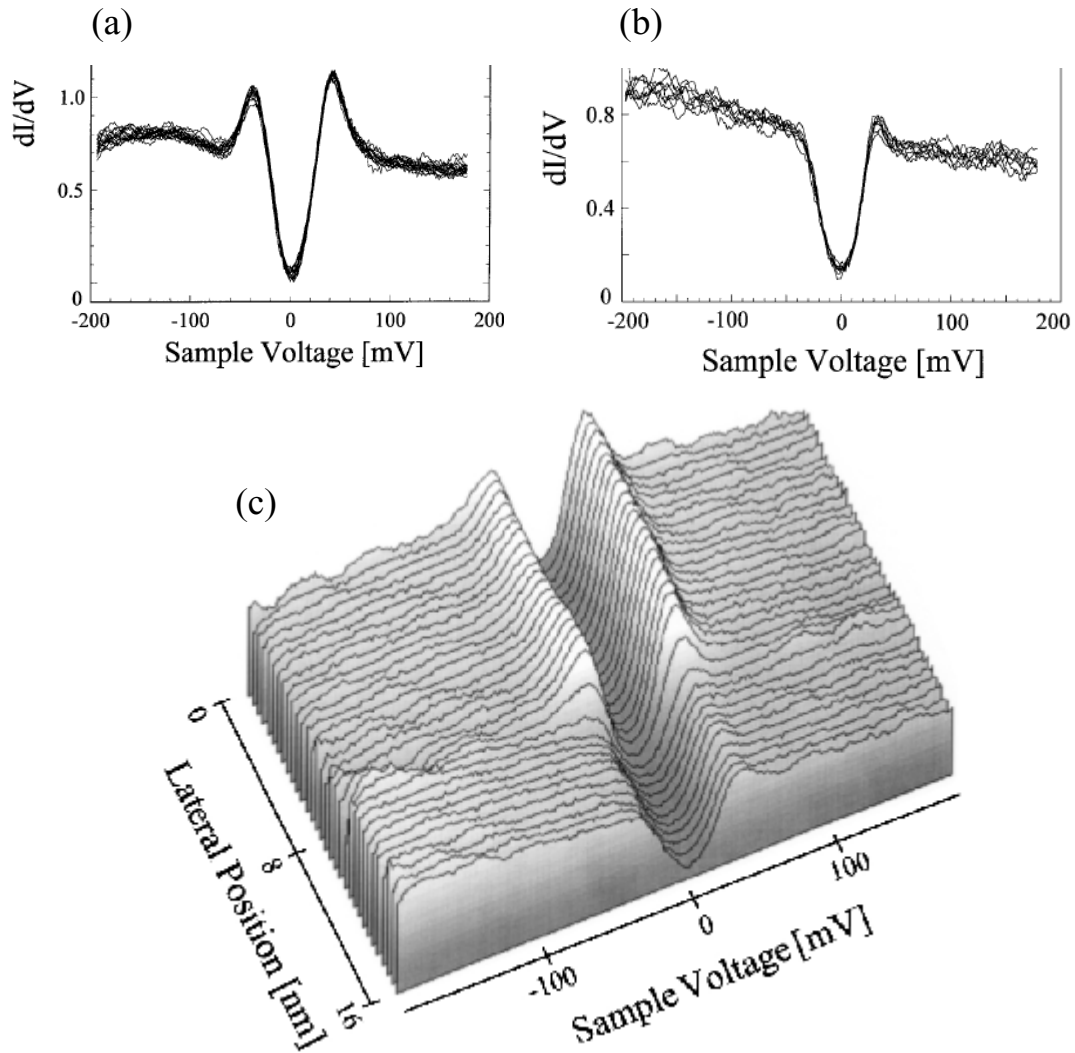


Figure 4.3: Spectra and linecut from the Klein group illustrating two observed spectral types and the transition between them. This data was taken at 4.2 K on MBE grown thin films of $\text{Bi}_2\text{Sr}_2\text{CaCu}_2\text{O}_{8+\delta}$. (a) Spectrum illustrating “superconducting” type. (b) Spectrum illustrating “pseudogap” type. (c) Line illustrating the transition between a “superconducting” region seen at the rear and the “pseudogap” region seen in front. The two spectral types illustrated in (a) and (b) are qualitatively comparable in shape to our 2HS and 2LB types respectively, which are shown in Figure 3.8 of this thesis. The linecut of (c) should be compared to our linecuts of Figure 3.4 and 5.1. The transition between the two regions shown here is similar to what we observe in that the coherence peaks rise as the “superconducting” region is entered. However, the size of their “superconducting” region, which appears here to be at least 80 Å, is rather larger than the 28 Å diameter regions we observe (see Section 5.3). Reference: Figures 1, 2, & 3 from Cren 2000.

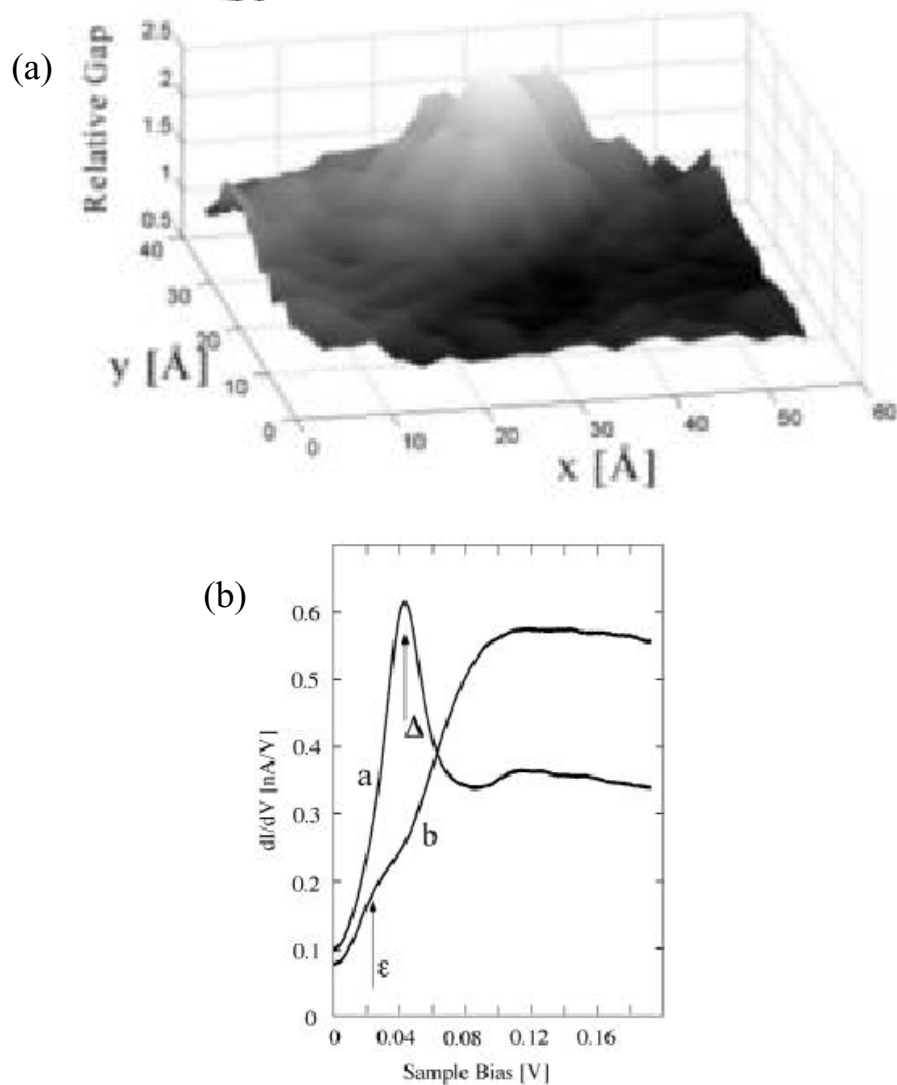


Figure 4.4: Gapmap and spectra from the Kapitulnik group illustrating the spatial variations in Δ and the two observed extremal spectral types. This data was taken at 8 K on single crystal $\text{Bi}_2\text{Sr}_2\text{CaCu}_2\text{O}_{8+\delta}$. (a) Gapmap on a 60 Å square region showing spatial variation in Δ . The size of the central high Δ region shown here is about 30 Å, which is comparable to the our reported length scale of 28 Å (see Section 5.3.1). (b) Two observed extremal spectral types. The two spectral types illustrated in ‘a’ and ‘b’ are qualitatively comparable to our 2HS and 2LB types respectively, which are shown in Figure 3.8 of this thesis. Reference: Figures 2 & 3 from Howald 2001.

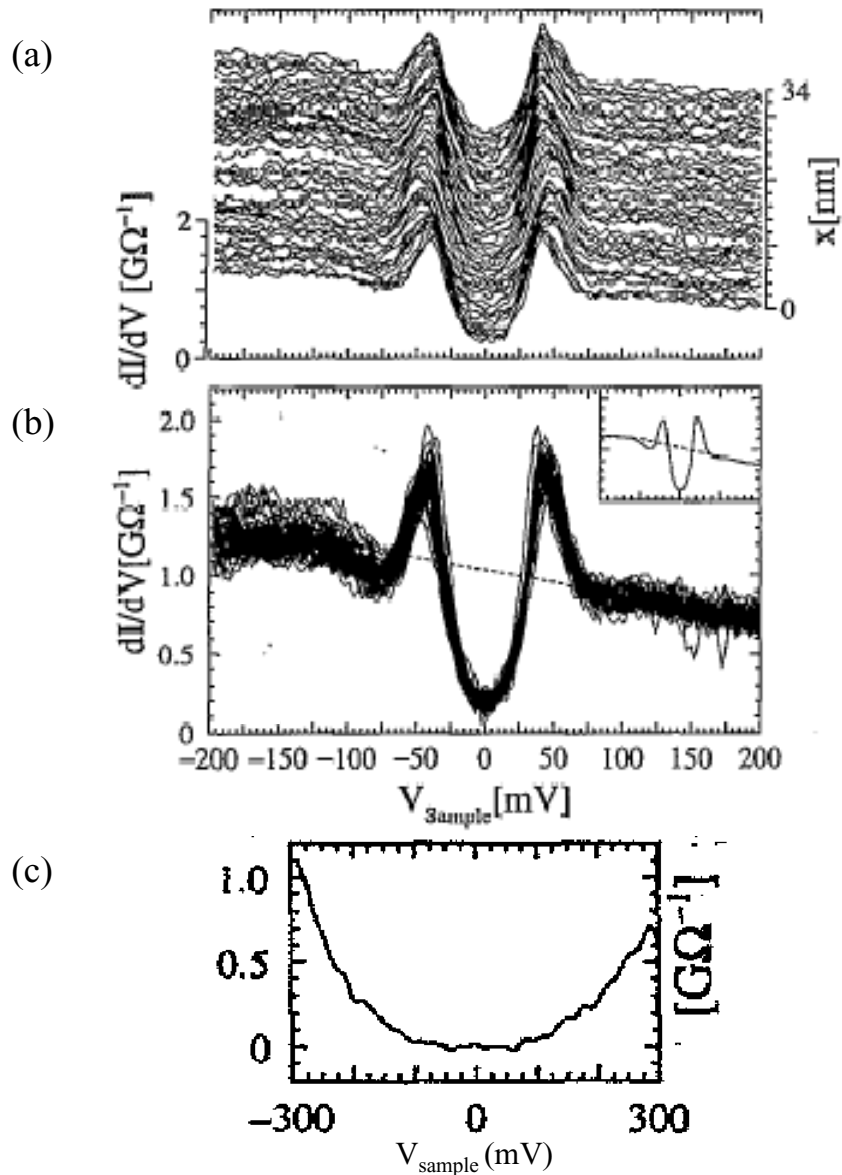


Figure 4.5: Data from the Fischer group showing spatially homogeneous spectroscopy. This data was taken at ~ 4.2 K on single crystal $\text{Bi}_2\text{Sr}_2\text{CaCu}_2\text{O}_{8+\delta}$. The spectra shown in (a) and (b) were measured along a 340 \AA line, and they show little spatial variation. In (a) the spectra are vertically offset, whereas in (b) the same spectra are plotted on top of each other. The inset in (b) gives the average spectrum. In addition to the type of spectrum shown in (a&b), a second spatially invariant spectral type is observed on some crystals. This “semiconducting” spectral type is shown in (c). These spatially homogeneous results from the Fischer group were obtained on crystals which were annealed just prior to study. Our observations are on crystals which were annealed some weeks or months prior to study. The Fischer group finds some (unpublished) spatial variation in spectroscopy on crystals not recently annealed [Fischer 2001]. Reference: Figures 2 & 6 from Renner 1995.

Chapter 5

Granularity and Segregation in the Electronic Structure of Underdoped $\text{Bi}_2\text{Sr}_2\text{CaCu}_2\text{O}_{8+d}$

In Chapter 3 I presented evidence that the local density of states⁵⁴ in $\text{Bi}_2\text{Sr}_2\text{CaCu}_2\text{O}_{8+\delta}$ is spatially inhomogeneous, and I described the phenomenology of the spatial variation. In addition I presented some preliminary evidence to support the assertion that the spatial variation in the LDOS is not continuous, but rather is suggestive of *granularity*⁵⁵ in this material. I further suggested that there is some evidence for *segregation*⁵⁵ into two distinct types of grains.

In this chapter I will provide additional evidence to support the assertions of granularity and segregation in $\text{Bi}_2\text{Sr}_2\text{CaCu}_2\text{O}_{8+\delta}$. This evidence comes from very high spatial resolution ($\leq 1 \text{ \AA}$ separation between spectra) linecuts and spectral-surveys taken on *underdoped* ($T_c \approx 79 \text{ K}$) pure single crystal BSCCO. Such detail allows one to see very clearly the spatial evolution of the LDOS spectrum as a whole, and in particular one may carefully examine the evolution of Δ , $A(\Delta)$, and Σ . Such detailed studies provide strong evidence for both granularity and segregation in this material.

Rationale for Studying Underdoped Samples

As mentioned above, all the high-resolution data presented in this chapter was taken on *underdoped* BSCCO. We chose underdoped samples for our detailed studies because we suspected that in this regime we might observe more significant variation in the LDOS for a number of reasons.

First, if one imagines that the inhomogeneity arises from variations in the local oxygen doping level [See Section 6.1.3], then at lower doping-levels the variations become fractionally more significant. From a simplistic viewpoint, one can imagine that the difference between 0 and 1 local dopant oxygen atoms might be more significant than the distinction between 1 and 2 local dopant oxygen atoms, which would be more significant than the difference between 2 and 3 local dopant oxygen atoms and so on. Lower global

⁵⁴ Although all the data presented in this thesis comprises measurements of the local *differential conductance*, nonetheless in this chapter and subsequently in this thesis, *local density of states (LDOS)* will be used synonymously with *differential conductance (dI/dV)*. The clarity and comprehensibility of presenting a discussion in terms of the physically meaningful quantity LDOS is the impetus for this nomenclature. The strictly proportional relationship between differential conductance and LDOS is the justification. Details of the relationship between differential conductance and LDOS are given in Chapter 1, and in particular the reader's attention is directed to Section 1.10 which discusses how to interpret inter-comparisons between distinct spectra.

⁵⁵ The terms *granularity* and *segregation* are used here and throughout this thesis to mean something very specific. This meaning is defined in Sections 5.1, 5.2 & P.4 and in the thesis glossary.

oxygen doping leads to lower local oxygen doping, and by this argument then, also to more significant variations in the local oxygen density and hence the LDOS. Thus were we motivated to study underdoped samples.

A second motivation for studying underdoped samples is the appearance of the unexplained pseudogap above T_c with underdoping. While the origin and significance of the pseudogap is unknown, recently there have been suggestions that it may be due to a competing order parameter (e.g. that proposed in Chakravarty 2001) which produces a quantum critical point near optimal doping [Tallon 2001]. If this suggestion is correct, at doping-levels less than the critical doping, we might hope to find some signature of these two order parameters in the LDOS.

Finally, theories of frustrated phase separation (often known as ‘stripe’ theories) predict that for low hole doping-levels there is a tendency of the material to locally order into hole-rich superconducting regions and hole-poor antiferromagnetic regions [Emery 1999]. One would imagine that these regions should be spectroscopically distinct and therefore distinguishable by STS.

General Comments About the Data Presented in This Chapter

Much of the data presented in this chapter is contained in the Data Catalog in Chapter 2. The re-rendering of specific examples permits the reader to more clearly see the evidence for a given assertion⁵⁶. Although selected data has been re-rendered to highlight specific features of the data, in general the reader may refer to the figures in Chapter 2 for further support for any assertion. In some cases specific references will be made to figures from that chapter which are particularly illuminating.

All the data presented in this entire chapter was taken on 79 K T_c underdoped BSCCO. The reader should be aware that many of the maps and plots in this chapter should be viewed as a set as either they were derived from the same spectral-survey or linecut, or they cover the same area despite being different files. This was done to facilitate cross comparison between the different views of the data presented. The figures which should be viewed as a set are:

Relevant Chapter 2 Data Catalog figure number	Chapter 5 figures which should be viewed as a set
2.17	5.1, 5.2, 5.3 & 5.18
2.3, 2.6	5.6, 5.7 & 5.8
2.4, 2.10	5.9, 5.10 & 5.11
2.5	5.12, 5.13, 5.14 & 5.15
2.15	3.5 & 5.17

⁵⁶ The data file numbers, which are given in all figure captions, permit a comparison between the present figure and any previous presentation of the same data.

5.1 Linecuts Illustrating Granularity and Segregation

The purpose of this chapter is to demonstrate and describe both the granularity and the segregation into two distinct grain types, which has been observed in the electronic structure of BSCCO. In this first section I will present raw data in the form of linecuts in order to illustrate these points. As these selected linecuts do not represent a very large area of the sample, they cannot establish the general validity of these observations. For this purpose, in Section 5.3 I will show maps of various spectral parameters to support the assertions made in this section.

5.1.1 Existence of Grains

Given that the LDOS of BSCCO is spatially varying as was shown in Chapter 3, one might then inquire as to the nature of the variation. One possibility is that the variation is continuous. That is to say, the overall shape of the spectral curves, including the values of Δ , $A(\Delta)$, and Σ , would change slowly but constantly throughout the crystal.

Figure 5.1 illustrates that this is clearly not the case. In this linecut there are eight regions each with distinct properties which distinguish it from its neighbors. The arrows, which point to the gap-edge peaks, indicate roughly the middle of each region.

It is useful to ask what it is about these regions that makes them appear so distinct. Most immediately apparent is that the value of Δ is different for the different regions, but relatively constant within a given region. A second distinctive quality preserved within a given region is, qualitatively speaking, the shape of the gap-edge peaks. In some regions there are relatively high sharp peaks and in other regions there are much lower broader peaks, and this shape is consistent within the given region.

Several of the linecuts shown Chapter 3 also clearly illustrate distinct regions. In particular, Figure 3.4 contains five very clearly differentiated regions as indicated by five arrows which point to the different Δ values present. In Figure 3.2 there are five distinct regions as well as a portion which runs along the edge of several regions and is thus somewhat less uniform in its properties.

The distinct regions which are apparent in these linecuts imply that the LDOS of $\text{Bi}_2\text{Sr}_2\text{CaCu}_2\text{O}_{8+\delta}$ is *granular*. In other words, there are regions in the material within which the local density of states exhibits a common set of characteristics, which are distinct from the characteristics exhibited by neighboring regions. An individual distinct region will henceforward be referred to as a *grain*, and *granular* will be taken to mean that the material consists of a multitude of these grains.

5.1.2 Existence of Segregation

Given that the electronic structure of BSCCO is granular, one might then inquire as to the nature of the grains. This sections concerns itself with this question.

An Analogy for Understanding Segregation

One possibility is that the observed grains, although distinct, share enough characteristics to be classified as all the same type. To use an analogy, this would be the case for distinct grains of sand on the beach.

A second possibility is that there are numerous types of grains which would be identified by their shape, spatial interrelationship with other grains, and by the characteristics of the spectra they contain. Continuing with the analogy, this would be the case if there were either little pebbles and seeds mixed into the beach sand or if the sand were in slurry mixed with water.

In both cases the grains present (sand, pebbles, seeds, water) can be distinguished by their constitutive material. However, in the former case, all the grains (sand, pebbles, seeds) have roughly the same shape and spatial interrelationship. In contrast, in the latter case the two materials present, sand and water, have different shapes and spatial interrelationships. We find for the electronic structure of BSCCO a situation analogous to the latter case of a slurry of sand and water.

Specifically, we find that in the electronic structure of BSCCO it is generally possible to classify a given grain or region into one of two types. As in the analogy above, the classification is based primarily on the constitutive LDOS structure of the region, and in particular it is based on a number of characteristics of the spectra found within the given grain. For the spatial interrelationship between grains, we find that it is analogous to that of water and sand mixed into a slurry. Namely, one of the BSCCO grain types is compact and circumscribed, and this grain type is embedded into a matrix of the other type.

For convenience the two types of grains observed in the electronic structure of BSCCO will be referred to as ***a**-grains* and ***b**-grains*. The α -grains are those which are analogous to the sand, and the β -grains are analogous to the water. Given the spatial structure of the respective grains, they will also be referred to as ***a**-domains* and ***b**-regions*. The remainder of this section is concerned with describing the LDOS characteristics of the α -domains and β -regions.

Distinguishing Grains by the Value of D

In Chapter 3 it was established that regions with lower values of Δ have different characteristics than those with higher Δ values. So it seems that one variable which could distinguish the two types of grains one from the other is the value of Δ . Since Δ represents an energy scale, this is a very intuitive variable to use. Later in this chapter I will justify this statement, but for the moment I shall just state that *the low- D regions are identified with the **a**-domains and the high- D regions with the **b**-regions*. Roughly speaking, *low- D* is taken to mean less than about 42 meV and *high- Δ* to mean greater than about 42 meV.

The number given for Δ , 42 meV, should be taken as a guideline rather than as a rigid definition of a threshold in Δ which distinguishes the grains. In practice, the value of Δ alone cannot identify a grain, but rather the value of Δ in concert with the other characteristics described later in this section should be used. This is particularly true for grains with $34 \text{ meV} \leq \Delta \leq 50 \text{ meV}$. Grains with Δ outside this range can be more reliably identified using only the value of Δ .

Distinguishing Grains by the Value and Spatial Variability of $A(\Delta)$

The α -domains and β -regions can be distinguished using the magnitude and spatial variation of the gap-edge peak height for spectra within the regions. *Specifically, for a high- D β -region, the height of the gap-edge peak, $A(\Delta)$, is relatively constant and low, whereas for a low- D α -domain, $A(\Delta)$ varies dramatically starting low on the perimeter of the domain and rising towards the center.*

Figure 5.2/5.3 shows a short section taken from near the bottom/top of the linecut of Figure 5.1. These figures illustrate the observation stated above regarding the characteristic behavior of $A(\Delta)$ for the two regions.

At the front of both these linecuts is a β -region which has a larger value of Δ , low broad gap-edge peaks, and little variation in the height of those peaks. The value of Δ for the β -region of Figure 5.2/5.3 is about 60meV/55meV, and the constant $A(\Delta)$ value is about 0.8 nS in both cases.

The red curve roughly marks the boundary between the β -region and the α -domain which is seen at the rear of both linecuts. Above the red curve the α -domain exhibits its characteristic low value of Δ and much sharper gap-edge peaks which rise dramatically in height as the domain is entered. The value of Δ for the α -domain of Figure 5.2/5.3 is about 46meV/32 meV. $A(\Delta)$ rises to a maximum height of about 1.4nS/1.9nS, a change of about 75%/137% above the relatively constant β -region height given above.

Several other linecuts also clearly illustrate this characteristic difference in $A(\Delta)$ spatial variability between α - and β - regions. Although it can be a bit difficult to see in a Figure such as 5.1 in which the spectra are not horizontally offset, it is nonetheless true that the five α -domains (2,3,5,7 and 8) and the three β -regions (1,4, and 6) demonstrate this characteristic $A(\Delta)$ behavior. Figure 3.5, which does have a horizontal offset, has a β -region at the front, an α -domain in the middle, and a second β -region at the back which clearly demonstrate this characteristic $A(\Delta)$ behavior as well.

Distinguishing Grains by the Spatial Variability of D

Figure 5.4 illustrates another characteristic that distinguishes the α - from the β - grains. *In the α -domains the value of D is constant to within a meV or two. However, in the β regions D can vary by up to ~ 10 meV within the grain.* Generally, Δ starts at its lowest

value on the edge of a β -region and slowly increases, reaching a maximum near the center of the grain and then decreases again to the other edge.

The bottom panel in Figure 5.4, which shows a different view of the linecut in the top panel, allows one to see most clearly the distinction between the behavior of the spatial variability of Δ in the two grains. The top of the linecut is an α -grain, and it is clearly seen that the yellow regions, which are the gap-edge peaks, demonstrate that Δ is constant and low. The middle region is a β -grain with a larger value of Δ . In this region the gap-edge peaks are lower and are the pink regions which gently bow outward across the grain. The lower region is again an α -grain with a low value of Δ in which the yellow peak regions are seen to be constant in energy.

Figure 5.1 also illustrates this characteristic difference in Δ spatial variability between α - and β - regions although it can be difficult to see in this type of figure. Region #1 is a β -region in which the value of Δ is seen to change gradually across the region. This is in contrast to the #2 α -domain in which Δ is constant. β -region #4 and α -domain #5 also illustrate this point.

Distinguishing Grains by Spectral Shape

All three of the figures thus far presented in this section serve to illustrate another distinction between the α - and the β - grains. *Qualitatively speaking, the gap-edge peaks in the α -grains are generally high and sharp, whereas in the β -grains the gap-edge peaks are low and broad.*

In Section 3.3 I described the variety of spectra which can be found in a study of BSCCO, and I stated that they could be classified as one of six types: 2LB, 4LB, 2HS, 4HS, 4LB-HS, and NP. Recall that LB means low broad gap-edge peaks, HS means high sharp gap-edge peaks, NP means no peaks and 2 or 4 refers to the total number of peaks in the spectrum.

Based on the discussion in this section, it now seems clear that the 2LB spectra are to be found in a β -grain whereas the 2HS spectra are to be found in an α -grain. Where then do the 4LB, 4HS, and 4LB-HS spectra fit in? This question will be addressed in the next section.

5.1.3 Boundaries Between the Grains

Thus far I have not discussed boundaries between grains. Clearly if there are grains, unless there is a discontinuous jump in properties, there must be some region in which there is a transition from one grain to the next. *These regions are the boundary regions which have distinct characteristics of their own, the primary one being the presence of four peaks in spectra which are located in that region.* Thus, the 4LB, 4HS, and 4LB-HS spectra are generally to be found on the boundaries between grains.

In general there can be three types of boundaries- one that separates two α -regions (α - α boundary), one that separates two β -regions (β - β boundary) and one that separates an α - from a β region (α - β boundary). In general, boundary regions shall be referred to as γ -regions.

In practice β - β boundaries are not found. As was discussed in the previous section, within a β -region, Δ varies gradually as a function of position and $A(\Delta)$ is constant. Given these facts a β - β boundary is essentially not definable. The other two types of boundaries are however easily identifiable and will be discussed in the remainder of this section.

Figure 5.5 is a linecut the most of which was taken, not through the middle of grains, but rather through two boundary regions. The schematic illustrates a path that could produce a linecut such as this one. The trajectory of the linecut begins in a β -region shown by the black curves. It then moves into a α - β boundary region shown by the green curves. In this region there are four clear peaks in the spectrum. Two of the peaks are at the energy $\pm\Delta_\beta$, the gap which corresponds to the bordering β region. The other two peaks are at $\pm\Delta_{\alpha 1}$, the gap corresponding to the bordering α region. When the linecut trajectory first encounters the edge of the $\alpha 1$ region, the spectra are 4LB class. Moving further toward the center of the $\alpha 1$ region, the peaks given by $A(\pm\Delta_{\alpha 1})$ increase, and the spectra transition to 4LB-HS class. Finally as the $\alpha 1$ region is exited the spectra transition back to 4LB class again.

Subsequently, the linecut trajectory enters an α - α boundary region shown by the red curves. Again there are four distinct peaks in the spectra now at energies $\pm\Delta_{\alpha 2}$ and $\pm\Delta_{\alpha 3}$. Except for the curves which are near the β region, all curves in this α - α boundary region are 4HS class. In general $A(\pm\Delta_\alpha)$ does not decrease across an α - α border as it does across an α - β border since $A(\Delta)$ decreases only upon encountering a β region.

5.1.4 Conventions for the Use of Color to Indicate Grain Type

In this section I have used linecuts to demonstrate that the LDOS of BSCCO consists of distinct grains (granularity) which can be categorized as one of two types (segregation). These distinct grain types have been termed α -domains and β -regions. In addition, there are regions which are on the border between distinct grains, and these have been termed γ -regions. In order to facilitate recognition of the regions in the figures in this thesis, roughly speaking a single color scheme is used throughout this document to distinguish the three regions.

The same color-palette has been used throughout this thesis for all Δ , $A(\Delta)$, and Σ maps which are presented in color. In this palette, roughly speaking, the α regions appear in red, orange or yellow and the β regions appear in dark green, blue, or black. Lighter green regions can fall into either the α or β camp and can also often be γ regions.

For linecuts or individual spectra which are deliberately colored, a similar color scheme has been followed. Red curves are in α regions, blue in β regions and green in γ regions

Although, the use of this color scheme should be considered more of a guide to the eye than a rigorous definition; nonetheless, the reader should know that care has been taken by the author to use these colors consistently throughout the thesis. Thus they can be used to assist the reader in appreciating the points being made.

5.2 Maps Demonstrating Granularity and Segregation

While the linecuts in the previous section permit a look at raw data which allows one to see the existence of both granularity and segregation, nonetheless they show the characteristics of only a small region of the sample along a one-dimensional line. In order to establish the existence of granularity and segregation, we should examine a two-dimensional region of the sample which is large compared to the size of the grains. If we see the same characteristic phenomena in these areas as we have observed in the linecuts, then it is possible to conclude that granularity and segregation are everywhere manifested in this material⁵⁷. Thus the purpose of this section is to present such two-dimensional data sets which support the assertions of granularity and segregation made in the previous sections.

Although the data we have typically consists of 128x128 spectra for each distinct area presented, it is not possible to present so many complete spectra. Thus the data presented in this section consists of various parameters extracted from those spectra by a computer program⁵⁸. The parameters are then presented in a series of Δ , $A(\Delta)$, Σ , and ∇ maps. These maps are described in more detail in Section 1.9. As in this entire chapter, all the data presented here was taken on 79 K T_c underdoped BSCCO.

5.2.1 Gapmap on Large Field of View

Figure 5.6 consists of a 589 Å square map of Δ together with a histogram of the Δ values which comprise this map. This figure is consistent with those presented in Figure 3.6 in terms of the observations that can be made about it. In particular, the Δ -map demonstrates granularity in that Δ is not a continuously varying quantity. The histogram once more demonstrates a decided lack of symmetry as evidenced by the good gaussian fit for the falloff on the large Δ side and the relatively poor gaussian fit for the small Δ falloff.

Although this figure presents striking evidence for granularity, evidence for segregation is difficult to observe due to the relatively low spatial resolution (4.6 Å/ pixel) and large area. Evidence for segregation is more easily seen by viewing a smaller area with higher

⁵⁷ A more conservative statement would be that we can then show that these phenomena are manifested on the surface of the material since STM is a surface probe. However other bulk experimental methods provide compelling evidence to support the assertion that this is a bulk phenomena. See Section 1.11 for a discussion.

⁵⁸ See appendix 1 for a description of the algorithms used.

(1.1 Å/pixel) spatial resolution. Consequently, several maps of the white-boxed area of Figure 5.6 are presented in Figure 5.7.

5.2.2 High Spatial Resolution Maps on Small Field of View

D-map

Panel 5.7(a) shows a 128x128 pixel Δ -map of a 147 Å square region. In this smaller field of view the spatial interrelationship between the regions is now more clear. The compact ‘islands’ (red, orange, and yellow) are the α -domains which have low- Δ and a well defined shape and border. The percolative ‘seas’ (dark green, blue, and black) between the α islands are the high- Δ β -regions.

These observations are reinforced by Figure 5.8(a) which shows the Δ -trace along the white line in Figure 5.7(a). This trace shows three clearly distinct grains, two α -domains and one β -region.

Now consider this figure in the light of the observations about the spatial variability of Δ in the α vs. the β regions. The trace begins in an α region where Δ is observed to be low (40 meV) and constant to within ± 2 meV (error in the measurement). Then the trace moves into a β region in which Δ is larger and is seen to vary gradually from ~ 50 meV on the edge of the region to ~ 60 meV in the center and back to ~ 50 meV again on the other edge. The trace ends in a second α region in which Δ is again observed to be 40 meV and constant.

$|\tilde{\nabla} \Delta|$ -map

Figure 5.7(b) provides evidence which validates the ‘islands’ and ‘seas’ observations of the α and β regions respectively. This figure is a $\tilde{\nabla}$ map of the Δ map from Figure 5.7(a). The white lines in the $\tilde{\nabla}$ map show where there is a large jump (> 8 meV) in Δ from one pixel ($=1.1$ Å) to the next. Thus the white lines generally indicate the borders between α and β regions. One can see that these borders form closed contiguous loops around the compact α islands.

A(Δ)-map

In addition to characteristics exhibited in the value and spatial evolution of Δ , the α and β regions are also distinguished by behavior manifested by $A(\Delta)$. Thus, a map of $A(\Delta)$ for this same region is presented in Figure 5.7(c). In this map $A(\Delta)$ is seen to be low for those regions where Δ is high. This is validation of the previous observation that $A(\Delta)$ is generally low in a β -region. For a given α -domain where Δ is low, $A(\Delta)$ is seen to vary from a low value at the perimeter of the region to a maximum in the middle of the region. Again, this validates previous observations for the behavior of $A(\Delta)$ in an α -domain.

The evolution of $A(\Delta)$ along the white trace of Figure 5.7(c) is given in Figure 5.8(b). This trace clearly shows $A(\Delta)$ rising and then falling in the initial α -domain. Then $A(\Delta)$ is constant and low in the middle β -region. Finally in the third α -domain, $A(\Delta)$ again exhibits a dramatic rise and fall, achieving at the center of this grain a value 80% higher than that measured at the edge of the grain.

$|\tilde{\nabla} A(D)|$ -map

Yet another view of the spatial variability of $A(\Delta)$ is presented in Figure 5.7(d). This panel is a $\tilde{\nabla}$ -map of the $A(\Delta)$ map presented in 5.7(c). In 5.7(d) it is seen that in those regions where Δ is high and $A(\Delta)$ is low, there is also little spatial variability in $A(\Delta)$. These are the stated characteristics of the β -region. Conversely, in those regions where Δ is low, $A(\Delta)$ is seen to have a large gradient. In other words, in the α -domains, $A(\Delta)$ is spatially varying as discussed previously.

S-map

An additional parameter which distinguishes the α and β regions is Σ . A $\Sigma(\Delta)$ -map for this same area is presented in Figure 5.7(e). This parameter was not discussed in Section 5.1 because it is not so apparent in a linecut, but here we see clear evidence that Σ is low in β -regions and higher and more variable in α -domains. In addition, since Σ is a parameter which is derived independently of the peak-finding computer algorithm, a correlation between the Σ -map and the other maps in this panel provides confirmation of the validity of the algorithm.

Analogous Set of Images

Figure 5.9, 5.10, and 5.11 are analogous figures to those presented in 5.6, 5.7 and 5.8 respectively. The figures 5.9-5.11 present a second distinct area which serves to further illustrate the points made in this section in regards to Figures 5.6-5.8. The reader is left to examine these figures in the context of the preceding discussion and without further comment from the author.

5.3 Quantifying the Properties of the α - and β - regions

Having qualitatively described the properties of the α - and β - regions using the linecuts and maps of the previous two sections, in this section I quantify some of those descriptions. Note that all the analysis in this section was performed on data from a 79 K T_C underdoped sample. Some of the values given may change with doping. Doping dependent studies will be necessary to make this determination.

5.3.1 Size of the α -Domains

In the previous section I showed that the α -domains appear as compact domains of constant Δ in the gapmaps. The question then arises as to the average size of those domains.

To determine this we performed a two-point correlation on several gapmaps. The results for one gapmap are shown in Figure 5.12 (black circles). We then fit a Lorentzian to these points (red curve) and determined its width. This width is related to the size of the domains. We now need to determine the relationship between the width of the Lorentzian fit of Figure 5.12 and the α -domain size.

To do this we created images containing multiple circular domains of a known diameter, and then performed the same analysis, as described above, on them as on the gapmaps. We were thus able to determine a relationship between the known diameters of the artificial circular domains and the width of the Lorentzian fit of these simulated maps. Using this relationship we were able to determine the diameter of the α -domains.

After performing this analysis on three 589 Å square gapmaps from an underdoped BSCCO sample, we obtain an average α -domain diameter of 28 Å.

This analysis was checked by measuring about 30 randomly selected α -domains by hand, which produced a size consistent with that determined as described above.

5.3.2 Separation of the α -Domains

The compact α -domains are separated by some average distance from one another, and the purpose of this section is give that distance and the means by which it was determined.

Using both the Δ -map and the $A(\Delta)$ -map for the 589 Å square field of view shown in Figures 3.6(a) (Δ -map) and 3.13(a) ($A(\Delta)$ -map), we found the centers of the α -domains. The determination of the centers was done by hand primarily by choosing the local maxima in the $A(\Delta)$ -map. In choosing the centers, some consideration was also given to the shape of the regions in both the Δ - and $A(\Delta)$ -maps and to the local value of Δ . The chosen centers are shown in Figure 5.13 (a&b) as small black dots on both maps.

Once the centers were determined, a Voronoi analysis was performed to determine the minimum size cells which each contain one center. Recall that a Voronoi cell is just a generalized Wigner-Seitz cell, and that it is determined by drawing perpendicular bisecting lines to the lines which separate the centers. The outlines of the Voronoi cells are shown as thin white lines on both the Δ - and $A(\Delta)$ - map of Figure 5.13.

The separation between the centers is then given by the size of the Voronoi cells. Given the area of the cells, and assuming that the cells are roughly circular, we find the

histogram shown in Figure 5.13(c). This histogram gives the diameter of the cells or correspondingly the separation between the centers.

From this analysis we obtain the mean separation between the centers of the \mathbf{a} -domains in underdoped BSCCO is 56.4 Å with a standard deviation of 8.7 Å.

5.3.3 Characteristics of the \mathbf{a} -Domains and \mathbf{b} -Regions

I now turn to the question of quantifying the behavior of the spectral parameters inside the α -domains and β -regions. All the analysis described here was done using the same field of view as that shown in Figure 5.13 and the α -domain centers determined as described in Section 5.3.2.

b-Regions

To determine the properties of the β -regions, we begin by putting 41 Å diameter circles on the center of each α -domain as shown in Figure 5.14. These circles are about 1.5 times the average diameter of the α -domains. We assume that everything outside these circles is in a β -region, and we can thereby determine the average properties of the β -region by computing properties for all pixels which are not covered by the black circles.

The histogram of Δ values for all pixels in the regions is shown in Figure 5.15 in blue, and *the mean value of \mathbf{D} for the \mathbf{b} -regions in this underdoped sample is found to be 53.1 meV with a standard deviation of 8.9 meV. We may also determine the average value of $A(\mathbf{D})$ which is 0.92 nS with a standard deviation of 0.15 nS (16%) for these regions.*

a-Domains

To determine the properties of Δ in the core of the α -domains, we find the average and standard deviation for Δ in a 3x3 pixel (13.8 Å x 13.8 Å) region around each α -domain center. The histogram of Δ values thus obtained is given by the red curve in Figure 5.15. *The mean value of \mathbf{D} for the \mathbf{a} -domains in this underdoped sample is found to be 38.6 meV with a standard deviation of 3.5 meV.*

We can also ask whether Δ is constant in the core of the domains by analyzing the standard deviation. *We find a standard deviation which is less than 5% (8%) of the mean value of \mathbf{D} for 71% (84%) of the \mathbf{a} -domains.* Since the measurement error is approximately 5%, this implies that Δ is constant in the core of the α -domains within measurable limits.

Finally, we may determine the properties of $A(\Delta)$ for the α -domains. Starting again with α -domain centers, we now find the maximum value of $A(\Delta)$ within the same 3x3 pixel region. We find this value to be 1.53 nS with a standard deviation of 0.21 nS. *This means that $A(\mathbf{D})$ in the center of the \mathbf{a} -domains has increased by 66% (\pm the 23%*

standard deviation) above the mean **b**-region background which is itself only varying by 16% of its mean value.

5.4 Conclusion

5.4.1 Summary of α , β , γ Region Characteristics

In the previous sections I have used linecuts and maps to demonstrate the characteristics of the α , β , and γ regions. Figure 5.16 shows representative spectra for each of the regions, and the following charts summarize the observations for the characteristics of each region.

Table 5.1: Summary of α - and β - region characteristics

Variable ↓	α -domain		β -region	
Δ value	low	≤ 50 meV	high	≥ 34 meV
Δ varies spatially	no	within 13 Å of center of domain Δ is constant to within 5%	yes	varies by ~10 meV between two α -domains
$A(\Delta)$ value	low at domain perimeter, high at domain center	at center of α -domain $A(\Delta)$ is 66% ($\sigma=23\%$) above β -region background	low everywhere	
$A(\Delta)$ varies spatially	yes		no	
Σ value	varies across domain		low	
Spectra class ⁵⁹	2HS		2LB	
Characteristic color ⁶⁰	red/orange/yellow		blue/black	

Table 5.2: Summary of γ - boundary region characteristics

Type of Boundary ⇒	α - α	α - β	β - β
Variable ↓			
Identifiable	Yes	Yes	No
$A(\Delta)$ value	High	Range	N/A
$A(\Delta)$ varies spatially	No	Yes	N/A
Spectra class ⁵⁹	4HS	4LB, 4LB-HS	N/A
Characteristic color for linecuts only ⁶⁰	green	green	N/A

⁵⁹ See Figure 3.8 for definition.

⁶⁰ See Section 5.1.4 for clarification.

5.4.2 A Few Concluding Remarks on the Observation of Inhomogeneity, Granularity and Segregation

This chapter and the previous one have presented arguments and evidence which indicate that observation of the electronic structure of $\text{Bi}_2\text{Sr}_2\text{CaCu}_2\text{O}_{8+\delta}$ implies that this material is not only *inhomogenous*, but is also *granular* and *segregated* into two distinct types of grains. The primary evidence for these phenomena is derived from the data presented in this chapter which I took on underdoped 79 K T_c $\text{Bi}_2\text{Sr}_2\text{CaCu}_2\text{O}_{8+\delta}$. However, these phenomena have been seen as well in other data taken over multiple years by multiple operators on multiple samples with multiple oxygen-doping levels⁶¹.

Figures 5.17 and 5.18 show two linecuts previously presented which are now colored to show the distinct regions suggested by the observations made in this thesis. The complicated set of observations which have been described in this and the previous chapter, and which have lead to the ability to identify the distinct α , β and γ regions as in Figures 5.17 and 5.18, constitute the core of this thesis and the contribution of this author to the field of high temperature superconductivity.

This and the preceding chapters have been strictly concerned with presentation of the data and commentary on observations which can be made about it. The lack of commentary on the possible implications of these observations has been deliberate.

Given the lack of consensus in the field of high T_c , I wished to separate the experimental facts presented in this and the previous chapters, from the much more speculative interpretation of the data. This interpretation will presented in the next chapter of this thesis.

⁶¹ See Table 2.1 for a summary of these data runs.

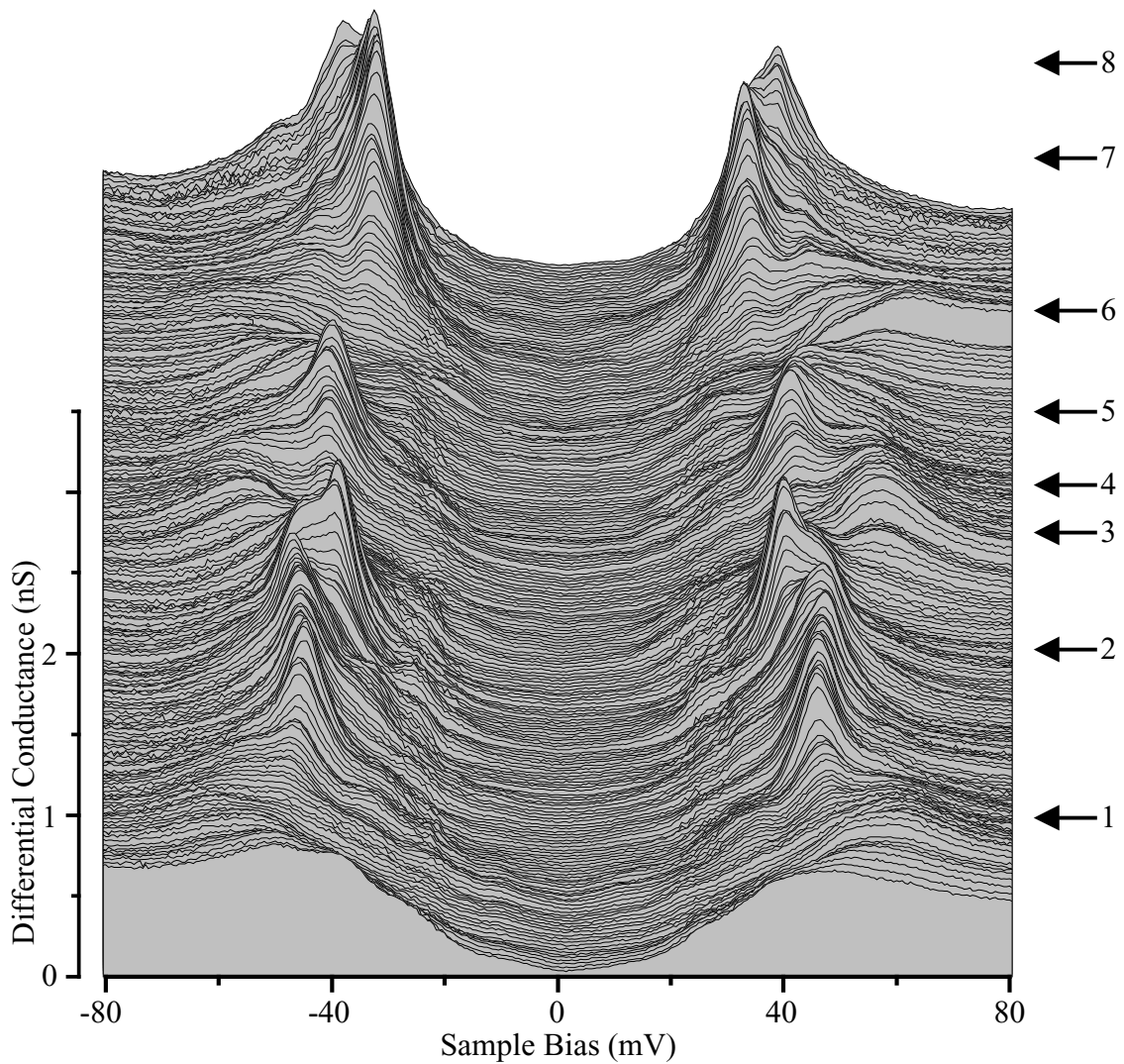


Figure 5.1: Linecut illustrating the observation of granularity in underdoped BSCCO.

The spectra were taken at 0.58 \AA intervals along a 133 \AA line. The spectra are vertically offset for clarity. The trajectory of the line is approximately along the x-axis. The line passes through eight distinct regions as indicated by the arrows. The regions are distinguished one from the other both by the value of Δ within the region and by the qualitative shape of the spectrum. This linecut, and all the data in this chapter, was taken on an underdoped BSCCO sample containing no deliberately doped impurities.

Run = 159, File = 01109c00-464 every 2nd curve, $V_{\text{set}} = -200 \text{ mV}$, $I_{\text{set}} = 200 \text{ pA}$

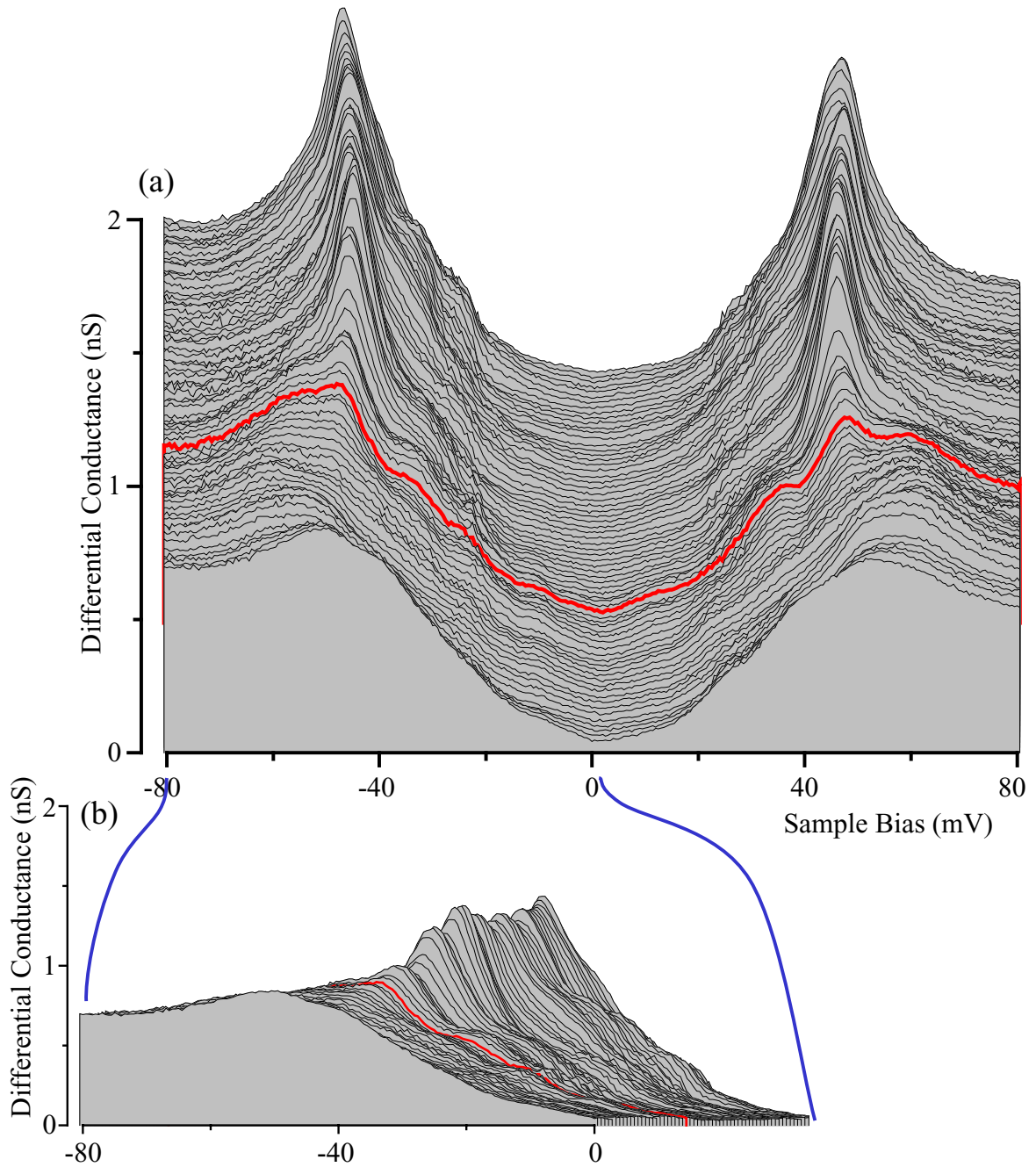


Figure 5.2: Linecut illustrating the behavior of Δ and $A(\Delta)$ in α - and β - grains. The front of the linecut from Figure 5.1 is re-rendered here in two different views. In (a) the spectra are vertically offset and in (b) horizontally offset for clarity. The spectra were taken at 0.58 \AA intervals along a 40 \AA line whose trajectory was approximately along the x-axis. The linecut shows a β -region at the front with its characteristic high- Δ and low constant $A(\Delta)$. The red curve marks the edge of this region, and an α -domain is shown at the rear with characteristic low- Δ and variable $A(\Delta)$.

Run = 159, File = 01109c320-458 every 2nd curve, $V_{\text{set}} = -200 \text{ mV}$, $I_{\text{set}} = 200 \text{ pA}$

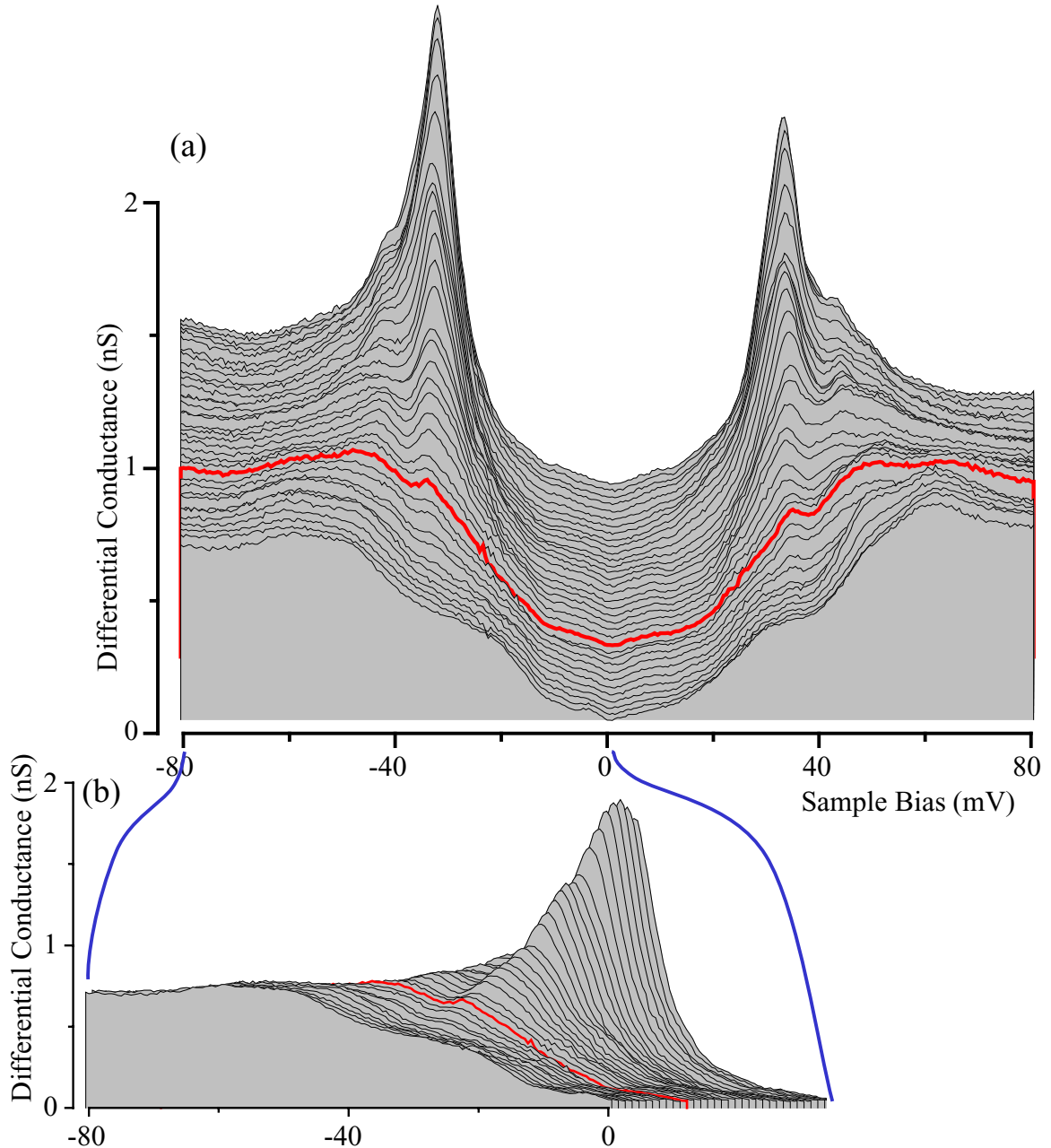


Figure 5.3: Second linecut illustrating the behavior of Δ and $A(\Delta)$ in α - and β -grains.

The rear of the linecut from Figure 5.1 is re-rendered here in two different views. In (a) the spectra are vertically offset and in (b) horizontally offset for clarity. The spectra were taken at 0.58 \AA intervals along a 19 \AA line whose trajectory was approximately along the x-axis. The linecut shows a β -region at the front with its characteristic high- Δ and low constant $A(\Delta)$. The red curve marks the edge of this region, and an α -domain is shown at the rear with its characteristic low- Δ and variable $A(\Delta)$.

Run = 159, File = 01109c42-108 every 2nd curve, $V_{\text{set}} = -200 \text{ mV}$, $I_{\text{set}} = 200 \text{ pA}$

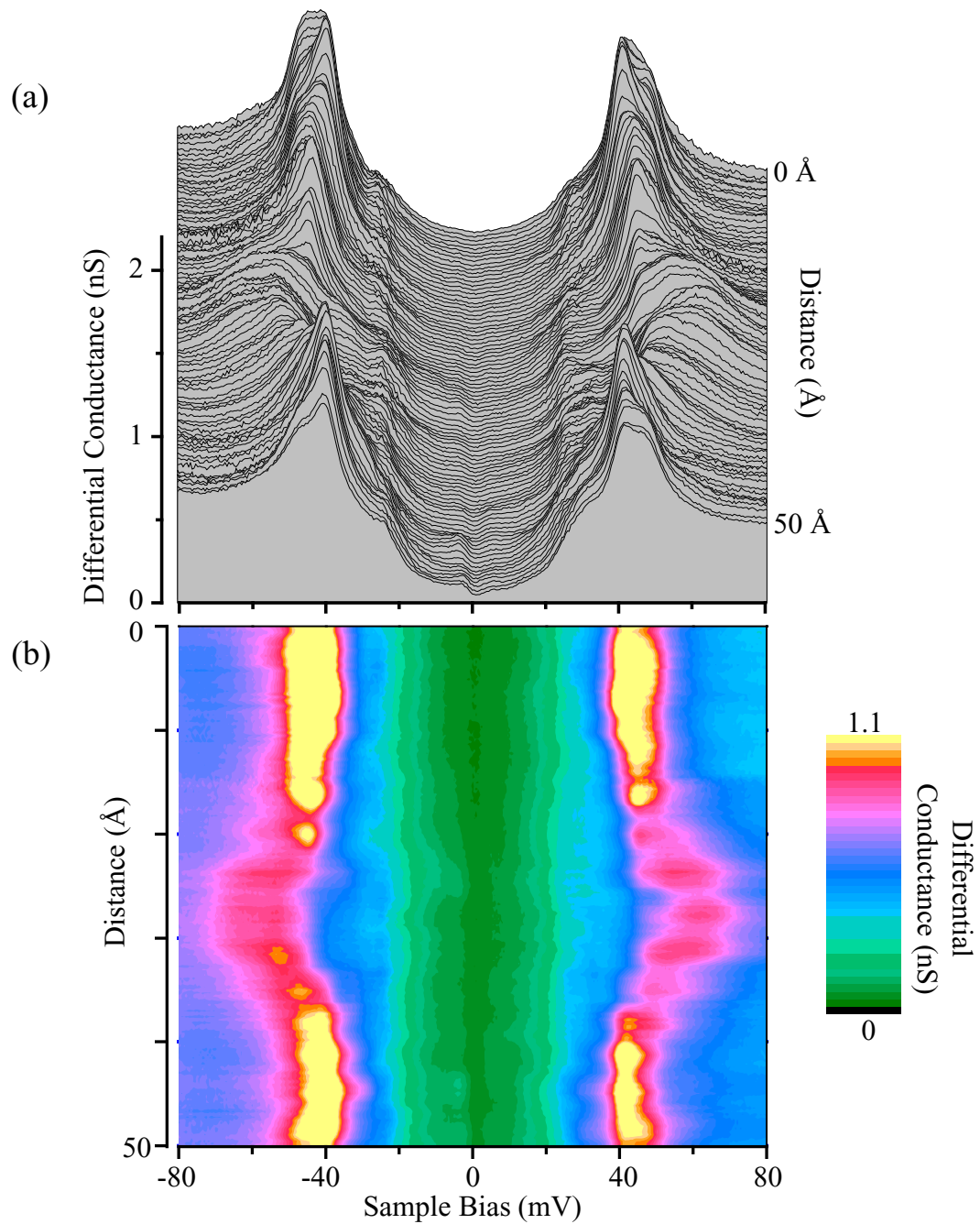


Figure 5.4: Linecut illustrating the spatial variability of Δ in α - and β - grains. The same linecut is shown in both (a) and (b) in two different representations. In (a) the spectra are vertically offset for clarity, so in this panel both differential conductance and distance are given by the vertical dimension. In (b) distance is given along the vertical direction and differential conductance is given by color as the legend indicates. The linecut has an α -domain at the front and back, and within these domains Δ is observed to be constant to within a couple meV. However, in the β -region at the center of the linecut, Δ is seen to vary by approximately 10 meV, being largest in the center of the region.
 Run = 159, File = 01108c200-376 every 2nd curve, $V_{\text{set}} = -200$ mV, $I_{\text{set}} = 200$ pA

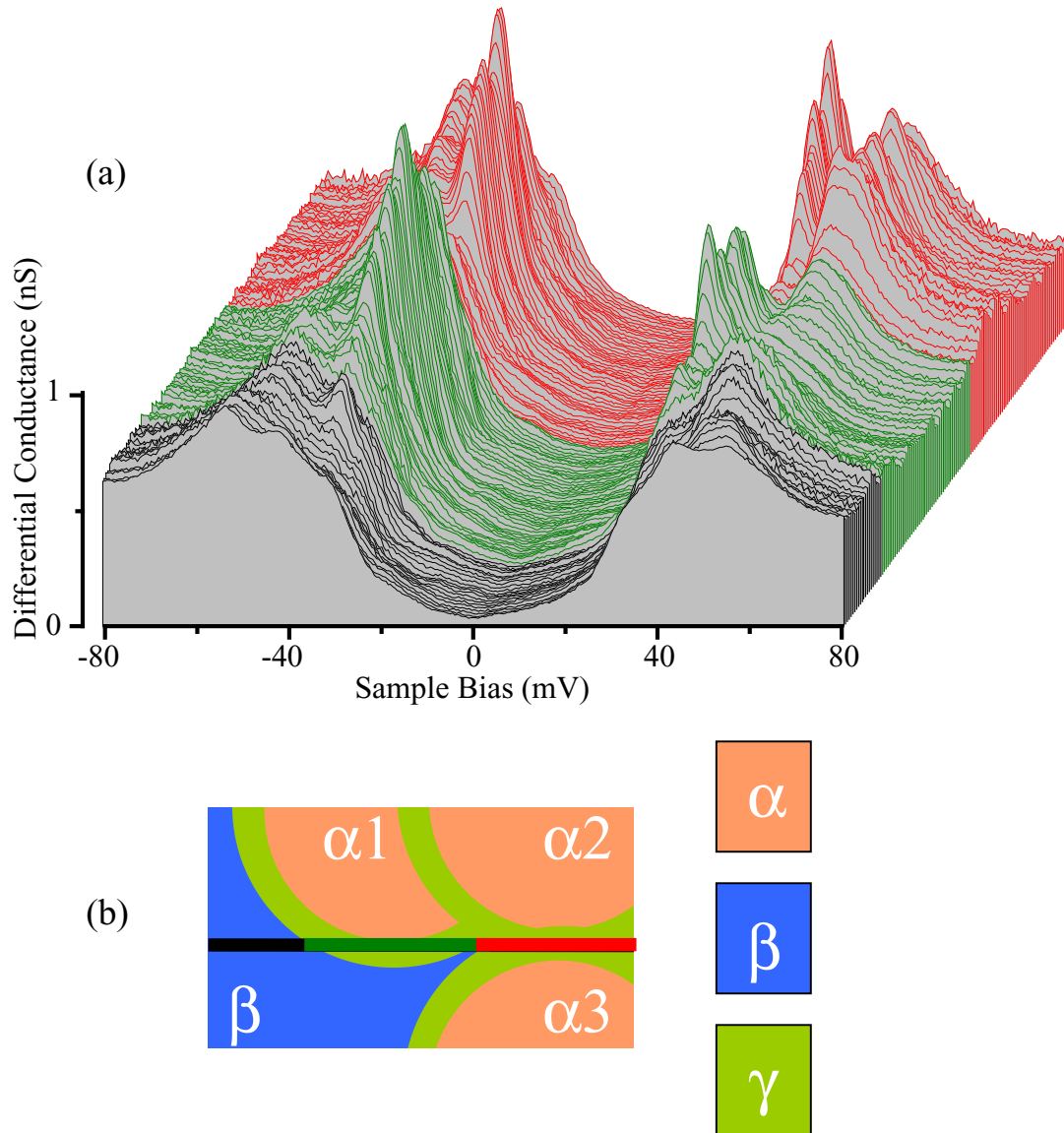


Figure 5.5: Linecut illustrating the border regions which exist between grains. The spectra in (a) were taken at 0.58 \AA intervals along a 69 \AA line. The spectra are both vertically and horizontally offset for clarity. The trajectory of the line is approximately along the x-axis, and runs along the edge of several distinct regions as indicated by the schematic in (b). As illustrated here, the spectra found on borders contain four peaks, where each set of two corresponds to a neighboring region. At the front of the linecut the black curves, which are of 2LB type, (see Figure 3.8 and text) are in a β -region. The linecut subsequently enters a region on the border between a β -region and an α -domain as seen in the green curves which are of 4LB-HS and 4LB type. Finally the linecut enters a region on the border between two α -domains as seen in the red curves, which are of 4HS type. Run = 159, File = 01129b150-390 every 2nd curve, $V_{\text{set}} = -200 \text{ mV}$, $I_{\text{set}} = 200 \text{ pA}$

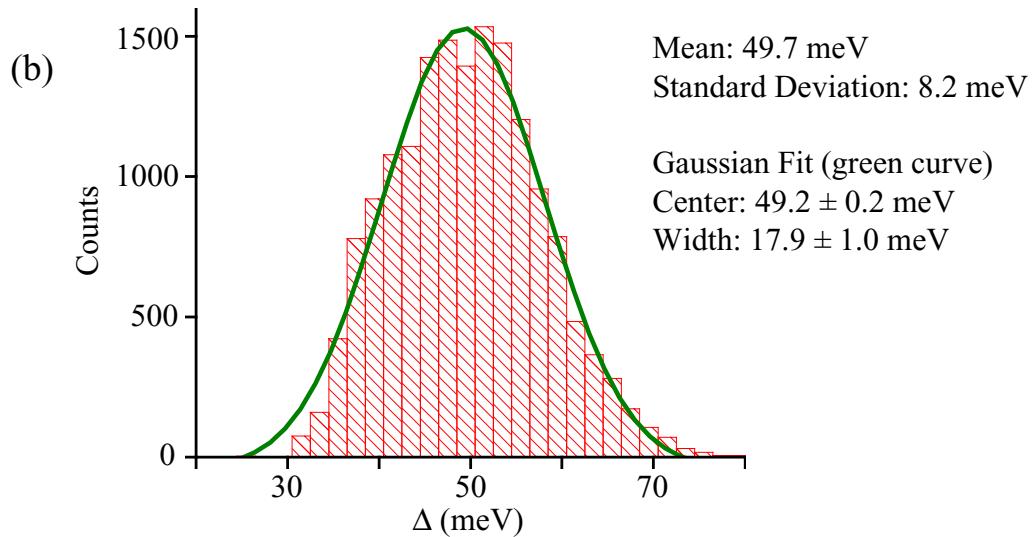
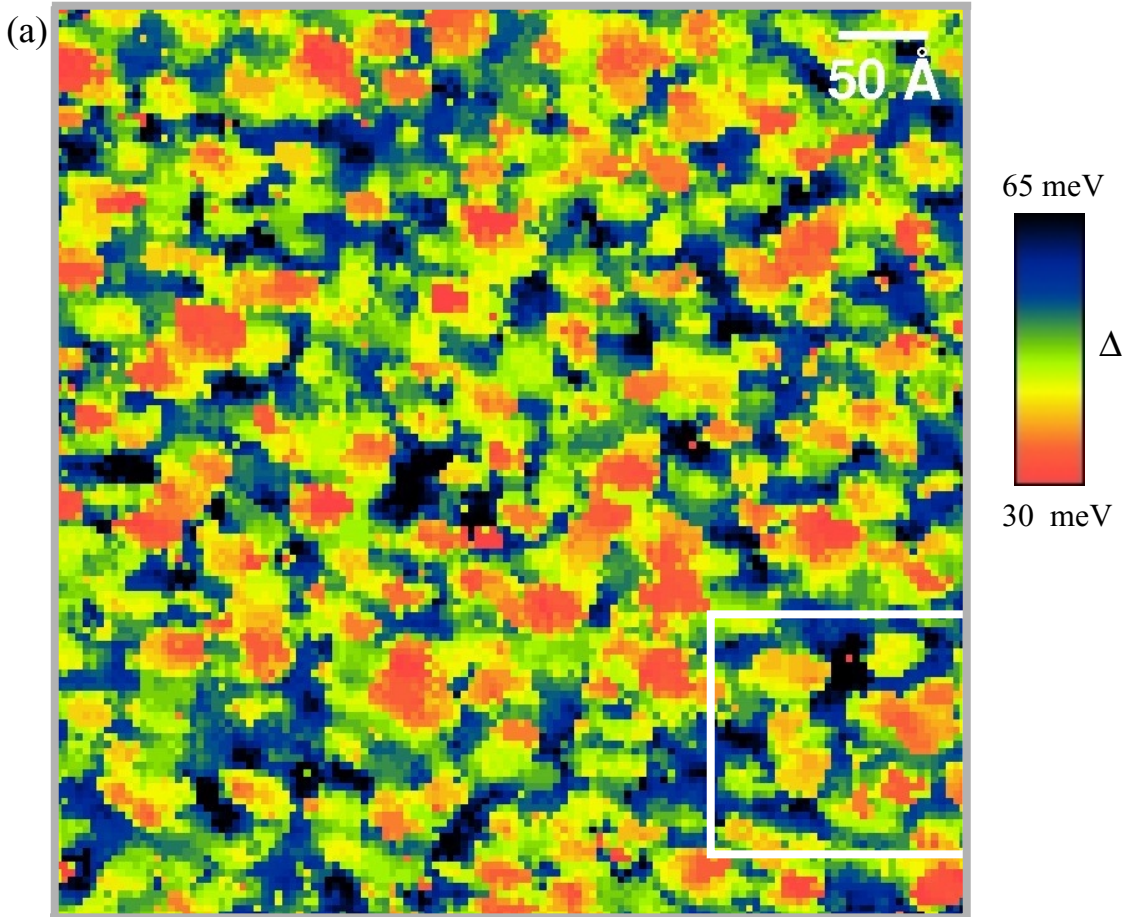


Figure 5.6: Large field of view gapmap and histogram on underdoped BSCCO. (a) shows a map of Δ for a 589 Å square region of an underdoped BSCCO sample. This map was extracted from a 128x128 pixel spectral-survey. The white box on the figure shows the location of the maps of Figure 5.7. (b) shows the histogram of Δ values for the entire large field of view.

Run = 159, File = 01019c02, $V_{\text{set}} = -100$ mV, $I_{\text{set}} = 100$ pA

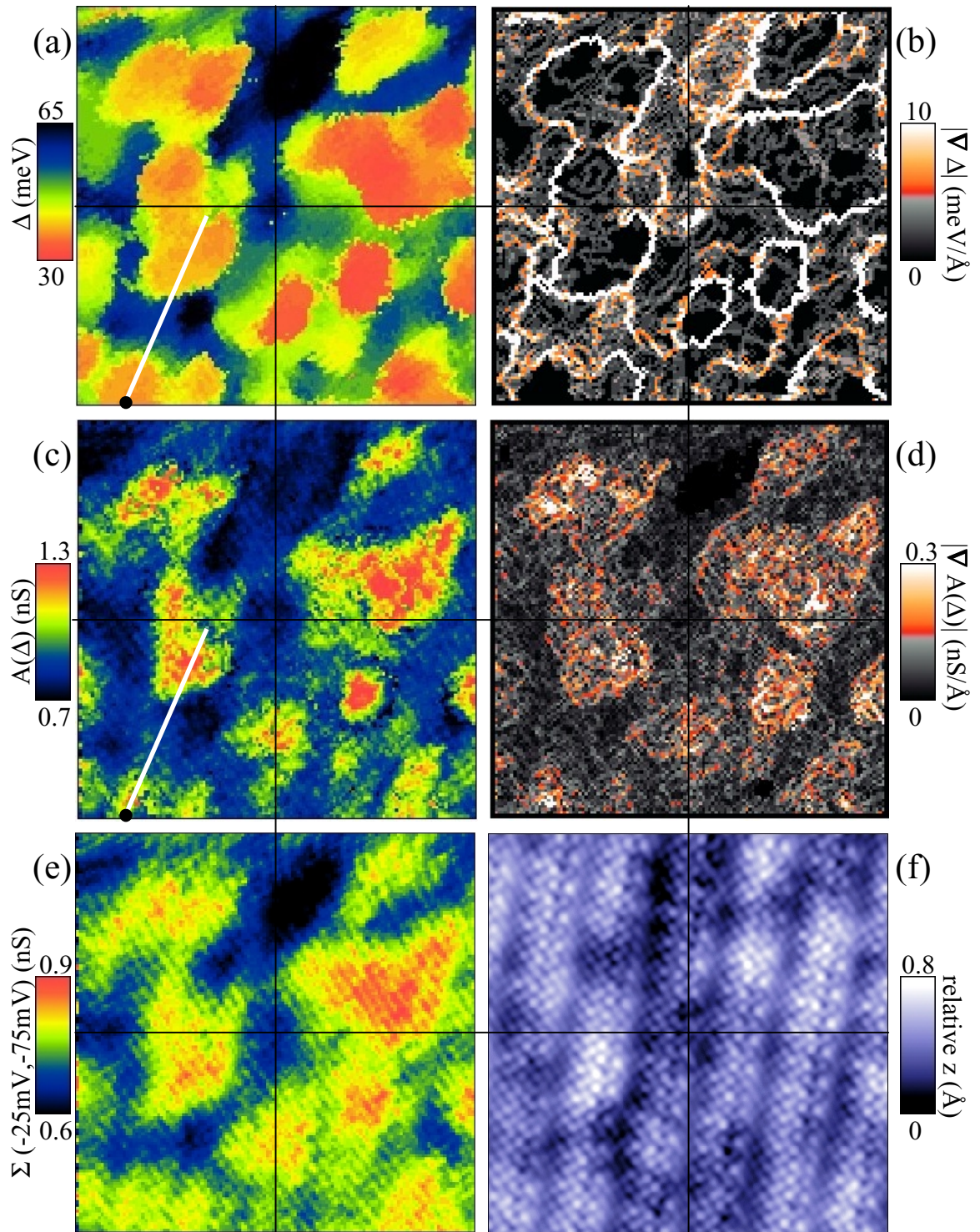


Figure 5.7: High resolution maps of multiple spectral parameters on a small field of view. This series of 147 \AA square maps was extracted from a single 128×128 pixel spectral-survey. The identity of each map is indicated next to its respective color bar. The spatial correlations between these images illustrate the properties of granularity and segregation in BSCCO as discussed in the text.

Run = 159, File = 01104b03 & 01105a00, $V_{\text{set}} = -200 \text{ mV}$; $I_{\text{set}} = 200 \text{ pA}$

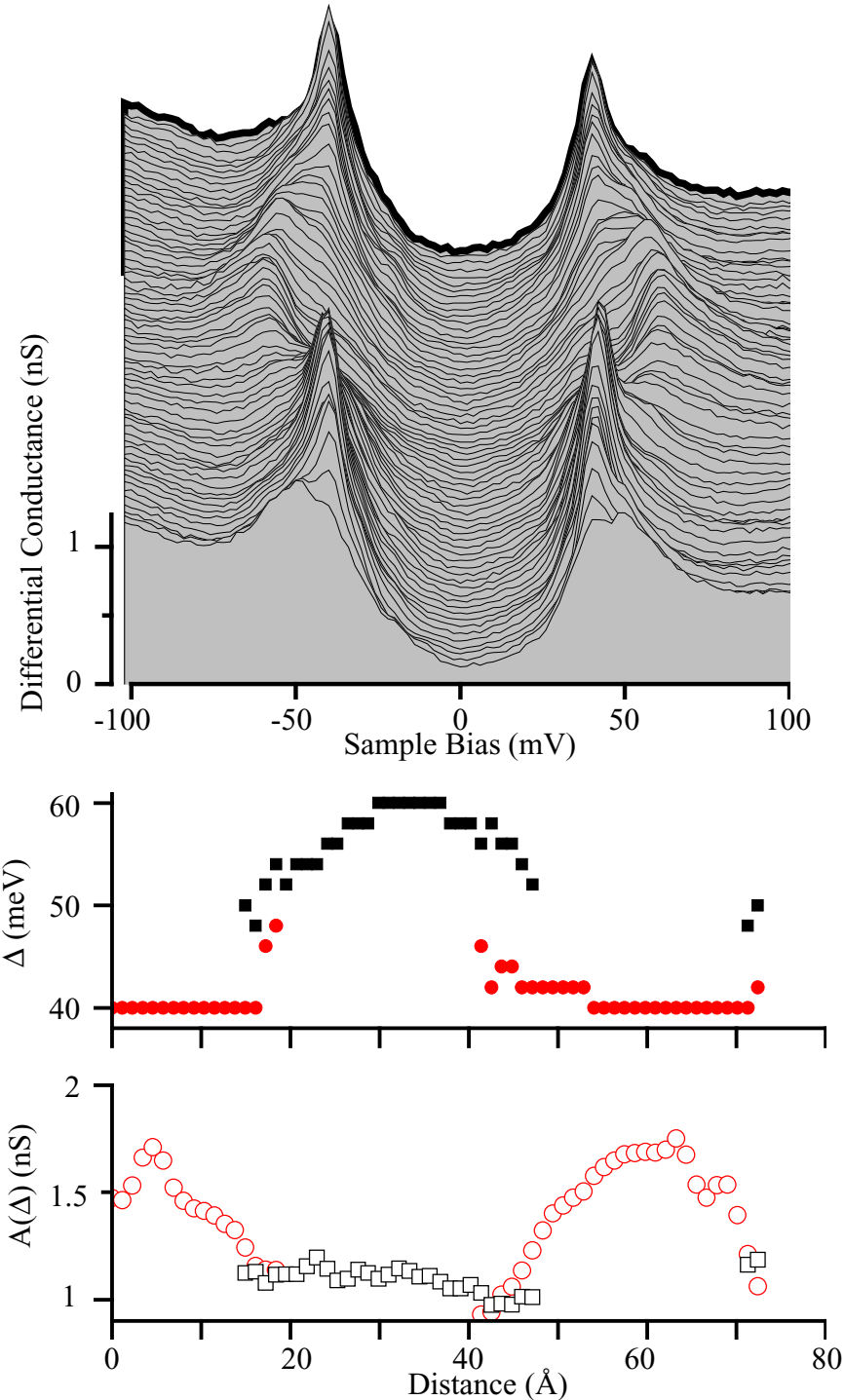


Figure 5.8: Set of Δ & $A(\Delta)$ traces and a linecut which correlate with the maps of the previous small field of view.

(a) shows the spectra and (b) & (c) the trace of Δ and $A(\Delta)$ respectively for the white line shown on Figure 5.7 a&b. The thick black curve at the rear of the linecut in (a) and 0 \AA in (b) & (c) correspond to the location of the black dot on Figure 5.7 a&b. The spectra in (a) are separated by 1.1 \AA and are offset vertically for clarity.

Run =159, File = 01104b03 pixels from 17,127 to 42,69, $V_{\text{set}} = -200$ mV, $I_{\text{set}} = 200$ pA

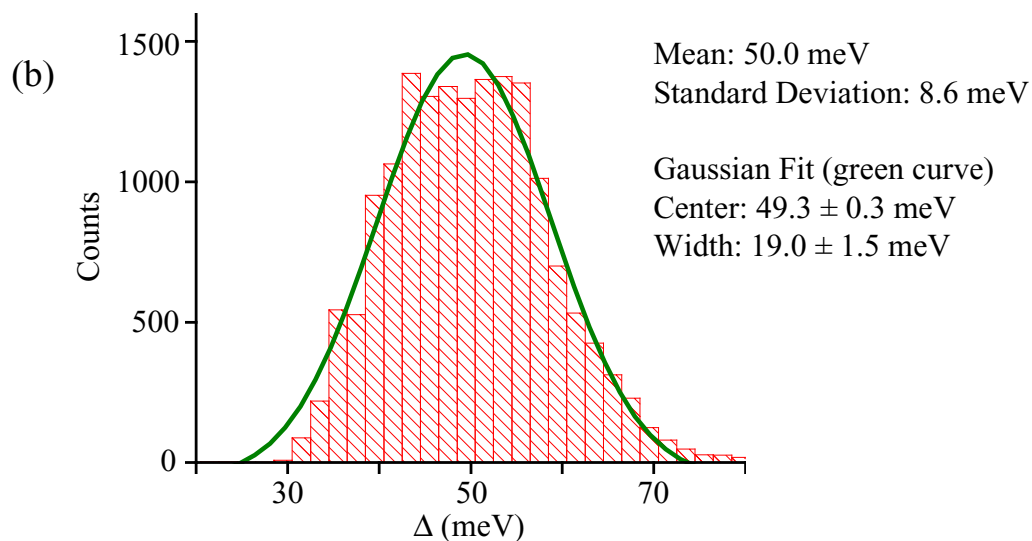
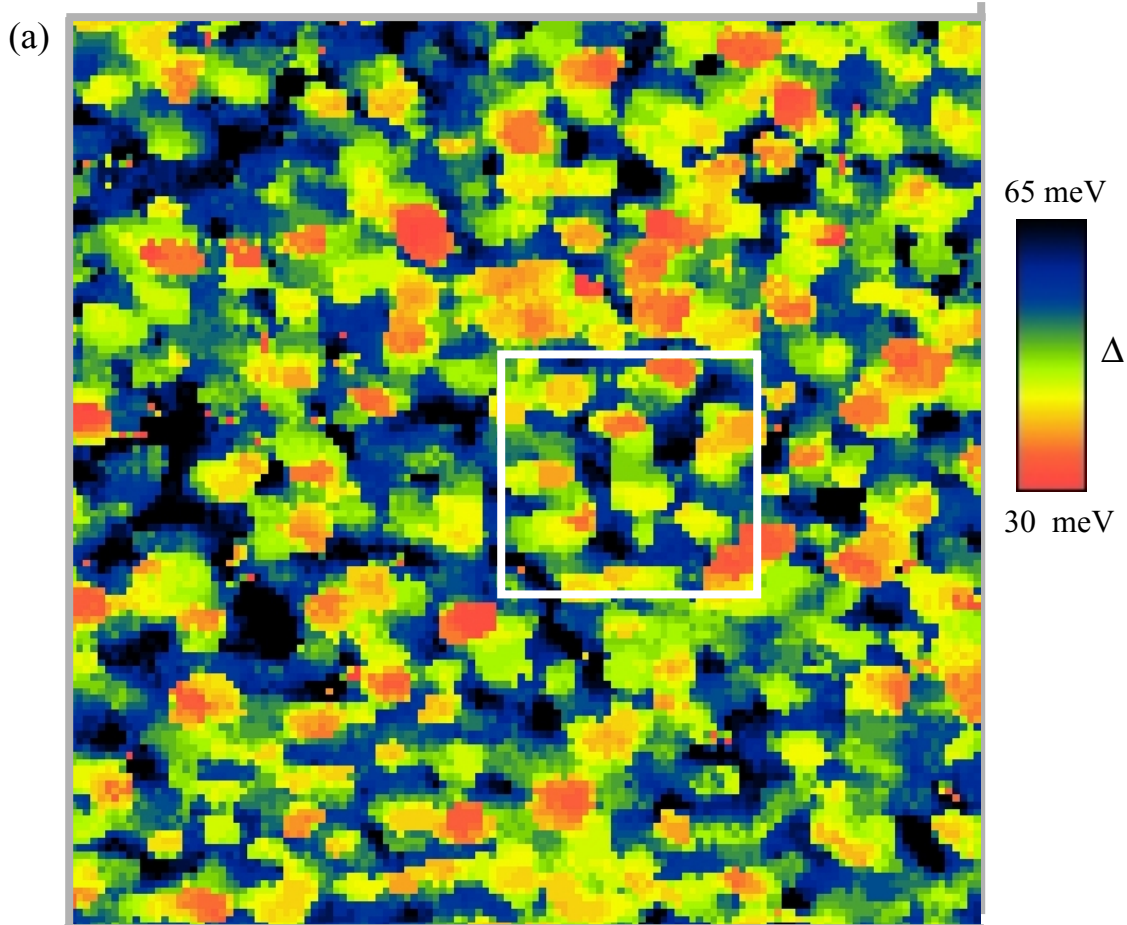


Figure 5.9: Second large field of view gapmap and histogram on underdoped BSCCO. (a) shows a map of Δ for a 589 \AA square region of an underdoped BSCCO sample. This map was extracted from a 128×128 pixel spectral-survey. The white box on the figure shows the location of the maps of Figure 5.10. (b) shows the histogram of Δ values for the entire large field of view.

Run = 159, File = 01020c02, $V_{\text{set}} = -100 \text{ mV}$, $I_{\text{set}} = 100 \text{ pA}$

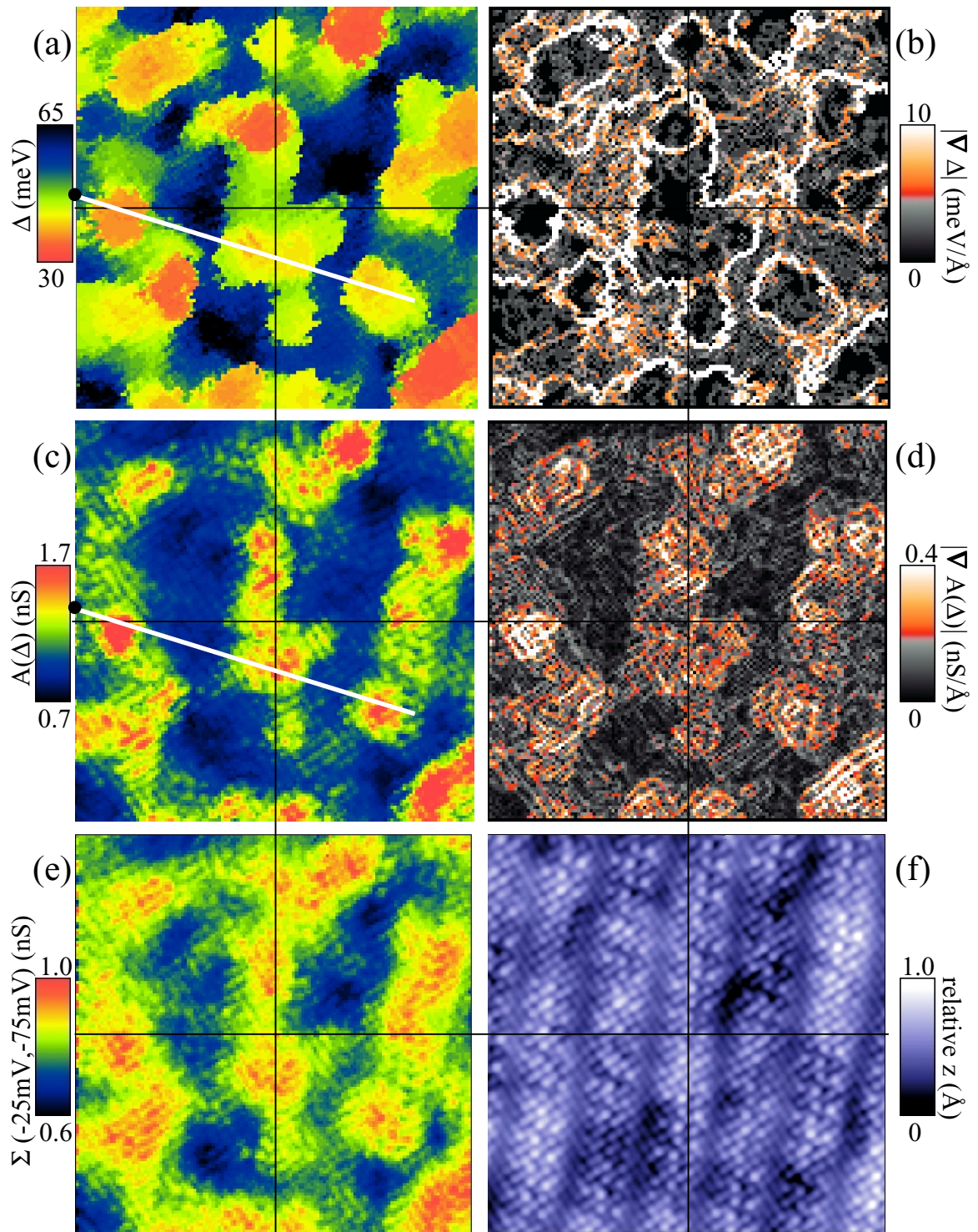


Figure 5.10: Set of high resolution maps of multiple spectral parameters on a second small field of view.

This series of 147 \AA square maps was extracted from a single 128×128 pixel spectral-survey. The identity of each map is indicated next to its respective color bar. The spatial correlations between these images illustrate the properties of granularity and segregation in BSCCO as discussed in the text.

Run = 159; File = 01025d02 & 01026a00, $V_{\text{set}} = -200 \text{ mV}$, $I_{\text{set}} = 200 \text{ pA}$

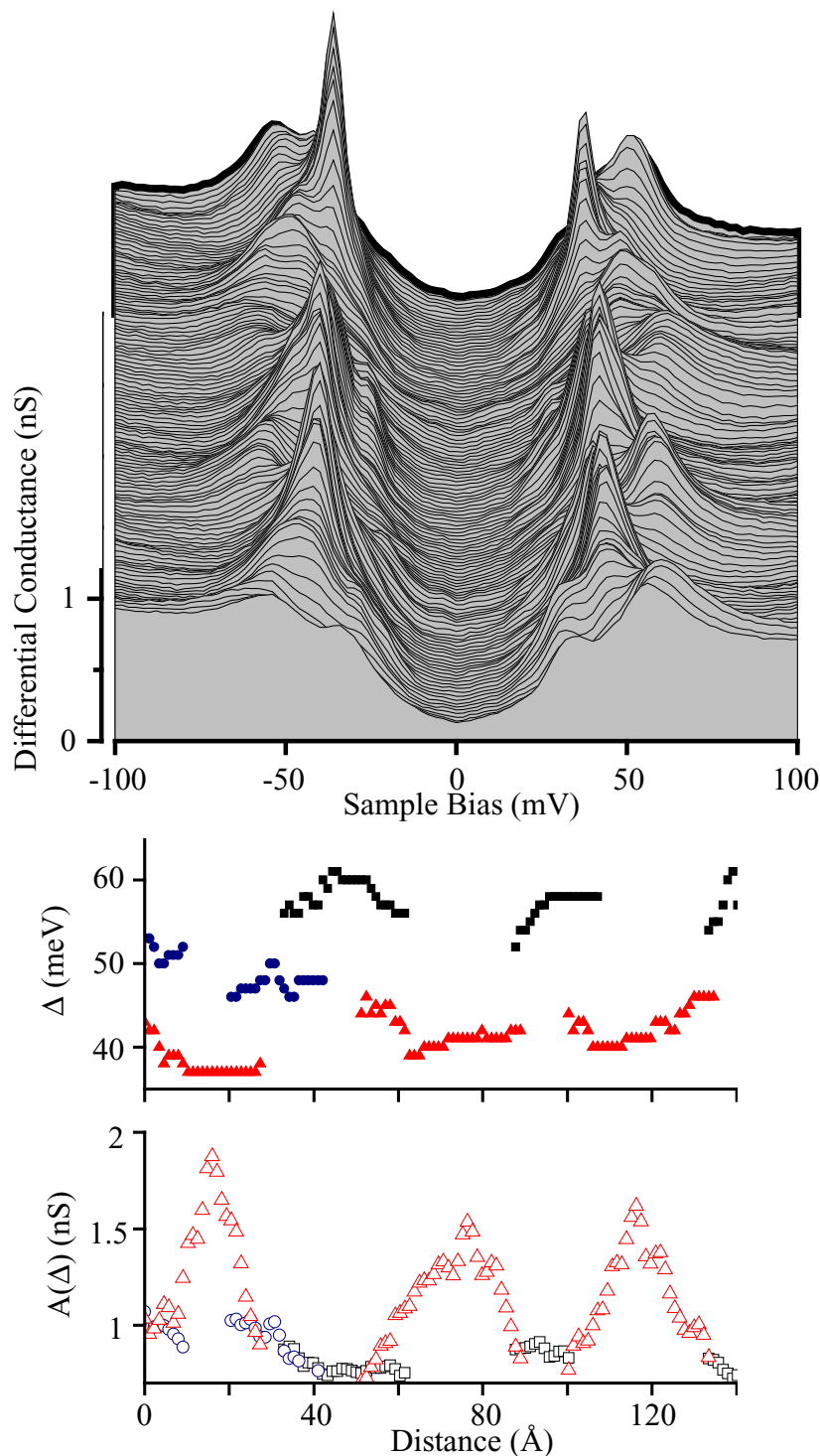


Figure 5.11: Set of Δ & $A(\Delta)$ traces and a linecut which correlate with the maps of the second small field of view.

(a) shows the spectra and (b) & (c) the trace of Δ and $A(\Delta)$ respectively for the white line shown on Figure 5.10 a&b. The thick black curve at the rear of the linecut in (a) and 0 \AA in (b) & (c) correspond to the location of the black dot on Figure 5.10 a&b. The spectra in (a) are separated by 1.1 \AA and are offset vertically for clarity.

Run =159, File = 01025d02 pixels from 0,61 to 119,98, $V_{\text{set}} = -200$ mV, $I_{\text{set}} = 200$ pA

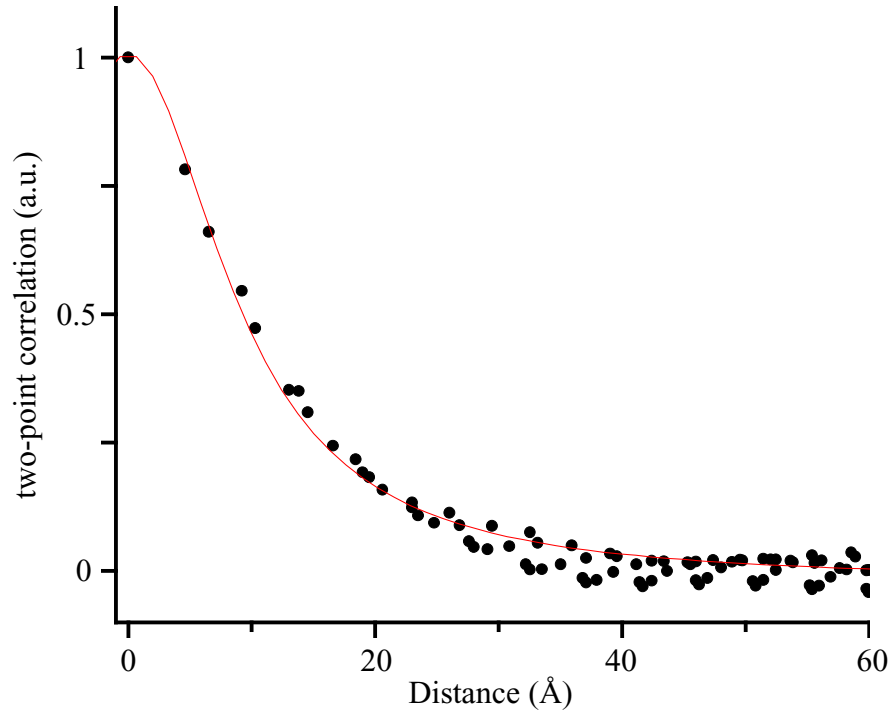


Figure 5.12: Two-point correlation of a gapmap.

A two-point correlation was performed on the gapmap of Figure 3.6(a&b). The result is shown as the black circles above. A Lorentzian was fit to this correlation as shown by the red curve. Given the width of this Lorentzian (18.8 Å) and a relationship between that width and the domain size (determined as described in the text), we find that the average α -domain size for this underdoped BSCCO sample is 28 Å.

Run =159, File = 01113b02, $V_{\text{set}} = -200$ mV, $I_{\text{set}} = 200$

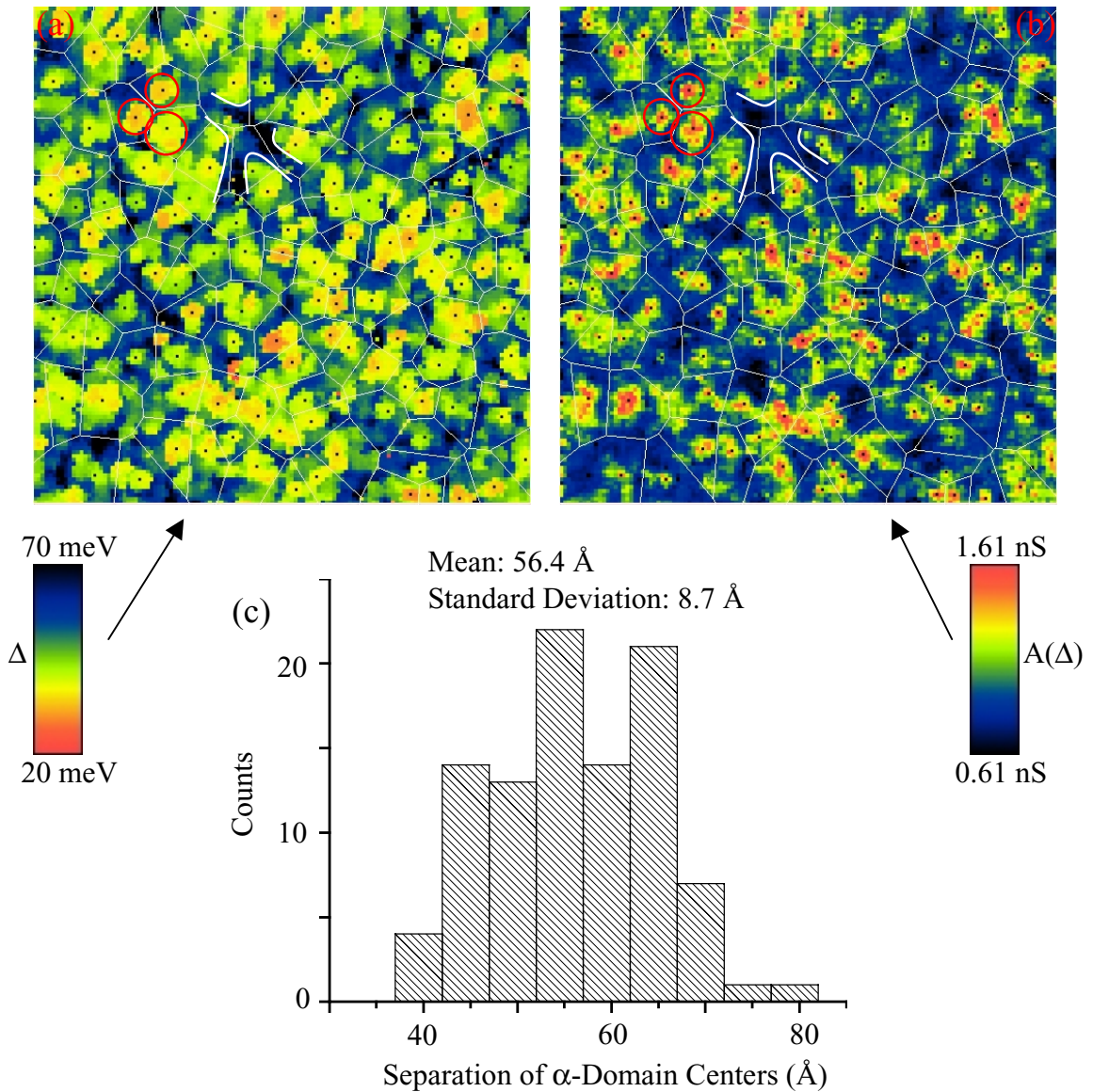


Figure 5.13: Δ - and $A(\Delta)$ -maps with α -domains indicated.

The 589 Å square (a) Δ -map and (b) $A(\Delta)$ -map from Figure 3.6 and 3.13 respectively are shown here. The small black dots mark the centers of the α -domains which were determined as discussed in the text. The fine white lines show the Voronoi cells based on these centers. Given the areas of the Voronoi cells, and assuming that they are circular, in (c) we show the histogram of diameters of those cells or correspondingly the separation between α -domain centers. The histogram of local- Δ values found at the α -domain centers is given by the red curve of Figure 5.15. Other properties of the α -domains are discussed in quantitative terms in the text.

Run = 159, File = 01113b02, $V_{\text{set}} = -200$ mV, $I_{\text{set}} = 200$ pA

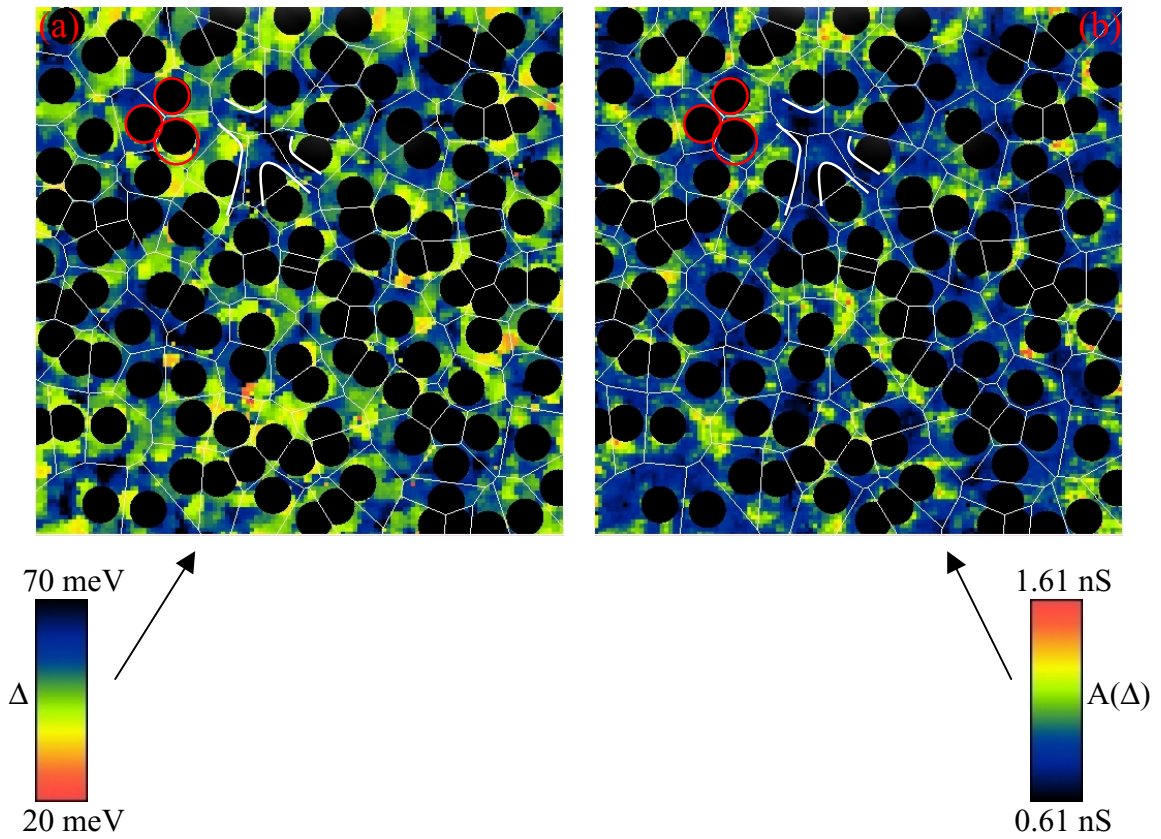


Figure 5.14: Δ - and $A(\Delta)$ -maps with β -regions indicated.

The (a) Δ - and (b) $A(\Delta)$ -maps shown here are the same as those of the previous figure. In this figure a black circle of diameter 41 Å has been placed at the location of each α -domain center shown by a black dot on the maps of the previous figure. The regions not covered by the black circles are assumed to represent the β -regions. The histogram of Δ values found in these regions is given by the blue curve in the next figure. Other properties of these regions are discussed in quantitative terms in the text.

Run = 159, File = 01113b02, $V_{\text{set}} = -200$ mV, $I_{\text{set}} = 200$ pA

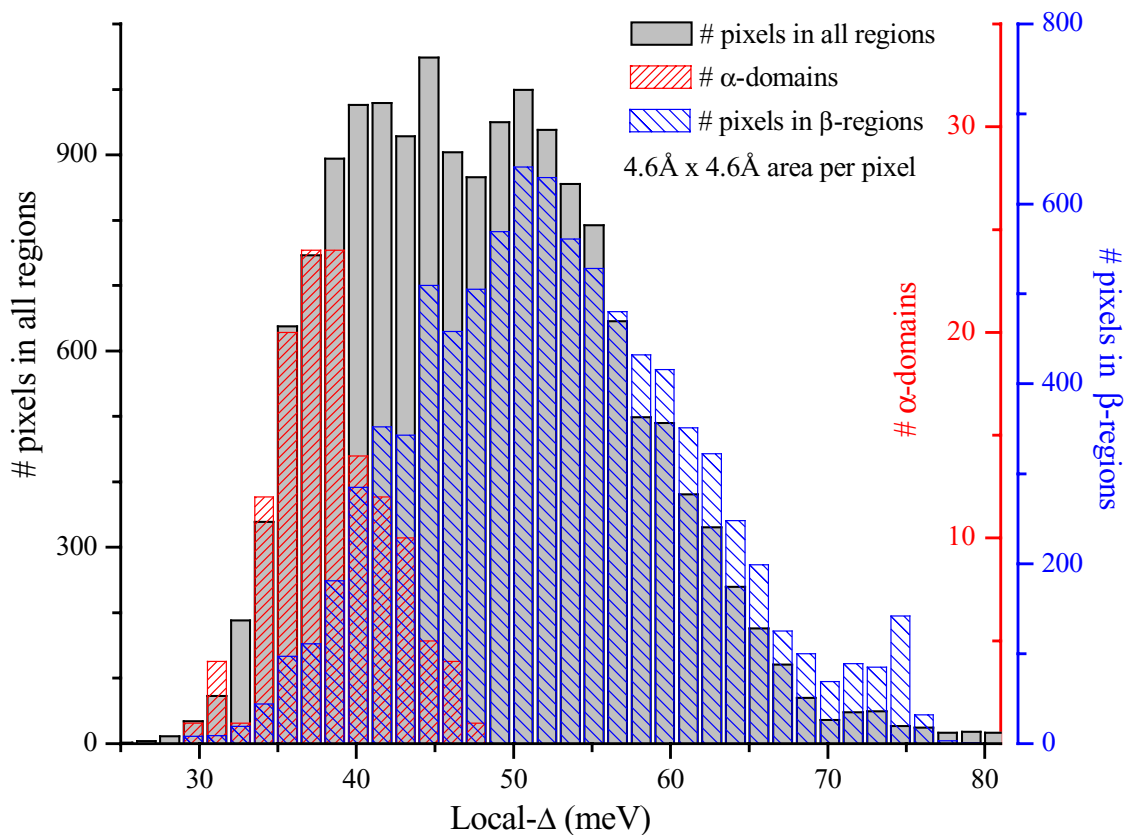


Figure 5.15: Histogram of Δ values for α -domains, β -regions, and all regions. These histograms are derived from the maps shown in Figures 5.13 and 5.14 as described in the captions to those figures and in the text. The gray curve is the histogram of Δ values for the entire 589 Å square field of view. The red curve is the histogram of Δ values found at α -domain centers. The blue curve is the histogram of Δ values found in the β -regions.

Run =159, File = 01113b02, $V_{\text{set}} = -200$ mV, $I_{\text{set}} = 200$ pA

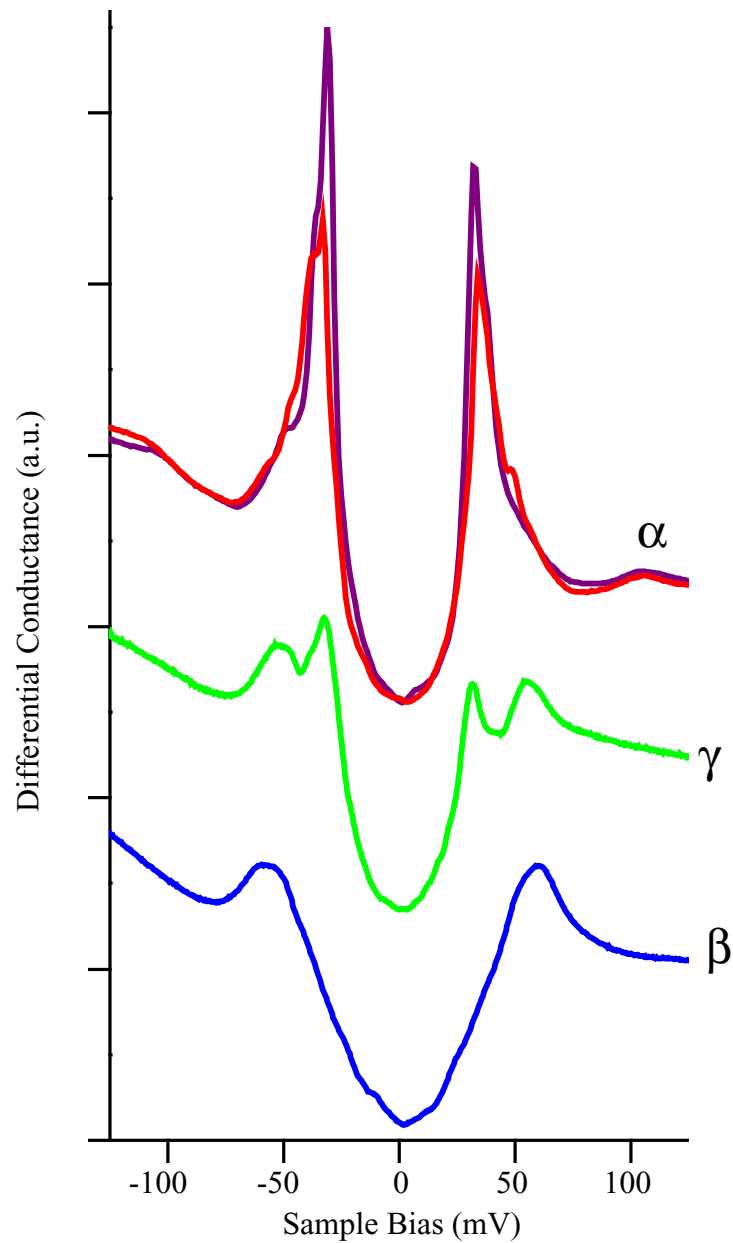


Figure 5.16: Representative α , β , and γ spectra.

The spectra shown here are representative of the qualitative spectral shape which is found in the respective regions. The spectra are vertically offset for clarity.

α spectra: Run = 159, File = 01029m00-13 and 01029k00-15, $V_{\text{set}} = -200$ mV, $I_{\text{set}} = 200$ pA

β spectrum: Run = 159, File = 01101d, $V_{\text{set}} = -200$ mV, $I_{\text{set}} = 200$ pA

γ spectrum: Run = 159, File = 01109c431-450, $V_{\text{set}} = -200$ mV, $I_{\text{set}} = 200$ pA

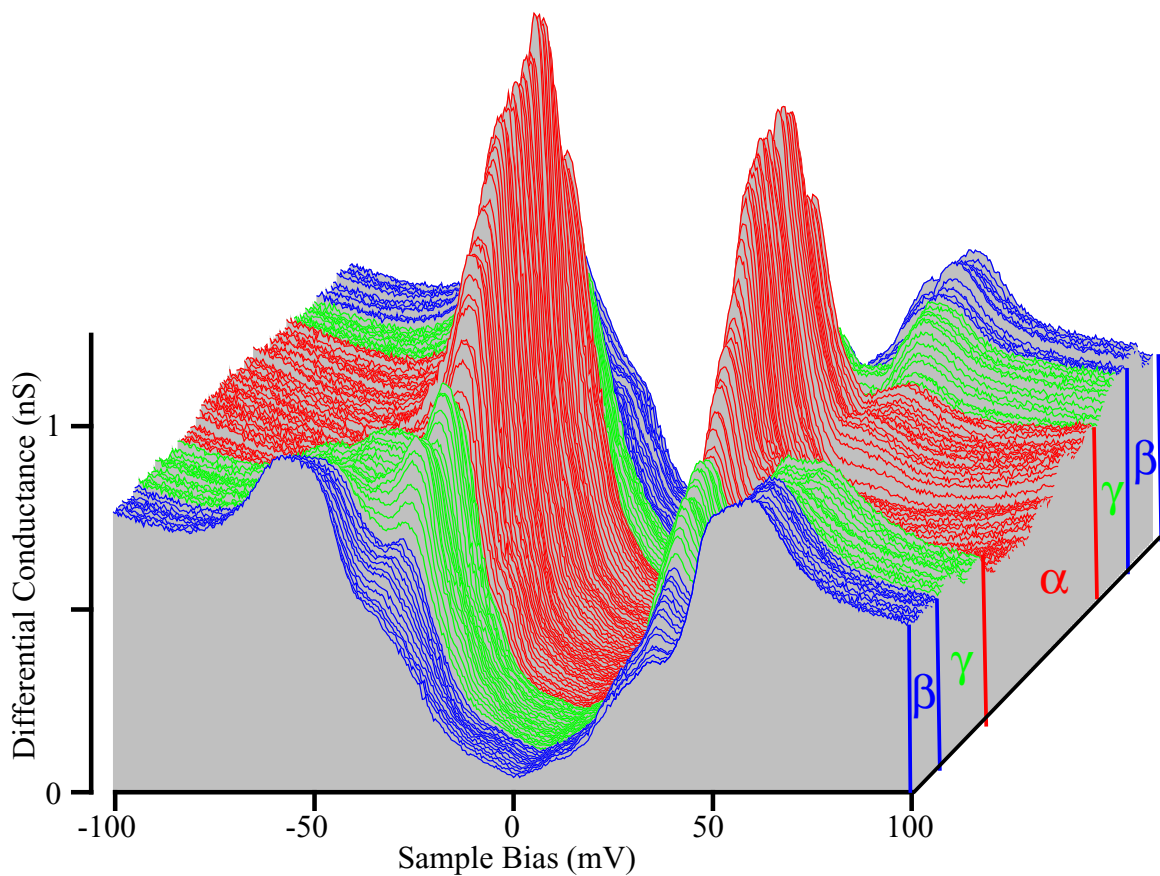


Figure 5.17: Linecut showing color coded α , β , and γ regions. This linecut is the same as the linecut of Figure 3.5 except here the spectra are color coded to indicate which region they belong to: α = red, β = blue, and γ = green. The spectra were taken at 0.29 \AA intervals along a 37 \AA line and are both vertically and horizontally offset for clarity. The trajectory of the line is approximately along the x axis.
 Run =159, File = 01101d104-233, $V_{\text{set}} = -200 \text{ mV}$, $I_{\text{set}} = 200 \text{ pA}$

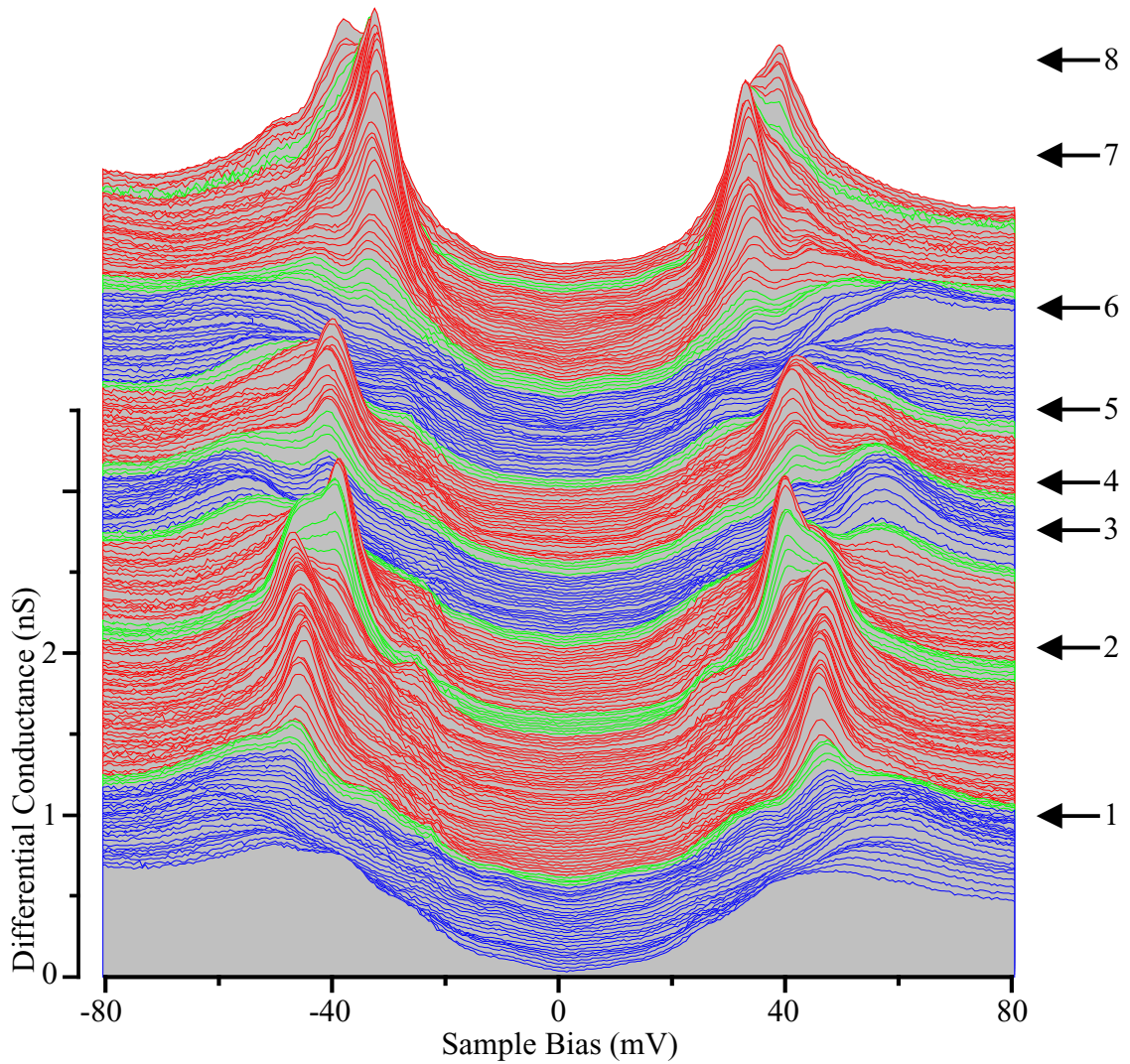


Figure 5.18: Second linecut showing color coded α , β , and γ regions. This linecut is the same as the linecut of Figure 5.1 except here the spectra are color coded to indicate which region they belong to: α = red, β = blue, and γ = green. The spectra were taken at 0.58 \AA intervals along a 133 \AA line. The spectra are vertically offset for clarity. The trajectory of the line is approximately along the x-axis. Run = 159, File = 01109c00-464 every 2nd curve, $V_{\text{set}} = -200 \text{ mV}$, $I_{\text{set}} = 200 \text{ pA}$

Chapter 6

Origin and Significance of Inhomogeneity, Granularity, and Segregation

The preceding three chapters have been dedicated to a demonstration of inhomogeneity, granularity and segregation in the electronic structure of BSCCO. Inhomogeneity has been observed in our data, as presented in Chapter 3, and in the data of others, as presented in Chapter 4. Granularity and segregation have been observed in our data, as presented in Chapter 5. Having thus demonstrated the existence of these three phenomena, I would now like to turn to a discussion of both the origin and significance of these observations.

I will begin this chapter with a brief and selected discussion of the current state of knowledge in the field of HTSC. I will then present three sections which discuss the origin of inhomogeneity, granularity, and segregation respectively. Finally, I will discuss the significance of these observations for the overall properties of the material.

A Comment on the Basis for the Discussion in this Chapter

The observations and suggestions which will be advanced in this chapter are on a different basis than those in previous chapters.

The findings in previous chapters constitute a careful and detailed description of the phenomenology of repeated and repeatable empirical observations of the electronic structure of BSCCO. As such, I believe that they are on a firm evidential foundation.

However, in this chapter much of what I will present (subsequent to Section 6.1) consists of deductions and speculations which are based on limited evidence, physical intuition, logical arguments, and educated guesses. I present these deductions as one suggestion of how to fit the new observations presented in previous chapters of this thesis into the overall framework of the phenomenology of the HTSCs. Although the interpretation presented in this chapter is, I believe, logically internally consistent, I do not claim that it is the only interpretation possible. However, the opportunity to make such educated speculation is one of the most exciting aspects of working in such a dynamic and unresolved field as high- T_c superconductivity.

6.1 A Brief and Selected Discussion of the Current State of Knowledge in HTSC

Much of the knowledge and many of the mysteries of HTSC are contained in the familiar temperature vs. doping HTSC phase diagram. A schematic of this phase diagram is presented in Figure 6.1. The remainder of this section will be concerned with a discussion of the aspects of this diagram which are most relevant to the subsequent

sections in this chapter. Additional discussion of these issues and others can be found in two recent (and very readable) reviews of HTSC [Batlogg 2000, Orenstein 2000].

6.1.1 Phenomenology as a Function of Doping

I begin the discussion of this diagram by considering the phenomenology of HTSC materials as a function of doping, which is given along the x-axis. For the general case of HTSC, doping-level means the number of excess holes per Cu atom. For the particular case of $\text{Bi}_2\text{Sr}_2\text{CaCu}_2\text{O}_{8+\delta}$, the number of excess holes is proportional to the number of non-stoichiometric oxygen atoms, and in particular one oxygen atom donates approximately two holes [Ghigna 1998]. Given the unit cell structure of this material, shown in Figure 1.6, this means that the δ in $\text{Bi}_2\text{Sr}_2\text{CaCu}_2\text{O}_{8+\delta}$ gives both the hole-doping level and the number of excess oxygen atoms per unit cell. Note that while the non-stoichiometric oxygen atoms are known to reside in the BiO plane [Yamamoto 1990], the resultant holes are found in the CuO_2 plane.

Having dispensed with the definition of doping, let us now discuss the effect of doping on HTSCs and in particular on the critical temperature. The undoped parent compounds of the HTSCs are antiferromagnetic Mott insulators. This is the phase given by ‘AF’ at the left of the diagram. Moving along the x axis, as holes are added, superconductivity turns on and T_C begins to increase. This is the *underdoped* region. At *optimal doping*, T_C reaches a maximum and then begins to decrease again in the *overdoped* region. Although there are many theories, the reason why T_C waxes and then wanes as a function of increasing hole doping remains a mystery.

Since much of this thesis is given to a discussion of the behavior of Δ , which we can measure by STM, it is useful to examine the trend in the spatially averaged value of $\Delta(x,y) (\equiv \bar{\Delta})$ as a function of doping. Direct measurements of $\bar{\Delta}$ can be executed by tunneling (break junction, point contact, planar, spatially averaged STS), ARPES⁶², and other spatially averaged spectroscopic methods. Several groups have published compilations of these measurements [Miyakawa 1998, Nakano 1998, Tallon 2001], and the compilation by Miyakawa *et al* is reproduced in Figure 6.2(a). The trend in $\bar{\Delta}$ is that it decreases monotonically as the doping level increases.

If one assumes that the measured $\bar{\Delta}$ in Figure 6.2(a) is the superconducting gap, then the observation of a monotonic trend in $\bar{\Delta}$ is rather unexpected since T_C is not monotonic in doping. In the weak coupling limit of the BCS theory for conventional superconductors $\bar{\Delta}/k_B T_C = 1.76$, and intuitively one might expect such a proportional relation between $\bar{\Delta}$ and T_C to hold in any superconductor. However, in the HTSCs $\bar{\Delta}/k_B T_C$ decreases monotonically as the doping-level increases as shown in Figure 6.2(b), which is reproduced from the paper by Nakano *et al* [1998]. Although there are

⁶² ARPES = angle resolved photoemission spectroscopy

many theories, the reason for the non-constancy of $\bar{\Delta}/k_B T_C$ in the HTSCs remains a mystery.

A second variable which can be measured locally by STM and which has been discussed in this thesis is the height of the gap-edge peak, $A(\Delta)$. It is useful then to examine the trend in the spatially averaged value of $A(\Delta, x, y)$ ($\equiv \bar{A}(\Delta)$) as a function of doping. Feng *et al* [2000] give a graph of the magnitude of the gap-edge peak at $(\pi, 0)$ as a function of oxygen-doping for $T \ll T_C$ as measured by ARPES. Subject to the assumption that the trend in the ARPES peak (\equiv SPR) is not significantly different for other k values, their signal should be proportional to $\bar{A}(\Delta)$. Their graph is reproduced in Figure 6.3(a), and it shows that the SPR increases with increasing doping until near optimal doping, at which point the SPR begins to decrease with increasing doping. Thus the magnitude of the gap-edge peak qualitatively tracks both the T_C , as seen in 6.3(a), and superfluid density, as seen in 6.3(b), vs. doping curves. The implication is that the value of SPR, and by extension, $\bar{A}(\Delta)$ is related to the amount of ‘superconductivity’ of the material, although why this should be true is unknown.

6.1.2 Phenomenology as a Function of Temperature

I would now like to consider the phenomenology of the HTSC materials as a function of temperature, which is given along the y -axis. For comparison, recall that a conventional superconductor below T_C has zero resistance, exhibits the Meissner effect, and manifests an energy gap (centered around the Fermi energy) in its density of states. These three phenomena are often considered as hallmarks of the existence of superconductivity, although superconductivity as such is the manifestation of zero resistance. The energy gap is due to Cooper pairing of the electrons, and the energy scale for this gap will be referred to as Δ_{SG} . The zero-resistance state and the Meissner effect arise from phase coherence of the Cooper-paired electrons, and the energy scale for this phase coherence will be given as E_{PC} . For a conventional superconductor $\Delta_{SG} \sim E_{PC} \sim k_B T_C$ which is why all three of these hallmarks of superconductivity disappear abruptly at T_C .

The situation is more complicated for the HTSCs. Overdoped samples of the HTSCs exhibit a behavior much like conventional superconductors in that the gap, the zero-resistance state, and the Meissner effect all turn off abruptly as T exceeds T_C .

Presumably this implies that for overdoped samples $\Delta_{SG} \sim E_{PC} \sim k_B T_C$.

However, for an underdoped sample things are different. At T_C only the zero-resistance state and the Meissner effect turn off; however, a gap remains above T_C , persisting until a temperature T^* is reached at which point it disappears. The gap which exists between T_C

and T^* for underdoped samples is generally called the *pseudogap*⁶³, a name which in itself indicates some ambivalence about the significance of this gap. The energy scale of the pseudogap is designed as $\Delta_{PG} \sim k_B T^*$. A recent and quite comprehensive review of experimental evidence for the pseudogap is given by Timusk and Statt [1999].

Generally speaking, there are currently two competing theories about the significance of the pseudogap. In one theory, often referred to as the “precursor pairing theory”, the pseudogap and the superconducting gap are one and the same, or $\Delta_{PG} \equiv \Delta_{SG}$. According to this school of thought then, for $T < T_C$ in an underdoped sample all three characteristics of superconductivity are present. As T exceeds T_C both the zero-resistance state and the Meissner effect disappear because $E_{PC} \sim k_B T_C$. However the superconducting/pseudo gap persists above T_C until T^* because $\Delta_{SG/PG} \sim k_B T^* > k_B T_C$. A summary of this theory and the evidence for it is given by Deutscher [1999].

The second theory about the significance of the pseudogap could be called the “competing gaps” theory. In this theory the pseudogap and the superconducting gap represent two separate and competing order parameters and $\Delta_{PG} > \Delta_{SG}$. According to this school of thought then, for $T < T_C$ in an underdoped sample all three characteristics of superconductivity are present, and in addition the pseudogap is present. As T exceeds T_C the zero-resistance state, the Meissner effect and the superconducting gap all disappear because $\Delta_{SG} \sim E_{PC} \sim k_B T_C$. However, the pseudogap persists above T_C until T^* because $\Delta_{PG} \sim k_B T^* > k_B T_C$. A summary of this theory and the evidence for it is given by Tallon and Loram [2001].

6.1.3 Papers Addressing Inhomogeneity, Granularity and/or Segregation

Recently there have been a number of papers which addressed inhomogeneity, granularity and/or segregation in the electronic structure of BSCCO. Essentially all these papers postulate that local disorder, presumed to be due to the dopant oxygen atoms for BSCCO, creates variations in the local density of states. In addition, different papers address different aspects of the observations presented in this thesis. Although this section is not meant to be a thorough review of such papers, selected ones which are known at this time to this author are briefly summarized here in alphabetical order of the first author’s last name.

Burgy *et al* [2001] *et al* use a two dimension (2D) toy model of Ising spins to suggest that the “*underdoped cuprate state is not homogeneous but results from the SC-AF*

⁶³ For the record, *superconducting gap* is taken to refer to the gap which is a manifestation of Cooper pairing and is thus ultimately responsible for the phase coherent properties of zero resistance and the Meissner effect. Although the superconducting gap is always present below T_C , this definition of superconducting gap is based on its role and significance and not on its position in the phase diagram. *Pseudogap* is taken to refer to the gap which exists in underdoped samples between T_C and T^* . This definition of pseudogap is then independent of this gap’s role or significance, and purely based on its position in the phase diagram.

[superconducting-antiferromagnetic] competition after disorder is considered.” This results in “a mixture of insulating and preformed SC islands” on a nanometer length scale.

Ghosal *et al* [2000] “*study a simple model of a two-dimensional s-wave superconductor in the presence of a random potential in the regime of large disorder. [They] use the Bogoliubov-de Gennes (BdG) approach to show that, with increasing disorder the pairing amplitude becomes spatially inhomogeneous...*” [p. 1] They further state that, “*we find that the system breaks up into superconducting islands (with large pairing amplitude) separated by an insulating sea.*” [p.1]

Martin *et al* [2001] state that the “*effect of carriers and intrinsic disorder produced by the very same doping are inseparable in underdoped and possibly overdoped cuprates.*” Starting with this postulate, they construct a semi-phenomenological model to predict the distribution of gaps to be found in a single sample as a function of global oxygen doping level.

Ovchinnikov *et al* [2001] comment on the implications of inhomogeneity for the origin of the pseudogap state saying, “*inhomogeneity leads to a spatial dependence of the critical temperature, so that $T_c \propto T_c(\mathbf{r})$. As a result, it is realistic to imagine the sample containing regions with different values of local critical temperature (T_c^L). Of course, for some of them $T_c^L > \bar{T}_c$, where \bar{T}_c is the average value of the critical temperature.*” In these regions pairing stills exists and would be manifest in spectroscopy, but if “*the distance between the clusters L exceeds some value L_0 ...then the compound is in the normal resistive state.*”

Pan *et al* [2001] present experimental data⁶⁴ which, “*lead[s] one to relate the magnitude of the integrated local DOS to the local oxygen doping concentration.*” The arguments used to substantiate this statement include a comparison of this data to ARPES data, as well as a comparison of the length scale of the observed LDOS variation with other relevant length scales.

Q.-H. Wang *et al* [Wang 2001A] use the t-J model in the presence of random disorder potential to find both the local hole density and the associated tunneling spectra. They find that the local gap varies with local hole density. In addition they address the issue of how the local hole density affects the integrated value of the spectra.

Z. Wang *et al* [Wang 2001B] present theoretical support for, “*[the] conjecture that the inhomogeneity arises from variations in the local oxygen doping level...*” [p. 1] by employing a numerical simulation using the t-J model plus randomly distributed ionic Coulomb potentials to “*calculate the LDOS spectrum, the integrated LDOS, and the local superconducting gap as those measured by STM, make detailed comparisons to experiments, and find remarkable agreement with the experimental data.*” [p. 1]

⁶⁴ The data presented in this paper has also been presented in this thesis since this data was taken while S.H. Pan was a postdoc at Berkeley. The specific file number of the data presented in this paper is: 90304c00.

6.2 Origin of Inhomogeneity

Having established some essential phenomenology of HTSC, I would now like to discuss the data presented in this thesis in the context of the overall framework of HTSC. In particular, I would like to begin with a discussion of the origin of the observed inhomogeneity of the electronic structure as described in Chapters 3 and 4.

I suggest that the electronic structure inhomogeneity observed in BSCCO originates in the random distribution of x,y positions of the non-stoichiometric dopant oxygen atoms. A schematic of this proposal is given in Figure 6.4 which shows several regions each with different local oxygen dopant density, accordingly different local hole density, and thus different local LDOS spectra⁶⁵.

The most straightforward way to verify this assertion would entail a direct measurement of the position of the oxygen atoms, and a correlation of that measurement with the parameter maps presented in the previous chapter. Unfortunately, the oxygen atoms are not visible in the topographies, and so such a direct verification is not possible. In lieu of this, I will offer several plausibility arguments in the remainder of this section. Although, I do not claim that such arguments can establish this assertion, I believe that they strongly suggest its validity. As many of these discussions hinge on the *local oxygen/hole doping level*, prior to presenting the plausibility arguments, I will begin this section with a careful definition of this quantity.

6.2.1 Definition of Local Doping Level

A logical definition of the *local doping level* and its synonym, *local density*, is given as follows. Consider a given x,y location on the sample surface and draw a circle which is centered on this location. The circle will be referred to as an *influence circle*, and the radius of this circle will be referred to as the *influence radius*.

The reason why an influence circle, rather than an influence sphere, is defined is the following. For $\text{Bi}_2\text{Sr}_2\text{CaCu}_2\text{O}_{8+\delta}$, each CuO_2 plane has one nearest neighbor BiO plane. The location of the dopant oxygen atoms in this one BiO plane (and resulting hole locations in the CuO_2 plane) are assumed to be the dominant factor which determines the spectral properties of the superconducting CuO_2 plane. Thus, to first order, we only consider the two-dimensional local density in the this single BiO plane, and so need only a circle, rather than a sphere, of influence.

⁶⁵ To clarify the arguments in this section, I postulate that the two holes donated by each oxygen atom are arranged such that the *local oxygen density* is always strictly half of the *local hole density* at all locations. Thus in this section *local oxygen density* and *local hole density* should be considered essentially interchangeable in the text. In the next section I explicitly discard this postulate in favor of the more physically plausible assumption that the holes somewhat rearrange themselves locally for several reasons. This hole rearrangement implies that the *local oxygen density* and the *local hole density* are no longer related by the same factor of two which nonetheless still relates the *global oxygen density* to the *global hole density*. Discarding this postulate can lead one to an understanding of the observed granularity in the electronic structure.

A simplistic definition of local doping-level would entail the following. Count the number of oxygen atoms/holes in a given influence circle, divide by the area of the circle, and the result is the local oxygen/hole density for the point located at the center of the circle.

A physically more plausible definition, and the one which should be kept in mind in the remainder of the discussion, would entail a slightly more complicated calculation as follows. Calculate the distance of each object (oxygen atom or hole) from the center of a given influence circle. Then define a function which determines a weighting factor for an object, such that objects further away from the circle center have lower weights. Note that both the size of the influence circle and the weighting function are both *material* dependent properties which can presumably be measured or calculated. Finally, add up all the weighted objects inside the circle, divide by the area of circle, and the result is the local doping-level for the point located at the center of the circle.

6.2.2 Global Causality Implies Local Causality

The data presented in this thesis and elsewhere establishes that Δ is a spatially varying quantity. For a random distribution of oxygen atoms, the local oxygen doping level will also be a spatially varying quantity. While *a priori* one might not assume that these two spatially varying quantities had a causal interrelationship, there exists one additional observation which suggests that they might. Figure 6.2(a) in the previous section established that the global oxygen doping, \bar{p} , controls the global value of the gap, $\bar{\Delta}$. Such global causality between these two variables renders the suggestion of local causality more plausible.

The ‘global causality implies local causality’ argument is more readily understood if one considers the following gedanken experiment. Let us assume that we have a macroscopic sample of a HTSC material, in which we have arranged the non-stoichiometric oxygen atoms in some regular array within the crystal. We measure global \bar{p} vs. global $\bar{\Delta}$ by some non-spatially resolved spectroscopic means like break junction or ARPES. Some relationship is found between these variables. Now cut that crystal in half and make the same measurement. It seems improbable that the relationship between \bar{p} and $\bar{\Delta}$ (both global variables) could change just from cutting the crystal in half. Then cut one half of the original crystal in half a second time and make the same measurement. If the relationship between \bar{p} and $\bar{\Delta}$ did not change due to the first cut, it seems improbable that it should change due to this second cut. Now repeat this experiment again and again with ever smaller crystals. At each juncture one finds that the relationship between \bar{p}

and $\bar{\Delta}$ remains the same as it was for the entire crystal⁶⁶. Thus does one arrive at the idea that ‘global causality implies local causality.’

In summary, non-spatially resolved spectroscopic techniques establish a global causal relationship between \bar{p} and $\bar{\Delta}$. This global causal relationship implies a local causal relationship between p and Δ , which suggests that the local value of Δ is determined by the local doping-level.

6.2.3 Comparison of Global and Local Spectral Shapes

A second justification for the assertion that local oxygen doping controls the local Δ value is derived from a comparison of spectral shapes as described below.

We begin by assuming what we are trying to demonstrate, namely that the local oxygen doping level determines the local value of Δ . Given this assumption, if we take a spectral-survey map on a given large ($\sim 550 \text{ \AA}$ square) region, and sort the spectra in that map by the parameter Δ , then we are effectively sorting those spectra on the doping-level, p . We then take all the spectra in a given range of Δ (Δ -bin) and average them together to get one spectrum which represents the properties of a given doping-level. We can do this for multiple ranges of Δ , and thus acquire a series of spectra which represent the different doping levels present in our single sample.

Point contact spectroscopy can be used to take a series of spectra on different samples with different global doping-levels. These spectra should be qualitatively comparable in shape to the series of spectra we created by Δ -binning and averaging in our spectral-surveys. A comparison between these two series of spectra is presented in Figure 6.5. Qualitatively speaking, the same trends are present in the two series. In particular, spectra with higher values of Δ have lower and broader gap-edge peaks and conversely spectra with lower values of Δ have higher and sharper gap-edge peaks.

This observation implies that the variety of shapes of our local spectra from a single sample are reflected in the variety of shapes of global spectra from multiple samples with different global oxygen doping-levels. This suggests that oxygen doping is the origin of the variation in spectral shape which we have observed in BSCCO.

6.3 Origin of Granularity

If one assumes that the non-stoichiometric oxygen atoms in the crystal are truly randomly distributed, then this distribution produces a *continuously* varying local oxygen doping-level in the sample according to the definition of local doping given in Section 6.2.1.

⁶⁶ One might argue that at some point one of the small pieces of the crystal will contain a different doping-level than the global doping of the original macroscopic crystal. While this is true it does not invalidate the argument. It just means that the small crystal in question will give a different point on the \bar{p} vs. $\bar{\Delta}$ curve than the macroscopic crystal it came from. However, the point given by this microscopic crystal will still be on the same curve because we could have started with a different macroscopic crystal which had that global doping to begin with.

Granularity is observed precisely because various parameters assume discrete values within a given region of the sample and then change over some short length to a different discrete value. How then does one account for this discreteness given a continuous variation in the oxygen atom doping-level?

I suggest that self-organization of mobile holes, donated by relatively immobile oxygen atoms, is the origin of the observed granularity. Essentially, the holes rearrange themselves to produce a non-uniform and relatively discontinuous local hole density, despite the relatively uniform continuous local oxygen density. Assuming that it is the local *hole* density (and not the local *oxygen* density) which determines the local spectral shape, including the local value of Δ , then the non-uniform local hole density produces discrete grains in which a given spectral shape predominates.

Given that a non-uniform local hole distribution can account for the observed granularity, one is then led to wonder what could produce such a distribution. This question will be addressed next. I subsequently present a discussion to clarify how this non-uniform hole distribution can lead to the observed granularity.

6.3.1 Origin of Non-Uniform Local Hole Distribution

A schematic of the proposed oxygen and hole distributions is given in Figure 6.6. Panel 6.6(a) shows a relatively uniform distribution of oxygen atoms. Panel (c) shows one possible distribution of holes which illustrates the postulated non-uniform hole distribution. Panel (b) shows the relative positions of these two distributions. Two representative influence circles are shown in all three panels. The shading inside the circles indicates schematically the weighting factor discussed in Section 6.2.1.

The next task is to physically motivate this non-uniform hole distribution given the oxygen distribution. I begin by discussing a mechanism which can drive the holes to cluster in general (and in the absence of the oxygen atoms), and then I discuss what effect the oxygen atoms have on this clustering.

The theory of why holes might cluster in a HTSC is often known as *stripe theory*. There is a large body of literature on this topic, so for brevity I shall only give a very few references which I have found useful in understanding this theory from an intuitive standpoint [Emery 1993, Emery 1999, Orenstein 2000]. The essential physics behind the stripe theory is depicted in Figure 6.7 and is as follows.

There are either one or zero itinerant electrons on each Cu atom in the CuO_2 plane. The number of sites with zero electrons is equivalent to the number of holes and is thus determined by the doping level. To give a sense of the numbers, approximately 1 in 6 Cu sites have a hole for optimal doping. Each of these itinerant electron carries a spin. An antiferromagnetic ordering of these spins lowers the energy of the system and so is preferred by nature. However, the presence of a hole locally jumbles this ordering and thus can raise the energy of the system. In order to minimize the disordering effect of the holes and achieve a state of minimum energy, the holes cluster together into stripes as

shown in the Figure 6.7. The intervening regions between the stripes can then have perfect antiferromagnetic order and thus is the energy of the system lowered.

Of course, the energy of the system is raised by the Coulomb repulsion energy of having so many positively charged holes in one region. It is this Coulomb repulsion between the holes which prevents total phase separation in which *all* the holes in the sample end up clustered together. Instead the phase separation is driven by the energy savings found in antiferromagnetic order among the electrons, but is frustrated by the energy cost of Coulomb repulsion between the holes. This balancing act leads to the compromise position of partial phase separation as manifested in the stripes.

Stripe theories are typically predicated in a system in which the holes are free to move wherever they choose, and stripes are the state of minimum energy under this condition. However, this condition does not hold in the HTSCs, because in these materials the positively charged holes are donated by relatively immobile negatively charged oxygen atoms. Given this, the energy of the system is raised by moving a hole far from its donor oxygen atom. Essentially, a lower energy state for the system is one which is locally charge neutral.

In this scenario there are now three competing factors, phase separation which lowers the energy, Coulomb repulsion of the holes which raises the energy, and local neutrality which lowers the energy. Under these three competing conditions, I suggest that the following scenario will minimize the energy. The holes will cluster in order to achieve phase separation, and that clustering will cost about the same Coulomb repulsion energy no matter how it occurs (as long as it is on about the same length scale as the previous stripes). However, subject to the constraint of local charge neutrality, the holes will stay within a given radius of their dopant oxygen atoms. In addition, again due to the constraint of local charge neutrality, regions with slightly higher local oxygen doping density are preferable for the clusters. These three competing phenomena can then produce a hole distribution such as that shown in Figure 6.6(b), in which slight fluctuations in the local oxygen density produce highly magnified fluctuations in the local hole density, resulting in a very non-uniform hole distribution.

The scenario in which a non-uniform hole distribution arises from a random, and fairly uniform, distribution of oxygen atoms has been seen in numerical simulations by Lee *et al* [Wang 2001A] using a t-J model Hamiltonian. They find that regions with unusually high hole density are found near the Coulomb centers which represent the oxygen atoms. These numerical simulations are concordant with the scenario shown in Figure 6.6(b) which I have motivated using physically intuitive arguments in this section.

6.3.2 Non-Uniform Hole Distribution Implies Granularity

The schematic in Figure 6.8(a) illustrates how a non-uniform distribution of holes can lead to the observed granularity. In this figure several representative influence circles are shown, and the spectrum obtained at the center of each circle is indicated.

In Figure 6.8(a), circles a and b each contain approximately the same number of holes, and thus result in the same spectrum, 1, as indicated. This implies that at points between the centers of circles a and b, and in general at any point nearby for which the influence circle contains approximately the same number of holes, a similar spectrum would be obtained. *Thus is a contiguous region established in which similar spectra are obtained at every point within the region. This contiguous region is a grain.* The outline of this grain, 1, is given very roughly in Figure 6.8(b).

The same argument can be applied to circles c & d (e, f, & g) which each contain approximately the same number of holes, and thus result in the same spectrum, 2 (3), as indicated. This produces grains 2 (3) as indicated in Figure 6.8(b).

There is one difference between grains 1 or 2 and grain 3 which is worth noting at this point. Namely, grains 1 and 2 are contiguous bounded regions, whereas grain 3 is a contiguous unbounded region, where bounded means that one can draw a closed contiguous boundary around the grain. While the existence of unbounded grains is not a necessity for granularity, I have shown one because I believe that such unbounded grains exist in underdoped BSCCO, as discussed in Section 6.5.

6.4 Origin of Segregation

Figure 6.8 suggests a local hole density distribution which could account for the observed granularity in the electronic structure of BSCCO. A further observation that could be made about this distribution is that, although there are contiguous regions in which the hole density is locally relatively constant, sometimes that locally constant hole density is near zero and sometimes it is finite.⁶⁷ I will refer to regions with near-zero local hole density as NZ grains and to regions with finite local hole density as F grains.

The question then arises, in the NZ grains vs. the F grains is the local excitation spectrum the same? I suggest that the answer to this question is no. I believe that this then is the origin of the observed segregation of the electronic structure of BSCCO into the two distinct regions. *The local electronic structure derives from the local hole density, such that electronic structure **a**-domains are associated with local hole density F regions, and electronic structure **b**-regions are associated with local hole density NZ regions.*

6.5 Implications for Segregation

In the previous section it was suggested that the origin of segregation is variations in the local hole density. In this section I would like to address the related question of the implication of segregation for the global properties of the crystal.

⁶⁷ Obviously the quantities “near-zero” and “finite” are not quantitatively well defined here, and they are not meant to be. However, the point is that in Figure 6.6 the local hole density of region 3 could be viewed as qualitatively distinct from the local hole density of regions 1 or 2.

To consider the implications of segregation, first consider the properties of a macroscopic crystal which has a *uniform* local hole density throughout. What would be the transport properties of this crystal as a function of that uniform local hole density? I believe that a macroscopic crystal which contained a ‘finite’ hole density, such as is found in α -regions, would be superconducting. In contrast, a crystal which contained a ‘near-zero’ hole density, such as is found in a β -region, would not be superconducting. These statements are motivated by the following: 1) a HTSC crystal with identically zero hole doping, which is by definition a uniform local doping, is not superconducting, and 2) adding holes to a HTSC crystal, whatever the local doping density distribution, renders it a global superconductor.

Now imagine that there existed many of these uniform local hole density crystals, some which had finite local hole density and were thus entirely α type and some which had near-zero local hole density and were thus entirely β type. Then imagine that the crystals were randomly arranged and subsequently fused together and shrunk down, so that the distinct α and β regions were only a few nanometers across. This is the situation as observed by STM. What now are the transport properties of the nanoscale α - and β -regions? Are the α -regions still superconducting and the β -regions still not?

The question in this context is much more complicated since the α - and β - region properties should not change discontinuously on the boundary between the two regions, and even the concept of a boundary is itself somewhat ill defined. However, ignoring these complications, I speculate that the α -domains still retain some vestige of their superconducting origin and likewise the β -regions retain some vestige of their non-superconducting origin. If this is the case, then the situation in BSCCO is that which has been conventionally referred to as granular superconductivity⁶⁸.

Recall that a granular superconductor is a system which contains droplets of a superconductor in a non-superconducting matrix. Although the superconducting droplets are physically separated from one another, the system as a whole can superconduct if the droplets are close enough to one another to be Josephson coupled. A model granular superconducting system is studied and discussed in the context of HTSC in the paper by Merchant *et al* [2001].

6.6 Summary

The speculations put forth in this chapter to address both the origin and significance of the STM observations presented in this thesis are summarized as follows.

The frustrated tendency of the holes to completely phase separate, due to mutual Coulomb repulsion and attraction to the relatively immobile oxygen dopant atoms, yields

⁶⁸ Note that *granular superconductivity* should not be taken as synonymous to *granularity*. While the former implies something about the nature of the distinct regions (namely that one is superconducting and the other is not), the latter merely describes the structure of the electronic local density of states with no implications as to the nature of the distinct regions.

regions with ‘near-zero’ or ‘finite’ local hole density. Regions with finite local hole density yield the α -domains observed by STM, and regions with near-zero local hole density yield the observed β -regions. The α -regions are superconducting, whereas the β -regions are not. This results in a situation which has been conventionally referred to as granular superconductivity, with superconducting droplets in a non-superconducting matrix. The material as a whole will superconduct if the superconducting α -domains are spaced closely enough so as to be Josephson coupled with one another.

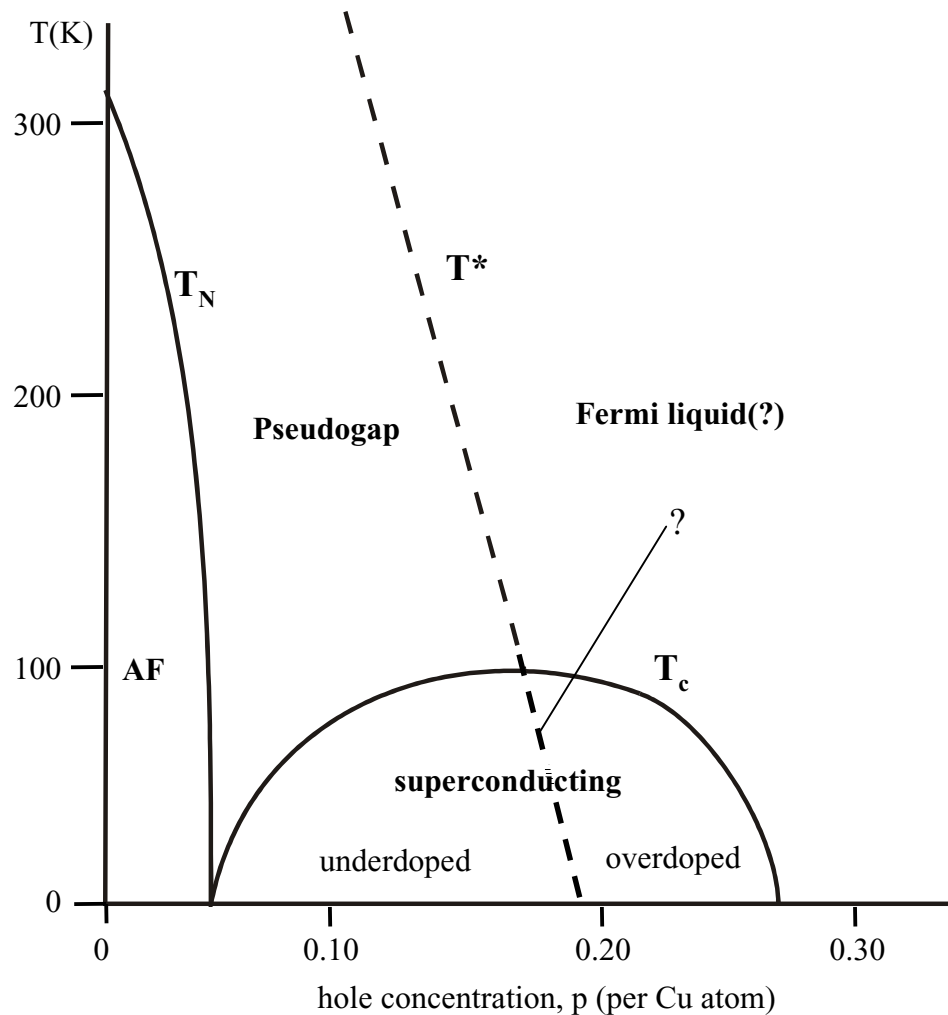


Figure 6.1: High temperature superconductivity phase diagram.

This diagram shows the different known phases of a high temperature superconductor as a function of hole-doping (p) and temperature (T). At very low dopings, these materials are antiferromagnetic Mott insulators as indicated by the AF on the diagram. When the doping-level is increased, they superconduct for a range of temperatures as indicated by the T_c dome. In the pseudogap phase, these materials exhibit a gap in their density of states, but do not superconduct. It is currently not known whether the T^* line continues to $T=0$ as shown or whether its slope is shallower such that it reaches 0 outside the overdoped side of the superconducting dome.

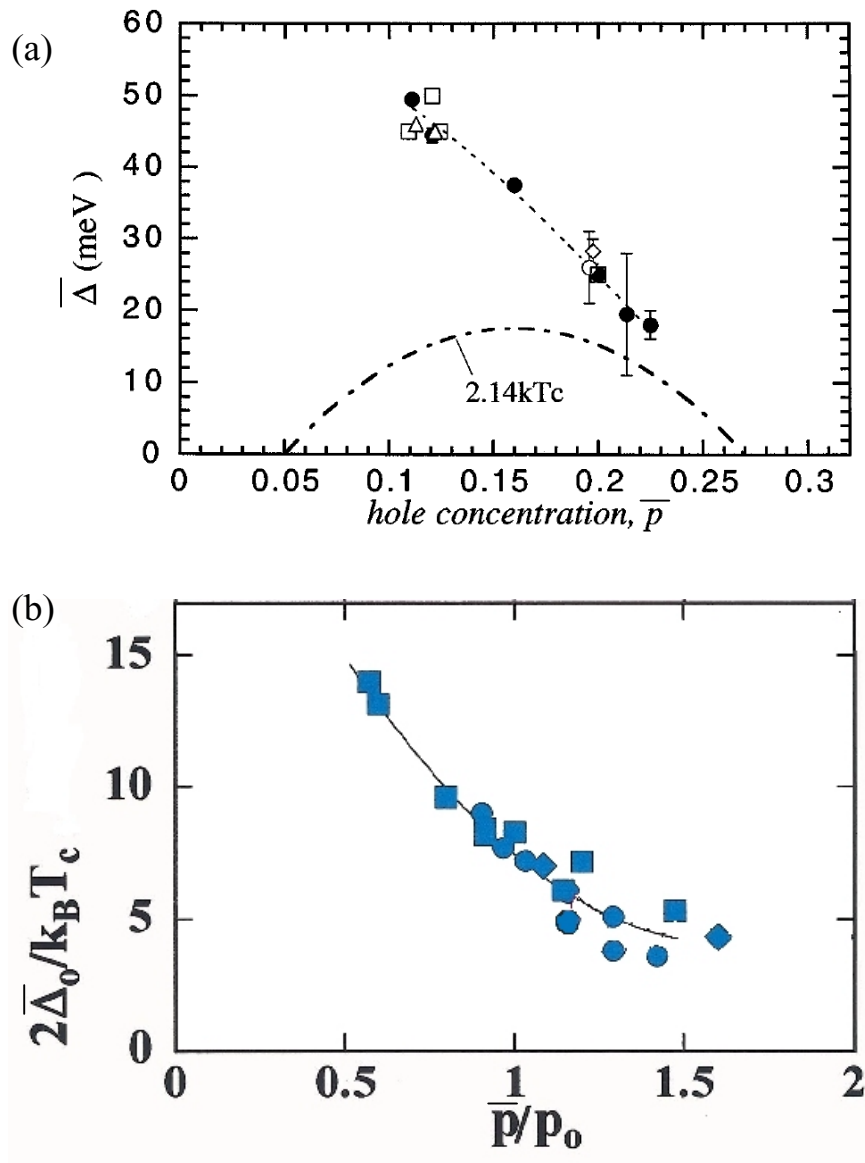


Figure 6.2: Trend in the spatially averaged value of Δ as a function of oxygen-doping. (a) shows the trend in spatially averaged Δ as a function of oxygen doping. The measurements shown in this plot were made by SIS tunneling and ARPES on BSCCO. Δ is seen to be monotonically decreasing with increasing doping. Given the dome shape of the T_c curve, this trend in Δ implies that $2\Delta/k_b T_c$ is also monotonically decreasing with increasing doping as seen in (b). This is in contrast to conventional superconductors in which $2\Delta/k_b T_c$ is a constant. The measurements in (b) were made by STS, Raman and break junctions on BSCCO (squares) and $\text{La}_{2-x}\text{Sr}_x\text{CuO}_4$ (circles).

(a) Reference: Figure 3 from Miyakawa 1998.

(b) Reference: Figure 3(b) from Nakano 1998.

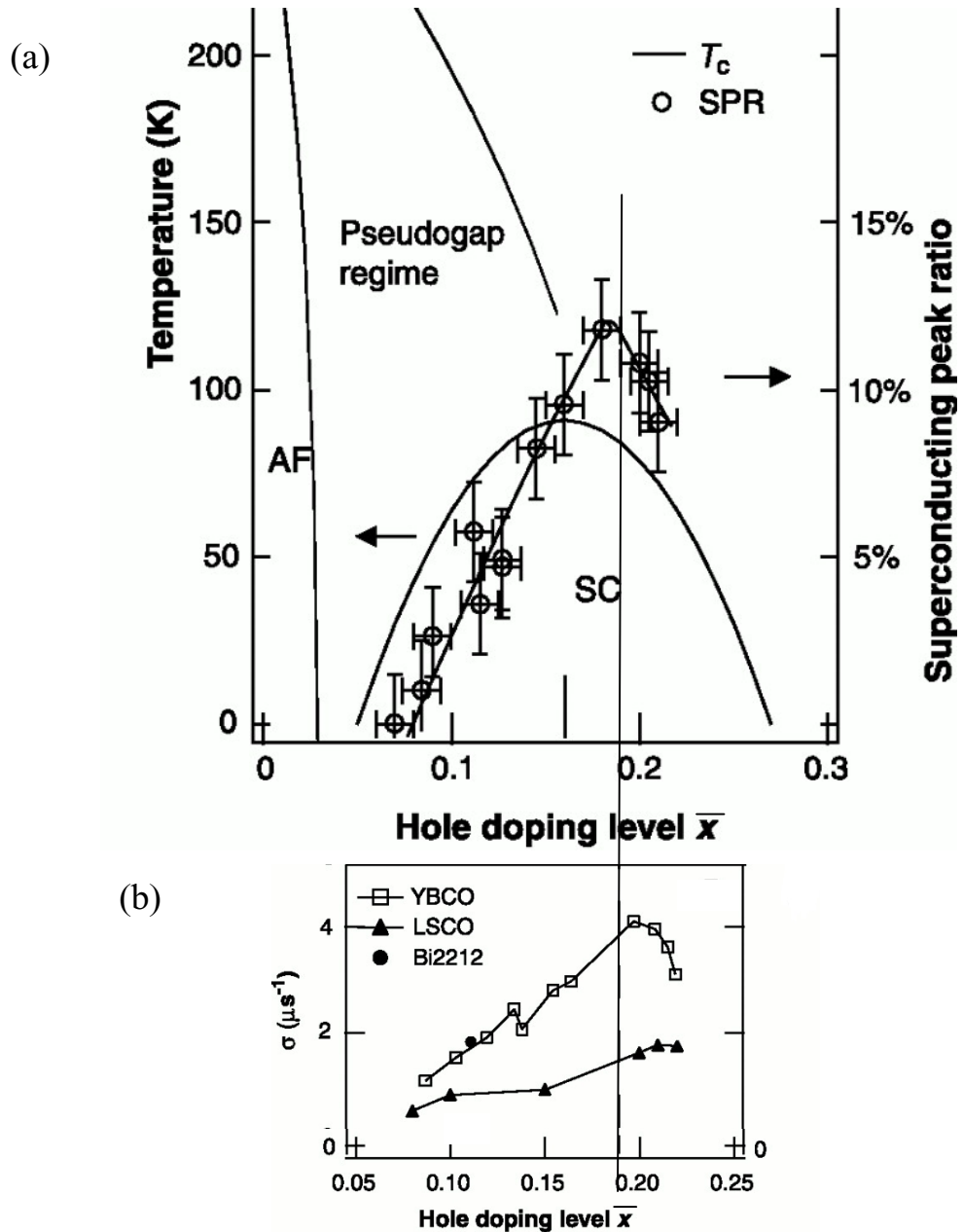


Figure 6.3: Trend in the spatially averaged value of $A(\Delta)$ as a function of oxygen-doping. (a) shows the trend with oxygen-doping in the “superconducting peak ratio” (SPR) as measured on BSCCO by ARPES near $(\pi, 0)$, the gap maximum direction. The SPR is the magnitude of the gap-edge peak after background subtraction. Assuming that the same trend (or no trend) in the SPR occurs in other k -space directions, then k -averaged spectra would show this same trend. Given that tunneling is a k -averaged measurement, this plot then represents the trend in spatially averaged $A(\Delta)$ ($\equiv \bar{A}(\Delta)$). These observations are qualitatively consistent with the trend seen in SIN tunneling spectra as a function of doping, as seen in Figure 6.5. It is remarkable that $\bar{A}(\Delta)$ tracks both the (a) T_c and (b) superfluid density, the latter of which was measured by the μSR relaxation rate. Reference: Figure 3B and 4B from Feng 2000.

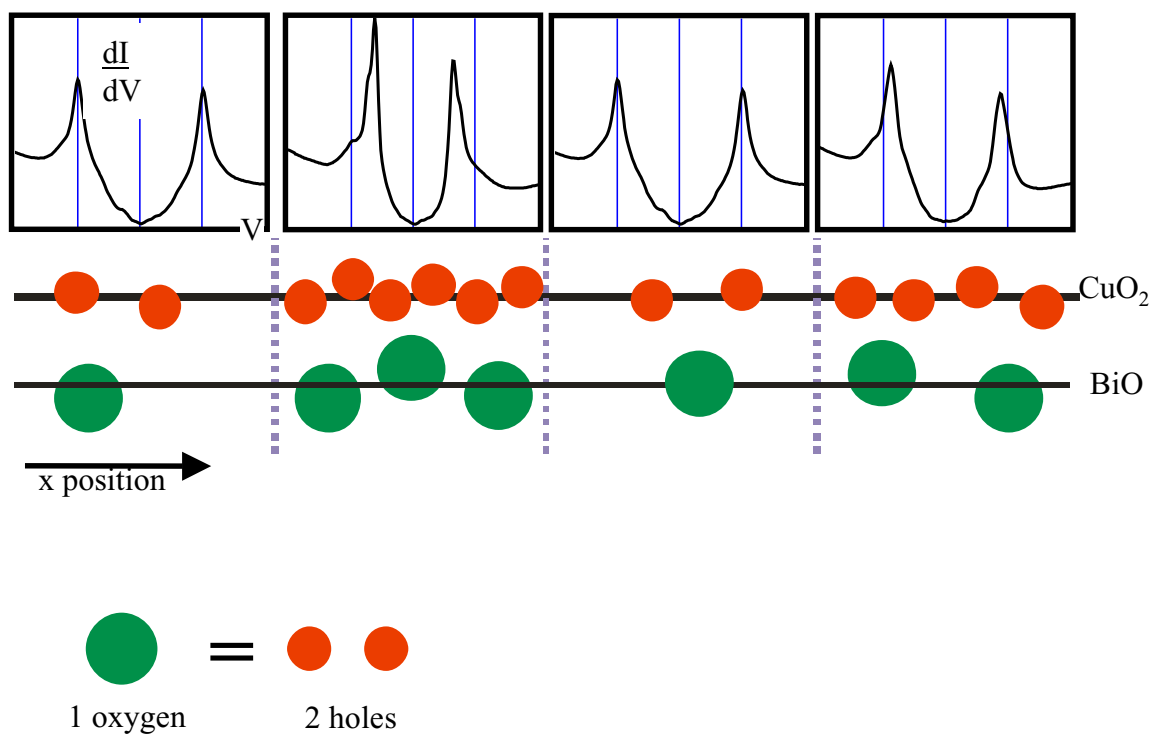


Figure 6.4: Schematic illustrating the proposed relationship between local oxygen doping and local spectral properties.

It is proposed that the local oxygen doping level in the BiO plane controls the local hole doping level in the CuO_2 plane, which in turn controls the local spectral properties. The simplistic schematic shown here illustrates the general trend in spectral properties which might result from this scenario. In accordance with both theory and experiment, it is expected that lower local doping levels would result in spectra with higher Δ and lower $A(\Delta)$, and conversely, as schematically shown. Note that this figure is not meant to convey quantitative information, but rather only qualitative trends.

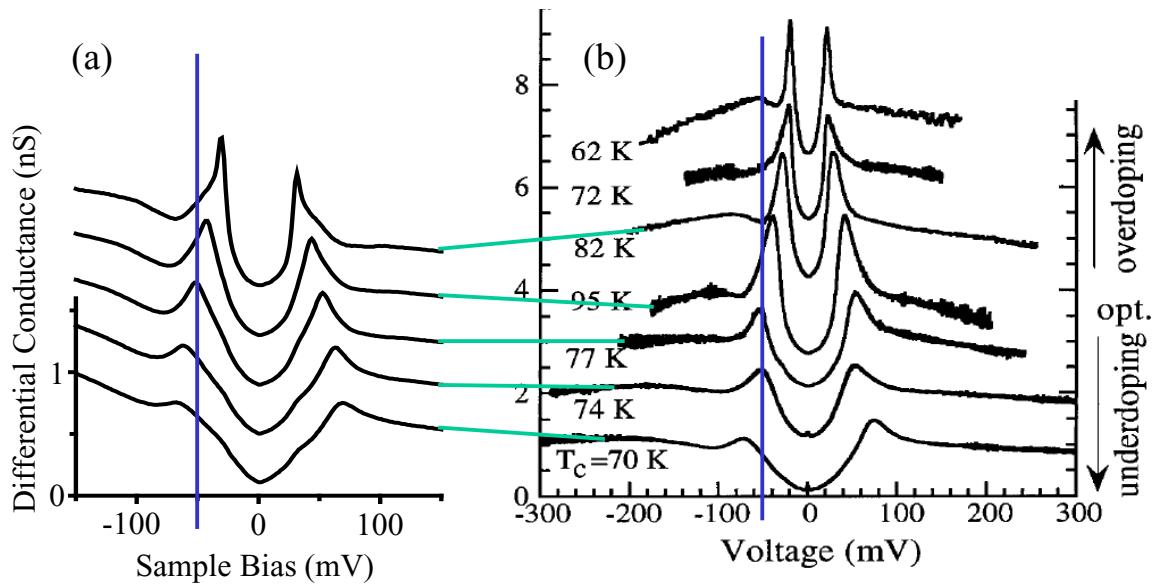


Figure 6.5: Trend in the spectral shape as a function of doping- local vs. global measurements.

The spectra in (a) were generated from a single 589 Å square spectral-survey. This plot was created by first sorting all the spectra in the survey on their respective value of Δ , and then subsequently averaging all spectra within each Δ -bin. Of the average spectra thus generated, selected ones are presented here. On the assumption that the local doping level controls the local value of Δ , then the spectra in (a) represent different local doping levels present in this single sample. The spectra in (b) were taken by point contact SIN tunneling on different crystals with different global doping levels. It is seen that the qualitative trend in spectral shape with doping is the same for the local spectra of (a) and the global spectra of (b). Note that this figure is not meant to convey quantitative information, but rather qualitative trends.

(a) Run =159, File = 01113b02, $V_{\text{set}} = -200$ mV, $I_{\text{set}} = 200$ pA

(b) Reference: Figure 1 from Miyakawa 1999.

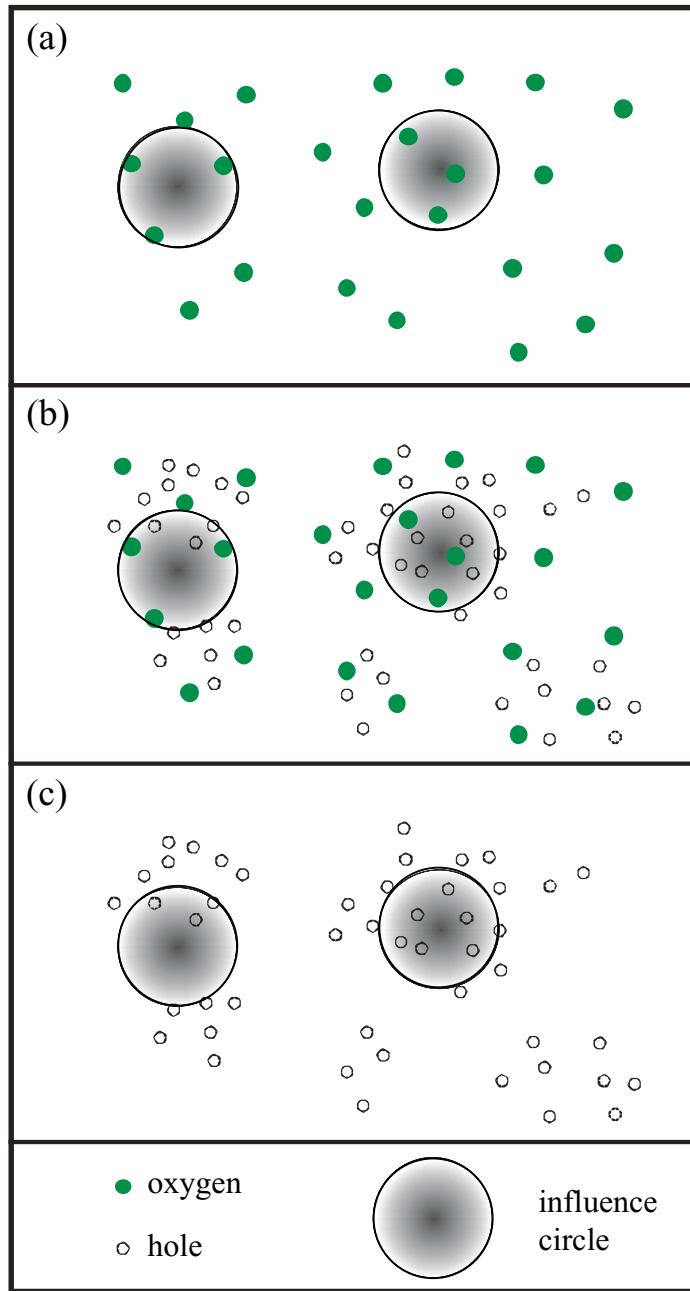


Figure 6.6: Schematic showing local oxygen atom distribution and proposed resulting local hole distribution.

Assuming an oxygen atom distribution as shown in (a), and assuming the holes exhibit a tendency to phase separation, together with a long range mutual Coulomb repulsion and an attraction to the relatively immobile oxygen dopant atoms that prohibits this total phase separation, the resulting hole distribution may appear as shown in (c). (b) shows the relative positions of these two distributions. *Influence circle* is defined in Section 6.2.1.

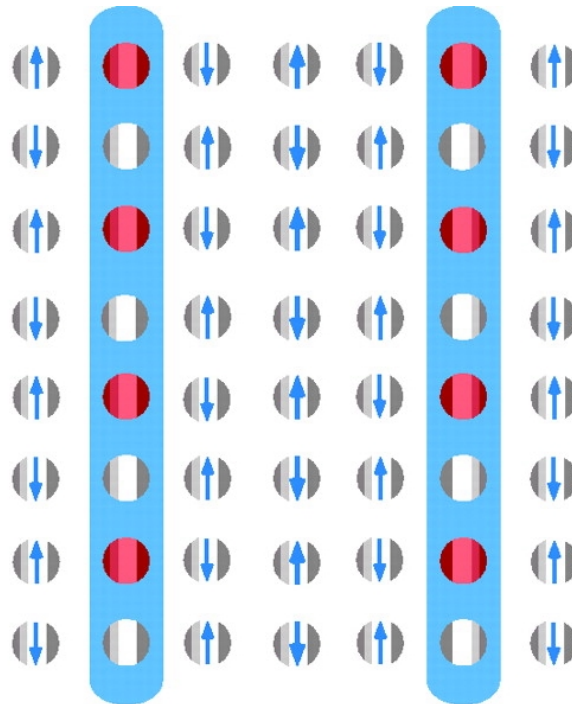


Figure 6.7: Schematic illustrating stripe ordering.

In this schematic all the holes (red circles) are confined to the blue shaded regions.

This allows the electrons (white & gray circles) in the non-shaded regions to assume perfect antiferromagnetic order as indicated by the up and down arrows representing their spins. This configuration of holes and electrons is predicted to lower the overall energy of the system as discussed in the text.

Reference: Figure 3B from Orenstein 2000.

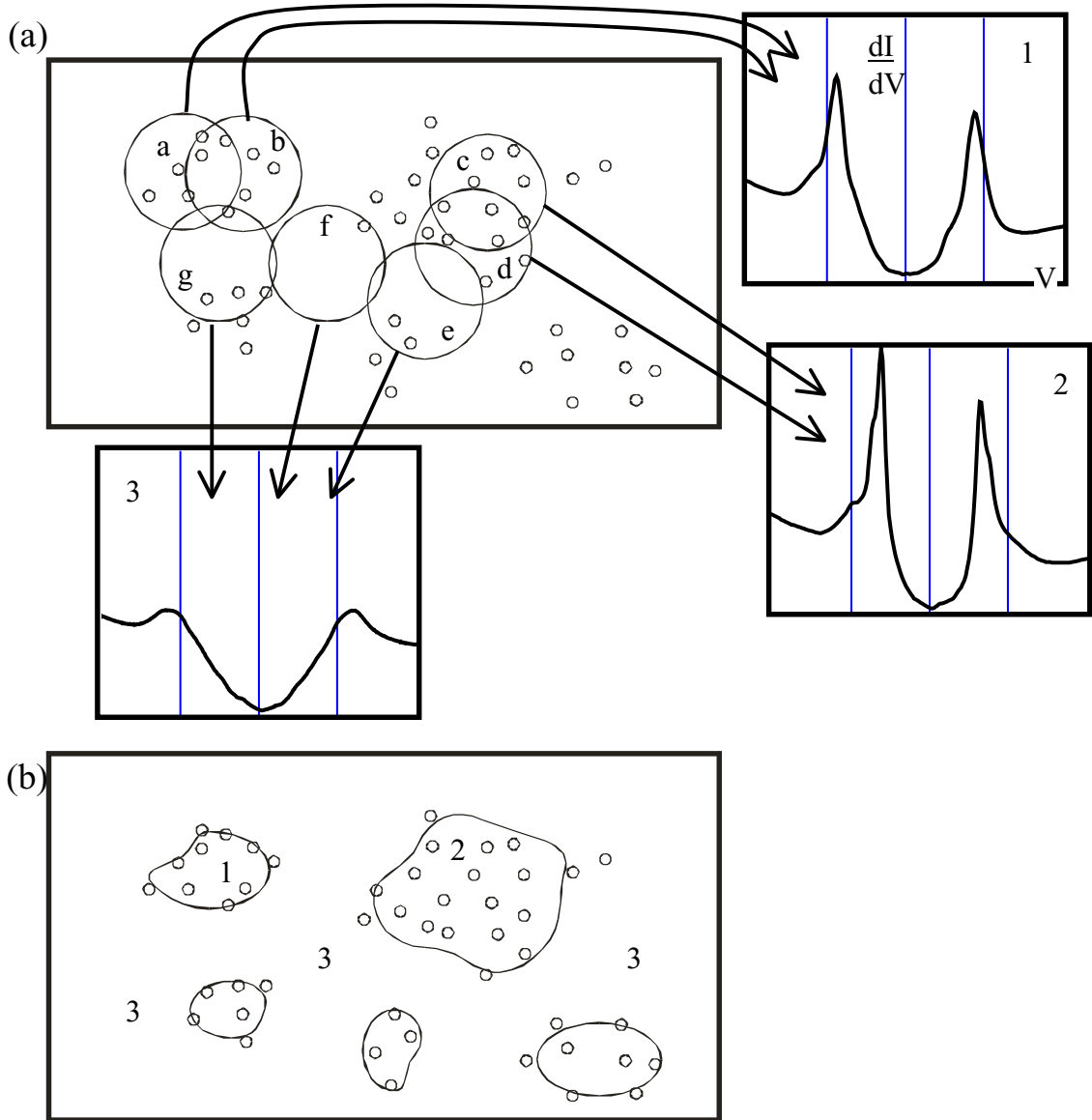


Figure 6.8: Schematic illustrating how LDOS granularity can arise from a clustered distribution of holes.

The same distribution of holes from Figure 6.6 is shown in (a) and (b). In (a) several circles of influence are shown and the spectrum measured at the center of each is indicated. Consider two circles, (e.g. a and b), which each contain approximately the same number of holes, and thus result in the same spectrum (1). This implies that at points between the centers of circles, and in general at any point nearby for which the influence circle contains approximately the same number of holes, the same spectrum would be obtained. Thus are regions obtained, as indicated in panel (b), in which the same spectrum would be measured throughout the region. In short, there are regions in the material within which the local density of states exhibits a common set of characteristics, which are distinct from the characteristics exhibited by neighboring regions. This is the situation which has been termed *granularity* in this thesis. Note that this figure is not meant to convey quantitative information, but rather qualitative trends.

Conclusion

In this thesis my focus has been to present as complete a description as possible of the phenomenology of *inhomogeneity*, *granularity* and *segregation* which have been observed by STM in the electronic structure of $\text{Bi}_2\text{Sr}_2\text{CaCu}_2\text{O}_{8+\delta}$. These observations raise many questions, some of which are addressed in this chapter and in a forthcoming paper on this topic [Lang 2001]. However, many questions remain unanswered.

Returning once more to the analogy presented in the Preamble of this thesis, high temperature superconductivity is like a disassembled jigsaw puzzle. We possess many of the pieces of the HTSC puzzle. Some of the puzzle pieces have been fit together to produce small bits of the overall picture. A grasp of the whole picture seems tantalizingly close at hand. And yet, the puzzle remains disassembled and the image recorded in its pieces is still unknown. It is my hope that the experiments presented in this thesis may provide definitive new pieces of the puzzle, which in turn may help clarify the picture of high temperature superconductivity.

Appendix 1

Peak Picking Algorithm

This appendix describes the algorithm which was used for picking the energetic location of the gap-edge peaks in the BSCCO differential conductance spectra (*peak picking algorithm*). In short, given a differential conductance spectrum, the algorithm was used to determine Δ for that spectrum. When implemented by a computer for every spectrum in a spectral-survey, the algorithm enabled us to extract parameter maps and histograms of Δ (and by extension of $A(\Delta)$, $\nabla \Delta$, and $\nabla A(\Delta)$) from those surveys. These maps and histograms are shown throughout this thesis.

A.1 Description of the Peak Picking Algorithm With Examples

Figure A.1(b) shows five spectra which are part of the linecut of A.1(a) as indicated by the color of the spectra. The linecut of A.1(a) is the same as that of Figure 5.8, and ultimately these spectra came from the spectral-survey whose parameters maps are shown in Figure 5.7. The spectra are typical of those obtained in a spectral-survey and represent examples of the different types found.

I will use these spectra to demonstrate how the computer algorithm picks Δ for each curve. In this section, I will describe the algorithm in detail using Spectrum 1, as shown in Figure A.2, as an example. Spectra #2 - #5 are further examples and are presented in Figure A.3.

Referring to Figure A.2, the algorithm works as follows.

1. Find the gap-edge peak at positive bias.
 - a) Given a spectrum, calculate the two point derivative for each point. The two point derivative for the point P_2 is defined as $G(P_3)-G(P_1)$.
 - b) Beginning at a positive bias near 0 mV⁶⁹ walk toward higher values of the bias (towards the right on the curve, i.e. first P_1 , then P_2 , etc.) considering the value of the derivative at that point and the four subsequent points (i.e. for P_1 consider P_1 , P_2 , P_3 , P_4 and P_5).
 - c) When a point is found such that 3 out of the 5 points considered show a negative value of the derivative then stop walking. For the purposes of reference I will call that point P_D . P_D is shown as a blue square on the curve of Figure A.2.
 - d) Starting at P_D , walk again toward higher values of the bias looking for the local maximum. Do this by asking for each point if $G(P)<G(P+1)$. When this condition is false, stop walking and call that point P_{LM} , the locally maximal point. P_{LM} is shown on Figure A.2 as a green triangle.

⁶⁹ We generally look for peaks in a bias range which would encompass every value of Δ which we could expect to find in that sample given its doping. There is some iteration involved in determining the best range, but in practice the range goes from 15-20 mV on the low end to 80-100mV on the high end.

- e) Find the global maximum for the positive bias energy range in which we looked for a peak, $G_{\max+}$.
 - f) If $G(P_{\text{LM}}) > 0.9 * G_{\max+}$, then the energy associated with the point at P_{LM} is defined as Δ_+ .
 - g) If $G(P_{\text{LM}}) < 0.9 * G_{\max+}$, then start walking again toward higher voltages starting at P_{LM} and follow instructions starting at step c.
 - h) If the end of the data is reached and no peak has been found, then write an error code as Δ for that spectrum. See Section A.2 for a discussion of this.
2. Find the gap-edge peak at negative bias.
Repeat step 1 for the peak at negative bias. Everything works the same except mirrored in voltage. For example the two point derivative is defined as $G(P1)-G(P3)$, the walking goes toward lower values of the bias (towards the left on the curve), the program looks for 3 out of 5 positive derivatives, and so on. In this way, find $G(\Delta_-)$.
 3. Calculate $\Delta \equiv \frac{\Delta_+ - \Delta_-}{2}$.

In practice this algorithm was implemented in a stand-alone computer program that I wrote in the C programming language. Two other members of the Davis group, Eric Hudson and Jenny Hoffman, also contributed to the development and coding of the algorithm.

A.2 Dealing With Spectra Which Have No Peaks Out To the Highest Measured Energy

The algorithm detailed in Section A.1 obviously will not find a peak in spectra which have no peaks out to the highest measured energy. An example of such a spectrum is found in Figures 3.9 and A.4. Such spectra are generally not isolated cases, but rather are found together patches. Such a patch is observed Figure A.5, and it appears as the extended black region which is roughly outlined in red. All the spectra inside the white box were averaged to produce the spectrum shown in Figure A.4.

The spectral-surveys presented in this thesis generally have a few percent of their area occupied by patches containing these no-peak, or NP, type spectra. The only spectral-survey where this fraction was significantly larger is shown in Figure A.5.

Given that these NP-spectra regions are such a small fraction of the total area, in the case when they are encountered, Δ_{\pm} is assigned to be the energy of global maximum for the \pm bias energy range in which we looked for a peak. In practice given the shape of these spectra, this means that Δ is assigned to be the largest voltage at which we looked for a peak. Given this assignment, these NP regions are assigned a larger value of Δ than all other regions in the field of view and thus appear black in all Δ , $\nabla\Delta$, $A(\Delta)$, and $\nabla A(\Delta)$ maps for all color scales used in this thesis. In addition, the NP regions have lower integrated LDOS, and thus appear as black regions in maps of Σ and in the topographies for all color scales used in this thesis.

A.3 Estimate of the Error in the Value of Δ Chosen by the Peak Picking Algorithm

To determine the error in the value of Δ chosen by the peak picking algorithm for non NP type spectra, we looked by hand at 40 selected spectra from each of two spectral-surveys and compared the value of Δ thus found to the value of Δ chosen by the algorithm.

For the first map the energetic spacing between measurements of dI/dV was 2 meV. In this map the RMS difference between the hand-picked Δ and algorithm-picked Δ is 2.6 meV.

For the second map the energetic spacing between measurements of dI/dV was 1.2 meV. In this map the RMS difference between the hand-picked Δ and the algorithm-picked Δ is 0.9 meV.

In both cases then the difference between the two methods of choosing Δ is comparable to the energetic spacing between measurements of dI/dV . Thus, the error in the value of Δ as chosen by the algorithm described above, is estimated to be approximately equal to the energy spacing between points of the spectra being analyzed. Note that most spectral-surveys presented in this thesis contained spectra with energy spacing of 2 meV. The two exceptions are file numbers 01113b02 with energy spacing 1.5 meV and 91114i04 with energy spacing 1.2 meV.

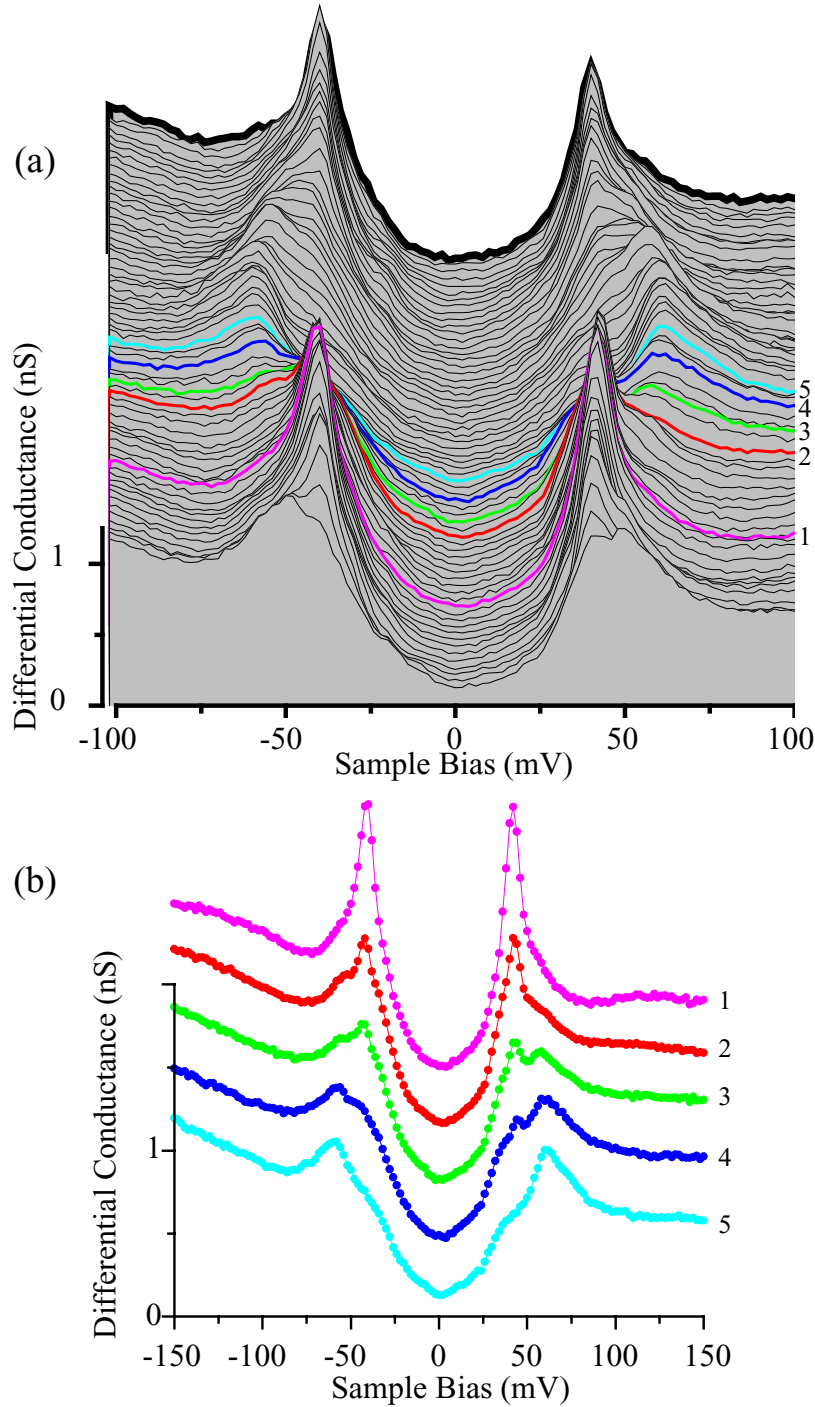


Figure A.1: Selected spectra for illustration of the peak picking algorithm.

(a) shows the same 72 Å linecut as Figure 5.8, which came from the spectral-survey whose parameter maps are shown in Figure 5.7. Selected spectra are colored and numbered in the linecut, and those spectra are reproduced in (b) vertically offset from one another. These spectra represent the different types which are typically found in a spectral-survey. They will be used to illustrate the peak picking algorithm in the subsequent figures.

(a) Run =159, File = 01104b03 pixels from 17,127 to 42,69, $V_{\text{set}} = -200$ mV, $I_{\text{set}} = 200$ pA

(b) Selected spectra at pixels (30,97); (31,94); (32,91); (33,89); (37,80)

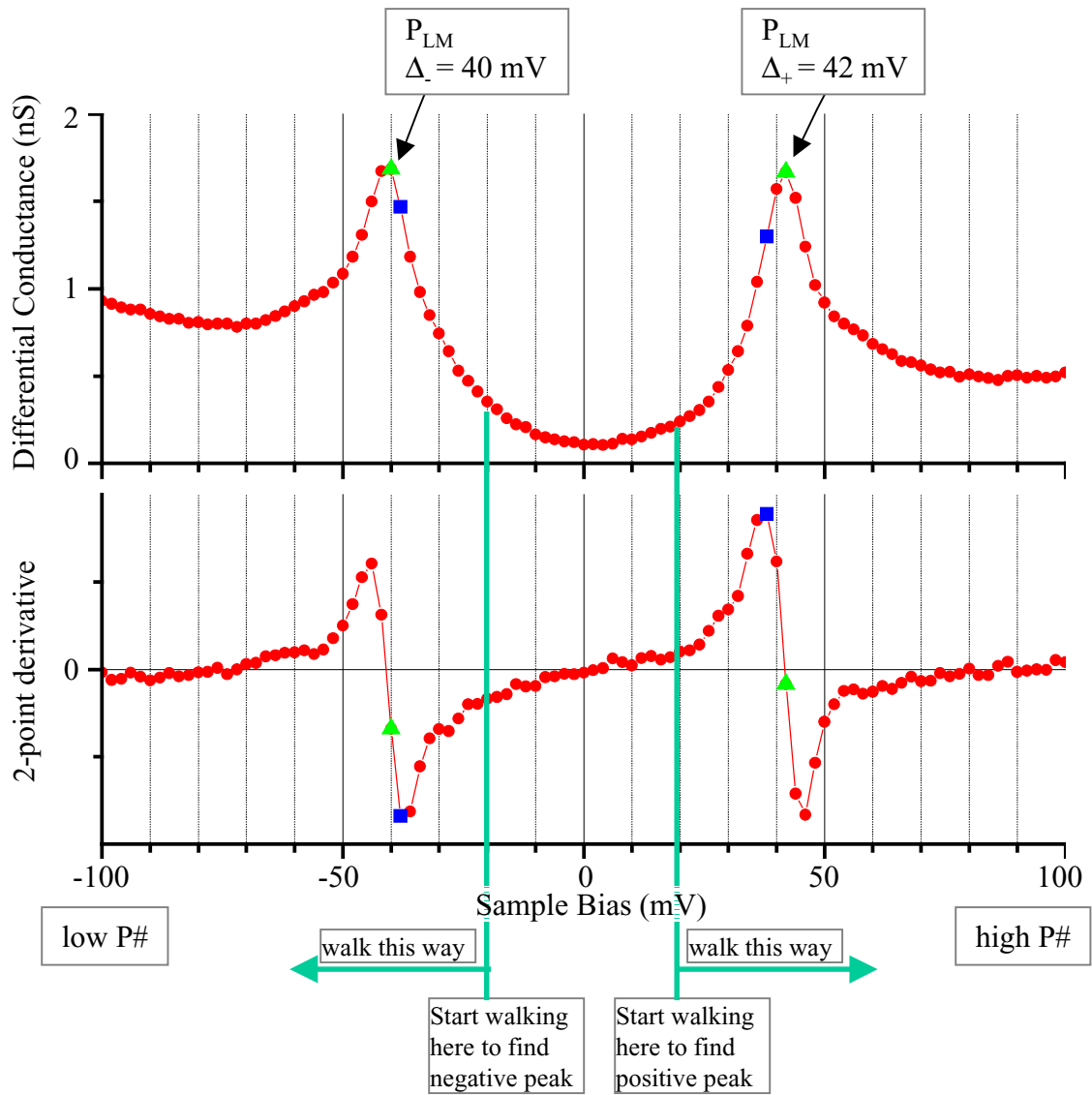


Figure A.2: Detailed illustration of algorithm using single spectrum. Spectrum #1 of Figure A.1 is reproduced here to demonstrate how the peak picking algorithm works for the large majority of spectra in a spectral-survey. The blue square indicates the point which meets the requirement that considering the point itself and four subsequent points, 3 out of 5 of these points show a $-/+$ derivative given $+/-$ sample bias. This point is called P_D in the text. The green triangle indicates the point (P_{LM}) which is the local maximum of the curve as found from walking out starting at P_D . In most cases the energetic value at P_{LM} determines Δ . In some cases, further processing is required as detailed in the text Section A.1 points 1.g & 1.h. Further processing is often necessary for spectra on boundaries between two regions (e.g. Spectrum # 4 from Figure A.3), for spectra showing impurity resonance peaks, or for NP type spectra (see Figure A.4).

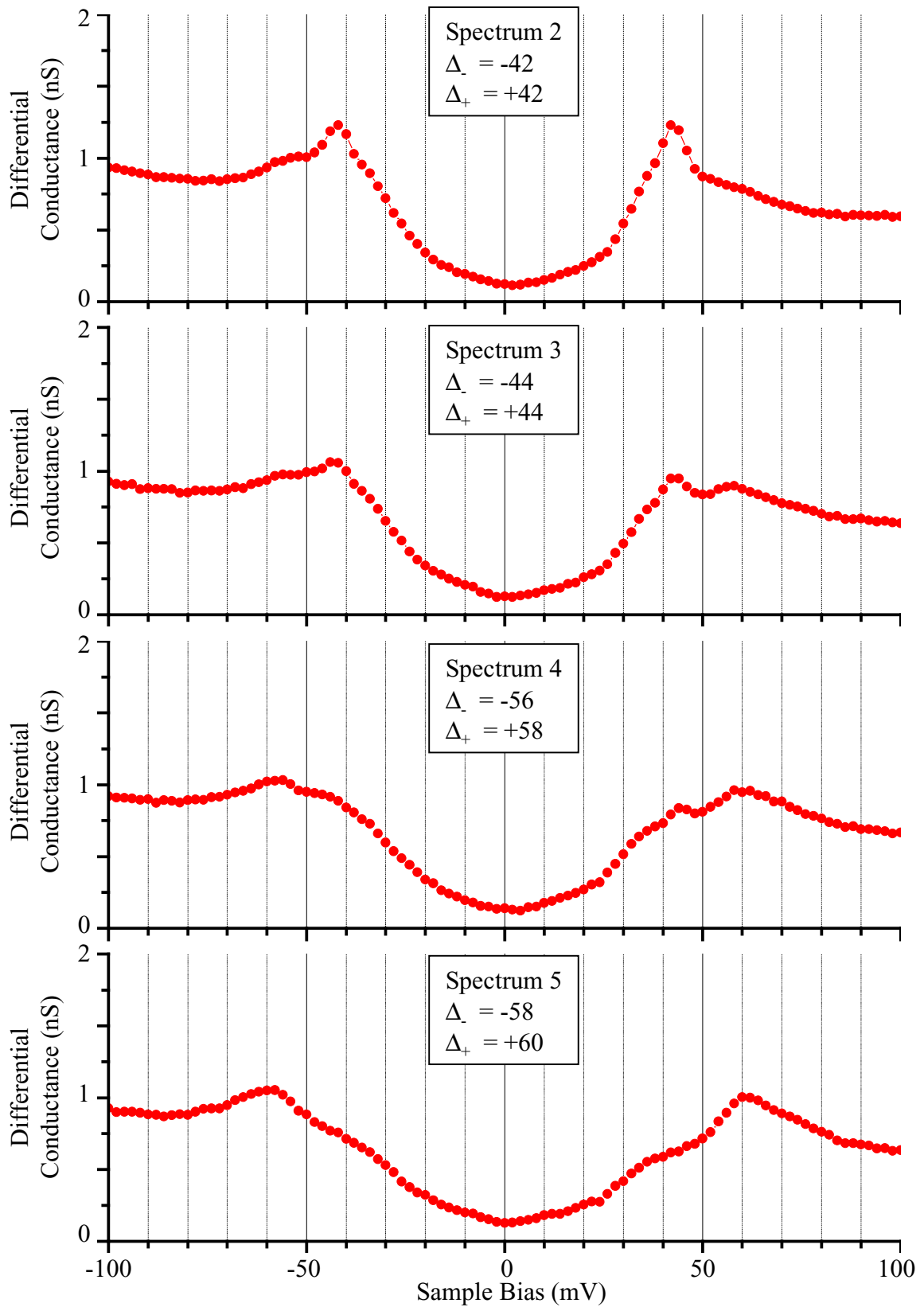


Figure A.3: Additional example spectra to demonstrate general functionality of algorithm. The spectrum numbers are the same as those of Figure A.1. The values of Δ_{\pm} in the box are those which were chosen by the peak picking algorithm.

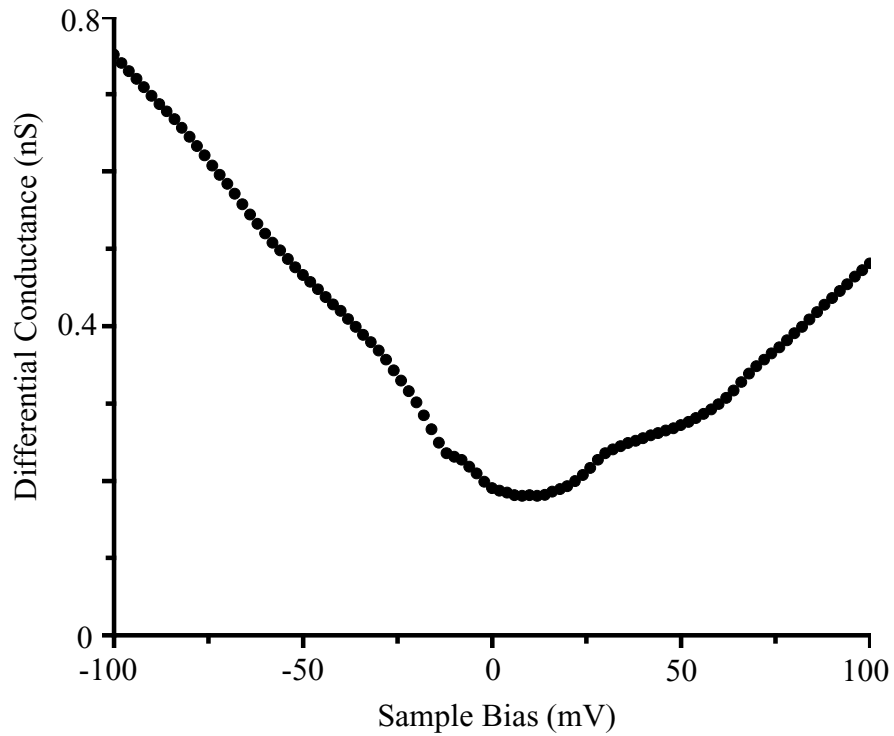


Figure A.4: Spectrum with no peaks to highest measured energy. This spectrum is an average of all the spectra measured inside the white box seen on Figure A.5. Such a spectrum, which has no peaks out to the highest measured energy (generally ± 100 - 150 meV), is found in about 1.5% of the measured areas for all fields of view and samples. Figure 3.9 presents an additional example of this spectrum which has been termed NP type. Given the relative infrequency of this type of spectrum, the peak picking algorithm assigns Δ to be the highest examined energy, as discussed in the text. This means that patches containing spectra such as this one will appear black on all Δ , $\nabla\Delta$, $A(\Delta)$, and $\nabla A(\Delta)$ maps for all color bars used in this thesis. These patches will also appear black on Σ maps and topographies due to the relatively lower integrated LDOS of these spectra.

Run = 159, File = 01103b02 avg all spectra in the box defined by pixels
 (51,98) & (75,122), $V_{\text{set}} = -100$ mV, $I_{\text{set}} = 100$ pA

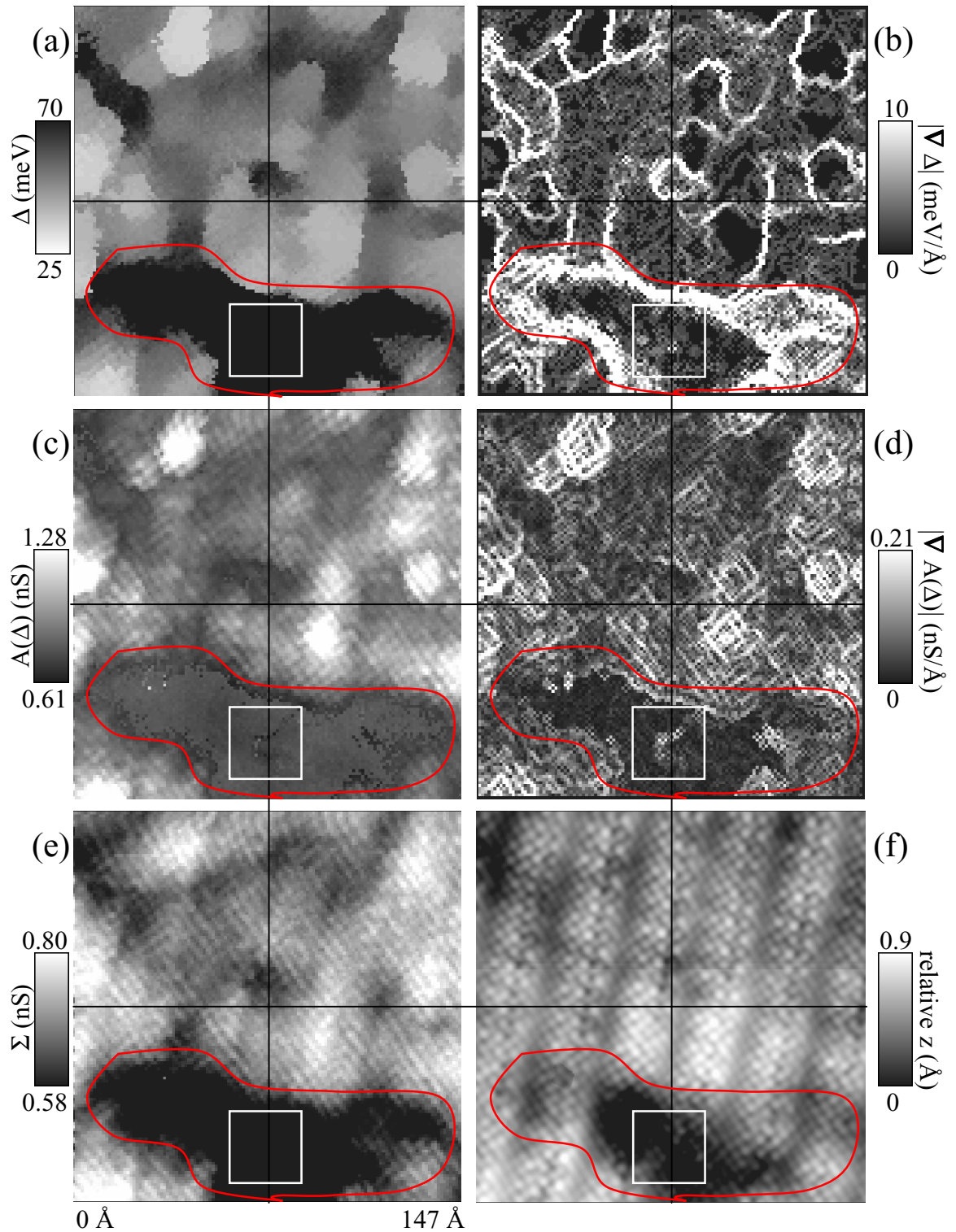


Figure A.5: Parameter maps showing a patch of NP type spectra. These parameter maps and topography, which are all of the same region, show a large black region, roughly outlined in red, which derives from NP type spectra. The average spectrum inside the white box is seen in Figure A.4.

Run = 159, File = 01103b02 & 01104a00, $V_{\text{set}} = -100$ mV, $I_{\text{set}} = 100$ pA

Appendix 2

Data Acquisition Parameters

This appendix details the explicit acquisition parameters for all data and samples presented in this thesis.

Material	$\text{Bi}_2\text{Sr}_2\text{CaCu}_2\text{O}_{8+\delta}$	
Composition	single crystal	
Fabrication method	floating-zone furnace	
Source	Uchida group, Tokyo University	
Oxygen doping	either as-grown or underdoped as stated. underdoped samples have $T_c = 79$ K as-grown doped samples are near optimal	
Timing of annealing	when the oxygen doping has been deliberately changed, such annealing has been done several weeks to months prior to study of the samples	
Surface prep	crystals are cold-cleaved in cryogenic UHV	
Direction of tunneling	c-axis	
Tip	etched W cleaned by field emission against an Au target	
Work function of tip	3 eV to 4 eV	
Ambient STM working environment		
	Vacuum	cryogenic UHV
	Temperature	4.2 K
	Magnetic field	0 T
Set point sample bias voltage	-100 mV to -200 mV as stated	
Set point current	10 pA to 200 pA as stated	
Normalization scheme	constant current. See Section 1.5.1 and 1.10.	

Bibliography

- Bardeen 1957** J. Bardeen, L.N. Cooper, and J.R. Schrieffer. Theory of superconductivity. *Physical Review* **108** (5), 1175-1204 (1957).
- Bardeen 1960** J. Bardeen. Tunneling from a many-body point of view. *Physical Review Letters* **6** (2), 57-59 (1960).
- Batlogg 2000** B. Batlogg and C. Varma. The underdoped phase of cuprate superconductors. *Physics World* **13** (2), 33-37 (2000).
- Bednorz 1986** J. G. Bednorz and K. A. Müller. Possible high- T_c superconductivity in the Ba-La-Cu-O system.. *Zeitschrift für Physik B* **64** (2), 189-193 (1986).
- Burgy 2001** J. Burgy, M. Mayr, V. Martin-Mayor, A. Moreo and E. Dagotto. Colossal Effects in Transition Metal Oxides Caused by Intrinsic Inhomogeneities. Preprint cond-mat/0107300 at <xxx.lanl.gov> (2001).
- Chakravarty 2001** S. Chakravarty, R.B. Laughlin, D.K. Morr, and C. Nayak. Hidden order in the cuprates. *Physical Review B* **63** (9), 094503/1-10 (2001).
- Chang 1992** A. Chang, Z.Y. Rong, Y.M Ivanchenko, F. Lu, and E.L. Wolf. Observation of large tunneling-conductance variations in direct mapping of the energy gap of single-crystal $\text{Bi}_2\text{Sr}_2\text{CaCu}_2\text{O}_{8-x}$. *Physical Review B* **46** (9), 5692-5698 (1992).
- Chen 1993** C. Julian Chen. *Introduction to Scanning Tunneling Microscopy*, Oxford University Press, New York (1993).
- Cren 2000** T. Cren, D. Roditchev, W. Sacks, J. Klein, J.-B. Moussy, C. Deville-Cavellin, and M. Laguës. Influence of Disorder on the Local Density of States in High- T_c Superconducting Thin Films. *Physical Review Letters* **84** (1), 147-150 (2000).
- Cren 2001** T. Cren, D. Roditchev, W. Sacks, and J. Klein. Nanometer scale mapping of the density of states in an inhomogenous superconductor. *Europhysics Letters* **54** (1), 84-90 (2001).

- Deutscher 1999** G. Deutscher. Coherence and single-particle excitations in the high-temperature superconductors. *Nature* **397** (6718), 410-412 (1999).
- Emery 1993** V.J. Emery and S.A. Kivelson. Frustrated Electronic Phase Separation and High Temperature Superconductors. *Physica C* **209** (4), 597-621 (1993).
- Emery 1999** V.J. Emery, S.A. Kivelson, and J.M. Tranquada. Stripe phases in high-temperature superconductors. *Proceedings of the National Academy of Sciences of the United States of America* **96** (16), 8814-8817 (1999).
- Feng 2000** D.L. Feng, D.H. Lu, K.M. Shen, C. Kim, H. Eisaki, A. Damascelli, R. Yoshizaki, J.-i. Shimoyama, K. Kishio, G.D. Gu, S. Oh, A. Andrus, J. O'Donnell, J.N. Eckstein, and Z.-X. Shen. Signature of Superfluid Density in the Single-Particle Excitation Spectrum of $\text{Bi}_2\text{Sr}_2\text{CaCu}_2\text{O}_{8+\delta}$. *Science* **289** (5477), 277-281 (2000).
- Fischer 1998** Ø. Fischer, Ch. Renner, and I. Maggio-Aprile. Scanning Tunneling Microscopy on High Temperature Superconductors in *The Gap Symmetry and Fluctuations in High- T_c Superconductors*, edited by J. Bok, G. Deutscher, D. Pavuna, and S.A. Wolf, pp. 487-502, Plenum Press, New York (1998).
- Fischer 2001** Private communication.
- Ghigna 1998** P. Ghigna, G. Spinolo, G. Flor, and N. Morgante. Correlation between hole density and oxygen excess in the $\text{Bi}_2\text{Sr}_2\text{CaCu}_2\text{O}_{8+\delta}$ superconductor. *Physical Review B* **57** (21), 13426-13429 (1998).
- Ghosal 2000** A. Ghosal, M. Randeria, and N. Trivedi. Inhomogeneous Pairing in Highly Disorderd s-wave Superconductors. Preprint cond-mat/0012304 at <xxx.lanl.gov> (2001).
- Ginzburg 1994** V.L. Ginzburg and E.A. Andryushin. *Superconductivity*, World Scientific, Singapore (1994).
- Howald 2001** C. Howald, P. Fournier, and A. Kapitulnik. Inherent Inhomogeneities in Tunneling Spectra of BSCCO Crystals in the Superconducting State. Preprint cond-mat/0101251 at <xxx.lanl.gov> (2001).

- Hudson 1999A** E.W. Hudson, S.H. Pan, A.K. Gupta, K.-W. Ng, and J.C. Davis. Atomic-Scale Quasi-Particle Scattering Resonances in $\text{Bi}_2\text{Sr}_2\text{CaCu}_2\text{O}_{8+\delta}$. *Science* **285** (5424), 88-91 (1999).
- Hudson 1999B** E.W. Hudson. Investigating High- T_c Superconductivity on the Atomic Scale by Scanning Tunneling Microscopy. Ph.D. Thesis, University of California, Berkeley, CA, USA (1999).
- Hudson 2001** E.W. Hudson, K.M. Lang, V. Madhavan, S.H. Pan, H. Eisaki, S. Uchida, and J.C. Davis. Interplay of magnetism and high- T_c superconductivity at individual Ni impurity atoms in $\text{Bi}_2\text{Sr}_2\text{CaCu}_2\text{O}_{8+\delta}$. *Nature* **411**, 920-924 (2001).
- Kaneko 1998** S. Kaneko, N. Nishida, K. Mochiku, and K. Kadowaki. Scanning tunneling spectroscopy of $\text{Bi}_2\text{Sr}_2\text{CaCu}_2\text{O}_{8+\delta}$. *Physica C* **298** (1-2), 105-114 (1998).
- Kirk 1988** M.D. Kirk, J. Nogami, A.A. Baski, D.B. Mitzi, A. Kapitulnik, T.H. Geballe, and C.F. Quate. The origin of the superstructure in $\text{Bi}_2\text{Sr}_2\text{CaCu}_2\text{O}_{8+\delta}$ as revealed by scanning tunneling microscopy. *Science* **242** (4886), 1673-1675 (1988).
- Lang 2001** K.M. Lang, V. Madhavan, J.E. Hoffman, E.W. Hudson, H. Eisaki, S. Uchida, and J.C. Davis. Imaging the granular structure of high- T_c superconductivity in underdoped $\text{Bi}_2\text{Sr}_2\text{CaCu}_2\text{O}_{8+\delta}$. *Nature* **415** (6870), 412-416 (2002).
- Lindberg 1989** P.A.P. Lindberg, Z.X. Shen, B.O. Wells, D. Dessau, D.B. Mitzi, I. Lindau, W.E. Spicer, and A. Kapitulnik. Reaction of Rb and oxygen overlayers with single crystalline $\text{Bi}_2\text{Sr}_2\text{CaCu}_2\text{O}_{8+\delta}$ superconductors. *Physical Review B* **39** (4), 2890-2893 (1989).
- Liu 1991** J.X. Liu, J.C. Wan, A.M. Goldman, Y.C. Chang, and P.Z. Jiang. Features of the Density of States of High- T_c Superconductors Probed by Vacuum Tunneling. *Physical Review Letters* **67** (16), 2195-2198 (1991).
- Liu 1994** J. Liu, Y. Li, and C. Lieber. Intrinsic features of $\text{Bi}_2\text{Sr}_2\text{CaCu}_2\text{O}_{8+\delta}$ tunneling spectra: Scaling and symmetry of the energy gap. *Physical Review B* **49** (9), 6234-6238 (1994).
- Maeda 1988** H. Maeda, Y. Tanaka, M. Fukutomi, and T. Asano. A new high- T_c oxide superconductor without a rare earth element. *Japanese Journal of Applied Physics Letters* **27** (2), L209-L210 (1988).

- Martin 2001** I. Martin and A.V. Balatsky. Doping-induced inhomogeneity in high- T_c superconductors. To appear in *Physica C* (2001). Also preprint cond-mat/0011252 at <xxx.lanl.gov> (2000).
- Merchant 2001** L. Merchant, J. Ostrick, R.P. Barber, Jr., and R.C. Dynes. Crossover from phase fluctuation to amplitude-dominated superconductivity: A model system. *Physical Review B* **63** (13), 134508/1-6 (2001).
- Miyakawa 1998** N. Miyakawa, P. Guptasarma, J.F. Zasadzinski, D.G. Hinks, and K.E. Gray. Strong Dependence of the Superconducting Gap on Oxygen Doping from Tunneling Measurements on $\text{Bi}_2\text{Sr}_2\text{CaCu}_2\text{O}_{8-\delta}$. *Physical Review Letters* **80** (1), 157-160 (1998).
- Miyakawa 1999** N. Miyakawa, J.F. Zasadzinski, L. Ozyuzer, P. Guptasarma, D.G. Hinks, C. Kendziora, and K.E. Gray. Predominantly Superconducting Origin of Large Energy Gaps in Underdoped $\text{Bi}_2\text{Sr}_2\text{CaCu}_2\text{O}_{8-\delta}$ from Tunneling Spectroscopy. *Physical Review Letters* **83** (5), 1018-1021 (1999).
- Nagamatsu 2001** J. Nagamatsu, N. Nakagawa, T. Muranaka, Y. Zenitani, and J. Akimitsu. Superconductivity at 39 K in magnesium diboride. *Nature* **410** (6824), 63-64 (2001).
- Nakano 1998** T. Nakano, N. Momono, M. Oda, and M. Ido. Correlation between the Doping Dependences of Superconducting Gap Magnitude $2\Delta_0$ and Pseudogap Temperature T^* in High- T_c Cuprates. *Journal of the Physical Society of Japan* **67** (8), 2622-2625 (1998).
- Onnes 1911** H. Kamerlingh Onnes. On the sudden change in the rate at which the resistance of mercury disappears. *Communications from the Physical Laboratory of the University of Leiden*, No. 124c (25 Nov 1911); H. Kamerlingh Onnes. *Akad.van Wetenschappen* **14** (113), 818.
- Orenstein 2000** J. Orenstein and A.J. Millis. Advances in the Physics of High-Temperature Superconductivity. *Science* **288** (5465), 468-474 (2000).
- Ovchinnikov 2001** Y.N. Ovchinnikov, S.A. Wolf, and V.Z. Kresin. Intrinsic inhomogeneities in superconductors and the pseudogap phenomenon. *Physical Review B* **63** (6), 064524/1-6 (2001).

- Pan 1993** S.H. Pan. International Patent Publication Number WO 93/19494, International Bureau, World Intellectual Property Organization, 30 Sept. 1993.
- Pan 1998** S.H. Pan, E.W. Hudson, J. Ma, and J.C. Davis. Imaging and identification of atomic planes of cleaved $\text{Bi}_2\text{Sr}_2\text{CaCu}_2\text{O}_{8+\delta}$ by high resolution scanning tunneling microscopy. *Applied Physics Letters* **73** (1), 58-60 (1998).
- Pan 1999** S.H. Pan, E.W. Hudson, and J.C. Davis. ^3He refrigerator based very low temperature scanning tunneling microscope. *Review of Scientific Instruments* **70** (2), 1459-1463 (1999).
- Pan 2000A** S.H. Pan, E.W. Hudson, K.M. Lang, H. Eisaki, S. Uchida, and J.C. Davis. Imaging the effects of individual zinc impurity atoms on superconductivity in $\text{Bi}_2\text{Sr}_2\text{CaCu}_2\text{O}_{8+\delta}$. *Nature* **403**, 746-750 (2000).
- Pan 2000B** S.H. Pan, E.W. Hudson, A.K. Gupta, K.-W. Ng, H. Eisaki, S. Uchida, and J.C. Davis. STM Studies of the Electronic Structure of Vortex Cores in $\text{Bi}_2\text{Sr}_2\text{CaCu}_2\text{O}_{8+\delta}$. *Physical Review Letters* **85** (7), 1536-1539 (2000).
- Pan 2001** S.H. Pan, J.P. O'Neal, R.L. Badzey, C. Chamon, H. Ding, J.R. Engelbrecht, Z. Wang, H. Eisaki, S. Uchida, A.K. Gupta, K.-W. Ng, E.W. Hudson, K.M. Lang, and J.C. Davis. Discovery of microscopic electronic inhomogeneity in the high- T_c superconductor $\text{Bi}_2\text{Sr}_2\text{CaCu}_2\text{O}_{8+x}$. To appear in *Nature* (2001).
- Renner 1994** Ch. Renner and Ø. Fischer. Non BCS IV characteristics of superconducting $\text{Bi}_2\text{Sr}_2\text{CaCu}_2\text{O}_{8+\delta}$ single crystals. *Physica C* **235-240** (1), 53-56 (1994).
- Renner 1995** Ch. Renner and Ø. Fischer. Vacuum tunneling spectroscopy and asymmetric density of states of $\text{Bi}_2\text{Sr}_2\text{CaCu}_2\text{O}_{8+\delta}$. *Physical Review B* **51** (14), 9208-9218 (1995).
- Renner 1998** Ch. Renner, B. Revaz, J.-Y. Genoud, K. Kadowaki, and Ø. Fischer. Pseudogap Precursor of the Superconducting Gap in Under- and Overdoped $\text{Bi}_2\text{Sr}_2\text{CaCu}_2\text{O}_{8+\delta}$. *Physical Review Letters* **80** (1), 149-152 (1998).
- Simon 1988** R. Simon and A. Smith. *Superconductors: Conquering Technology's New Frontier*, Plenum Press, New York (1988).

- Stroschio 1986** J.A. Stroschio, R.M. Feenstra, and A.P. Fein. Electronic structure of the Si(100)2x1 surface by scanning tunneling microscopy. *Physical Review Letters* **57** (20), 2579-2582 (1986).
- Subramanian 1988** M.A. Subramanian, C.C. Torardi, J.C. Calabrese, J. Gopalakrishnan, K.J. Morrissey, T.R. Askew, R. B. Flippen, U. Chowdhry, and A.W. Sleight. A New High-Temperature Superconductor: Bi₂Sr_{3-x}Ca_xCu₂O_{8+y}. *Science* **239** (4843), 1015-1017 (1988).
- Tallon 2001** J.L. Tallon and J.W. Loram. The doping dependence of T*- what is the real high-T_C phase diagram?. *Physica C* **349** (1-2), 53-68 (2001).
- Tersoff 1983** J. Tersoff and D.R. Hamann. Theory and Application for the Scanning Tunneling Microscope. *Physical Review Letters* **50** (25), 1998-2001 (1983).
- Tersoff 1985** J. Tersoff and D.R. Hamann. Theory of the scanning tunneling microscope. *Physical Review B* **31** (2), 805-813 (1985).
- Timusk 1999** T. Timusk and B. Statt. The pseudogap in high-temperature superconductors: an experimental survey. *Reports on Progress in Physics* **62** (1), 61-122 (1999).
- Wang 1990** C. Wang, B. Giambattista, C.G. Slough, R.V.Coleman, and M.A. Subramanian. Energy gaps measured by scanning tunneling microscopy. *Physical Review B* **42** (14), 8890-8906 (1990).
- Wang 2001A** Q.-H. Wang, J.H. Han, and D.-H. Lee. Pairing in the spin sector. Preprint.
- Wang 2001B** Z. Wang, J.R. Engelbrecht, S. Wang, H. Ding, and S.H. Pan. Inhomogeneous d-wave superconducting state of a doped Mott insulator. Preprint cond-mat/0107004 at <xxx.lanl.gov> (2001).
- Wolf 1994** E.L. Wolf, A. Chang, Z.Y. Rong, Y.M. Ivanchenko, and F. Lu. Direct STM Mapping of the Superconducting Energy Gap in Single Crystal Bi₂Sr₂CaCu₂O_{8+x}. *Journal of Superconductivity* **7** (2), 355-360 (1994).
- Wolf 1996** E.L. Wolf. Scanning tunneling spectroscopy of a superlattice superconductor: Bi₂Sr₂CaCu₂O₈. *Superlattices and Microstructures* **19** (4), 305-312 (1996).

- Wu 1991** X.L. Wu, Y.L. Wang, Z. Zhang, and C. Lieber. Electronic and structural effects of oxygen doping in $\text{Bi}_2\text{Sr}_2\text{CaCu}_2\text{O}_x$ superconductors characterized by tunneling microscopy. *Physical Review B* **43** (10), 8729-8732 (1991).
- Yamamoto 1990** A. Yamamoto, M. Onoda, E. Takayama-Muromachi, and F. Izumi. Rietveld analysis of the modulated structure in the superconducting oxide $\text{Bi}_2(\text{Sr,Ca})_3\text{Cu}_2\text{O}_{8+x}$. *Physical Review B* **42** (7), 4228-4239 (1990).
- Zhang 1993** Z. Zhang and C. Lieber. Measurement of the energy gap in oxygen-annealed $\text{Bi}_2\text{Sr}_2\text{CaCu}_2\text{O}_{8+\delta}$ high- T_c superconductors by tunneling spectroscopy. *Physical Review B* **47** (6), 3423-3426 (1993).

Glossary

2HS	class of spectrum which has two high sharp gap-edge peaks and is generally found in an α -domain. See Figure 3.8 for an example.
4HS	class of spectrum which has four high sharp gap-edge peaks and is generally found on the border between two α -domains. See Figure 3.8 and Figure 5.5 for examples.
2LB	class of spectrum which has two low broad gap-edge peaks and is generally found in a β -region. See Figure 3.8 for an example.
4LB	class of spectrum which has four low broad gap-edge peaks and is generally found on the border between an α -domain and a β -region. See Figure 3.8 and Figure 5.5 for examples.
4LB-HS	class of spectrum which has two high sharp gap-edge peaks and two low broad gap-edge peaks and which is generally found on the border between an α -domain and a β -region. See Figure 3.8 and Figure 5.5 for examples.
α - α boundary	the border γ -region which is found between two α -domains. See Table 5.2 and Figure 5.5.
α - β boundary	the border γ -region which is found between an α -domain and a β -region. See Table 5.2 and Figure 5.5.
α -domain	region characterized by a low constant value of Δ and gap-edge peaks which vary in height from low on the perimeter to high in the center of the grain. See Table 5.1.
Å	10^{-10} meters.
$A(\Delta)$	the height of the gap-edge peak. See Figure 1.13 and Section 1.8.2.
as grown [oxygen doping]	oxygen doping level which has not been deliberately altered by annealing. Generally crystals with as-grown doping are near optimally doped.
β -region	region characterized by a high variable value of Δ and gap-edge peaks which are constant. See Table 5.1.

BSCCO	$\text{Bi}_2\text{Sr}_2\text{CaCu}_2\text{O}_{8+\delta}$. Although there are other compounds with the same constitutive atomic species but different stoichiometry, in this thesis BSCCO is always taken to refer to the above stoichiometry. See Figure 1.6 for the structure.
Δ	half the size of the energetic region centered around the Fermi energy in which there is a depletion of states in a BSCCO LDOS spectrum. See Figure 1.13 and Section 1.8.1.
doping [-level]	always taken to refer to the fractional number of excess (not present in the undoped parent compound) holes. For BSCCO the number of holes is directly proportional to the number of non-stoichiometric oxygen atoms present, so in this case doping-level also refers to the number of these O atoms. Doping of anything else will be explicitly named, for example Zn-doping, impurity-doping, etc.
∇	gradient. See Section 1.9.2 for a definition.
gap	see Δ .
gapmap	plot which shows the magnitude of Δ for all points in a given planar region. See Section 1.9.1.
granularity	inhomogeneity plus the existence of regions within which spectral parameters such as the energy gap and the height of the gap-edge peak exhibit a common set of characteristics, which are distinct from the characteristics exhibited by neighboring regions. The distinct regions are termed <i>grains</i> and the material is termed <i>granular</i> . See Section P.4 and Chapter 5.
γ -region	region which forms the boundary between two grains. The spectra in this region typically have 4 or more peaks. Each set of two peaks corresponds to the peaks in a neighboring grain. See Section 5.1.3 for more information.
h	height of the structural features (e.g. atomic corrugation and supermodulation) above an arbitrary reference plane parallel to the sample surface. See Figure 1.2 and Figure 1.8 for a schematic definition.
HTSC	high temperature superconductor/superconductivity.
I_{set}	set point current. In constant current imaging, the current which the feedback system seeks for each x,y position. See Section 1.5.1.

inhomogeneity	the existence of spatial variation of the LDOS spectral parameters such as the energy gap and the height of the gap-edge peak. See Section P.4 and Chapter 3.
LDOS	local density of electronic states. This quantity is proportional to the differential conductance which is measured by STS. See Section 1.6 and 1.10.
linecut	series of spectra taken at discrete sequential positions as the tip is moved along a line on the sample surface. See Figure 1.12 and Section 1.7.3.
native	not having to do with impurities, grain boundaries, or other such non-essential perturbations
optimally-doped	having a doping-level such that $T_c = T_{cmax}$.
overdoped	having a higher oxygen dopant concentration than optimally-doped.
parameter	generic word for Δ , $A(\Delta)$, ∇ or Σ .
parameter map	plot which shows the magnitude of a spectral characteristic such as Δ , $A(\Delta)$, ∇ or Σ for all points in a given planar region. See Section 1.9.
$\Sigma(\Delta)$	integral of the area under a differential conductance curve for the energetic range near Δ . See Section 1.8.3 and Section 3.4.1.
$\Sigma(\leq \Delta)$	integral of the area under a differential conductance curve for only energies less than Δ . See Section 3.4.1.
$\Sigma(V_1, V_2)$	integral of the area under a differential conductance curve between the two specified voltages. See Figure 1.13 for a graphical definition. Also see Section 1.8.3 and Section 3.4.1.
s	distance between the end of the tip and the point on the sample surface which is directly beneath tip. Also called the tip-sample separation. See Figure 1.2 and Figure 1.8 for a schematic definition.
segregation	inhomogeneity and granularity plus the existence of a finite number of distinct grain-types such that each observed grain may be classified as one of these types. In this thesis, the types of grains observed in BSCCO are referred to as α , β and γ . See Section P.4 and Chapter 5.

set point current	see I_{set}
set point voltage	see V_{set}
spectral-survey	measurement of the differential conductance at all x,y positions within some area and at all energies within some range. Equivalently, taking a complete dI/dV spectrum for every position in a given field of view. See Figure 1.12 and Section 1.7.1.
spectral-parameter	generic word for Δ , $A(\Delta)$, ∇ or Σ .
spectrum	measurement of the differential conductance at a single x,y position for all voltages within a certain range. For this thesis generally the voltage range is ± 100 mV or ± 200 mV. See Figure 1.12 and Section 1.7.2.
STM	scanning tunneling microscope/microscopy.
STS	scanning tunneling spectroscopy. Measurement of the differential conductance as a function of tip-sample voltage for individual x,y points on the sample surface. See Section 1.6.
T_c	the critical temperature, the temperature below which the material superconducts.
$T_{c\text{max}}$	for a given material, the highest critical temperature which can be achieved.
tip	the metal wire held over the sample surface which forms a tunnel junction with the sample.
tip-sample separation	distance between the end of the tip and the point on the sample surface which is directly beneath tip. Also called s. See Figure 1.2 and Figure 1.8 for a schematic definition.
underdoped	having a lower oxygen dopant concentration than optimally-doped.
V	sample bias
V_{set}	set point voltage. In constant current topographic imaging, the voltage the tip is held at throughout the scan. See Section 1.5.1.
x,y	lateral position of the tip on the sample surface. See Figure 1.2 and Figure 1.8 for a schematic definition.

z

perpendicular distance between the tip and a given reference plane parallel to the sample surface. See Figure 1.2 and Figure 1.8 for a schematic definition.